DISSERTATION

submitted to the

Combined Faculty of Mathematics, Engineering and Natural Sciences

of the Ruperto-Carola University of Heidelberg, Germany

for the degree of

Doctor of Natural Sciences

put forward by

Viktoria Noel

Born in: Salgótarján, Hungary

Oral examination: 07-05-2025

Far-from-equilibrium universality and dynamics of nonequilibrium quantum many-body systems

Referees: Prof. Dr. Jürgen Berges

Prof. Dr. Tilman Enss

“True strength lies not in one’s power,
but in one’s way of being.”

—*Shadow*, in *The Eminence in Shadow*

Abstract

Far from equilibrium, quantum many-body systems can exhibit emergent structures and universal behaviour that require effective descriptions capturing their macroscopic dynamics. Such descriptions must identify the relevant degrees of freedom, emergent symmetries, and collective excitations that govern the long-time evolution of these systems. This thesis investigates how these features manifest in strongly correlated quantum field theories by extracting nonequilibrium symmetries and developing methods to characterise their universal scaling behaviour.

First, the restoration of symmetries in isolated quantum systems is examined. By deriving Ward identities for correlation functions, a method for extracting symmetries from experimental and numerical data is established. Applying this framework to ultracold atomic gases, it is demonstrated that explicitly broken symmetries are effectively restored long before thermalisation. The approach is also used to define spontaneous symmetry breaking in a nonequilibrium system.

Subsequently, the role of emergent quasiparticles and defect-driven dynamics is investigated in a single-component scalar field theory with a focus on their connection to nonthermal fixed points, which arise as attractor solutions with universal scaling behaviour. Through real-time lattice simulations, unequal-time correlation functions are extracted to identify the dominant infrared excitations, which are connected to Kelvin waves propagating along vortex lines. Beyond correlation functions, a geometric approach is introduced to study topological structures directly. Using tools from topological data analysis, robust, nonlocal observables are defined that capture the coarsening dynamics of topological defects. These observables exhibit a distinct scaling behaviour compared to traditional correlation functions, highlighting the multiscaling nature of universal dynamics near nonthermal fixed points.

Furthermore, the thesis explores the emergence of universal scaling behaviour in relativistic scalar field theories using an approach that goes beyond scaling analyses. By explicitly solving a self-consistent equation derived from the two-particle irreducible effective action, nonthermal scaling solutions are extracted. The results indicate a stationary transport regime characterised by a universal quadratic scaling.

Zusammenfassung

Außerhalb des Gleichgewichts können Quanten-Vielteilchensysteme emergente Strukturen und universelles Verhalten aufweisen, die eine effektive Beschreibung ihrer makroskopischen Dynamik erfordern. Eine solche Beschreibung muss die relevanten Freiheitsgrade, emergente Symmetrien und kollektive Anregungen identifizieren, die die langfristige Entwicklung dieser Systeme bestimmen. Diese Dissertation untersucht, wie sich diese Merkmale in stark korrelierten Quantenfeldtheorien manifestieren. Dazu extrahieren wir Symmetrien außerhalb des Gleichgewichts und entwickeln Methoden zur Charakterisierung universellen Skalierungsverhaltens.

Zunächst konzentrieren wir uns auf die Wiederherstellung von Symmetrien in isolierten Quantensystemen. Wir leiten Ward-Identitäten für Korrelationsfunktionen her und entwickeln daraus eine Methode, um Symmetrien aus experimentellen und numerischen Daten zu extrahieren. Die Anwendung dieses Ansatzes auf ultrakalte Atomgase zeigt, dass explizit gebrochene Symmetrien lange vor der vollständigen Thermalisierung des Systems effektiv wiederhergestellt werden. Zudem wird der Ansatz genutzt, um spontane Symmetriebrechung in einem Nichtgleichgewichtssystem zu definieren.

Anschließend untersuchen wir die Rolle emergenter Quasiteilchen und defektgetriebener Dynamik in einer skalaren Feldtheorie mit einer Komponente. Besonderes Augenmerk liegt auf der Verbindung zu nichtthermischen Fixpunkten, die als Attraktor-Lösungen mit universellem Skalierungsverhalten auftreten. Mittels Echtzeit-Gittersimulationen extrahieren wir Korrelationsfunktionen für verschiedene Zeitargumente, um die dominanten Infrarotanregungen zu identifizieren, die wiederum mit Kelvin-Wellen entlang von Vortexlinien zusammenhängen. Über die Untersuchung von Korrelationsfunktionen hinaus führen wir einen geometrischen Ansatz ein, um topologische Strukturen direkt zu analysieren. Mithilfe der topologischen Datenanalyse definieren wir robuste, nichtlokale Observablen, welche die Vergröberungsdynamik topologischer Defekte erfassen. Diese Observablen zeigen ein deutlich anderes Skalierungsverhalten als herkömmliche Korrelationsfunktionen und stellen die Multiskalennatur der universellen Dynamik in der Nähe nichtthermischer Fixpunkte deutlich heraus.

Abschließend untersucht diese Dissertation das Auftreten von universellem Skalierungsverhaltens in relativistischen skalaren Feldtheorien mit einem Ansatz, der über einfache Skalengesetze hinausgeht. Durch die explizite Lösung einer selbstkonsistenten Gleichung, die aus der zweiteilchen-irreduziblen effektiven Wirkung abgeleitet wird, bestimmen wir nichtthermische Skalierungslösungen. Die Ergebnisse deuten auf ein stationäres Transportregime hin, das durch eine universelle quadratische Skalierung charakterisiert ist.

List of publications

In this thesis, I present the findings of my research conducted throughout my doctoral studies, as detailed in the publications [1, 2] and preprint [3]:

[1] V. Noel, D. Spitz, *"Detecting defect dynamics in relativistic field theories far from equilibrium using topological data analysis"*, arXiv:2312.04959, Phys. Rev. D 109, 056011 (2024),

[2] A. N. Mikheev, V. Noel, I. Siovitz, H. Strobel, M. K. Oberthaler, J. Berges, *"Extracting the symmetries of nonequilibrium quantum many-body systems"*, arXiv:2407.17913, SciPost Phys. 18, 044 (2025),

[3] V. Noel, T. Gasenzer, K. Boguslavski, *"Kelvin waves in nonequilibrium universal dynamics of relativistic scalar field theories"*, arXiv:2503.01771.

Additionally, results are presented from the following ongoing work:

[4] V. Noel, A. N. Mikheev, C. Huang, J. Berges, *"Nonthermal scaling phenomena with the two-particle irreducible effective action"*.

For [1, 3], I took a leading role in the projects and contributed with many of the main ideas, performed all practical computations, and wrote large parts of the manuscripts. Ref. [2] was a collaborative project where I contributed with key ideas, developed and performed the framework for the data analysis presented, and wrote large parts of the published manuscript. In [4], I played a significant role in the development of the project and carried out the analytical computations, while the numerical analysis was a joint effort. During my doctoral studies, I was also involved in

[5] V. de Jonge, V. Noel, Jan M. Pawlowski, F. Sattler, *"Far-from-equilibrium universality in driven-dissipative scalar fields"*,

which is currently being prepared for a publication, and is not included in this thesis. This was the Master's degree project of V. de Jonge, for which I acted as a co-supervisor, providing technical guidance and contributing central ideas. The following manuscript was published as a preprint during my doctoral studies based on work I completed before starting my doctoral research, and is not part of this thesis:

[6] A. Molle, J. P. Drennhaus, V. Noel, N. Kolev, A. Bande, *"Time-resolved rubidium-assisted electron capture by Barium (II) cation"*, arXiv:2306.09580.

Contents

Chapter 1

Introduction and outline of thesis

The study of isolated nonequilibrium quantum many-body systems lies at the forefront of theoretical and experimental physics. Far from equilibrium, these systems can reveal extraordinary dynamics shaped by emergent symmetries, conservation laws, and universal scaling behaviour. A central challenge in the study of these systems lies in understanding how they evolve over time and approach equilibrium. In this context, one of the most pressing directions in quantum many-body physics is the search for effective theories that describe the emergent, macroscopic nonequilibrium dynamics at large scales and provide insight into how this behaviour arises from underlying microscopic laws. For isolated quantum systems evolving under unitary dynamics, equilibrium in the conventional sense cannot be reached globally, as the evolution preserves all information about the initial state. However, in general systems can exhibit an effective loss of detailed memory, with observables becoming indistinguishable from their corresponding equilibrium values over time [7–10]. There are intriguing scenarios in this setting that may occur on the way to thermalisation, such as quasi-stationary prethermalised states [11, 12], many-body oscillations [13] and revivals [14], and notably, in some cases thermalisation may be avoided altogether [15–18].

One of the important phenomena that can happen during the approach towards thermal equilibrium is given by *nonthermal fixed points*. These are nonequilibrium attractors characterised by universal self-similar scaling behaviour in time and space [19–22]. The approach to a nonthermal fixed point happens in far-from-equilibrium systems for a wide range of initial conditions on the way to thermal equilibrium, as illustrated in Fig. 1.1. Universality refers to the concept that seemingly distinct physical systems can display the same large-scale or macroscopic behaviour under certain conditions, despite having very different microscopic details. It allows connections to be drawn between phenomena that appear vastly different and span a wide range of energy scales. In the case of nonthermal fixed points, this includes experiments with ultracold atoms where they have been observed [21–27], heavy-ion collisions [28, 29], and early-universe cosmology [30, 31]. These systems offer a rich playground to explore fundamental questions about quantum dynamics, as explained in the following paragraphs, and far-from-equilibrium universality can provide a powerful tool to understand the otherwise complex relaxation dynamics of isolated quantum many-body systems.

Tabletop experiments using ultracold atomic gases can largely be isolated from the environment, making them suitable for the study of the dynamics of closed quantum systems.

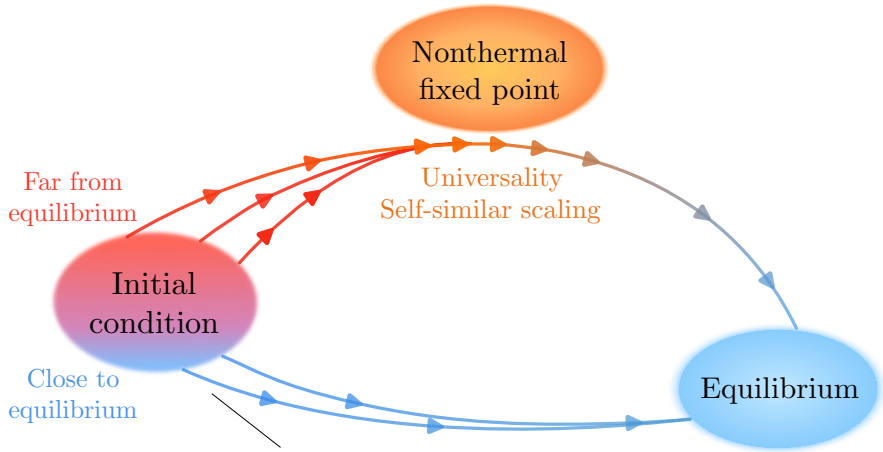

Figure 1.1. Illustration of various pathways towards thermal equilibrium: a system starting from a wide range of far-from-equilibrium initial conditions can approach a nonthermal fixed point on its path to equilibrium. In practice, this often involves extreme overoccupation initially. Near a nonthermal fixed point, the dynamics exhibits universal behaviour. When the initial conditions are near equilibrium, the system may directly evolve into the thermal state.

These platforms can realise a wide range of Hamiltonians with different symmetries, variable interactions, and degrees of freedom via atomic, molecular, and optical physics engineering [32, 33]. As a prominent example, ultracold Bose gases have been instrumental in researching fundamental phenomena such as thermalisation [34], spontaneous symmetry breaking [35, 36], and quantum phase transitions [37]. A well-studied case involves a *strong cooling quench* applied to a dilute Bose gas, where the system is rapidly cooled to temperatures near or below the Bose-Einstein condensation threshold [38]. This abrupt temperature drop brings the gas far from equilibrium, leading to highly populated states at low momenta as the particles condense into the lowest energy modes. Such an initial condition has allowed for the experimental study of the aforementioned universal scaling laws and the approach to nonthermal fixed points [21, 22], thus providing a versatile platform for exploring far-from-equilibrium dynamics and testing theoretical predictions in controlled experimental settings.

Within the realm of high-energy physics, ultrarelativistic heavy-ion collision experiments conducted at the Large Hadron Collider at CERN and the Relativistic Heavy Ion Collider at Brookhaven provide a crucial platform for probing the strong interaction, described by Quantum Chromodynamics, under extreme conditions reminiscent of the early universe. At sufficiently high temperatures, quarks and gluons, typically confined within hadrons like protons and neutrons, become deconfined to form the *quark–gluon plasma* (QGP). In the early stages of a collision, large gluon fields dominate the system. These fields are unstable and give rise to rapid plasma instabilities, leading to the amplification of fluctuations and the generation of highly occupied low-momentum modes [29]. This initially far-from-equilibrium state rapidly expands and undergoes a (cross-over) transition back to the hadronic phase before it can be directly detected, with strong experimental ev-

idence supporting the existence of the QGP [39–41]. Understanding the nonequilibrium evolution leading to QGP formation is crucial for interpreting its observable signatures. In this context, nonthermal fixed points have been demonstrated in longitudinally expanding non-Abelian plasmas [42], offering valuable insights into the universal dynamics during the initial stages of high-energy collisions.

There is a similar scenario in inflationary cosmology, which describes the exponential expansion of space in the very early universe [43, 44]. Inflation provides explanations for several key cosmological observations, such as the isotropy of the universe, the uniform distribution of the cosmic microwave background, and the flatness of space [45]. The exponentially fast expansion is often modelled by a slowly rolling scalar field called the *inflaton*. Following inflation, the universe continued expanding at a slower rate, with its entire energy density stored in a macroscopic inflaton field, representing a highly nonequilibrium state. In this subsequent phase, known as reheating, the inflaton field decayed into elementary particles, eventually creating the matter and radiation that form the universe we observe today [46]. In many models of reheating, an intermediate stage called preheating occurs, where the inflaton decays into scalar fluctuations and other particles through nonlinear processes [47]. During this stage, instabilities amplify long-wavelength modes, leading to an exponential growth of fluctuations, resulting in an overoccupied scalar system. Notably, nonthermal fixed points have also been identified in such overoccupied scalar fields [20, 48], revealing universal scaling behaviour and self-similar dynamics during the far-from-equilibrium evolution of the system.

The primary aim of this thesis is to advance the development of effective theories that describe the emergent macroscopic dynamics of isolated quantum many-body systems far from equilibrium. This is done by investigating *nonequilibrium symmetries* and their connection to thermalisation, exploring universality in systems far from equilibrium in the context of nonthermal fixed points, as well as nontrivial field configurations associated with topological defects. Nonequilibrium symmetries are studied in a spinor Bose gas using lattice simulations, in addition to experimental data with measurements from an *analogue quantum simulator* with ultracold atomic gases. The rest of the thesis investigates relativistic scalar fields, which are directly relevant for early universe cosmology in three spatial dimensions. Moreover, relativistic and nonrelativistic scalar fields have been shown to share a universality class [48], therefore, the results are also important for nonrelativistic scalar fields, for instance, in the description of Bose gases.

1.1 Symmetries of nonequilibrium quantum many-body systems

Symmetry principles play a central role in laying the foundation for the fundamental theories of modern physics. Its aspects are already present in the dynamical laws known from classical physics, in the form of Galilean invariance in Newton's laws of mechanics and Lorentz and gauge invariance in Maxwell's equations. Appreciating that symmetry principles are the fundamental features that constrain the allowable dynamics, Einstein formulated special relativity and later general relativity, where the principle of equivalence played a central

role. Building upon the significance of such principles, Noether discovered the important relation between the symmetries of a physical system and conservation laws: for every continuous symmetry, there exists a conserved charge [49]. If such a symmetry is preserved at the quantum level, it implies relationships between correlation functions, known as Ward–Takahashi identities [50, 51], often discussed in the context of quantum electrodynamics. The equivalent identities for non-Abelian theories are known as Slavnov–Taylor identities [52, 53].

Such symmetry constraints play an important role in understanding quantum field theories, where the framework of effective field theories has long been a powerful tool for describing the macroscopic behaviour of equilibrium many-body systems. In such systems, the symmetries of the underlying Hamiltonian or action, combined with the identification of the relevant order-parameter field, allow for the construction of consistent effective descriptions [54, 55]. However, in nonequilibrium scenarios, it becomes essential to distinguish between the symmetries of a state and those of the Hamiltonian. For instance, even simple nonequilibrium states with an order-parameter field not in their free-energy ground state can explicitly break a symmetry of the Hamiltonian. This distinction raises significant questions about the effective or emergent symmetries of nonequilibrium systems, including when and how explicitly broken symmetries may be dynamically restored. Addressing such questions requires quantifying the symmetry properties of nonequilibrium states, which is also a necessary step for deriving effective field theories. Recent investigations have explored dynamical symmetry restoration using methods based on entanglement asymmetry [56, 57] and single-body density matrices [58].

In this thesis, a general approach is outlined for determining the effective symmetries of nonequilibrium quantum many-body systems using correlation functions. These relations can be interpreted as nonequilibrium counterparts of Ward identities, which are particularly suitable for the analysis of measured or simulated data at different snapshots in time. Using a spinor Bose gas as an example, it is demonstrated that for an initial state that explicitly breaks the symmetry of the Hamiltonian governing the dynamics, effective symmetry restoration can occur long before thermalisation in an isolated system. While the full restoration of a symmetry explicitly broken by the initial state cannot fundamentally occur in closed quantum systems, it is shown that effective restoration can be observed at the level of lower-order correlation functions, akin to how local observables in thermalisation mimic equilibrium behaviour despite the underlying unitary evolution. These elements are essential for effective descriptions of nonequilibrium dynamics, often constructed using lower-order correlation functions, such as the Boltzmann equation for single-particle distribution functions derived from two-point correlations.

1.2 Nonthermal fixed points and universality far from equilibrium

The notion of universality refers to the fact that certain properties, like scaling exponents or amplitude ratios, remain the same across a broad range of systems, regardless of their specific dynamical details. We can group these systems into universality classes based on their

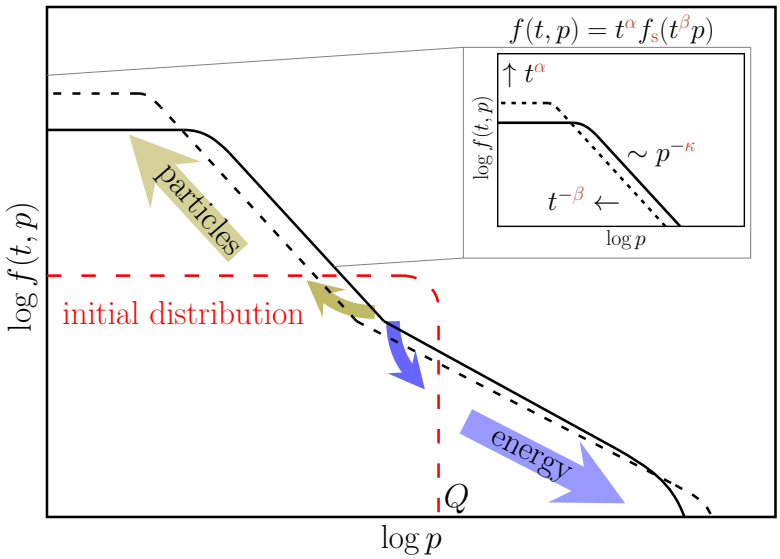

Figure 1.2. Distribution function $f(t,p)$ near a nonthermal fixed point, shown at two subsequent times (dashed later than solid). The scaling exponents α, β, and κ characterise the self-similar scaling, where particle number is transported towards the infrared, leading to a Bose-Einstein condensate, while energy is transported towards the ultraviolet. Figure adapted from [59].

behaviour near fixed points of renormalisation group flows. Near such a fixed point, scale invariance and the divergence of correlation length are observed, and while these systems can behave vastly different at finite scales, their behaviour will become increasingly similar as this fixed point is approached. The development of these ideas owes much to the pioneering work of researchers such as Widom, who formulated scaling laws that connect critical exponents [60], and Kadanoff, who introduced the concept of block spin transformations to explain scale invariance [61]. Wilson's renormalisation group theory provided a unifying framework for understanding universality, demonstrating how the microscopic details of a system become irrelevant near a critical point [62, 63]. These concepts have been instrumental in describing systems near a second-order phase transition, as summarised by the theory of dynamical critical phenomena [64]. Crucially, such universality classes describe systems close to thermal equilibrium and require fine-tuning of parameters to reach the fixed point.

Out of equilibrium, while a comprehensive framework for universality is yet to be established, universal scaling phenomena have been identified in a variety of contexts, including turbulence [65, 66], coarsening dynamics [67], ageing phenomena [68, 69], and driven-dissipative systems [70]. Universality classes have also been observed in far-from-equilibrium isolated systems in the context of nonthermal fixed points [20], which form nonequilibrium attractor solutions characterised by emergent universal self-similar scaling and the transport of conserved quantities. The approach to a nonthermal fixed point happens for a wide range of initial conditions on the way to thermal equilibrium, such that no fine-tuning is needed to reach it, as opposed to criticality in equilibrium systems.

Typically, to observe self-similar scaling behaviour, an initial state with extreme overoccupation is prepared up to some characteristic momentum scale, as depicted in Fig. 1.2,

along with the subsequent time evolution. For such an initial condition, the system quickly redistributes modes at early times, which is followed by the slowing down of the dynamics and the self-similar scaling regime. The latter is characterised by the emergence of a universal scaling function for the occupation number distribution function $f(t,p) = t^{\alpha} f_S\left(t^{\beta} p\right)$ with universal scaling exponents α and β that can be related to different conservation laws. Nonthermal fixed points are characterised by a dual cascade, where particle number is transported towards the infrared leading to a Bose-Einstein condensate, while energy is transported towards the ultraviolet. The universal properties are different for different inertial ranges: in the infrared, the exponents α, β and the scaling function f_S that characterise the particle transport do not agree with the exponents and scaling function in the energy cascade towards higher momenta. Much of this thesis focuses on the dynamics in the infrared regime, where large occupancies at low momenta result in strongly nonlinear dynamics despite a weak coupling, making standard perturbative approaches invalid. In such highly occupied systems, the quantum dynamics can be accurately mapped onto a *classical-statistical* theory [71], which can be solved using real-time lattice simulation techniques, providing a powerful nonperturbative approach. This method successfully described the particle transport in the strongly correlated regime at low momenta and the energy transport at higher momenta; however, at even higher momenta, where occupations are on the order of the *quantum half*, this approximation no longer works.

Another standard approach to studying the underlying dynamics is based on *kinetic theory*. In this context, a related phenomenon is *wave turbulence*, which shares features with the dynamics near nonthermal fixed points. Both phenomena involve the transport of conserved quantities across scales and can be analysed using kinetic equations. Wave turbulence can be understood in terms of transport processes across different scales by the presence of a source driving, for instance, energy into a system and a sink dissipating it [65, 66]. The scaling laws and exponents in stationary turbulence have been successfully described by approaches based on kinetic theory and Boltzmann-type equations. However, sources and sinks are absent in an isolated system. Instead of the occupation number $f(t,p)$ describing stationary transport, it evolves self-similarly in time, conserving particle number and energy across different momentum ranges [19, 48]. Notably, one of the standard approaches to studying scaling at nonthermal fixed points involves deriving evolution equations for the dynamics of correlation functions within a given model and analysing their scaling behaviour. On this basis, kinetic theory provides a framework for tracking the evolution of the distribution function $f(t,p)$ by accounting for different collision events [72]. This approach results in a Boltzmann-type equation, which has been particularly successful in explaining the observed scaling behaviour and exponents in both the perturbative regime characterised by weak wave turbulence and the nonperturbative regime associated with strong wave turbulence [48, 72–74].

More specifically, N-component scalar fields with quartic interactions provide a useful paradigm for the study of universality classes far from equilibrium. For such models, techniques like the large-N expansion can be used to yield *large-N kinetic theory*. The analytic derivation of scaling exponents related to nonthermal fixed points gives $\beta = 0.5$ and $\alpha = d\beta$, up to a potential *anomalous dimension* η [48, 73]. The exponents $\beta \approx 0.55$ and $\alpha \approx d\beta$ have been successfully found in numerical simulations with a remarkable in-

sensitivity to the number of field components, including even at low N [48]. In fact, the corresponding universality classes appear to be surprisingly large; for instance, relativistic and nonrelativistic scalar fields for any number of field components N form a universality class [48], and gauge and scalar fields have been found to form another one [75, 76].

However, the scaling analysis based on large-N kinetic theory leads to integer or rational scaling exponents when assuming an anomalous dimension of $\eta = 0$. Without this assumption, the approach does not predict a specific value for η, which, if nonzero, is expected to be small, as numerical results remain close to $\beta = 0.5$. This raises the question of whether such approaches fully capture the range of possible scaling behaviours at nonthermal fixed points. Numerical simulations, including real-time classical-statistical simulations, provide an alternative means of investigating these systems by tracking their evolution from an initially highly occupied state towards a nonthermal fixed point, where self-similar scaling emerges dynamically. However, these methods also have limitations in extracting scaling properties, as the results can depend on numerical implementation details, show sensitivity to initial conditions, and are affected by uncertainties in self-similar fitting procedures. The existing methods also focus on attractor solutions, where the system dynamically approaches a self-similar scaling regime, further raising the question of whether the full range of possible scaling behaviours is captured. Therefore, there is a need for alternative approaches that not only refine the precision of scaling exponent extraction but also extend the study of nonthermal scaling beyond conventional attractor solutions.

This thesis presents an approach conceptually similar to large-N kinetic theory for relativistic scalar fields with O(N) symmetry in three dimensions, but extending significantly beyond previous scaling analyses. Explicit calculations are carried out to obtain scaling solutions to self-consistent equations derived from effective actions. The method is first validated against known analytic solutions at the critical point for scalar fields undergoing a second-order phase transition, and subsequently, it is used to extract scaling solutions in nonequilibrium dynamics. The results indicate a stationary transport regime characterised by a universal quadratic scaling, offering valuable insights into strong-wave turbulence.

1.2.1 Nontrivial field configurations

Another related phenomenon to nonthermal fixed points is coarsening and *phase-ordering kinetics* [67], which describes the growth of order through coarsening dynamics when a system is quenched across a phase transition. In this process, the evolution of the order parameter is governed by the dynamics of domains and topological defects, which grow, merge, or decay over time. The associated scaling exponents and functions depend on the structure of the order parameter and the nature of the topological defects. The formation of a Bose-Einstein condensate via the inverse particle cascade near a nonthermal fixed point bears a strong resemblance to this kind of physics, where topological defects might be created following the initial quench. Throughout this process, particles are gradually transferred to low-momentum modes, ultimately building a condensate at zero momentum. However, causality imposes a limit on the rate at which information and correlations can propagate, preventing the instantaneous formation of a uniform condensate. Therefore, the condensate initially lacks long-range order, which it will gradually develop through ordering dynam-

ics. In fact, topological defects have been shown, in certain cases, to provide an effective framework for understanding the dynamics close to a nonthermal fixed point [77–79].

For relativistic O(N) theories, a number of different, N-dependent topological defects are expected to contribute to the dynamics in the infrared, including vortices for $N = 1, 2, 3$, domain walls for $N = 2$ and monopoles for $N = 4$ [80]. As highlighted in the previous section, however, it was found that the scaling dynamics and the scaling exponents, even for low N, are consistent with the large-N limit predicted from large-N kinetic theory, which assumes elastic collisions of quasiparticles with free dispersion, a result further corroborated by numerical simulations. While the large-N description works remarkably well, it remains unclear why its predictions should hold for the scaling behaviour and exponents at low N, especially given the N-dependent topological defects. However, the study of far-from-equilibrium universality in isolated systems has mostly been focused on properties of the distribution function $f(t, p)$ of particles with momentum p at time t, which might not be particularly sensitive to topological features. Hence, there is a need for topologically sensitive and computationally accessible observables in order to investigate the connection between nonthermal fixed points and coarsening dynamics more thoroughly.

In this work, two distinct approaches are employed to address this. First, *unequal time correlation functions* are investigated to study the different excitations in relativistic scalar fields at low N. The previously studied *equal-time* distribution function, defined based on $f(t, p) = \langle a_p^\dagger(t) a_p(t) \rangle$ where $a_p^\dagger(t)$ and $a_p(t)$ are the usual creation and annihilation operators,[1] can provide valuable insights into the underlying dynamics of scattering processes between quasiparticles. However, this particle picture is only well understood in the large-N limit. Previous works have shown that for $N = 1$, the dominant quasiparticle in the infrared regime differs significantly from the one assumed in large-N theories [81, 82]. This raises the question of what the relevant degrees of freedom are for O(1) and U(1) scalar fields. Identifying these is a crucial step towards constructing a low-energy effective theory that captures their macroscopic dynamics and would complement existing large-N descriptions. While $f(t, p)$ reflects the momentum dependence of excitations, unequal-time correlations provide additional information by resolving their frequency dependence, making it possible to distinguish between different excitations in the system. This thesis demonstrates that the dominant quasiparticle can be understood as excitations arising from vortex interactions for $N = 1$.

Subsequently, topologically sensitive observables are defined using *persistent homology*, the main toolbox from *topological data analysis* (TDA) [83, 84]. These can provide complementary information to correlation functions by giving access to the topology of the data on the lattice obtained from numerical simulations. Observables based on TDA offer a versatile and nonlocal approach for probing mechanisms and signatures of collective quantum field-theoretic phenomena, with robust mathematical properties such as stability under data perturbations [85] and ergodicity [86]. This approach allows for a deeper understanding of the emergent structures in nonequilibrium dynamics and offers a novel perspective on the

[1] In a nonequilibrium interacting theory, the interpretation of the same object is more subtle in terms of the total number of (quasi)particles, however, even in the nonperturbative highly occupied regime, the distribution function can be well-defined in terms of simple correlation functions, which has been successfully used to characterise the system [81].

role of topology in far-from-equilibrium quantum systems. The observables defined based on persistent homology reveal universal scaling exponents and dynamics that are driven by vortex defects with the exponent $\beta_{\mathrm{L}} \approx 0.2$ for $N = 1, 2$ and $\beta_{\mathrm{L}} \approx 0.4$ for $N = 3$ in relativistic scalar fields. These are distinct from the usual $\beta = 0.5$, which characterises the scaling of the distribution function $f(t, p)$. This indicates the presence of multiscaling phenomena, where distinct observables constructed from the same data set are sensitive to different underlying physical processes. These results emphasise the importance of topologically sensitive observables for uncovering subdominant defect dynamics in universal regimes far from equilibrium, particularly in three-dimensional systems where such dynamics may be suppressed in overoccupied scenarios.

1.3 Outline of thesis

This thesis is divided into seven chapters. Here, a brief outline is given for each chapter.

Chapter 2 introduces the foundational tools of nonequilibrium quantum field theory that are employed in the study of the dynamics of quantum systems later in this work. This includes the classical-statistical approximation and functional field-theoretic methods, along with further approximations it can be combined with.

Chapter 3 explores the role of effective symmetries in nonequilibrium quantum many-body systems. The symmetry restoration of explicitly broken symmetries is investigated and compared with thermalisation time scales. It is found that effectively, symmetries are restored long before equilibration in an isolated system on the level of lower-order correlation functions, with higher-order ones retaining memory of the initial condition. The approach is also used to identify spontaneous symmetry breaking far from equilibrium, which is of great relevance for applications to nonequilibrium phase transitions.

Chapter 4 examines the different degrees of freedom that could play a role in the relevant low-energy effective theory of the universal dynamics in far-from-equilibrium $\mathrm{O}(1)$ scalar theories. The primary quasiparticle excitations are associated with vortex defects and their dynamics. These excitations are identified as Kelvin waves, or kelvons, in three dimensions, which are quantised helical perturbations propagating along vortex strings. In two dimensions, similar vortex-boundary excitations are conjectured alongside phonons generated through vortex-antivortex annihilation.

Chapter 5 studies the influence of topological defects on universal scaling far from equilibrium, with a focus on the dynamics of defect-driven coarsening. This is done by defining observables based on persistent homology, which provide complementary information to well-known correlation functions. These observables reveal a different scaling behaviour from that of correlation functions, confirming the existence of multiple scaling phenomena coexisting in the vicinity of nonthermal fixed points.

Chapter 6 explores universal scaling behaviour in relativistic $\mathrm{O}(N)$ scalar field theories, going beyond the standard scaling analyses typically employed in kinetic theory. The approach relies on explicitly solving a self-consistent equation and evaluating self-energy integrals. The numerical approach presented is benchmarked using existing analytic solutions for equilibrium critical behaviour, after which it is used to extract scaling solutions for

nonthermal phenomena. The results provide valuable insights into stationary nonequilibrium dynamics, particularly in the context of strong-wave turbulence.

Chapter 7 provides a conclusion where the results are discussed, and an outlook is given for possible future directions.

Chapter 2

Functional methods in nonequilibrium quantum field theory

In this chapter, the main tools and techniques used in the study of nonequilibrium quantum fields are discussed that will be used in the subsequent chapters. The description is largely based on the lecture notes [87], titled *Nonequilibrium Quantum Fields: From Cold Atoms to Cosmology*, where more details can be found. First, the functional integral representation of nonequilibrium quantum fields is introduced, followed by the classical-statistical approximation, which is a useful method to study the dynamics of quantum fields in the regime of large occupations. Afterwards, effective actions are considered, with an emphasis on the two-particle irreducible (2PI) effective action. In the context of the 2PI formalism, the large-N expansion is also discussed as a powerful nonperturbative approximation scheme. The focus will be on scalar field theories with quartic self-interactions, which are used as a paradigm for understanding far-from-equilibrium dynamics in most chapters of this thesis.

2.1 Nonequilibrium quantum fields

Nonequilibrium quantum systems can be described by specifying an *initial condition* at some time t_0, typically represented via a *density operator* $\hat{\rho}\,(t_0) \equiv \hat{\rho}_0$, whose time evolution is given by the operator $U(t, t_0)$. Equivalently, the initial state can be specified by providing all initial *correlation functions*; e.g., the one-point function $\mathrm{Tr}\,\{\hat{\rho}_0 \hat{\varphi}\,(t_0, \mathbf{x})\}$, the two-point function $\mathrm{Tr}\,\{\hat{\rho}_0 \hat{\varphi}\,(t_0, \mathbf{x})\,\hat{\varphi}\,(t_0, \mathbf{y})\}$, and all higher n-point functions, where $\hat{\varphi}\,(t_0, \mathbf{x})$ represents a real, bosonic scalar field operator at a spacetime point $(t_0, \mathbf{x})$. Lower-order correlation functions are often sufficient to approximate the initial state, and higher-order correlators tend to build up during the system's subsequent evolution $t > t_0$. This approximation is equivalent to assuming the density operator $\hat{\rho}_0$ is Gaussian when the description is restricted to only the one- and two-point functions. Once the initial state is specified, the time-evolution of an isolated quantum system is unitary and fully determined by its Hamiltonian. This evolution can then be reformulated on a closed time contour in the path integral formalism, as detailed in the following.

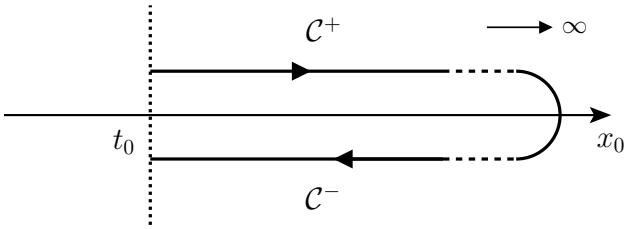

Figure 2.1. The Schwinger-Keldysh contour on a closed time path.

2.1.1 Functional integral representation of quantum fields

Computing observables is a crucial step for any theory since they provide measurable quantities that connect theoretical predictions with experimental results. Considering the above density matrix $\hat{\rho}_0$ at the initial time t_0 with the time evolution operator $U(t, t_0)$, in the Heisenberg picture, the expectation value of an *observable* is given by

$$\langle \hat{O}(t) \rangle = \mathrm{Tr} \left\{ \hat{\rho}_0 U\left(t_0, t\right) \hat{O} U\left(t, t_0\right) \right\}, \tag{2.1}$$

where $\hat{O}(t)$ is some local operator corresponding to an observable quantity and is time-dependent, while the density matrix in this picture is time-independent. We can see that the initial density matrix is evolved forward in time by $U(t, t_0)$ and then back in time by $U(t_0, t)$, acted upon by the observable $\hat{O}$ and finally traced over. Thus, the dynamical evolution of the system generally involves the evolution of the density matrix in both forward and backward time directions. This can be naturally described by the *Schwinger-Keldysh contour* [88, 89], as illustrated in Fig. 2.1 by the symbol $\mathcal{C}$, which is a closed contour in the complex time plane. It consists of two branches, $\mathcal{C}^+$ and $\mathcal{C}^-$, corresponding to the forward and backward time evolution, respectively. This description is particularly useful for nonequilibrium systems, as it is not restricted to computations of scattering matrix elements of asymptotic states, and at the same time, it also allows for the study of vacuum as well as thermal field theory.

Any quantum system can be completely described by the knowledge of all correlation functions, which are represented as the trace over time-dependent Heisenberg field operators for a given density matrix $\hat{\rho}_0$. Since observables are often computed from correlation functions, accurately determining these is an important step. The *generating functional* of correlation functions contains all information about the quantum system and is given by

$$Z\left[J; \hat{\rho}_0\right] = \mathrm{Tr} \left\{ \hat{\rho}_0 \mathcal{T}_{\mathcal{C}} \exp\left(\mathrm{i} \int_{x,\mathcal{C}} J(x) \hat{\varphi}(x) \right) \right\}, \tag{2.2}$$

which is the generalisation of the *partition function* for nonequilibrium systems in the presence of the source term $J(x)$, with the normalisation $\mathrm{Tr}\{\hat{\rho}_0\} = 1$. Here, $\mathcal{T}_{\mathcal{C}}$ is the time-ordering operator, which arranges field operators according to their time arguments (from right to left in increasing time), along the $\mathcal{C}^+$ branch, and reversed ordering along the $\mathcal{C}^-$ part. This can be rewritten as a path integral using the eigenstates of the Heisenberg operator $\hat{\varphi}(x)$, i.e. $\hat{\varphi}(x)|\varphi\rangle = \varphi(x)|\varphi\rangle$. The standard procedure divides the time interval into infinitesimally small chunks and a complete set of coherent states are inserted between the slices. In this case, it is useful to write $\varphi(x) = \varphi^{\pm}(x)$ if $x_0 \in \mathcal{C}^{\pm}$, as one needs to indicate if

the coherent state belongs to a forward or backward branch on the Schwinger-Keldysh contour. Therefore, at the reference time t_0, the eigenstates of the field operator can be defined as

$$\hat{\varphi}^{\pm}\left(t_0, \mathbf{x}\right)\left|\varphi^{\pm}\right\rangle = \varphi_0^{\pm}(\mathbf{x})\left|\varphi^{\pm}\right\rangle. \tag{2.3}$$

The generating functional can then be equivalently written as

$$Z\left[J;\hat{\rho}_0\right] = \int \left[d\varphi_0^{+}\right]\left\langle\varphi^{+}\right|\hat{\rho}_0\mathcal{T}_{\mathcal{C}}\exp\left[\mathrm{i}\int_{x,\mathcal{C}} J(x)\hat{\varphi}(x)\right]\left|\varphi^{+}\right\rangle, \tag{2.4}$$

with the integration measure

$$\left[d\varphi_0^{\pm}\right] \equiv \prod_{\mathbf{x}} d\varphi_0^{\pm}(\mathbf{x}). \tag{2.5}$$

Using the insertion

$$\int \left[\mathrm{d}\varphi_0^{-}\right]\left|\varphi^{-}\right\rangle\left\langle\varphi^{-}\right| = \mathbb{1}, \tag{2.6}$$

one obtains

$$Z\left[J;\hat{\rho}_0\right] = \int \left[d\varphi_0^{+}\right]\left[d\varphi_0^{-}\right]\left\langle\varphi^{+}\right|\hat{\rho}_0\left|\varphi^{-}\right\rangle\left(\varphi^{-}, t_0 \mid \varphi^{+}, t_0\right)_J. \tag{2.7}$$

The quantity given by

$$\left(\varphi^{-}, t_0 \mid \varphi^{+}, t_0\right)_J = \left\langle\varphi^{-}\right|\mathcal{T}_{\mathcal{C}}\exp\left[\mathrm{i}\int_{x,\mathcal{C}} J(x)\hat{\varphi}(x)\right]\left|\varphi^{+}\right\rangle \tag{2.8}$$

is the transition amplitude in the presence of the source J. Similarly to the standard vacuum quantum field theory, this can be also written as a functional integral over *classical* fields $\varphi(x)$ with the classical action $S[\varphi]$ as

$$\left(\varphi^{-}, t_0 \mid \varphi^{+}, t_0\right)_J = \int_{\varphi_0^{+}}^{\varphi_0^{-}} \mathcal{D}'\varphi\exp\left[\mathrm{i}S[\varphi] + \mathrm{i}\int_{x,\mathcal{C}} J(x)\varphi(x)\right]. \tag{2.9}$$

The classical action is given by integrating over the respective Lagrangian density $\mathcal{L}(x)$, i.e. $S = \int_{\mathcal{C}} \mathrm{d}x^0 \int \mathrm{d}^d x\mathcal{L}(x)$. The path integral goes over the field configurations $\varphi(x)$ depending on space and times $x^0 > t_0$ that satisfy the boundary conditions $\varphi^{\pm}\left(x^0 = t_0, \mathbf{x}\right) = \varphi_0^{\pm}(\mathbf{x})$ for x^0 on $\mathcal{C}^{\pm}$. The prime on $\mathcal{D}'\varphi$ indicates that the integration over the fields at $x^0 = t_0$ is excluded. Bringing everything together, the path integral representation of the generating functional can be written as

$$Z\left[J;\hat{\rho}_0\right] = \underbrace{\int \left[d\varphi_0^{+}\right]\left[d\varphi_0^{-}\right]\left\langle\varphi^{+}\right|\hat{\rho}_0\left|\varphi^{-}\right\rangle}_{\text{initial conditions}}\underbrace{\int_{\varphi_0^{+}}^{\varphi_0^{-}} \mathcal{D}'\varphi\mathrm{e}^{\mathrm{i}\left\{S[\varphi]+\int_{x,\mathcal{C}} J(x)\varphi(x)\right\}}}_{\text{quantum dynamics}}. \tag{2.10}$$

The above expression highlights two key components of nonequilibrium quantum field theory: quantum fluctuations, represented by the functional integral over the action $S[\varphi]$, and statistical fluctuations, captured through the averaging process involving the matrix elements of the initial density operator $\hat{\rho}_0$.

Regarding initial conditions, in general, a density matrix is given by

$$\left\langle \varphi^{+}\right| \hat{\rho}_{0} \left|\varphi^{-}\right\rangle = \mathcal{N} \mathrm{e}^{\mathrm{i}h_{c}[\varphi]}, \tag{2.11}$$

with normalisation $\mathcal{N}$ and $h_{\mathcal{C}}[\varphi]$ expanded in terms of the fields

$$\begin{aligned} h_{\mathcal{C}}[\varphi] =& \alpha_{0} + \int_{x,\mathcal{C}} \alpha_{1}(x)\varphi(x) + \frac{1}{2}\int_{xy,\mathcal{C}} \alpha_{2}(x,y)\varphi(x)\varphi(y) \\ &+ \frac{1}{3!}\int_{xyz,\mathcal{C}} \alpha_{3}(x,y,z)\varphi(x)\varphi(y)\varphi(z) \\ &+ \frac{1}{4!}\int_{xyzw,\mathcal{C}} \alpha_{4}(x,y,z,w)\varphi(x)\varphi(y)\varphi(z)\varphi(w) + \ldots \end{aligned} \tag{2.12}$$

and coefficients α_n. The integrals are evaluated along the forward branch $\mathcal{C}^+$ and the backward branch $\mathcal{C}^-$ of the closed time path with $\varphi^{+}\left(t_{0}, \mathbf{x}\right) = \varphi_{0}^{+}(\mathbf{x})$ and $\varphi^{-}\left(t_{0}, \mathbf{x}\right) = \varphi_{0}^{-}(\mathbf{x})$. Since the density matrix is specified at the initial time t_0 only, the time integrals only contribute at the endpoints of the contour, and therefore the coefficients $\alpha_1(x), \alpha_2(x,y), \alpha_3(x,y,z)$ vanish for $t \neq t_0$, such that

$$\int_{x,\mathcal{C}} \alpha_{1}(x)\varphi(x) \equiv \int \mathrm{d}^{d}x \left\{\alpha_{1}^{+}(\mathbf{x})\varphi_{0}^{+}(\mathbf{x}) + \alpha_{1}^{-}(\mathbf{x})\varphi_{0}^{-}(\mathbf{x})\right\}, \tag{2.13}$$

$$\begin{aligned} \int_{xy,\mathcal{C}} \alpha_{2}(x,y)\varphi(x)\varphi(y) \equiv \int \mathrm{d}^{d}x\, \mathrm{d}^{d}y \{&\alpha_{2}^{++}(\mathbf{x},\mathbf{y})\varphi_{0}^{+}(\mathbf{x})\varphi_{0}^{+}(\mathbf{y}) + \alpha_{2}^{+-}(\mathbf{x},\mathbf{y})\varphi_{0}^{+}(\mathbf{x})\varphi_{0}^{-}(\mathbf{y}) \\ &+ \alpha_{2}^{-+}(\mathbf{x},\mathbf{y})\varphi_{0}^{-}(\mathbf{x})\varphi_{0}^{+}(\mathbf{y}) + \alpha_{2}^{--}(\mathbf{x},\mathbf{y})\varphi_{0}^{-}(\mathbf{x})\varphi_{0}^{-}(\mathbf{y})\Big\}, \end{aligned} \tag{2.14}$$

and similarly for α_n. For a physical density matrix $\rho_0 = \rho_0^\dagger$, the coefficients have to satisfy $i\alpha_1^+ = \left(i\alpha_1^-\right)^*, i\alpha_2^{++} = \left(i\alpha_2^{--}\right)^*, i\alpha_2^{+-} = \left(i\alpha_2^{-+}\right)^*$, and so forth. There can be further constraints on the coefficients arising from spacetime symmetries. For the most general initial density matrix, the generating functional can be written as

$$Z\left[J;\hat{\rho}_{0}\right] = \int \mathcal{D}\varphi \mathrm{e}^{\mathrm{i}\left\{S[\varphi] + \int_{x,\mathcal{C}} J(x)\varphi(x) + \frac{1}{2}\int_{xy,\mathcal{C}} R(x,y)\varphi(x)\varphi(y) + \frac{1}{3!}\int_{xyz,\mathcal{C}} \alpha_{3}(x,y,z)\varphi(x)\varphi(y)\varphi(z) + \ldots\right\}}, \tag{2.15}$$

where we shifted the source terms $J(x) + \alpha_1(x) \to J(x)$, $R(x,y) + \alpha_2(x,y) \to R(x,y)$ and neglected the irrelevant normalisation constant. This shows that the sources J and R can be used to absorb the linear and quadratic contributions from the initial density matrix, and as a result, the initial generating functional may be fully determined by the initial-time sources. In general, one could specify an arbitrarily complex initial density matrix. However, in practice, particularly in experimental settings, initial conditions are often characterised by only a few lower-order correlation functions. For many practical applications, the initial density matrix can be effectively approximated by a Gaussian form, which corresponds to states fully determined by one- and two-point correlation functions. In this case, one has $\alpha_n\left(x_1, \ldots, x_n\right) \equiv 0, n \geq 3$, and the generating functional simplifies to

$$Z^{(\text{Gauss})}[J,R] = \int \mathcal{D}\varphi \mathrm{e}^{\mathrm{i}\left\{S[\varphi] + \int_{x,\mathcal{C}} J(x)\varphi(x) + \frac{1}{2}\int_{xy,\mathcal{C}} \varphi(x)R(x,y)\varphi(y)\right\}}. \tag{2.16}$$

2.1.2 Correlation functions

We obtain the correlation functions by taking the functional derivative of $Z\left[J;\hat{\rho}_0\right]$ with respect to the source term $J(x)$. For instance, the one-point function is obtained for a vanishing source $J(x)$ as

$$\left.\frac{\delta Z\left[J;\hat{\rho}_0\right]}{\mathrm{i}\delta J(x)}\right|_{J=0} = \mathrm{Tr}\left\{\hat{\rho}_0\hat{\varphi}(x)\right\} \equiv \left\langle\hat{\varphi}(x)\right\rangle \equiv \phi(x), \tag{2.17}$$

and the time-ordered two-point correlator is

$$\left.\frac{\delta^2 Z\left[J;\hat{\rho}_0\right]}{\mathrm{i}\delta J(x)\mathrm{i}\delta J(y)}\right|_{J=0} = \mathrm{Tr}\left\{\hat{\rho}_0\mathcal{T}_{\mathcal{C}}\hat{\varphi}(x)\hat{\varphi}(y)\right\} \equiv \left\langle\mathcal{T}_{\mathcal{C}}\hat{\varphi}(x)\hat{\varphi}(y)\right\rangle. \tag{2.18}$$

Higher-order correlation functions $\left\langle\mathcal{T}_{\mathcal{C}}\hat{\varphi}\left(x_1\right)\ldots\hat{\varphi}\left(x_n\right)\right\rangle$ can be obtained by taking further derivatives. One can introduce the *connected two-point function* by

$$G(x,y) \equiv \left\langle\mathrm{T}_{\mathcal{C}}\hat{\varphi}(x)\hat{\varphi}(y)\right\rangle - \phi(x)\phi(y), \tag{2.19}$$

which removes the contribution that is reducible to disconnected terms, thereby isolating the genuine, *connected* two-point correlations. Since the function $G(x,y)$ is defined along the contour $\mathcal{C}$, the time-ordering of the fields $\mathcal{T}_{\mathcal{C}}\hat{\varphi}(x)\hat{\varphi}(y)$ depends on the relative arrangement of their time arguments on this contour. Using the Heaviside step function $\theta(x^0-y^0)$, this relationship can be expressed explicitly as

$$\begin{aligned}\mathcal{T}_{\mathcal{C}}\hat{\varphi}(x)\hat{\varphi}(y) = &\begin{cases}\hat{\varphi}(x)\hat{\varphi}(y)\theta\left(x^0-y^0\right)+\hat{\varphi}(y)\hat{\varphi}(x)\theta\left(y^0-x^0\right), & \text{for } x^0,y^0 \text{ on } \mathcal{C}^+,\\ \hat{\varphi}(x)\hat{\varphi}(y)\theta\left(y^0-x^0\right)+\hat{\varphi}(y)\hat{\varphi}(x)\theta\left(x^0-y^0\right), & \text{for } x^0,y^0 \text{ on } \mathcal{C}^-,\\ \hat{\varphi}(y)\hat{\varphi}(x), & \text{for } x^0 \text{ on } \mathcal{C}^+, y^0 \text{ on } \mathcal{C}^-,\\ \hat{\varphi}(x)\hat{\varphi}(y), & \text{for } x^0 \text{ on } \mathcal{C}^-, y^0 \text{ on } \mathcal{C}^+,\end{cases}\\ &\equiv \hat{\varphi}(x)\hat{\varphi}(y)\theta_{\mathcal{C}}\left(x^0-y^0\right)+\hat{\varphi}(y)\hat{\varphi}(x)\theta_{\mathcal{C}}\left(y^0-x^0\right),\end{aligned} \tag{2.20}$$

in terms of the contour step function $\theta_{\mathcal{C}}\left(x^0-y^0\right)$. Making use of the $\pm$ indices introduced above, nonequilibrium correlation functions can be computed by taking functional derivatives with respect to $J^+(x)$ and $J^-(x)$. In this case, the one-point correlation function

$$\left.\frac{\delta Z\left[J;\hat{\rho}_0\right]}{\mathrm{i}\delta J_{\pm}(x)}\right|_{J=0} = \mathrm{Tr}\left\{\hat{\rho}_0\hat{\varphi}(x)\right\} \equiv \phi(x) \tag{2.21}$$

is the same whether it is obtained from J^+ or J^- in the absence of any sources since time-ordering plays no role. On the other hand, there are four possible options for a two-point function, namely

$$\begin{aligned}\left.\frac{\delta^2 Z\left[J;\hat{\rho}_0\right]}{\mathrm{i}\delta J^+(x)\mathrm{i}\delta J^+(y)}\right|_{J=0} &= \left\langle\hat{\varphi}(x)\hat{\varphi}(y)\right\rangle\theta\left(x^0-y^0\right)+\left\langle\hat{\varphi}(y)\hat{\varphi}(x)\right\rangle\theta\left(y^0-x^0\right)\\ &\equiv G^{++}(x,y)+\phi(x)\phi(y),\\ \left.\frac{\delta^2 Z\left[J;\hat{\rho}_0\right]}{\mathrm{i}\delta J^-(x)\mathrm{i}\delta J^-(y)}\right|_{J=0} &= \left\langle\hat{\varphi}(x)\hat{\varphi}(y)\right\rangle\theta\left(y^0-x^0\right)+\left\langle\hat{\varphi}(y)\hat{\varphi}(x)\right\rangle\theta\left(x^0-y^0\right)\\ &\equiv G^{--}(x,y)+\phi(x)\phi(y),\\ \left.\frac{\delta^2 Z\left[J;\hat{\rho}_0\right]}{\mathrm{i}\delta J^+(x)\mathrm{i}\delta J^-(y)}\right|_{J=0} &= \left\langle\hat{\varphi}(y)\hat{\varphi}(x)\right\rangle \equiv G^{+-}(x,y)+\phi(x)\phi(y),\\ \left.\frac{\delta^2 Z\left[J;\hat{\rho}_0\right]}{\mathrm{i}\delta J^-(x)\mathrm{i}\delta J^+(y)}\right|_{J=0} &= \left\langle\hat{\varphi}(x)\hat{\varphi}(y)\right\rangle \equiv G^{-+}(x,y)+\phi(x)\phi(y).\end{aligned} \tag{2.22}$$

While any nonequilibrium two-point correlator can be written in terms of these, not all the components are independent. Using the property $\theta\left(x^0-y^0\right)+\theta\left(y^0-x^0\right)=1$ of the Heaviside step function, one arrives at the identity

$$G^{++}(x,y)+G^{--}(x,y)=G^{+-}(x,y)+G^{-+}(x,y). \tag{2.23}$$

Furthermore, it can also be observed that $G^{+-}(x,y)=G^{-+}(y,x)$. Therefore, in general, a nonequilibrium two-point function can be parameterised by two independent functions.

Spectral and statistical functions

In the context of nonequilibrium field theory, it is often useful to define the commutator and anticommutator of fields

$$\begin{aligned} F(x,y)&=\frac{1}{2}\left\langle\{\hat{\varphi}(x),\hat{\varphi}(y)\}\right\rangle_c, \\ \rho(x,y)&=i\left\langle[\hat{\varphi}(x),\hat{\varphi}(y)]\right\rangle, \end{aligned} \tag{2.24}$$

where $F(x,y)$ is called the *statistical two-point function* and $\rho(x,y)$ is the *spectral function*. Loosely speaking, the former contains information about the average occupancy of available modes, while the latter contains information about the availability of modes. These two functions can be related to the time-ordered propagator $G(x,y)$ via

$$G(x,y)=F(x,y)-\frac{i}{2}\rho(x,y)\,\mathrm{sgn}_{\mathcal{C}}\left(x_0-y_0\right), \tag{2.25}$$

where $\mathrm{sgn}_{\mathcal{C}}\left(x_0-y_0\right)$ is $+1$ if $x_0>y_0$ and -1 if $x_0<y_0$.

For the case of thermal equilibrium, there is an important relationship between these two quantities in the form of the *fluctuation-dissipation theorem* [90] which relates the statistical and spectral functions via

$$F^{(\mathrm{eq})}(\omega,\mathbf{p})=-i\left(\frac{1}{2}+f_{\mathrm{BE}}(\omega)\right)\rho^{(\mathrm{eq})}(\omega,\mathbf{p}), \tag{2.26}$$

where $f_{\mathrm{BE}}(\omega)=\left(e^{\beta\omega}-1\right)^{-1}$ is the Bose–Einstein distribution function and $\beta=1/T$ is the inverse temperature. In the case of nonequilibrium systems, the fluctuation-dissipation relation is generally not valid and the statistical and spectral functions are independent quantities.

2.2 Classical-statistical approximation

Classical-statistical field theory is expected to be an adequate description of the quantum dynamics when the number of bosonic field quanta per mode is sufficiently large, as quantum fluctuations become suppressed compared to statistical ones. In this regime, the quantum system can be effectively described by an ensemble of classical field configurations. In the corresponding classical-statistical simulations, one samples over initial conditions, and each realisation is evolved according to the classical equation of motion. The advantage of this is that solving such equations can be straightforwardly implemented numerically on a discretised lattice, after which expectation values of observables are obtained by averaging

over their evaluations for the classical trajectories. This approximation provides a substantial simplification in complexity compared to the full quantum many-body problem and has wide-ranging applications in the context of cosmology [91], high-energy physics [29], and ultracold quantum gases [8].

In the following, the classical-statistical approximation and its range of validity are discussed, starting with the generating functional introduced in the previous section. We consider the paradigmatic example of an O(N) symmetric scalar field theory in $d = 3+1$ dimensions with fields $\varphi_a(x) \equiv \varphi_a(x_0, \mathbf{x})$ and quartic self-interaction. The action is given by

$$S[\varphi] = \int_{x,\mathcal{C}} \left[\frac{1}{2}\partial^\mu \varphi_a(x)\partial_\mu \varphi_a(x) - \frac{m^2}{2}\varphi_a(x)\varphi_a(x) - \frac{\lambda}{4!N}\left(\varphi_a(x)\varphi_a(x)\right)^2 \right], \tag{2.27}$$

where $\int_{x,\mathcal{C}} \equiv \int_{-\infty}^{\infty} \mathrm{d}^d\mathbf{x} \int_{\mathcal{C}} \mathrm{d}x_0$ denotes a closed time path contour. The fields $\varphi_a(x)$ are real and the index a runs from 1 to N.

2.2.1 Keldysh rotation

The classical action (2.27) for the N-component scalar field theory may be rewritten in terms of the fields taken on the positive and negative branches of the closed contour $\mathcal{C}^+$ and $\mathcal{C}^-$, respectively, as

$$\begin{aligned} &S\left[\varphi^+, \varphi^-\right] \\ &= \int_{x,t_0} \left\{ \frac{1}{2}\partial^\mu \varphi_a^+(x)\partial_\mu \varphi_a^+(x) - \frac{m^2}{2}\varphi_a^+(x)\varphi_a^+(x) - \frac{\lambda}{4!N}\left(\varphi_a^+(x)\varphi_a^+(x)\right)^2 \right. \\ &\quad \left. -\frac{1}{2}\partial^\mu \varphi_a^-(x)\partial_\mu \varphi_a^-(x) + \frac{m^2}{2}\varphi_a^-(x)\varphi_a^-(x) + \frac{\lambda}{4!N}\left(\varphi_a^-(x)\varphi_a^-(x)\right)^2 \right\}. \end{aligned} \tag{2.28}$$

It is insightful to introduce the linear transformation

$$\begin{pmatrix} \varphi \\ \tilde{\varphi} \end{pmatrix} \equiv \underbrace{\begin{pmatrix} 1/2 & 1/2 \\ 1 & -1 \end{pmatrix}}_{\equiv A} \begin{pmatrix} \varphi^+ \\ \varphi^- \end{pmatrix} \tag{2.29}$$

and the transformed scalar fields

$$\varphi = \frac{\varphi^+ + \varphi^-}{2}, \quad \tilde{\varphi} = \varphi^+ - \varphi^-, \tag{2.30}$$

as we will shortly see, this makes the comparison with classical-statistical field theory simpler. We arrive at the generating functional in terms of the rotated variables as

$$\begin{aligned} Z\left[J, \tilde{J}; \hat{\rho}_0\right] &= \int \mathcal{D}\varphi_0 \mathcal{D}\tilde{\varphi}_0 \left\langle \varphi_0 + \frac{\tilde{\varphi}_0}{2} \left| \hat{\rho}_0 \right| \varphi_0 - \frac{\tilde{\varphi}_0}{2} \right\rangle \\ &\times \int_{\varphi_0, \bar{\varphi}_0} \mathcal{D}'\varphi \mathcal{D}'\tilde{\varphi} \exp\left\{ iS[\varphi, \tilde{\varphi}] + i\int_x \left(\varphi_a(x)\tilde{J}_a(x) + \tilde{\varphi}_a(x)J_a(x) \right) \right\}, \end{aligned} \tag{2.31}$$

where the source terms have been analogously transformed according to

$$\begin{pmatrix} J \\ \tilde{J} \end{pmatrix} \equiv A \begin{pmatrix} J^+ \\ J^- \end{pmatrix}. \tag{2.32}$$

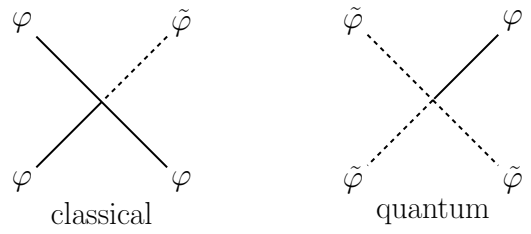

Figure 2.2. The classical and quantum vertices, corresponding to the different kinds of interaction terms $\sim \tilde{\varphi}\varphi^3$ and $\sim \tilde{\varphi}^3\varphi$, respectively.

The different connected two-point correlation functions in the rotated variables, obtained via the *Schwinger functional* $W[J,R] = -i \ln Z[J,R]$ are given by

$$\begin{aligned} F_{ab}(x,y) &= \left.\frac{\delta^2 W[J,R]}{i\delta\tilde{J}_a(x)\delta\tilde{J}_b(y)}\right|_{J=\tilde{J}=0}, \quad -iG^R_{ab}(x,y) = \left.\frac{\delta^2 iW[J,R]}{i\delta\tilde{J}_a(x)\delta J_b(y)}\right|_{J=\tilde{J}=0}, \\ -iG^A_{ab}(x,y) &= \left.\frac{\delta^2 W[J,R]}{i\delta J_a(x)\delta\tilde{J}_b(y)}\right|_{J=\tilde{J}=0}, \quad \tilde{F}_{ab}(x,y) = \left.\frac{\delta^2 W[J,R]}{i\delta J_a(x)\delta J_b(y)}\right|_{J=\tilde{J}=0}, \end{aligned} \tag{2.33}$$

where the retarded and advanced propagators are $G^R_{ab}(x,y) \equiv \theta(x_0-y_0)\,\rho_{ab}(x,y)$ and $G^A_{ab}(x,y) \equiv -\theta(y_0-x_0)\,\rho_{ab}(x,y)$, the spectral function is their difference $\rho_{ab}(x,y) = G^{\rm R}_{ab}(x,y) - G^{\rm A}_{ab}(x,y)$ and $\tilde{F}_{ab}$ is zero for vanishing sources. In the $\pm$ basis, the propagators are given by

$$\begin{pmatrix} F & -iG^{\rm R} \\ -iG^{\rm A} & \tilde{F} \end{pmatrix} = A \begin{pmatrix} G^{++} & G^{+-} \\ G^{-+} & G^{--} \end{pmatrix} A^T. \tag{2.34}$$

2.2.2 Relation to classical-statistical field theory

The action appearing in Eq. (2.31) above can then be split into

$$S[\varphi,\tilde{\varphi}] = S_0[\varphi,\tilde{\varphi}] + S_{\rm int,cl}[\varphi,\tilde{\varphi}] + S_{\rm int,q}[\varphi,\tilde{\varphi}], \tag{2.35}$$

where the different terms are given by

$$\begin{aligned} S_0[\varphi,\tilde{\varphi}] &= \int_{x,t_0} \partial^\mu\tilde{\varphi}_a(x)\partial_\mu\varphi_a(x) - m^2\tilde{\varphi}_a(x)\varphi_a(x), \\ S_{\rm int,cl}[\varphi,\tilde{\varphi}] &= -\frac{\lambda}{6N}\int_{x,t_0} \tilde{\varphi}_a(x)\varphi_a(x)\varphi_b(x)\varphi_b(x), \\ S_{\rm int,\,q}[\varphi,\tilde{\varphi}] &= -\frac{\lambda}{24N}\int_{x,t_0} \tilde{\varphi}_a(x)\tilde{\varphi}_a(x)\tilde{\varphi}_b(x)\varphi_b(x). \end{aligned} \tag{2.36}$$

There are two types of interaction vertices, namely, a "classical" one and a "quantum" one, as shown in Fig. 2.2. To illustrate the reason behind the naming of these terms, it is worth noting that the generating functional of the corresponding nonequilibrium classical-statistical field theory is rather similar to the quantum case, except that crucially, there is an additional quantum vertex corresponding to the interaction term $\sim \tilde{\varphi}^3\varphi$ that does not appear in the classical theory. The classical-statistical approximation is obtained by neglecting the

quantum interaction term $S_{\text{int, q}}[\varphi, \tilde{\varphi}]$ in the action. The generating functional is then given by

$$Z_{\text{cl}}\left[J, \tilde{J}; \rho_0\right] = \int \mathcal{D}\varphi_0 \mathcal{D}\pi_0 W\left[\varphi_0, \pi_0\right] \int_{\varphi_0, \pi_0} \mathcal{D}'\varphi \mathcal{D}\tilde{\varphi} e^{iS_{\text{cl}}[\varphi,\bar{\varphi}]+i\int_x \left(\varphi_a(x)\bar{J}_a(x)+\bar{\varphi}_a(x)J_a(x)\right)}, \tag{2.37}$$

where S_{cl} is the action containing S_0 and $S_{\text{int,cl}}$, and $W[\varphi_0, \pi_0]$ is the Wigner distribution functional of fields at t_0 defined via

$$\left\langle \varphi_0 + \frac{\tilde{\varphi}_0}{2} \left|\hat{\rho}_0\right| \varphi_0 - \frac{\tilde{\varphi}_0}{2} \right\rangle = \int \mathcal{D}\pi_0 W\left[\varphi_0, \pi_0\right] e^{i\int d^d x \pi_{0,a}(\mathbf{x})\bar{\varphi}_{0,a}(\mathbf{x})}. \tag{2.38}$$

Since the classical action $S_{\text{cl}}[\varphi, \tilde{\varphi}]$ is linear in $\tilde{\varphi}$, it can be written as

$$S_{\text{cl}}[\varphi, \tilde{\varphi}] = \int_x \tilde{\varphi}_a(x) \frac{\delta S_{\text{cl}}[\varphi, \tilde{\varphi}]}{\delta \tilde{\varphi}_a(x)}, \tag{2.39}$$

and analytically integrated over to yield

$$\int \mathcal{D}\tilde{\varphi} e^{iS_{\text{cl}}[\varphi,\bar{\varphi}]} = \delta\left[\frac{S_{\text{cl}}[\varphi, \tilde{\varphi}]}{\delta \tilde{\varphi}_a(x)}\right] = \delta\left[\varphi - \varphi^{\text{cl}}\right] \underbrace{\mathcal{J}^{-1}[\varphi]}_{=1}, \tag{2.40}$$

where the Jacobi determinant is equal to 1 due to the normalisation of Z. Here, φ^{cl} is the solution to the classical field equation of motion, which can be obtained by minimising the action (2.27) as $\delta S/\delta\varphi = 0$ to give

$$\left(\partial^\mu \partial_\mu + m^2 + \frac{\lambda}{6N}\varphi_c(x)\varphi_c(x)\right)\varphi_a(x) = 0. \tag{2.41}$$

The classical-statistical average of an observable $\mathcal{O}[\varphi]$ is given by the phase-space average over field trajectories that are solutions to the classical field equation

$$\langle O[\varphi, \pi]\rangle_{\text{cl}} = \int \mathcal{D}\varphi_0 \mathcal{D}\pi_0 W\left[\varphi_0, \pi_0\right] O\left[\varphi^{\text{cl}}\left(\varphi_0, \pi_0\right), \pi^{\text{cl}}\left(\varphi_0, \pi_0\right)\right], \tag{2.42}$$

with initial conditions given by φ_0, π_0.

The classical-statistical approximation discussed here is closely related to the Truncated Wigner Approximation (TWA) [71], which serves as a practical tool for studying quantum dynamics in the phase-space formalism. Both approaches involve initialising the system through the Wigner distribution, which captures quantum fluctuations at the initial time, and then evolving the system using classical equations of motion. In practice, this yields equivalent results for computed observables. However, TWA is formally derived from the Wigner representation of quantum mechanics and is obtained by neglecting higher-order quantum corrections in the evolution equations, whereas the classical-statistical approximation omits specific quantum terms in the action.

2.2.3 Classicality condition

In order to make the range of validity of this approximation more concrete, we first return to the different two-point functions in the rotated variables,

$$\begin{aligned} F_{ab}(x, y) &= \langle \varphi_a(x)\varphi_b(y)\rangle, \\ -iG^R_{ab}(x, y) &= \langle \varphi_a(x)\tilde{\varphi}_b(y)\rangle, \\ -iG^A_{ab}(x, y) &= \langle \tilde{\varphi}_a(x)\varphi_b(y)\rangle, \end{aligned} \tag{2.43}$$

given explicitly in terms of the rotated fields $\tilde{\varphi}, \varphi$. As discussed above, the interaction term in the action (2.35) contains two kinds of contributions, corresponding to a classical vertex $\sim \tilde{\varphi}\varphi^3$ and a quantum vertex $\sim \tilde{\varphi}^3\varphi$, as illustrated in Fig. 2.2. These vertices can generate additional sub-diagrams with loop corrections. However, in the classical-statistical approximation, quantum vertices are neglected, meaning that terms involving multiple $\tilde{\varphi}$ fields do not contribute. In contrast, including quantum vertices, which feature more dashed $\tilde{\varphi}$ legs, would introduce sub-diagrams with fewer F propagators and a higher proportion of ρ functions, as seen from Eq. (2.43). This naturally leads to the *classicality condition*

$$F_{ab}(x,y) \gg \rho_{ab}(x,y). \tag{2.44}$$

However, this requirement is difficult to fulfill for all space-time arguments, and can typically only be met for a limited amount of time and momenta. Equivalently, the condition can be restated in terms of the distribution function as

$$f(t,\mathbf{p}) \gg \frac{1}{2} \tag{2.45}$$

for the relevant time and momentum range. Therefore, the classical-statistical description accurately captures the quantum dynamics if the dominant momentum modes have occupancies much higher than the so-called *quantum half*.

Furthermore, we note that by rescaling the fields in the action (2.36) according to

$$\varphi_a(x) \to \varphi'_a(x) = \sqrt{\lambda}\varphi_a(x), \quad \tilde{\varphi}_a(x) \to \tilde{\varphi}'_a(x) = \frac{1}{\sqrt{\lambda}}\tilde{\varphi}_a(x) \tag{2.46}$$

the rescaled interaction terms are given by

$$S_{\rm int}[\varphi',\tilde{\varphi}'] = -\frac{1}{6N}\int_x \tilde{\varphi}'_a(x)\varphi'_a(x)\varphi'_b(x)\varphi'_b(x) - \frac{\lambda^2}{24N}\int_x \tilde{\varphi}'_a(x)\tilde{\varphi}'_a(x)\tilde{\varphi}'_b(x)\varphi'_b(x), \tag{2.47}$$

and the λ dependence is fully encoded in the quantum interaction term. As a result, in the classical-statistical approximation, the generating functional and the evolution equations governing the dynamics become independent of λ, with λ entering only through the initial conditions. This implies an additional constraint on the validity of the approximation: while the dynamics itself remains unaffected by λ, the approximation is expected to hold reliably only when interactions do not significantly alter the high-occupancy modes, which is typically the case at weak coupling $\lambda \ll 1$.

2.2.4 Scalar fields on a lattice

In practice, the classical field equations can be solved numerically on a discrete lattice by first sampling initial conditions from the Wigner distribution, evolving the fields according to the classical equations of motion and then averaging O over the different realisations

$$\langle O[\varphi,\pi]\rangle_{\rm cl} \approx \frac{1}{N_{\rm samp}} \sum_{(\varphi_0,\pi_0)} O\left[\varphi^{\rm cl}(\varphi_0,\pi_0), \pi^{\rm cl}(\varphi_0,\pi_0)\right], \tag{2.48}$$

where N_{samp} is the number of different runs. More concretely, first, the fields $\varphi_a(t_0, \mathbf{x})$ and conjugate momenta $\pi_a(t_0, \mathbf{x}) = \dot{\varphi}_a(t_0, \mathbf{x})$ are randomly initialised according to

$$\varphi_a(t_0, \mathbf{x}) = \phi_0 + \int \frac{\mathrm{d}^d p}{(2\pi)^d} \sqrt{\frac{f_{\mathbf{p}}(t_0) + 1/2}{\omega_{\mathbf{p}}(t_0)}} c_{a,\mathbf{p}} e^{i\mathbf{p}\mathbf{x}}, \tag{2.49}$$

$$\pi_a(t_0, \mathbf{x}) = \dot{\phi}_0 + \int \frac{\mathrm{d}^d p}{(2\pi)^d} \sqrt{(f_{\mathbf{p}}(t_0) + 1/2)\,\omega_{\mathbf{p}}(t_0)} \tilde{c}_{a,\mathbf{p}} e^{i\mathbf{p}\mathbf{x}}, \tag{2.50}$$

where $\phi(t_0) = \phi_0$ is a macroscopic field and its derivative is $\dot{\phi}(t_0) = \dot{\phi}_0$, $f_{\mathbf{p}}(t_0)$ is the distribution function, and the dispersion relation is $\omega_{\mathbf{p}}(t_0) = \sqrt{\mathbf{p}^2 + M^2}$. For Gaussian initial conditions, the coefficients $c_{a,\mathbf{p}}$ have to satisfy

$$\left\langle c_{a,\mathbf{p}} c^*_{b,\mathbf{p}'} \right\rangle_{\text{cl}} = (2\pi)^d \delta_{ab} \delta(\mathbf{p} - \mathbf{p}'), \quad \left\langle c_{a,\mathbf{p}} c_{b,\mathbf{p}'} \right\rangle_{\text{cl}} = \left\langle c^*_{a,\mathbf{p}} c^*_{b,\mathbf{p}'} \right\rangle_{\text{cl}} = 0, \tag{2.51}$$

and similarly for the coefficients $\tilde{c}_{a,\mathbf{p}}$. Moreover, since $c_{a,\mathbf{p}}$ and $\tilde{c}_{a,\mathbf{p}}$ are independent random numbers, we also have $\langle c_{a,\mathbf{p}} \tilde{c}_{b,\mathbf{p}'} \rangle_{\text{cl}} = 0$. This can be realised in practice by the formulation $c_{a,\mathbf{p}} = A(\mathbf{p}) e^{i2\pi\alpha(\mathbf{p})}$, where $A(\mathbf{p})$ is an amplitude drawn from a Gaussian distribution, and $\alpha(\mathbf{p})$ is a uniformly distributed phase between 0 and 1. The random numbers also have to satisfy $c^*_{a,-\mathbf{p}} = c_{a,\mathbf{p}}$ so that the fields are real-valued.

Subsequently, the classical fields $\varphi_a(\mathbf{x})$ and $\pi_a(\mathbf{x})$ are evolved according to the discretised version of the classical equations of motion

$$\begin{aligned} \partial_t \varphi_a(t, \mathbf{x}) &= \pi_a(t, \mathbf{x}), \\ \partial_t \pi_a(t, \mathbf{x}) &= \partial_i \partial^i \varphi_a(t, \mathbf{x}) - m^2 \varphi_a(t, \mathbf{x}) - \frac{\lambda}{6} \varphi_a(t, \mathbf{x})^3, \end{aligned} \tag{2.52}$$

on a spatial lattice with spacing a_s and volume $V = (N_s a_s)^d$ with a standard leapfrog algorithm. Moreover, in practice, the coupling λ is scaled out as discussed above.

Ensemble averages of classical fields can then be obtained by repeating the procedure of randomly initialising the classical fields and evolving them. The number of runs needed to accurately compute correlation functions depends on the lattice size and dimensionality of the investigated systems. For instance, even single-run simulations on a large lattice can give accurate results since systems have self-averaging properties. This is especially evident in three (and higher) dimensions, while in lower dimensions, larger ensembles of runs may be required to reduce statistical fluctuations and achieve accurate results due to reduced self-averaging effects.

2.3 Effective actions

Studying the dynamics of strongly correlated many-body systems is a notoriously difficult problem [92, 93], especially in a nonequilibrium time evolution. Usual perturbative approaches that rely on the expansion of the action in terms of the coupling constant are inefficient due to the large number of Feynman diagrams that need to be computed, and standard perturbative time evolution can also be affected by so-called secular terms, which grow with time and render the perturbative expansion invalid. The *two-particle irreducible*

effective action is a powerful tool that has been successfully used to study the dynamics of quantum fields in nonequilibrium systems in the strongly correlated regime. It provides a self-consistent treatment of initial value problems and is particularly useful in the context of large-N expansions, which we will discuss in this section.

2.3.1 One-particle irreducible effective action

As mentioned earlier, the generating functional Z is the nonequilibrium quantum field generalisation of the partition function. In thermodynamics, the logarithm of the partition function and its Legendre transforms provide alternative formulations of the physics of the system. Motivated by this, and taking the Legendre transform of the generating functional for connected correlation functions defined via $W = -i \ln Z$, we arrive at the *quantum effective action*

$$\Gamma[\phi] = W[J] - \int_{x,\mathcal{C}} J_a(x)\phi_a(x), \tag{2.53}$$

where $J(x)$ is the source for which the scalar field has the expectation value $\phi(x)$. Moreover, the expectation value $\phi(x) = \langle\hat{\varphi}(x)\rangle_J$, often referred to as the *classical field* can be identified as

$$\frac{\delta W[J]}{\delta J_a(x)} = \phi_a(x). \tag{2.54}$$

This quantity can be thought of as the weighted average over quantum fluctuations in the presence of $J(x)$. Taking the functional derivative of (2.53), one has

$$\left.\frac{\delta\Gamma[\phi]}{\delta\phi_a(x)}\right|_{\phi=\phi_J} = -J_a(x), \tag{2.55}$$

which shows that the vacuum expectation value of the fields minimises the quantum effective action, rather than the classical action. This reflects the principle of least action applied to the full quantum framework.

The functional in Eq. (2.53) is called *one-particle irreducible quantum effective action*, which can be understood by considering its functional derivatives with respect to the fields

$$\Gamma^{(n)}_{a_1\ldots a_n}(x_1,\ldots,x_n) \equiv \frac{\delta^n\Gamma[\phi]}{\delta\phi_{a_1}(x_1)\ldots\delta\phi_{a_n}(x_n)}. \tag{2.56}$$

This is the generator of *one-particle irreducible (1PI) vertices*, which correspond to diagrams that cannot be separated into two disconnected ones by cutting a line. Therefore, 1PI vertices are a more compact form of storing information, since the connected correlation functions generated by $W[J]$ still contain redundant information in the form of one-particle reducible diagrams.

There is an important relation, which can be seen by considering the following quantity in terms of the 1PI two-point function $\Gamma^{(2)}$, and the propagator $\delta W[J]/\delta J(y)\delta J(x_2)$,

$$\begin{aligned}\int_y \frac{\delta^2\Gamma[\phi]}{\delta\phi_a(x_1)\,\delta\phi_c(y)}\frac{\delta^2 W[J]}{\delta J_c(y)\delta J_b(x_2)} &= \int_y \frac{\delta}{\delta\phi_a(x_1)}\left(\frac{\delta\Gamma[\phi]}{\delta\phi_c(y)}\right)\frac{\delta}{\delta J_c(y)}\left(\frac{\delta W[J]}{\delta J_b(x_2)}\right)\\ &= -\int_y \frac{\delta J_c(y)}{\delta\phi_a(x_1)}\frac{\delta\phi_b(x_2)}{\delta J_c(y)} = -\delta_{ab}\delta(x_1-x_2).\end{aligned} \tag{2.57}$$

From this, we observe that the 1PI two-point function is in fact the inverse of the propagator.

2.3.2 Two-particle irreducible effective action

The above procedure can be repeated to obtain a functional, which is a generator of *two-particle irreducible (2PI) diagrams*. First we consider the generating functional to contain a bilinear source term $R(x,y)$ as well,

$$\begin{aligned} Z[J,R] &\equiv \exp(iW[J,R]) \\ &= \int \mathcal{D}\varphi \exp\left\{ i\left[S[\varphi] + \int_{x,\mathcal{C}} J_a(x)\varphi_a(x) + \frac{1}{2}\int_{xy,\mathcal{C}} \varphi_a(x) R_{ab}(x,y)\varphi_b(y)\right]\right\}, \end{aligned} \tag{2.58}$$

with the functional derivatives of $W[J,R]$ being

$$\begin{aligned} \frac{\delta W[J,R]}{\delta J_a(x)} &\equiv \phi_a(x), \\ \frac{\delta W[J,R]}{\delta R_{ab}(x,y)} &\equiv \frac{1}{2}\left(\phi_a(x)\phi_b(y) + G_{ab}(x,y)\right). \end{aligned} \tag{2.59}$$

The 2PI effective action $\Gamma[\Phi,\Delta]$ is defined as the double Legendre transform of $W[J,R]$ with respect to the source terms,

$$\begin{aligned} \Gamma[\phi,G] &= \Gamma[\phi] - \frac{1}{2}\int_{xy,\mathcal{C}} \left[\phi_a(x)\phi_b(y) + G_{ab}(x,y)\right] R_{ab}(x,y) \\ &= W[J,R] - \int_{x,\mathcal{C}} \phi_a(x) J_a(x) - \frac{1}{2}\int_{xy,\mathcal{C}} \left[\phi_a(x)\phi_b(y) + G_{ab}(x,y)\right] R_{ab}(x,y). \end{aligned} \tag{2.60}$$

The 2PI equations of motion are given by the stationary conditions of the 2PI effective action with respect to the fields ϕ and G, expressed as

$$\frac{\delta\Gamma[\phi,G]}{\delta\phi_a(x)} = -J_a(x), \quad \frac{\delta\Gamma[\phi,G]}{\delta G_{ab}(x,y)} = -\frac{1}{2}R_{ab}(x,y). \tag{2.61}$$

The 2PI effective action can be recast into a very convenient form, written as

$$\Gamma[\phi,G] = S[\phi] + \frac{i}{2}\,\mathrm{Tr}_{\mathcal{C}} \ln G^{-1} + \frac{i}{2}\,\mathrm{Tr}_{\mathcal{C}}\, G_0^{-1}(\phi)G + \Gamma_2[\phi,G] + \text{const}, \tag{2.62}$$

where $G_0^{-1}(\phi)$ is the classical inverse propagator. This has the form of a one-loop type expression, plus an additional term $\Gamma_2[\phi,G]$ which contains all 2PI contributions. Diagrammatically, this corresponds to all 2PI graphs, which are diagrams that do not become disconnected by cutting two lines open. Varying $\Gamma_2[\phi,G]$ with respect to G yields

$$G_{ab}^{-1}(x,y) = G_{0,ab}^{-1}(x,y) - \Sigma_{ab}(x,y) - iR_{ab}(x,y), \tag{2.63}$$

where the self-energy is defined as

$$\Sigma_{ab}(x,y;\phi,G) \equiv 2i\frac{\delta\Gamma_2[\phi,G]}{\delta G_{ba}(y,x)}. \tag{2.64}$$

The self-energy can be separated into a local and nonlocal part

$$\Sigma_{ab}(x,y) = -i\Sigma_{ab}^{(0)}(x)\delta(x-y) + \bar{\Sigma}_{ab}(x,y), \tag{2.65}$$

where the local contribution shifts the effective mass for which one can introduce the notation

$$M^2_{ab}(x) \overset{(\phi=0)}{=} m^2\delta_{ab} + \Sigma^{(0)}_{ab}(x). \tag{2.66}$$

The nonlocal contribution, similarly to the propagator (2.25), can be decomposed into spectral and statistical parts

$$\Sigma_{ab}(x,y) = \Sigma^F_{ab}(x,y) - \frac{i}{2}\Sigma^\rho_{ab}(x,y)\,\mathrm{sgn}_\mathcal{C}(x_0 - y_0)\,. \tag{2.67}$$

On the Keldysh contour, (2.63) can be formulated as

$$\begin{pmatrix} 0 & i\left(G^\mathrm{A}\right)^{-1} \\ i\left(G^\mathrm{R}\right)^{-1} & \left(G^\mathrm{R}\right)^{-1}\cdot F\cdot\left(G^\mathrm{A}\right)^{-1} \end{pmatrix} = \begin{pmatrix} 0 & G_0^{-1} \\ G_0^{-1} & 0 \end{pmatrix} - \begin{pmatrix} 0 & -i\Sigma^\mathrm{A} \\ -i\Sigma^\mathrm{R} & \Sigma^F \end{pmatrix}, \tag{2.68}$$

where the retarded, advanced, and statistical self-energies are obtained as

$$\begin{pmatrix} 0 & -i\Sigma^\mathrm{A} \\ -i\Sigma^\mathrm{R} & \Sigma^F \end{pmatrix} = \left(A^{-1}\right)^T \begin{pmatrix} \Sigma^{++} & -\Sigma^{+-} \\ -\Sigma^{-+} & \Sigma^{--} \end{pmatrix} A^{-1} \tag{2.69}$$

from the self-energies in the $\pm$ basis. Similarly to the 1PI two-point function and inverse propagator, the inverse of the 2PI propagators can also be equated with the corresponding two-point functions. This yields four equations for the two-point functions $\Gamma^F_{ab}, \Gamma^{\tilde{F}}_{ab}, \Gamma^R_{ab}, \Gamma^A_{ab}$, out of which only two are independent, as discussed in Sec. 2.1.2. Therefore, the number of degrees of freedom has doubled in going to the Keldysh description; however, this is essential in order to obtain a real equation of motion that has a causal structure, which is crucial for a real-time description.

2.3.3 Large-N expansion

Depending on the problem at hand, the 2PI effective action can be further combined with different approximation schemes to make it more tractable. One such approach is a perturbative coupling expansion, which can be applied to weakly coupled systems where power counting in the interaction coupling λ is appropriate. However, it is not always applicable. For instance, in the infrared regime of nonthermal fixed points where the occupation number grows very large, the system becomes strongly correlated despite the weak coupling, which invalidates perturbative approaches. The large-N expansion uses the number of field components N as an expansion parameter instead of a small coupling. Therefore, we consider the nonperturbative, systematic expansion of the 2PI effective action $\Gamma_2[\phi;G]$, in powers of $1/N$

$$\Gamma_2[\phi;G] = \Gamma_2^\mathrm{LO}[G] + \Gamma_2^\mathrm{NLO}[\phi;G] + \Gamma_2^\mathrm{NNLO}[\phi;G] + \ldots, \tag{2.70}$$

where $\Gamma_2^\mathrm{LO}[G]$ is the leading order (LO) contribution and scales as N^1, $\Gamma_2^\mathrm{NLO}[\phi;G]$ is the next-to-leading order (NLO) contribution and scales as N^0, and each successive term is down by an additional factor of $1/N$. In this work, we consider the expansion to NLO for the case of a vanishing field expectation value $\phi = 0$, where the relevant terms have been computed in [87].

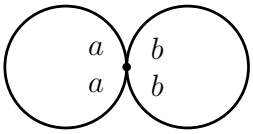

Figure 2.3. The double-bubble diagram that contributes at the leading order in the $1/N$ expansion of Γ_2.

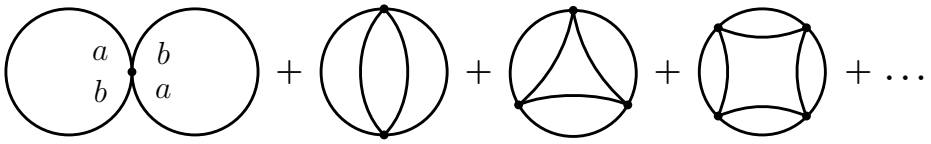

Figure 2.4. Diagrams summed by the NLO order in the $1/N$ expansion of Γ_2.

Diagrammatically, each vertex contributes a factor of $1/N$, while each trace over field indices, e.g., $\mathrm{Tr}(\phi\phi)$ or $\mathrm{Tr}(G^n)$ is proportional to N. The leading order contribution is

$$\Gamma_2^{\mathrm{LO}}[G] = -\frac{\lambda}{4!N}\int_x G_{aa}(x,x)G_{bb}(x,x), \tag{2.71}$$

given by the diagram in Fig. 2.3. At next to leading order, we have

$$\Gamma_2^{\mathrm{NLO}}[\phi, G] = \frac{1}{2}\,\mathrm{Tr}\ln[B(G)], \tag{2.72}$$

where we have defined

$$B(x,y;G) = \delta^d(x-y) + \frac{\lambda}{6N}G_{ab}(x,y)G_{ab}(x,y). \tag{2.73}$$

Eq. (2.72), together with (2.73) sums the infinite series of diagrams shown in Fig. 2.4, which can be observed by expanding (2.72). Regarding the self-energies, the local part is given by the space-time-dependent mass shift (2.66), while the nonlocal part can be decomposed into

$$\Sigma^F(x,y) = -\frac{\lambda}{3N}\left(F(x,y)I^F(x,y) - \frac{1}{4}\rho(x,y)I^\rho(x,y)\right), \tag{2.74}$$

$$\Sigma^\rho(x,y) = -\frac{\lambda}{3N}\left(F(x,y)I^\rho(x,y) + \rho(x,y)I^F(x,y)\right), \tag{2.75}$$

at NLO in the $1/N$ expansion. Here, the so-called summation function $I(x,y)$ can also be decomposed into spectral and statistical parts

$$I^F(x,y) = \Pi^F(x,y) - \int_{t_0}^{x^0} \mathrm{d}z I^\rho(x,z)\Pi^F(z,y) + \int_{t_0}^{y^0} \mathrm{d}z I^F(x,z)\Pi^\rho(z,y), \tag{2.76}$$

$$\begin{aligned} I^\rho(x,y) &= \Pi^\rho(x,y) - \int_{y^0}^{x^0} \mathrm{d}z I^\rho(x,z)\Pi^\rho(z,y) \\ &= \Pi^\rho(x,y) - \int_{t_0}^{x^0} \mathrm{d}z I^\rho(x,z)\Pi^\rho(z,y) + \int_{t_0}^{y^0} \mathrm{d}z I^\rho(x,z)\Pi^\rho(z,y), \end{aligned} \tag{2.77}$$

with $\int_{t_1}^{t_2} \mathrm{d}z \equiv \int_{t_1}^{t_2} \mathrm{d}z^0 \int_{-\infty}^{\infty} \mathrm{d}^d z$ and where

$$\Pi^F(x,y) = \frac{\lambda}{6N}\left(F_{ab}(x,y)F_{ba}(x,y) - \frac{1}{4}\rho_{ab}(x,y)\rho_{ba}(x,y)\right), \tag{2.78}$$

$$\Pi^\rho(x,y) = \frac{\lambda}{3N}F_{ab}(x,y)\rho_{ba}(x,y). \tag{2.79}$$

2.3.4 Gradient expansion and Wigner space quantities

The nonequilibrium evolution of a quantum system starting from a given initial state can involve rapid changes initially, followed by a more uniform evolution over time. As the dynamics slows down at intermediate and later times, low-order expansions in spatial and time derivatives can be applied to approximate the behaviour of observables through effective dynamic equations. This is the basis for effective kinetic descriptions, which have been successfully applied even in strongly correlated regimes and accurately predicted scaling exponents in the infrared region of nonthermal fixed points.

In the following, relevant quantities will be considered in Fourier space, which is often more convenient to work with for homogeneous systems. Due to homogeneity, one has translational invariance, and a two-point function $G(x,y)$ only depends on the difference of its arguments $x-y$, therefore, its Fourier transform would then only depend on a single momentum p. However, in general, time-translation invariance does not hold in a nonequilibrium system; e.g., a two-point function would depend on both the difference $t-t'$ and the sum $t+t'$ of its temporal arguments. Accordingly, we can then define the Wigner transform as the Fourier transform with respect to the relative coordinates $s=x-y$ only

$$f(u^0,\omega,\mathbf{p}) = \int_{-2u^0}^{2u^0} \mathrm{d}s^0 e^{i\omega s^0} \int_{-\infty}^{\infty} \mathrm{d}^d s e^{-i\mathbf{ps}} f\left(u+\frac{s}{2}, u-\frac{s}{2}\right), \tag{2.80}$$

and with $u=\frac{1}{2}(x+y)$ being centre coordinates. In Wigner space, the loop quantities in (2.78) and (2.79) are obtained as

$$\Pi^F(p) = \frac{\lambda}{6N}[(F_{ab} * F_{ba})(p)], \tag{2.81}$$

$$\Pi^\rho(p) = \frac{\lambda}{3N}[(F_{ab} * \rho_{ba})(p)], \tag{2.82}$$

where the $*$ symbol denotes a convolution integral, and the spectral term in $\Pi^F(p)$ has been dropped due to the classical-statistical limit. With a leading-order gradient expansion in time $t=(x_0+y_0)/2$, the summation functions take a simple form

$$I^F(p) = v_{\text{eff}}(p)\Pi^F(p), \tag{2.83}$$

$$I^\rho(p) = v_{\text{eff}}(p)\Pi^\rho(p), \tag{2.84}$$

with the four-vector $p\equiv(\omega,\mathbf{p})$. The *effective vertex* v_{eff} sums the infinite chain of diagrams appearing at NLO in the $1/N$ expansion and is given by

$$v_{\text{eff}}(p) = \frac{1}{|1+\Pi^R(p)|^2}. \tag{2.85}$$

The self-energies can also be obtained as

$$\Sigma^F_{ab}(p) = -\frac{\lambda}{3N}\left[F_{ab} * \left(\Pi^F \cdot v_{\text{eff}}\right)\right](p), \tag{2.86}$$

$$\Sigma^\rho_{ab}(p) = -\frac{\lambda}{3N}\left[F_{ab} * \left(\Pi^\rho \cdot v_{\text{eff}}\right) + \rho_{ab} * \left(\Pi^F \cdot v_{\text{eff}}\right)\right](p), \tag{2.87}$$

where similarly to (2.81), the spectral contribution has been dropped in $\Sigma^F_{ab}(p)$. These expressions will be used as the starting point towards the extraction of nonthermal scaling solutions in Chapter 6.

Chapter 3

Extracting the symmetries of nonequilibrium quantum many-body systems

This chapter is based on *"Extracting the symmetries of nonequilibrium quantum many-body systems"* by A. N. Mikheev, V. Noel, I. Siovitz, H. Strobel, M. K. Oberthaler, and J. Berges, arXiv:2407.17913, SciPost Phys. 18, 044 (2025).

Symmetries play a pivotal role in our understanding of the properties of quantum many-body systems. While there are theorems and a well-established toolbox for systems in thermal equilibrium, much less is known about the role of symmetries and their connection to dynamics out of equilibrium. This arises due to the direct link between a system's thermal state and its Hamiltonian, which is generally not the case for nonequilibrium dynamics. Here we present a pathway to identify the effective symmetries and to extract them from data in nonequilibrium quantum many-body systems. Our approach is based on exact relations between correlation functions involving different numbers of spatial points, which can be viewed as nonequilibrium versions of (equal-time) Ward identities encoding the symmetries of the system. We derive symmetry witnesses, which are particularly suitable for the analysis of measured or simulated data at different snapshots in time. To demonstrate the potential of the approach, we apply our method to numerical and experimental data for a spinor Bose gas. We investigate the important question of a dynamical restoration of an explicitly broken symmetry of the Hamiltonian by the initial state. Remarkably, it is found that effective symmetry restoration can occur long before the system equilibrates. We also use the approach to define and identify spontaneous symmetry breaking far from equilibrium, which is of great relevance for applications to nonequilibrium phase transitions. Our work opens new avenues for the classification and analysis of quantum as well as classical many-body dynamics in a large variety of systems, ranging from ultracold quantum gases to cosmology.

This chapter begins with an introduction in Sec. 3.1 and a general discussion on symmetries in many-body systems in Sec. 3.2, emphasising the differences between equilibrium

and nonequilibrium cases. Afterwards, our system of study, the spinor Bose gas is presented with a brief review of its mean-field approximation in Sec. 3.3. This is followed by the discussion of symmetry identities in Sec. 3.4 with different n-point correlation functions, which lead to our specific investigations, namely the restoration of explicitly broken symmetries throughout the dynamics in an isolated system in Sec. 3.5, and the exploration of spontaneous symmetry breaking under far-from-equilibrium conditions with cold atom experimental data in Sec. 3.6. We conclude with a discussion of our findings and an outlook in Sec. 3.7.

3.1 Introduction and overview

Important progress in our understanding of the complexity of macrophysics in quantum many-body systems has been achieved with classical computers for ground state or equilibrium properties. However, ab initio understanding of general dynamical or nonequilibrium behaviour is particularly scarce in situations that are not simple extensions of near-equilibrium properties, such as the emergence of instabilities or turbulent flows. The search for emergent theories that effectively describe nonequilibrium macroscopic behaviour, their classification, and justification from first principles is one of the most pressing research directions in quantum many-body physics [10, 29, 94].

The notion of effective field theories for macroscopic behaviour is a well-established powerful tool for equilibrium many-body systems, where the symmetries of the underlying Hamiltonian or action together with the knowledge of the order-parameter field allows one to construct the relevant description consistent with the symmetries [54, 55]. However, out of equilibrium it is especially important to distinguish the symmetries of a state from the symmetries of a Hamiltonian. In fact, even the simplest nonequilibrium states with an order-parameter field that is initially not in its free-energy ground state can explicitly break a symmetry of the Hamiltonian in general. This raises the important question about the effective or emergent symmetries of nonequilibrium systems and whether/when explicitly broken symmetries get dynamically restored. To address this question, one needs to be able to quantify the symmetry content of a nonequilibrium state. This is also a crucial prerequisite for extracting the effective field theory actions [95, 96] or Hamiltonians [97] from experimental or simulation data of quantum many-body systems. The question of dynamical symmetry restoration has been recently investigated based on entanglement asymmetry [56, 98] and single-body density matrix [58].

In this work, we describe a general pathway for extracting the effective symmetries of nonequilibrium quantum many-body systems using equal-time correlation functions. The approach takes into account that the density operator $\hat{\rho}_t$ describing a nonequilibrium state at any time t may not be directly related to the Hamiltonian $\hat{H}$, unlike in thermal equilibrium, where $\hat{\rho}_{\text{eq}} \sim \exp\left(-\beta \hat{H}\right)$ for the example of a canonical ensemble. Instead, we exploit that the symmetries can be classified on the level of observables, i.e., expectation values $\mathrm{Tr}\left[\hat{\rho}_t \, \hat{\mathcal{O}}(\boldsymbol{x}_1, \ldots, \boldsymbol{x}_n)\right]$ of n-point operators $\hat{\mathcal{O}}(\boldsymbol{x}_1, \ldots, \boldsymbol{x}_n)$. We derive exact relations between expectation values of operators involving different numbers n of spatial points, which encode the symmetry properties of the system. Our equations can be viewed as nonequi-

librium versions of (equal-time) Ward identities [50]. For the example of a spin-one Bose gas, we show that extracting the n-point functions from spatially resolved data allows one to efficiently uncover the presence or absence of a given symmetry. For this, we define symmetry witnesses and apply our approach to analyse the dynamical effective restoration of explicit symmetry breaking. Remarkably, we observe that effective symmetry restoration can occur long before the system equilibrates, which is a crucial ingredient for the construction of effective theories for nonequilibrium evolutions. Importantly, we also demonstrate how the method can be used to define and identify spontaneous symmetry breaking even far from equilibrium, opening up numerous applications for nonequilibrium phase transitions.

While the approach can be used for any analytical or classical simulation technique of quantum many-body systems, we emphasise that it is particularly well suited for large-scale (analogue) quantum simulations based on setups with ultracold quantum gases [32, 33]. These systems can realise a wide range of Hamiltonians with different symmetries, variable interactions, and degrees of freedom based on atomic, molecular, and optical physics engineering. They offer high control in the preparation and read-out of the quantum dynamics, with the ability to explore new regimes even far from equilibrium [21, 22, 24] that are otherwise difficult to access directly.

3.2 Symmetries and dynamics

For the following, it will be important to distinguish symmetries of a state or density operator from symmetries of the Hamiltonian that governs the equations of motion [99]. A Hamiltonian $\hat{H}$ is symmetric under the group of transformations G if $[U, \hat{H}] = 0$ for every $U \in G$. This group can be either discrete or continuous, with U forming an (anti-)unitary representation of G on the Hilbert space of the system [100, 101]. In this work, we focus on the case of continuous unitary symmetries. In addition, we assume that the considered continuous symmetries have the structure of a Lie group, whose elements can be written as

$$U = \exp(\mathrm{i}\alpha_k Q_k)\,, \quad [Q_i, Q_j] = \mathrm{i} f_{ijk} Q_k\,, \tag{3.1}$$

where f_{ijk} are the structure constants that characterise the underlying Lie algebra, and the operators Q_k are the generators of the group. For brevity, we have restricted ourselves to elements of G that are simply connected to the unity element. Since U is unitary, the operators Q_k are Hermitian and taken to correspond to physical observables. From Eq. (3.1) it immediately follows that $[Q_k, \hat{H}] = 0$, implying that the generators of G are conserved quantities.

On the other hand, the state at time t described by the density operator $\hat{\rho}_t$ is symmetric under G if $[U, \hat{\rho}_t] = 0$ for every $U \in G$. From this, one also concludes the following rigorous property for the unitary time evolution of quantum systems described by the von Neumann equation: if the density operator $\hat{\rho}_{t_0}$ explicitly breaks a symmetry of the Hamiltonian $\hat{H}$ at some given time t_0, then it cannot be restored on a fundamental level at any other time. Conversely, starting with a symmetric state and following a unitary evolution respecting the same symmetry, it will never be explicitly broken.

However, these strict statements are not in conflict with the assertion that typical observables may show emergent phenomena that involve the effective restoration of an initially broken symmetry or vice versa. In this work, we will consider expectation values $\mathrm{Tr}\left[\hat{\rho}_t\,\hat{\mathcal{O}}(\boldsymbol{x}_1,\ldots,\boldsymbol{x}_n)\right]$ of n-point operators $\hat{\mathcal{O}}(\boldsymbol{x}_1,\ldots,\boldsymbol{x}_n)$ as observables. An effective symmetry still remains a set of transformations that leave observable properties of the system unchanged, though the set of observables becomes restricted in practice, which in our case will be related to finite numbers for n. For instance, the notion of effective or relevant symmetries for observable properties is at the heart of macroscopic theories for nonequilibrium evolutions, such as effective kinetic theories or hydrodynamics describing the long-time and long-distance behaviour of an underlying microscopic many-body system in terms of few-point functions only [29]. In this respect, the discussion also closely resembles the one concerning thermalisation in closed quantum systems with unitary time evolution [10].

So far we have distinguished the symmetries of the state from those of the Hamiltonian with the possibility of explicit symmetry breaking. However, for many-body systems, it is also important to distinguish an explicit breaking of a symmetry from the phenomenon of spontaneous symmetry breaking. The latter is crucial, e.g., for our understanding of typical phase transitions where an order parameter can be defined to vanish on one side of the transition while taking on a nonzero value otherwise. Though this is of course well established in equilibrium, the definition and detection of spontaneously broken symmetries out of equilibrium is much less explored.

Spontaneous symmetry breaking implies that the symmetry of the system's state is reduced to a residual symmetry subgroup of G without explicit symmetry violation. Generally, the system will be in a superposition of degenerate states such that the symmetry breaking is not manifest. To efficiently characterise spontaneous symmetry breaking in terms of an order parameter, one needs to lift the degeneracy and favour one of the infinitely many symmetry-breaking configurations. This is typically achieved by adding a small symmetry-breaking perturbation to the Hamiltonian, such as $\hat{H} \to \hat{H} + \int J\,\hat{\mathcal{O}}$ for a given order-parameter operator $\hat{\mathcal{O}}$. To remove the explicit symmetry breaking in the end, such a bias is introduced as a limiting procedure. Spontaneous symmetry breaking is then identified by a nonvanishing expectation value

$$\lim_{J\to 0^+} \mathrm{Tr}\left[\hat{\rho}_t\,\hat{\mathcal{O}}(\boldsymbol{x})\right] = v_t(\boldsymbol{x})\,. \tag{3.2}$$

Crucially, in the case of spontaneous symmetry breaking, one finds a nonzero order parameter $v_t(\boldsymbol{x}) \neq 0$ even in the limit of a vanishing perturbation, $J \to 0^+$. On the other hand, $v_t(\boldsymbol{x})$ is zero in the symmetric state. The choice of an order parameter operator is not unique, although often suggested by the physics of the spontaneous symmetry breaking. Here, we have restricted ourselves to cases that can be characterised by a local order parameter. For translationally invariant systems in space and/or time, the function $v_t(\boldsymbol{x})$ naturally reduces to a respective constant.

For nonequilibrium systems, there are interesting further options to introduce a symmetry-breaking bias, e.g., through the choice of an explicit symmetry-breaking state at a given initial time t_0 with

$$[U,\hat{\rho}_{t_0}] \neq 0\,, \quad [V,\hat{\rho}_t] = 0\,, \tag{3.3}$$

while the symmetry of the Hamiltonian remains unaffected with $[U, \hat{H}] = 0$. In this case, the initial explicit symmetry breaking is not restricted to small perturbations. In situations where the explicitly broken symmetry gets effectively restored dynamically during the time evolution, spontaneous symmetry breaking is still signalled by the emergence of a nonzero order parameter (3.2). Typically, this requires an evolution of the system to sufficiently late times such that the initial explicit symmetry breaking is effectively reduced to a small perturbation. In the following sections, we will discuss how symmetry can be broken through the initial condition in systems out of equilibrium. Specifically, we will introduce relationships between different n-point functions to identify symmetries and to distinguish between explicit and spontaneous symmetry breaking.

3.3 Spinor Bose gas

Both experimentally and in our numerical simulations, we consider a homogeneous one-dimensional spin-1 Bose gas described by the Hamiltonian

$$\hat{H} = \int \mathrm{d}x \left[\hat{\boldsymbol{\psi}}^\dagger \left(-\frac{1}{2M}\frac{\partial^2}{\partial x^2} + q f_z^2 \right) \hat{\boldsymbol{\psi}} + \frac{c_0}{2} :\hat{n}^2: + \frac{c_1}{2} :\hat{\boldsymbol{F}}^2: \right], \tag{3.4}$$

where $\hat{\boldsymbol{\psi}} = (\hat{\psi}_1, \hat{\psi}_0, \hat{\psi}_{-1})^T$ is the three-component bosonic field representing the magnetic sub-levels $m_\mathrm{F} = 0, \pm 1$ of the $F = 1$ hyperfine manifold, M denotes the atom mass, and $\hat{n} = \hat{\psi}_m^\dagger \hat{\psi}_m$. The spin-changing collisions are described in terms of the spin operators $\hat{F}_i = \hat{\psi}_m^\dagger (f_i)_{mm'} \hat{\psi}_{m'}$, with $\boldsymbol{f} = (f_x, f_y, f_z)^T$ being the generators of the so(3) Lie algebra in the three-dimensional fundamental representation. The bosonic field operators obey the standard commutation relations $[\hat{\psi}_m(x), \hat{\psi}_{m'}^\dagger(x')] = \delta_{mm'}\delta(x - x')$, $[\hat{\psi}_m(x), \hat{\psi}_{m'}(x')] = 0$. Together with $[f_i, f_j] = \mathrm{i}\varepsilon_{ijk} f_k$, this readily implies $[\hat{F}_i(x), \hat{F}_j(x')] = \mathrm{i}\varepsilon_{ijk}\hat{F}_k(x)\,\delta(x - x')$. Here and in the following, Einstein's summation convention is implied and we use units where $\hbar = k_\mathrm{B} = 1$.

3.3.1 Mean-field phase diagram

In the mean-field approximation, the quantum field operator can be decomposed in terms of the mean value of the field and the fluctuations around it, $\hat{\psi}_m(x) = \psi_m(x) + \delta\hat{\psi}_m(x)$, where $\psi_m(x) = \left\langle \hat{\psi}_m(x) \right\rangle$ is the expectation value of the field. For the case of large densities and weak interactions, classical-statistical fluctuations become much larger than quantum fluctuations, and the ultracold quantum many-body system can be described by a classical field theory, where one drops the quantum fluctuations and the field operator is replaced by its expectation value $\hat{\psi}_m(x) \to \psi_m(x)$. Apart from requiring a large number of atoms and weak interactions, the system also needs to be at a low temperature such that thermal fluctuations can also be neglected. In the mean-field approximation, the complex-valued field $\psi_m(x)$ obeys the Gross-Pitaevskii equation (GPE) for the spinor condensate, which is given by

$$\mathrm{i}\partial_t \boldsymbol{\psi}(x,t) = \left[-\frac{1}{2M}\frac{\partial^2}{\partial x^2} + q f_z^2 + c_0 n(x,t) + c_1 \boldsymbol{F}(x,t)\cdot\boldsymbol{f} \right] \boldsymbol{\psi}(x,t). \tag{3.5}$$

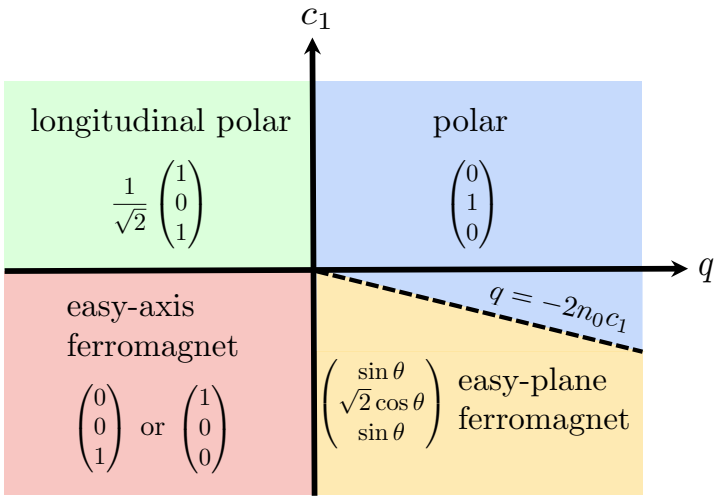

Figure 3.1. Mean-field phase diagram of a spin-1 Bose–Einstein condensate in the $q - c_1$ plane.

By determining the stationary solutions and the different regimes for which the solutions minimise energy, one can find the different ground states of the system for different values of the parameters. These different ground states can then be represented on a phase diagram, as depicted in Fig. 3.1. We also note that for stable Bose–Einstein condensates, density-density interactions are repulsive ($c_0 > 0$). The quadratic Zeeman shift q and the terms proportional to c_1 in the Hamiltonian give rise to competing energy scales that can lead to different phases in the system in the $q - c_1$ plane. For our case, the regime of interest is the ferromagnetic one with $c_1 < 0$, which favours spins to align when $q = 0$. The line $q = 2nc_1$ separates the polar and easy-plane phases. The polar phase shows no magnetisation and it is found in the parameter regime $q > 2nc_1$, while for $0 < q < 2nc_1$, the system is in the easy-plane phase, where there is a magnetisation transverse to the F_z axis, with a complex order parameter $F_\perp = F_x + \mathrm{i}F_y$ and with magnetisation $|F_\perp| = [1 - q^2/(2q)^2]^{1/2}$.

3.3.2 Experimental setup

We apply our analysis to measurements from a spinor Bose gas of ^{87}Rb, which features rotationally invariant ferromagnetic ($c_1 < 0$) spin-spin as well as repulsive ($c_0 > 0$) density-density interactions, with $|c_0/c_1| \approx 200$. As illustrated in Fig. 3.2(a), the condensate is confined in a quasi one-dimensional box trap. The quadratic Zeeman shift q is induced by an external magnetic field which shifts the energy of the $m_\mathrm{F} = \pm 1$ levels relative to the $m_\mathrm{F} = 0$ component, and is adjusted by using off-resonant microwave dressing, as depicted in Fig. 3.2(b). We will consider data where the system is initialised with zero average longitudinal (z-axis) spin such that only the $m_F = 0$ sublevel is populated. The microwave dressing initiates the spin-exchange dynamics by quenching from the polar to the easy-plane ferromagnetic phase, and excitations build up in the $F_x - F_y$ plane, with the spin acquiring a mean length with a random orientation in the $F_x - F_y$ plane. This transversal spin degree of freedom is examined by the spatially resolved detection of the complex valued field $F_\perp(x) = F_x(x) + \mathrm{i}F_y(x)$.

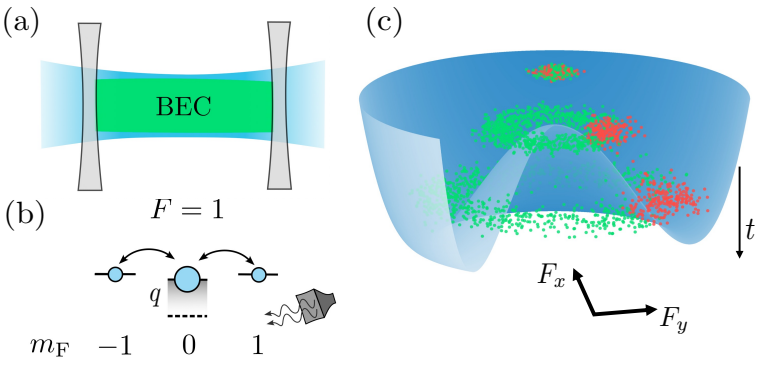

Figure 3.2. (a) Quasi one-dimensional Bose–Einstein condensate in a box-like potential formed by an elongated dipole trap (blue) with repulsive walls (light grey). The overall density (green) is approximately uniform throughout the cloud. (b) The effective quadratic Zeeman energy difference q between the $m_F = 0$ and $m_F = \pm 1$ levels is adjusted using off-resonant microwave dressing (grey). This enables the tuning of spin-changing collisions into resonance, which can redistribute population among the hyperfine levels. (c) Schematics of many individual realisations averaged over in green, with a single realisation highlighted in red in a "sombrero" potential associated with spontaneous symmetry breaking. The vertical t arrow indicates the evolution in time.

Experimentally, we simultaneously extract the spatial spin profiles $F_x(x)$ and $F_y(x)$ via spin rotations from the $F_x - F_y$ plane to the F_z direction and subsequent absorption imaging [21, 102]. For more details on the experimental setup and specific parameters, see App. A.1 and Ref. [25].

The Hamiltonian (3.4) is symmetric under SO(2) × U(1) transformations for $q \neq 0$, where SO(2) denotes the group of rotations about the F_z axis on the $F = 1$ hyperfine manifold. The spin operator $\hat{\boldsymbol{F}}$ can play the role of the order parameter for the symmetry breaking of the SO(2) group. In the case of spontaneous symmetry breaking, according to the definition (3.2), there is a nonzero expectation value $\langle \hat{F}_i \rangle$. This situation is illustrated in Fig. 3.2(c). Due to the underlying SO(2) symmetry, we can always align the expectation value along one of the axes, e.g., $\langle \hat{F}_x \rangle = 0$, $\langle \hat{F}_y \rangle = v_t$.

Establishing long-range coherence across the entire system requires some time. This is especially true for lower-dimensional systems with continuous symmetries, where fluctuations preventing the build-up of long-range order are very strong, as highlighted by the Mermin–Wagner theorem [103]. To ensure an adequate level of coherence across the system during the time of observation, we reduce our analysis to a finite central region of our data as specified in App. A.1. For this subsystem, the condensate builds up a constant phase across the sample, and the order parameter can be assumed to be approximately homogeneous for the considered evolution times.

3.4 Symmetry identities between equal-time correlation functions

We are probing the symmetry content of our system via equal-time correlation functions. Since such correlators can be extracted from measurements at different snapshots in time, they are particularly convenient for studying cold atom systems and matching theory to experiment. In spinor Bose gases, a convenient choice of experimentally accessible observables are spin operators $\hat{F}_i$. On a theoretical level, the corresponding equal-time correlation functions can then be conveniently extracted from the generating functional

$$Z_t[\boldsymbol{J}] = \mathrm{Tr}\left\{\hat{\rho}_t \exp\left[\int \mathrm{d}x\, \boldsymbol{J}(x)\cdot\hat{\boldsymbol{F}}(x)\right]\right\}, \tag{3.6}$$

where $\hat{\rho}_t$ is the density matrix of the system in the Schrödinger picture at time t, not necessarily normalised to unity. Symmetrically ordered equal-time spin correlation functions are obtained by taking derivatives with respect to $J_i(x)$ and setting the latter to zero:

$$\frac{Z^{(n)}_{t,i_1\ldots i_n}[0]\,(x_1,\ldots,x_n)}{Z_t[0]} = \frac{1}{n!}\sum_{\sigma\in S_n}\left\langle \hat{F}_{i_{\sigma_1}}(x_{\sigma_1})\ldots\hat{F}_{i_{\sigma_n}}(x_{\sigma_n})\right\rangle. \tag{3.7}$$

Here, the prefactor $1/Z_t[0]$ takes care of the density matrix normalisation, S_n denotes the set of all permutations of $\{1,\ldots,n\}$, $\langle\ldots\rangle \equiv \mathrm{Tr}\{\hat{\rho}_t\ldots\}$, and we have introduced the notation

$$Z^{(n)}_{t,i_1\ldots i_n}[\boldsymbol{J}]\,(x_1,\ldots,x_n) \equiv \frac{\delta^n Z_t[\boldsymbol{J}]}{\delta J_{i_1}(x_1)\ldots\delta J_{i_n}(x_n)}\,. \tag{3.8}$$

The correlation functions (3.7) contain disconnected, lower-order parts. To remove this redundant information and generate connected correlation functions, one can invoke an equal-time equivalent of the Schwinger functional,

$$E_t\,[\boldsymbol{J}] = \log Z_t\,[\boldsymbol{J}]\,. \tag{3.9}$$

As an example, a two-point connected symmetric spin correlation function generated by the functional E_t is given by

$$E^{(2)}_{t,xy}\,[0]\,(x_1,x_2) = \frac{1}{2}\left\langle \hat{F}_x(x_1)\,\hat{F}_y(x_2)+\hat{F}_y(x_2)\,\hat{F}_x(x_1)\right\rangle - \left\langle \hat{F}_x(x_1)\right\rangle\left\langle \hat{F}_y(x_2)\right\rangle,$$

and correspondingly for higher-order correlation functions.

Since the spin operators $\hat{F}_i$ transform trivially under $\mathrm{U}(1)$, we will focus on the $\mathrm{SO}(2)$ part and derive associated symmetry identities between different correlation functions. Following the discussion in the previous sections, we will assume that the initial state $\hat{\rho}_{t_0}$ is also $\mathrm{SO}(2)$-invariant, ensuring that the symmetry is fully respected on the dynamical level. In this case, the density matrix $\hat{\rho}_t$ remains formally symmetric at any time $t \geq t_0$, even in the case of spontaneous symmetry breaking. As pointed out above, to address the latter scenario, one has to introduce a symmetry-breaking bias to the system. In this work, the role of such a bias will be played by the sources J_i coupled to the spin operators in the definition (3.6) of the generating functional, which will be addressed in more detail in the following.

From (3.6) we conclude, together with $\hat{\rho}_t = U\,\hat{\rho}_t\,U^{-1}$ and with $U \in \mathrm{SO}(2)$, that

$$Z_t[\boldsymbol{J}] = \mathrm{Tr}\left\{\hat{\rho}_t \exp\left[\int \mathrm{d}x\, \boldsymbol{J}(x)\cdot\left(U^{-1}\,\hat{\boldsymbol{F}}(x)\,U\right)\right]\right\}, \tag{3.10}$$

where we have used the cyclic property of trace and $U^{-1}\exp(A)\,U = \exp(U^{-1}A\,U)$.

The spin operators $\hat{F}_i$ live in the fundamental representation of the rotation group and thus transform as

$$\hat{F}_i \to R_{ij}(\epsilon)\,\hat{F}_j = \hat{F}_i + \mathrm{i}\epsilon T_{ij}\hat{F}_j + \mathcal{O}\left(\epsilon^2\right),\ T = \begin{pmatrix} 0 & \mathrm{i} & 0 \\ -\mathrm{i} & 0 & 0 \\ 0 & 0 & 0 \end{pmatrix}, \tag{3.11}$$

where $R(\epsilon)$ denotes the rotation matrix by an angle ϵ about the F_z axis with its single generator T.

Together, Eqs. (3.6) – (3.11) imply $Z_t[\boldsymbol{J}] = Z_t[R^{-1}\boldsymbol{J}]$, and likewise $E_t[\boldsymbol{J}] = E_t[R^{-1}\boldsymbol{J}]$, where we have used the fact that $\boldsymbol{J}\cdot\left(R\hat{\boldsymbol{F}}\right) = (R^{-1}\boldsymbol{J})\cdot\hat{\boldsymbol{F}}$. Taking R to be infinitesimal, this yields $E_t[J_x - \epsilon J_y, J_y + \epsilon J_x] - E_t[J_x, J_y] = 0$. Expanding it to linear order in the rotation angle ϵ, we finally derive the master symmetry identity:

$$\int \mathrm{d}x'\left[J_x(x')\,E^{(1)}_{t,y}[\boldsymbol{J}](x') - J_y(x')\,E^{(1)}_{t,x}[\boldsymbol{J}](x')\right] = 0\,. \tag{3.12}$$

By taking further J-derivatives one can generate an infinite hierarchy of symmetry identities encoding the $\mathrm{SO}(2)$ symmetry of the system.

Here and in the following, we assume that the mean field does not break spatial homogeneity. To emphasise the distinction between the fields $\hat{F}_x$ and $\hat{F}_y$, we then introduce the notation $(F_x, F_y) \to (\pi, \sigma)$, $(J_x, J_y) \to (J_\pi, J_\sigma)$, and accordingly $\langle\hat{\pi}\rangle = 0$ and $\langle\hat{\sigma}\rangle = \nu_t$. To allow for a spontaneous symmetry-breaking scenario, we first explicitly break the symmetry via a linear source term $\int \mathrm{d}x\, J\,\hat{\sigma}(x)$, cf. the discussion in Sec. 3.2:

$$\langle\hat{\sigma}\rangle = \lim_{J\to 0^+} E^{(1)}_{t,\sigma}[J_\pi = 0, J_\sigma = J] = \nu_t\,. \tag{3.13}$$

The symmetry-breaking case corresponds to $\nu_t \neq 0$, whereas $\nu_t = 0$ in the symmetric phase. For spin systems, this symmetry-breaking term allows for a simple physical interpretation as a deformation of the initial density matrix, which is discussed in more detail in App. A.2.

Differentiating the master symmetry identity (3.12) once with respect to J_π we get

$$\int \mathrm{d}x'\left[\delta(x'-x'')\,E^{(1)}_{t,\sigma}[\boldsymbol{J}](x') + J_\pi(x')\,E^{(2)}_{t,\sigma\pi}[\boldsymbol{J}](x',x'') - J_\sigma(x')\,E^{(2)}_{t,\pi\pi}(x',x'')\right] = 0\,.$$

Setting the sources to $(0, J)$ and going to Fourier space, we obtain

$$E^{(1)}_{t,\sigma}[0,J] - J\,\tilde{E}^{(2)}_{t,\pi\pi}[0,J](p=0,-p=0) = 0\,, \tag{3.14}$$

where we have introduced the notation

$$E^{(n)}_{t,i_1\ldots i_n}(p_1,\ldots,p_n) \equiv 2\pi\delta\left(\sum_{i=1}^{n} p_n\right)\tilde{E}^{(n)}_{t,i_1\ldots i_n}(p_1,\ldots,p_n)\,. \tag{3.15}$$

Similarly, differentiating the master symmetry identity (3.12) once with respect to both J_π and J_σ and then setting the sources to $(0, J)$ yields

$$J \lim_{q\to 0} \tilde{E}^{(3)}_{t,\pi\pi\sigma}[0,J]\,(q,p,-p-q) = \tilde{E}^{(2)}_{t,\sigma\sigma}[0,J]\,(p,-p) - \tilde{E}^{(2)}_{t,\pi\pi}[0,J]\,(-p,p)\,.$$

Taking the $J \to 0^+$ limit and using (3.13) and (3.14) we then find

$$v_t \lim_{q\to 0} \frac{\tilde{E}^{(3)}_{t,\pi\pi\sigma}(q,p,-p-q)}{\tilde{E}^{(2)}_{t,\pi\pi}\,(q,-q)} = \tilde{E}^{(2)}_{t,\sigma\sigma}(p,-p) - \tilde{E}^{(2)}_{t,\pi\pi}(-p,p)\,, \tag{3.16}$$

with $\tilde{E}^{(n)}_t \equiv \tilde{E}^{(n)}_t[J_\pi = 0, J_\sigma = 0]$. Here, we have taken into account that only the quotient of $\tilde{E}^{(3)}_{t,\pi\pi\sigma}\,(q,p,-p-q)$ and $\tilde{E}^{(2)}_{t,\pi\pi}\,(q,-q)$ may have a finite $q \to 0$ limit. While Eq. (3.16) connects two- and three-point functions, additional symmetry identities relating higher-order correlation functions can be obtained by taking further derivatives:

$$\begin{aligned} v_t \lim_{k\to 0} \frac{\tilde{E}^{(4)}_{t,\pi\pi\sigma\sigma}\,(k,p,q,-k-p-q)}{\tilde{E}^{(2)}_{t,\pi\pi}\,(k)} &= \tilde{E}^{(3)}_{t,\sigma\sigma\sigma}\,(p,q,-p-q) \\ &\quad - \tilde{E}^{(3)}_{t,\pi\pi\sigma}\,(q,p,-p-q) - \tilde{E}^{(3)}_{t,\pi\pi\sigma}\,(p,-p-q,q)\,, \end{aligned} \tag{3.17a}$$

$$\begin{aligned} v_t \lim_{k\to 0} \frac{\tilde{E}^{(4)}_{t,\pi\pi\pi\pi}\,(k,p,q,-k-p-q)}{\tilde{E}^{(2)}_{t,\pi\pi}\,(k)} &= \tilde{E}^{(3)}_{t,\pi\pi\sigma}\,(p,q,-p-q) \\ &\quad + \tilde{E}^{(3)}_{t,\pi\pi\sigma}\,(p,-p-q,q) + \tilde{E}^{(3)}_{t,\pi\pi\sigma}\,(q,-p-q,p)\,, \end{aligned} \tag{3.17b}$$

and so forth.

Symmetry identities, akin to those derived in the present section, then serve as a manifestation of the system's symmetry properties on the level of correlation functions. Since n-point correlation functions can be readily extracted from numerically simulated data or experimental measurements, the symmetry identities can be explicitly checked. This makes them a powerful tool for analysing the symmetry content of quantum many-body systems, allowing to determine whether the symmetry is broken explicitly, spontaneously, or not broken at all.

Based on the above symmetry identities one can introduce symmetry witnesses, which provide efficient measures of the symmetry content of a given system. In particular, higher-order correlation functions are often difficult to visualise and the introduction of a norm as a measure can be very convenient. Defining the left- and right-hand sides of (3.16) as

$$\begin{aligned} f^{(3)}_{t,\pi\pi\sigma}(p) &= v_t \lim_{q\to 0} \frac{\tilde{E}^{(3)}_{t,\pi\pi\sigma}(q,p,-p-q)}{\tilde{E}^{(2)}_{t,\pi\pi}(q,-q)}\,, \\ f^{(2)}_{t,\pi\pi\sigma}(p) &= \tilde{E}^{(2)}_{t,\sigma\sigma}(p,-p) - \tilde{E}^{(2)}_{t,\pi\pi}(-p,p)\,, \end{aligned} \tag{3.18}$$

we may encode the symmetry content by measuring a distance between the two functions using the standard L_1-norm, $\|f\| = L^n \int \mathrm{d}p_1 \ldots \mathrm{d}p_n\, |f(p_1,\ldots,p_n)|$, with L being the system size setting the smallest unit of momentum $1/L$. To avoid biasing the infrared momentum region, where the correlation functions are typically larger, we normalise the difference by

dividing it by double the average value of $|f^{(3)}|$ and $|f^{(2)}|$, which yields

$$Q^{(3)}_{\pi\pi\sigma}(t) = \lim_{\varepsilon\to 0^+} \left\| \frac{f^{(3)}_{t,\pi\pi\sigma} - f^{(2)}_{t,\pi\pi\sigma}}{\left|f^{(3)}_{t,\pi\pi\sigma}\right| + \left|f^{(2)}_{t,\pi\pi\sigma}\right| + \varepsilon} \right\|. \tag{3.19}$$

Here, ε is a regularisation parameter ensuring that $Q^{(3)}_{\pi\pi\sigma} = 0$ when $f^{(3)}_{t,\pi\pi\sigma} = f^{(2)}_{t,\pi\pi\sigma} = 0$, i.e., in the absence of both explicit as well as spontaneous symmetry breaking. In practice, the choice of ε is motivated by the value of statistical error, inevitable in any experimental or numerical setup. Note that the normalisation choice implies $0 \leq Q^{(3)}_{\pi\pi\sigma} \leq 1$, with the upper bound following from the Cauchy–Schwarz inequality.

At each point in time, the quantity $Q^{(3)}_{\pi\pi\sigma}$, which we call a symmetry witness, connects one-, two-, and three-point correlation functions and quantifies the degree of violation of the symmetry identity (3.16). Analogously, one can introduce higher-order witnesses $Q^{(4)}_{\pi\pi\sigma\sigma}$ and $Q^{(4)}_{\pi\pi\pi\pi}$ using the identities (3.17a) and (3.17b), respectively, characterising the symmetry content with respect to the higher-order correlation functions. Geometrically, the connected correlation functions characterise the shape and the inner structure of the histograms, like the ones depicted in Fig. 3.3. Such histograms consist of "sub-histograms", one for each spatial point x_i, or momentum mode p_i, in the system. The one-point functions correspond to their positions, the two-point functions are related to their widths and heights, while higher-order n-point functions reflect cross-correlations between the sub-histograms. Symmetry then puts constraints on their allowed shapes and cross-correlations, and symmetry witnesses represent how well these constraints are satisfied. The spatial correlation functions can be extracted from numerical simulations or experimentally by sampling readouts of the transverse spin $F_\perp(x) = F_x(x) + \mathrm{i}F_y(x)$ [102]. As a result, probing the symmetry properties of the system via exact relations between observable correlation functions proves to be an effective approach, as demonstrated in the following sections.

3.5 Nonequilibrium symmetry restoration

In the following, we investigate the dynamics of a spinor Bose gas (3.4) prepared in an explicitly symmetry-broken state. Whether the initially explicitly broken symmetry gets effectively restored during the dynamics will be analysed using the symmetry witnesses introduced above. We employ the truncated Wigner approximation (TWA), which describes the dynamics for highly occupied systems at not too late times and weak couplings [71]. The numerical integration of the system is done via a pseudo-spectral split-step method and gives the time evolution of the full spinor state $\boldsymbol{\psi} = (\psi_1, \psi_0, \psi_{-1})^T$ comprised of the complex scalar Bose fields describing the three magnetic components of the spin-1 manifold.

We start from an initial state with nonvanishing n-point spin correlations that violate the SO(2) rotational symmetry in the $F_x - F_y$ plane. For this, we consider the spinor condensate in the mean-field ground state of the easy-plane phase, which is characterised by a well-defined spin length and orientation. In addition, we imprint a Gamma distribution function in momentum space in the fundamental fields and add noise in the Bogoliubov modes of the initial state to achieve a sizeable explicit symmetry breaking. We then quench

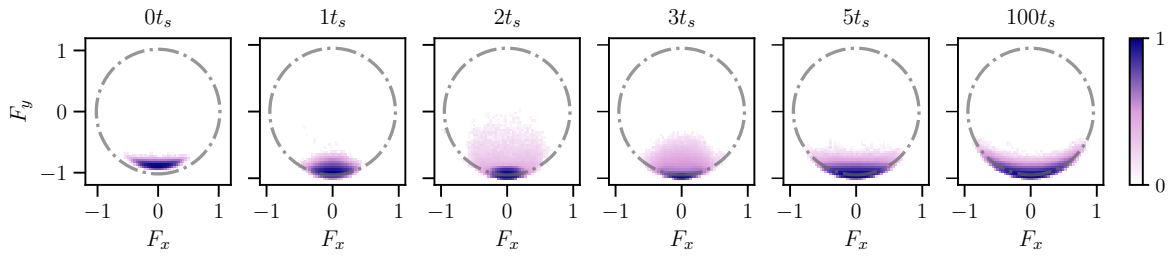

Figure 3.3. Histograms of the spin orientations in the $F_x - F_y$ plane normalised by the atom number for $q_f = 0.6n|c_1|$ and averaged over 10^3 runs. The dash-dotted line represents the average spin length $\langle |F_\perp| \rangle = \sqrt{1 - (q/2n|c_1|)^2} \sim 0.95$.

the quadratic Zeeman shift from $q_\mathrm{i} = 0.9n|c_1|$ to $q_\mathrm{f} = 0.6n|c_1|$, where we verified that no significant excitations of topological defects are excited in the system. We propagate this state according to the classical field equations of motion (3.5) with periodic boundary conditions.

The physical parameters of the simulations aim to resemble a cloud of ^{87}Rb atoms in a one-dimensional geometry as performed in the experiments [25, 96, 104], the main differences being an increased homogeneous density n compared to the experiment and a purely one-dimensional setting with no trapping potential. We simulate a cloud of $3 \cdot 10^6$ particles on a numerical grid containing $N = 4096$ points corresponding to a physical length of 220 µm. The spin healing length is given by $\xi_\mathrm{s} = 8$ lattice units, and spin-changing collisions occur on a timescale of $t_\mathrm{s} = 696$ in numerical time units. We give spatial length in terms of the spin healing length $\xi_\mathrm{s} = (2Mn|c_1|)^{-1/2}$ and time in units of the characteristic spin-changing collision time $t_\mathrm{s} = 2\pi/(n|c_1|)$. Furthermore, the field operators are normalised with respects to the total density $\tilde{\psi}_m = \psi_m/\sqrt{n}$, which results in a normalisation of the spin vector as well $\tilde{\boldsymbol{F}} = \boldsymbol{F}/n$. In the following, the tilde is omitted and all values are to be understood as normalised values unless explicitly stated otherwise. Upon extracting the spin degrees of freedom F_x and F_y, we compute the relevant two-, three-, and four-point correlation functions appearing in the identities (3.16), (3.17a), and (3.17b). Further technical details of these computations are given in App. A.3.

It is instructive to first examine the probability distribution of local spins in real space by averaging over many realisations. In Fig. 3.3, we depict an $F_z = 0$ cut of the probability density in spin configuration space. From the left graph, one observes that the initial state is characterised by a sizeable spin length with a rather well-defined orientation. As a consequence, one may separate two types of excitations for the transversal spin $\boldsymbol{F}_\perp$: a radial "Higgs"-like mode associated with perturbations of the spin length $|F_\perp|$, and a transverse "Goldstone"-like mode associated with perturbations of the angle φ_L, respectively. Since the state is initialised away from the minimum of the sombrero-shaped effective potential illustrated in Fig. 3.2, one observes dynamics in the radial direction, such that the spin length $|F_\perp|$ acquires a range of values that are also significantly smaller than the initial one. As seen in the histograms, this occurs predominantly during the first few characteristic spin-changing collision times t_s. During this time, the nonequilibrium "Higgs"-like mode explores the inner part of the effective potential, whose nonconvex shape is expected to

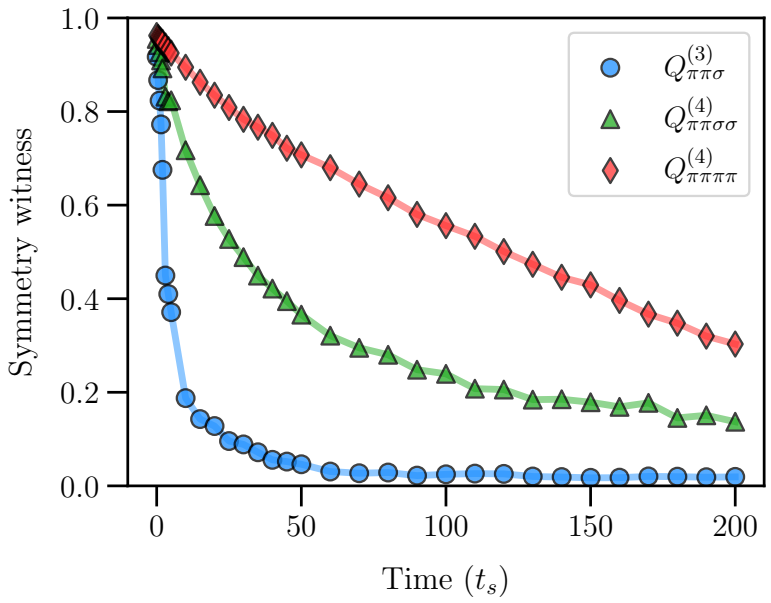

Figure 3.4. Evolution of the symmetry witnesses $Q^{(n)}$ for a system prepared in a state which explicitly breaks the SO(2) symmetry of the Hamiltonian with a subsequent quench from $q_\mathrm{i} = 0.9n|c_1|$ to $q_\mathrm{f} = 0.6n|c_1|$, where $0 \leq Q^{(n)} \leq 1$. The value of $Q^{(n)} = 0$ corresponds to the absence of explicit symmetry violation. Here, $Q^{(3)}_{\pi\pi\sigma}$ is the identity connecting two- and three-point functions appearing in Eq. (3.16), while $Q^{(4)}_{\pi\pi\sigma\sigma}$ and $Q^{(4)}_{\pi\pi\pi\pi}$ connect three- and four-point functions.

lead to a fast instability growth of the mode occupancy in a characteristic momentum range. However, after about $\sim 5\,t_s$, perturbations in $|F_\perp|$ are seen to become more and more suppressed. Instead, significantly slower dynamics for the transverse mode starts dominating, by which the spin distribution settles into a banana-like shape as it spreads out around the ring set by the minimum of the effective potential.

While the histograms indicate the different dominant excitations and timescales of the system, one needs further information to quantify the initial explicit symmetry breaking and its effective restoration. For instance, both the left graph of Fig. 3.3 at $0\,t_s$ and the right one at $100\,t_s$ indicate configurations with comparable spin length and rather small spread in the radial direction. However, their transverse extensions along the ring, which represent the "Goldstone"-like fluctuations, are significantly different. As described in Sec. 3.4, in the absence of explicit symmetry breaking there exists a well-defined relation between the spin length and the fluctuations, which we will use in the following to quantify the symmetry content of the data.

Fig. 3.4 shows the corresponding time evolution of the symmetry witnesses $Q^{(n)}$ defined in Eq. (3.19), where $0 \leq Q^{(n)} \leq 1$, with $Q^{(n)} = 0$ in the absence of explicit symmetry violation. The index n denotes the maximum number of spatial points involved in the correlation functions probing the symmetries. We show $Q^{(3)}_{\pi\pi\sigma}$ based on an identity connecting two- and three-point functions involving the "Goldstone"-like (π) and "Higgs"-like (σ) excitations appearing in Eq. (3.16), while $Q^{(4)}_{\pi\pi\sigma\sigma}$ and $Q^{(4)}_{\pi\pi\pi\pi}$ connect three- and four-point functions based on Eqs. (3.17a) and (3.17b), respectively.

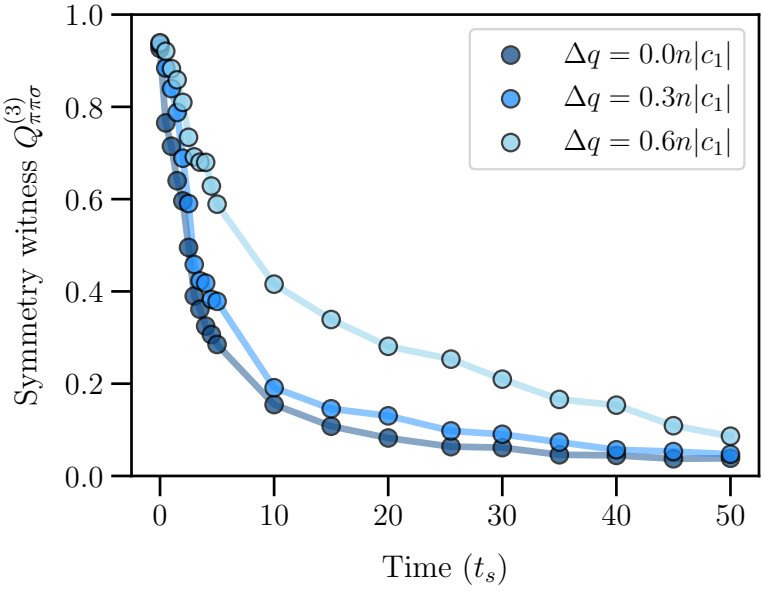

Figure 3.5. Evolution of the symmetry witness $Q^{(3)}_{\pi\pi\sigma}$ for three different systems prepared in a symmetry-broken state. The dark blue curve represents the symmetry witness for a system that is not quenched initially, while the medium and light blue curves correspond to initial quenches, with the light blue one being a stronger quench. The middle curve for $Q^{(3)}$ shows the same data as in Fig. 3.4, but only up to $50\,t_s$.

As seen in Fig. 3.4, the system starts out in a state that explicitly breaks the SO(2) symmetry of the underlying Hamiltonian very strongly, with the different $Q^{(n)}$ rather close to unity. While the unitary time evolution of the quantum system can never restore the symmetry exactly, one observes that important observable properties can nevertheless exhibit an effective symmetry restoration. The different witnesses based on n-point correlation functions probe more and more details as n increases. Correspondingly, we find that the lowest-order witness shown, $Q^{(3)}_{\pi\pi\sigma}$, approaches zero fastest (blue curve). In fact, after an initial rapid decrease until times of a few t_s, the restoration dynamics slows down, and the timescales are in close analogy to those observed from the histograms in Fig. 3.3.

The higher-order witnesses $Q^{(4)}_{\pi\pi\sigma\sigma}$ (green curve) and especially $Q^{(4)}_{\pi\pi\pi\pi}$ (red curve) exhibit a comparably slower effective restoration of the initially broken symmetry. While $Q^{(4)}_{\pi\pi\sigma\sigma}$ involving both σ and π excitations still shows a characteristic two-stage decay, which is relatively fast at early times and then slowing down at late times, this is much less pronounced in $Q^{(4)}_{\pi\pi\pi\pi}$, which involves predominantly the slow "Goldstone"-like modes. Nevertheless, all witnesses clearly exhibit the approach towards an effective restoration of the explicitly broken symmetry by the initial state. We emphasise that this is much shorter than the timescale on which the approach to thermal equilibrium is observed, as the power spectrum $\langle |F_\perp|^2 \rangle$ starts to develop a thermal tail at higher momenta around $\sim 1400\,t_s$. This separation of time scales between the effective restoration of an explicitly broken symmetry and thermalisation may, in principle, be further diminished for sufficiently high-order correlation functions. However, thermalisation time is defined with respect to characteristic thermodynamic observables that typically do not involve arbitrarily high-order details since the time-

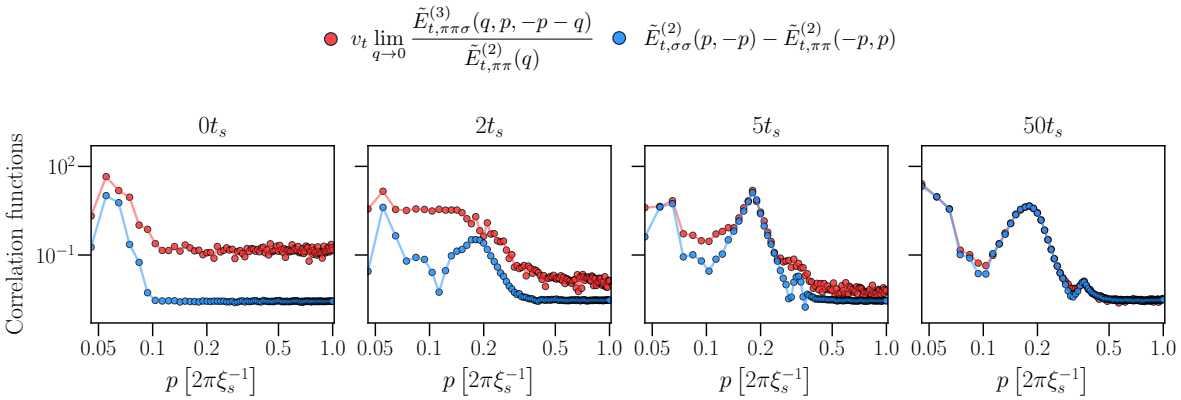

Figure 3.6. Data for the symmetry identity (3.16) with the correlation functions as a function of momentum at four different times during the dynamical evolution.

translation invariant thermal state can never be reached on a fundamental level in systems with unitary dynamics. In practice, emergent theories that effectively describe dynamical behaviour, such as effective kinetic theories, are based on a reduced set of low-order correlation functions. In this context, our results demonstrate that effective symmetry restoration can occur long before the system equilibrates. The situation is reminiscent of thermalisation in isolated quantum systems, where local observables of the system, prepared in a nonequilibrium quantum state, eventually behave as if sampled from a thermal distribution. In contrast, sufficiently global observables retain memory of the original nonequilibirum state and thus behave nonthermally even at very late times. Similarly, while low-order symmetry witnesses show effective restoration, some higher-order witnesses, which encode finer statistical details of the system, will show symmetry violations even at late times. This is in accordance with the general statement regarding how the symmetry can never be fully restored by means of a unitary time evolution governed by a symmetric Hamiltonian, cf. Sec. 3.2.

It remains to investigate to what extent the results depend on the details of the initial state. Here we consider variations in the initial quench of the quadratic Zeeman shift with different strengths or with no quench at all. As depicted in Fig. 3.5, we find that the stronger the quench, the longer it takes to restore the SO(2) symmetry, and not quenching at all restores it the fastest. The witness based on the correlation functions from Eq. (3.16), as seen in Fig. 3.4, corresponds to the middle curve, with an initial quench from $q_i = 0.9n|c_1|$ to $q_f = 0.6n|c_1|$. Quenching stronger than this, to $q_f = 0.3n|c_1|$, takes longer to restore the symmetry (light blue curve), and not doing a quench takes the shortest (dark blue curve). Irrespective of the strength of or the presence of the quench, the correlation functions and the restoration process look qualitatively very similar as shown in Fig. 3.5.

The symmetry witnesses provide an efficient means to quantify the symmetry content of the data. However, further details can be investigated by looking directly at the underlying momentum-resolved correlation functions in the identity (3.16). In Fig. 3.6, we plot both the left-hand side (red curve) and right-hand side (blue curve) of Eq. (3.16) for four different time steps. Initially, we observe that the symmetry is strongly broken signalled by the unequal different n-point correlation functions. Within the span of a few t_s, these different

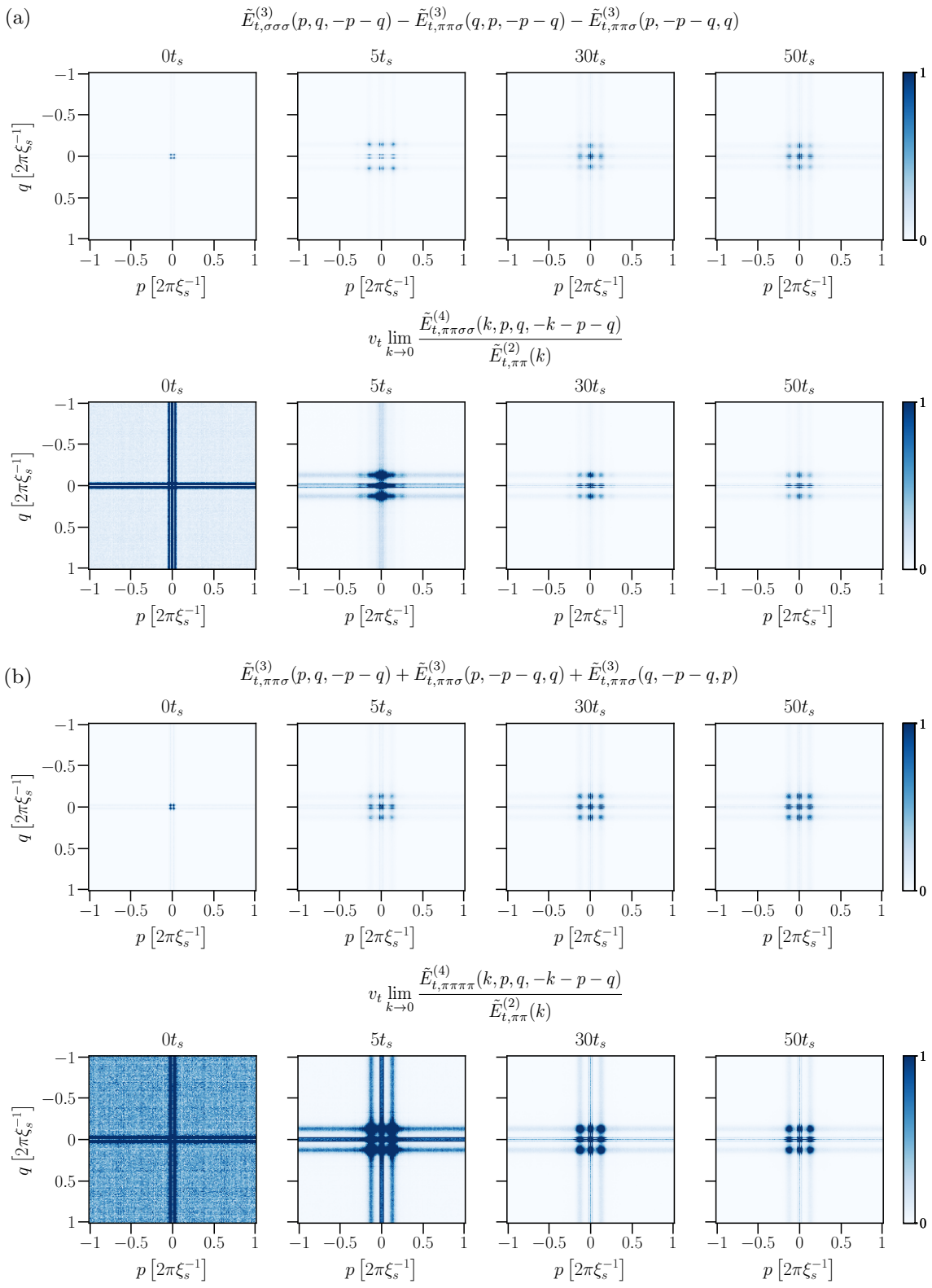

Figure 3.7. Momentum-conserving surfaces in the symmetry identities (3.17a) and (3.17b), respectively.

correlation functions quickly approach each other and by $\sim 50\,t_s$, they are nearly equal and the conclusions are as for the symmetry witnesses discussed before. In addition, one observes from the momentum-resolved correlation functions that, apart from the initial strong fluctuations at low momenta, an additional peak in the correlation functions develops at a higher momentum scale. The peak height settles quickly within a few t_s, during which the "Higgs"-like mode explores the inner part of the effective potential leading to a fast growth of fluctuations as discussed above.

The momenta of the correlation functions entering the identity (3.16) underlying $Q^{(3)}$ correspond to the momentum-conserving diagonals of the full momentum matrix. Likewise, the identities for $Q^{(4)}$ involve momentum-conserving surfaces. As an example, we show the surfaces of our numerical data corresponding to the symmetry identities (3.17a) in Fig. 3.7(a) and (3.17b) in Fig. 3.7(b). In both cases, we see strong initial symmetry violation signalled by the different unequal n-point correlator surfaces. The cross-like shape is the dominant feature of these surfaces and is already present initially, although much stronger in the four-point surfaces. The appearance of the surfaces becomes gradually more equal with time in both Fig. 3.7(a) and (b), however, we can visually confirm that it is not as quick as for the momentum-conserving diagonals above. Additionally, restoration is visibly slower for the identity (3.17b) since at $50\,t_s$ in Fig. 3.7(b) the dominant cross-like features are still at an increased amplitude in the four-point surface compared to the three-point one. This is consistent with what we have observed from the corresponding witnesses in Fig. 3.4.

3.6 Nonequilibrium spontaneous symmetry breaking

In the previous section, we discussed the explicit breaking of a symmetry of the Hamiltonian by the initial state, and its effective restoration long before the system equilibrates. However, even if explicit symmetry breaking is absent or dynamically restored, the symmetry may still be spontaneously broken. The notion of spontaneous symmetry breaking, in thermal equilibrium or dynamically even far from equilibrium, is a central ingredient for our understanding of phase transitions as explained in Sec. 3.2. Spontaneous symmetry breaking is signalled by a nonzero order parameter (3.2) using a bias that does not break the symmetry explicitly in the end.

To analyse spontaneous symmetry breaking out of equilibrium in more detail, in the following we consider experimental data from measurements of a spinor Bose–Einstein condensate of ^{87}Rb atoms as described in Sec. 3.3. The system is initialised in the $|F, m_\mathrm{F}\rangle = |1, 0\rangle$ state, the so-called polar state. Subsequently, the parameter q, which corresponds to the relevant energy difference between the $m_\mathrm{F} = 0$ and $m_\mathrm{F} = \pm 1$ levels, is quenched to a value within the easy-plane phase thereby initiating the dynamics. In contrast to the initial state investigated in Sec. 3.5 in the context of explicit symmetry breaking, in the present case there is initially no well-defined spin length, with fluctuations solely in the $F_x - F_y$ plane such that the initial state respects the $\mathrm{SO}(2)$ symmetry of the system. The initial conditions restrict the average longitudinal (z-axis) spin to be zero, and excitations build up in the $F_x - F_y$ plane. This transversal spin degree of freedom is examined by the spatially resolved detection of the complex-valued field $F_\perp(x) = F_x(x) + \mathrm{i}F_y(x)$ [25].

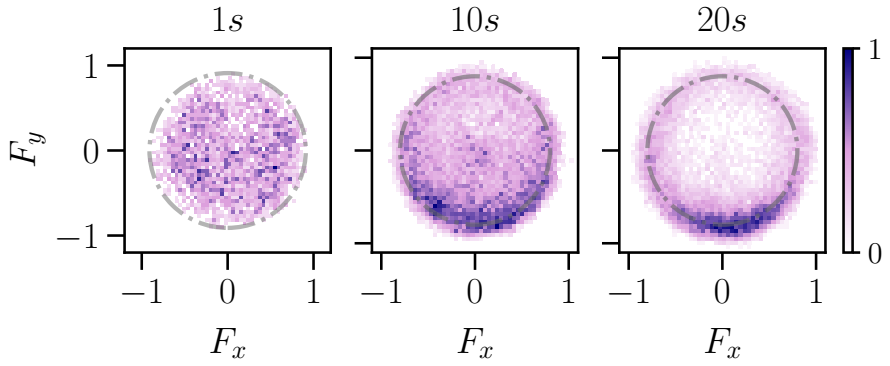

Figure 3.8. Histograms of the experimentally measured spin in the $F_x - F_y$ plane taken from a quasi one-dimensional ^{87}Rb experiment [25], normalised by the atom number, for different evolution times. The dash-dotted line represents $|F_\perp| = 0.85$.

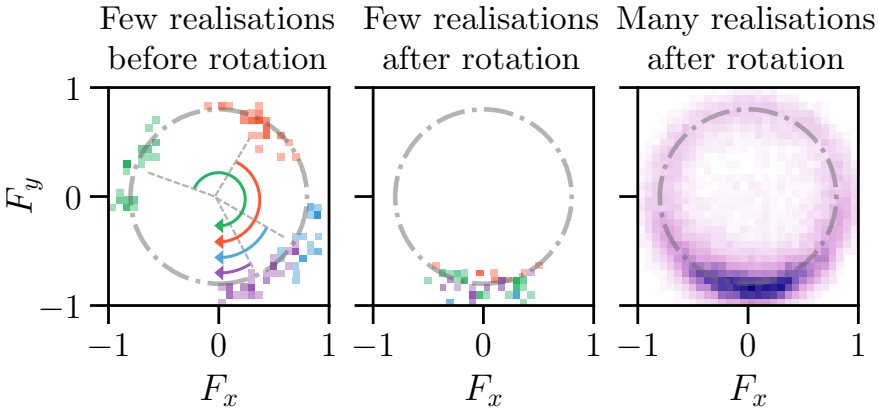

Figure 3.9. Histogram of the normalised spin at $t = 35$ s. The left and middle figures show four different experimental realisations, each in a different colour, before (left) and after (middle) the rotation by the mean phases for each realisation. On the right, the combination of all realisations with mean phase subtracted is displayed.

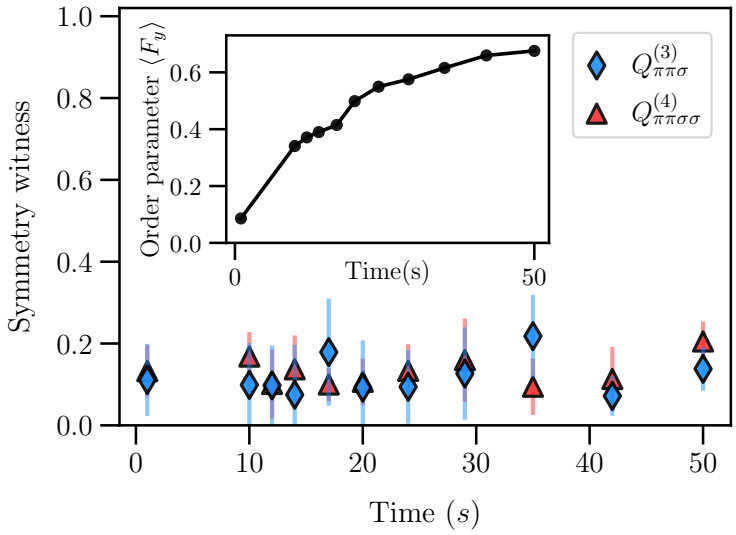

Figure 3.10. The symmetry witness based on two- and three-point correlation functions extracted from experimental data. The inset shows the average spin length $\langle F_y \rangle$. The witness $Q^{(4)}_{\pi\pi\pi\pi}$, which is not shown in order not to overcrowd the plot, gives comparable results to $Q^{(4)}_{\pi\pi\sigma\sigma}$. The error bars are obtained by bootstrapping and correspond to 80% confidence interval. The spin-changing collision time is $t_s = 2\pi/(n\,|c_1|) \sim 0.4\,\mathrm{s}$ for the experimental parameters used in this work.

Fig. 3.8 shows histograms of the measured spin orientations in the $F_x - F_y$ plane normalised by the atom number at different times. While initially the measured values scatter, such that the average spin length is practically zero, this changes at later times. The average spin length settles around $|F_\perp| = 0.85$ represented by the dash-dotted line in the figure. In this case, the nonzero average spin plays the role of the order parameter, signalling the spontaneous symmetry breaking of the SO(2)-symmetric system. Due to the underlying SO(2) symmetry, one can always align the expectation value along one of the axes, e.g., $\langle \hat{F}_x \rangle = 0$, $\langle \hat{F}_y \rangle = v_t$, which was done for Fig. 3.8.

The alignment procedure of the spin expectation value for the experimental data is illustrated in Fig. 3.9. In the left graph, data from four experimental realisations is shown at late time ($t = 35\mathrm{s}$). To understand the underlying dynamics leading to these configurations, it is helpful to consider them as corresponding to the top view of the pictorial representation of the sombrero effective potential sketched in Fig. 3.2(c). While in each realisation the spin distribution is expected to acquire a "blob" shape, as marked by red in the green ring of that figure, and settle in one of the many symmetry-breaking minima, many such blobs will form a symmetric ring. Hence, while there is a preferred direction in each experimental realisation individually, once we average over multiple realisations, the transverse spin is symmetrically distributed across the ring in the $F_x - F_y$ plane. Correspondingly, one observes the different experimental realisations distributed along the ring as seen in the left graph of Fig. 3.9. However, by rotating each individual realisation by the global phase as shown in the middle of Fig. 3.9, there is a nonzero expectation value $\langle \hat{F}_y \rangle \neq 0$ and $\langle \hat{F}_x \rangle = 0$ when averaged over all the realisations. This is shown in the right graph of Fig. 3.9, which gives the average over many realisations. We emphasise that the global-phase rotation an-

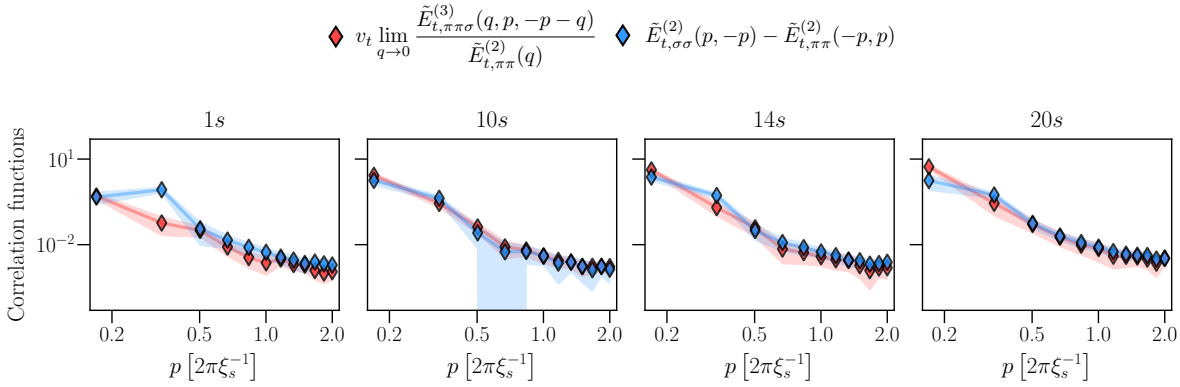

Figure 3.11. The left- and right-hand sides of the symmetry identity (3.16) using experimental data, with the momentum-resolved correlation functions at four different times during the dynamical evolution. The error bands represent 80% confidence intervals obtained from bootstrapping.

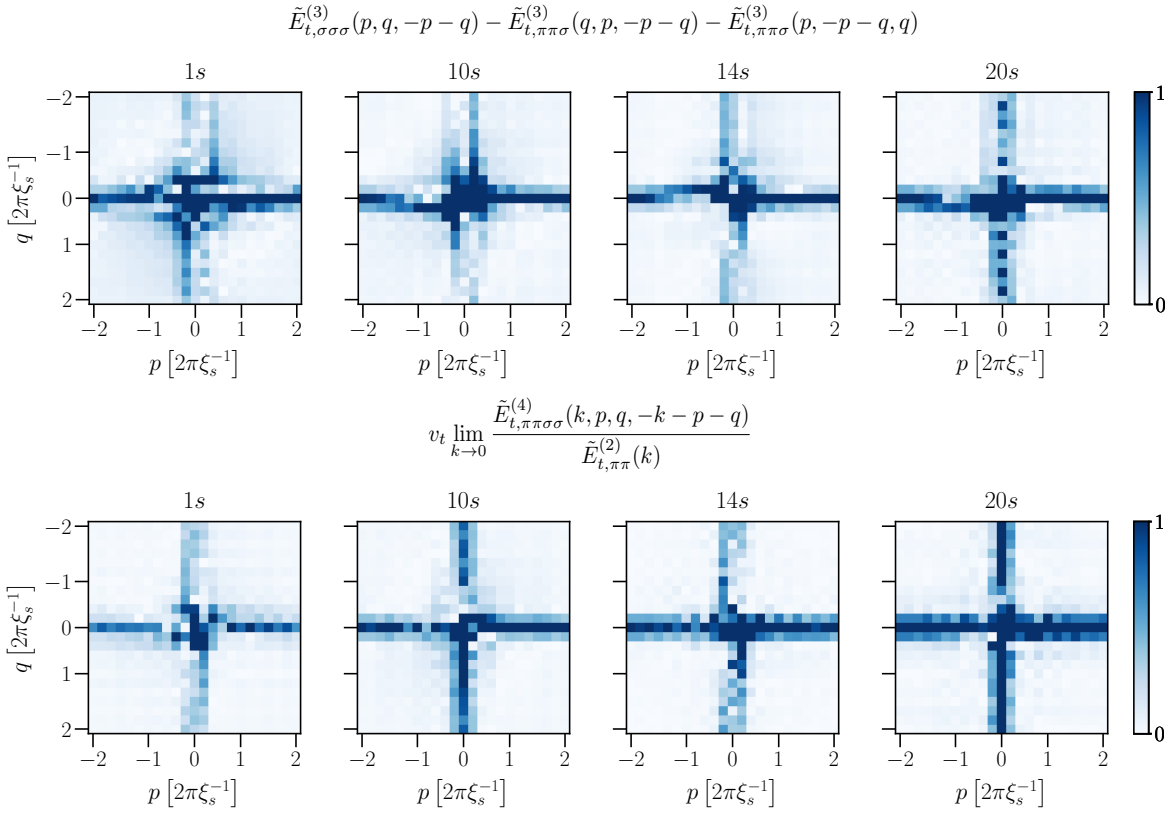

Figure 3.12. Data for the symmetry identity connecting two-, three-, and four-point correlation functions calculated from experimental measurements. The top four surface plots correspond to the right-hand side of the identity (3.17a), while the bottom ones correspond to the left-hand side of the equation. One observes the resemblance of these momentum-conserving surfaces, which involve different n-point correlation functions.

gle maintains translational invariance since this angle does not introduce any spatial bias, whereas, e.g., rotating by the phase of any specific point would do so.

While the histograms of Fig. 3.8 and 3.9 illustrate the dynamical buildup of a macroscopic spin length, a quantitative analysis of spontaneous symmetry breaking requires taking its fluctuations into account as well. In particular, the fluctuations can be used to distinguish data with underlying spontaneous symmetry breaking from situations where a macroscopic spin length arises due to explicit symmetry breaking, as exemplified on the left of Fig. 3.3. The fluctuations are encoded in the n-point correlation functions, which fulfil the symmetry identities for spontaneous symmetry breaking as derived in Sec. 3.4.

We examine the witnesses $Q^{(3)}_{\pi\pi\sigma}$ and $Q^{(4)}_{\pi\pi\sigma\sigma}$ according to Eq. (3.19) in Fig. 3.10. The minimum value of these quantities, and any of the higher-order witnesses is zero, which corresponds to a perfectly symmetric scenario, including that of a spontaneously broken symmetric state, while the upper value is unity, corresponding to a maximally and explicitly broken state. One observes that the value of the symmetry witnesses is clearly much smaller than unity, and near zero within errors. This indicates the absence of explicit symmetry breaking, which in principle can be improved with increasing statistics. We also give the average spin length $\langle F_y \rangle$ as an inset on top of the symmetry witness. The witness is seen to be near zero within errors independent of the magnitude of $\langle F_y \rangle$. One observes that the magnitude of $\langle F_y \rangle$ settles at later times, representing an order parameter for spontaneous symmetry breaking.

In order to test the momentum resolved symmetry identity (3.16), we consider the two- and three-point correlation functions by averaging over many realisations of single-shot measurements of the rotated $F_\perp(x)$. For more details on the data analysis procedure, see App. A.3. We plot four different time steps in Fig. 3.11 and observe that the left- and the right-hand sides of the identities are close within experimental errors at all times. Similarly, Fig. 3.12 shows momentum resolved surface plots for the symmetry identity (3.17a) connecting two-, three-, and four-point correlation functions calculated from experimental measurements. We emphasise once again that *a priori* there is no reason why these different n-point correlation functions should obey such equalities, representing a quantitative manifestation of the emergence of spontaneous symmetry breaking.

3.7 Discussion and outlook

While symmetries of a Hamiltonian that are explicitly broken by the initial state cannot be restored on a fundamental level in closed quantum systems, we have shown that their effective restoration can be quantified in terms of symmetry identities for correlation functions. In particular, our results demonstrate that properties involving lower n-point correlation functions exhibit dynamical symmetry restoration earlier than those involving higher-order correlations. Moreover, our findings for a spinor Bose gas show that an initial explicit symmetry breaking gets restored on timescales much before the system thermalises. These are important ingredients for effective descriptions of nonequilibrium evolutions, which are typically based on lower-order correlation functions, where kinetic theory or Boltzmann equations for single-particle distribution functions extracted from two-point correlation functions

represent a paradigmatic example [105].

Though the correlation functions appearing in the symmetry identities (3.16), (3.17a), and (3.17b) involve only a few spatial points, in general they also test extremely nonlocal properties, such as the ones encoded in their low-momentum behaviour in Fourier space. This is crucial for the identification of spontaneous symmetry breaking in the presence of a nonvanishing expectation value for the zero mode and condensation phenomena, which we have analysed for the example of the spinor Bose gas. In particular, our approach is not based on a spatial separation into subsystems, which can be difficult to define in fundamental descriptions, such as relativistic theories, and gauge theories implementing local symmetries. Though we have not described the approach for local symmetries explicitly in this work, the formulation of nonequilibrium (equal-time) versions of Ward identities for gauge theories [50–53] follows along the same lines as we described.

Our approach provides a general pathway to extract the symmetry content of nonequilibrium quantum as well as classical many-body systems based on a hierarchy of n-point correlation functions. This complements alternative approaches to the question of dynamical symmetry restoration, such as the entanglement asymmetry between spatial subsystems introduced as a measure of symmetry breaking in quantum systems [56, 57, 98, 106–111], which has also been experimentally applied [112–114]. It would be interesting to establish a direct link between our symmetry witnesses based on correlations and the entanglement measure of symmetry breaking for quantum systems. While our work primarily focused on ultracold atoms, the approach could also give important further insights into applications and experimental data across various systems, ranging from the detection of new nonequilibrium phases in condensed matter systems to preheating dynamics in inflationary early-universe cosmology [10, 29, 94].

Chapter 4

Kelvin waves in nonequilibrium universal dynamics of relativistic scalar field theories

This chapter is based on *"Kelvin waves in nonequilibrium universal dynamics of relativistic scalar field theories"* by V. Noel, T. Gasenzer, and K. Boguslavski, arXiv:2503.01771.

Understanding the relevant degrees of freedom in nonequilibrium quantum many-body systems is crucial for describing their long-time dynamics and emergent universal behaviour. In this chapter, we examine the scaling properties of a relativistic O(1) scalar field theory far from equilibrium, focusing on the nature of infrared excitations and their role in self-similar scaling. In such a strongly correlated many-body system, identifying the respective roles of nonlinear wave excitations and defect dynamics is a prerequisite for understanding the universal character of time evolution far from equilibrium and thus the different possible universality classes related to nonthermal fixed points. Using unequal-time correlation functions, we identify the dominant modes contributing to the observed dynamics and explore their connections to topological defects. Our study provides a detailed characterisation of these excitations in both two and three spatial dimensions, revealing distinct scaling properties and excitation spectra that contrast with predictions from large-N field theories. In three dimensions, the primary excitations are identified as kelvon quasiparticles, which are quantised Kelvin waves propagating along vortex lines, while in two dimensions, the infrared dynamics is dominated by bound-state like excitations similar to Kelvin waves. Our results underline the role of topological defects and their influence on the universal dynamics of strongly correlated systems near nonthermal fixed points, complementing the analysis of large-N models in O(N) systems.

This chapter is organised as follows: after an introduction in Sec. 4.1, Sec. 4.2 describes the lattice simulations and the different types of two-point correlation functions investigated. Sec. 4.3 provides an overview of the relevant degrees of freedom based on applicable low-energy effective theories of relativistic scalar fields. It discusses the expected N-dependence from both the quasiparticle picture and the possible topological defects. In Sec. 4.4, the main findings from real-time lattice simulations are presented. First, the self-similar scaling from

the (equal-time) distribution function is compared to that of vortex-antivortex annihilation-driven coarsening dynamics and then parallels are drawn to the excitations found in unequal-time correlation functions. The dispersion relation of these excitations is analysed to clearly pinpoint their nature. The conclusions are presented in Sec. 4.5.

4.1 Introduction

The concept of universality is a powerful framework for understanding complex many-body systems. Near equilibrium, it provides a way to associate phase transitions with universality classes based on a small set of system parameters, highlighting how vastly different systems can exhibit similar dynamical critical behaviour [64]. Beyond this, universal dynamics can also emerge far from equilibrium in isolated systems, in particular, nonthermal fixed points [19, 20, 48, 73, 77, 115, 116] give rise to nonequilibrium attractor solutions characterised by spatio-temporal self-similar scaling. Such far-from-equilibrium universality has been experimentally observed in ultracold atomic gases in different dimensions and trapping geometries [21–27, 96, 117, 118]. Many of the properties of this universal scaling dynamics have been theoretically predicted and studied in very different systems, ranging from ultracold gases over heavy-ion collisions to the early universe [48, 72–74, 77–79, 105, 115, 116, 119–131]. The broad range of systems in which this phenomenon has been proposed raises the question of what the relevant physics behind the apparent universality is.

The study of far-from-equilibrium universality in isolated systems has primarily focused on the properties of the equal-time momentum distribution function, $f(t,p)$, which describes the occupancy of momentum modes over time. These functions reveal self-similar scaling behaviour near nonthermal fixed points, characterised by universal scaling exponents that are largely independent of the systems' parameters or initial conditions [48]. Scalar field theories with O(N) symmetry, for example, exhibit universal dynamics at low momenta according to $f(t,p) = t^{\alpha} f_{\mathrm{s}}(t^{\beta}p)$, with the exponents $\alpha = d\beta$ and $\beta = 1/2$. The scaling function f_{s} is consistent across different values of N, whether in relativistic or nonrelativistic models, and the underlying physics is connected to the self-similar transport of particle numbers towards lower momenta and the growth of a quasi condensate in the long-wavelength modes below a characteristic scale $p_{\mathrm{IR}}(t) \sim t^{-\beta}$. Large-$N$ kinetic theories provide a successful description of this scaling dynamics and the exponents [19, 20, 48, 72–74, 105, 115, 122–124], which can be traced to the elastic collisions of quasiparticles with free dispersion [72]. For small values of N, however, the precise description of the universality remains unsatisfactory, and alternative mechanisms, such as coarsening dynamics of topological defects is anticipated to play a significant role [25, 26, 77–79, 116, 117, 119–121, 125, 127, 128, 132, 133]. Recent studies indicate that for systems with a small number of field components, distinct initial conditions may lead to different scaling exponents, [25, 79, 131, 134], where another scaling exponent, $\beta \approx 1/5$, has been associated with specific defect-driven dynamics for vortices in two spatial dimensions [1, 79, 117, 135].

For the O(N) vector models in both two and three spatial dimensions, a number of different, N-dependent topological defects are expected to contribute to the dynamics in the infrared [1, 80, 125], which includes vortex defects in O(1). However, for O(N) the-

ories in three (spatial) dimensions, including the case of $N = 1$, the self-similar scaling dynamics has been consistent with that of large-N descriptions and in agreement with nonrelativistic U(N) vector models [48, 73, 74, 80–82, 105, 115]. This has been corroborated by observing the scaling behaviour of $f(t, p)$ based on classical-statistical real-time lattice simulations. Nonetheless, unequal-time correlation functions, which also give information about the nonequilibrium excitation spectrum, have revealed markedly different dominant excitation peaks for $N = 1, 2$ compared to $N \geq 3$, where the large-N excitation indeed dominates [82].

Here we study the underlying mechanisms of the self-similar infrared transport for the relativistic single-component O(1) theory in two and three spatial dimensions using unequal-time two-point correlation functions. By providing information on both occupancies and dispersion relations, the latter observables allow us to distinguish the different excitations contributing to the scaling and also to ascertain which excitation is dominant. Based on numerical simulations in three spatial dimensions, the dominant excitation in such correlators at large N has been identified as the one with the quasiparticle dispersion [82, 136] that agrees with the kinetic theory picture. An excitation similar to the large-N excitation has also been found for the relativistic $N = 2$ case at low momenta [82], whereas it is absent for $N = 1$. On the other hand, a very specific, so-called "transport peak" has been identified for both nonrelativistic U(1) and in the nonrelativistic limit of relativistic O(1) models [81, 82], with the same momentum and time dependence of the dispersion relation, as well as damping rate, while being distinct from the large-N excitation. This peak appears to be present for the cases of O(2) and O(3) as well, however, it distinctly dominates only the $N = 1$ theory [82]. The origin of this transport peak has not been understood yet and is not predicted by any current kinetic or low-energy effective description of nonthermal fixed points.

In anticipation of its potential connection to topological defects, in this work, we also extract and analyse the vortex dynamics for the O(1) theory in both two and three dimensions using topological defect data extracted from lattice configurations. In the context of nonthermal fixed points, two-dimensional relativistic theories have not been extensively studied yet [119, 120, 125]. However, they do provide an interesting toy model since, intuitively speaking, topological effects are more important in lower dimensions and for lower N. By carefully investigating the transport peak, we find a direct connection between the self-similar infrared transport near nonthermal fixed points and vortex line defects in three dimensions in terms of Kelvin waves [137–140], which arise as quantised excitations on vortices present in scalar theories, and which are well-investigated in the context of vortex dynamics and quantum turbulence [141–149]. In two dimensions, we observe a similar transport peak, where the underlying physics is connected to the two-dimensional analogues of Kelvin waves, which arise as vortex-displacement excitations [150–152]. While the general picture of nonlinear wave propagation in the strongly correlated regime near a nonthermal fixed point still applies for both small and large values of N, with the present study, we distinctly identify the relevant degrees of freedom in these theories, highlighting the importance of topological defects for a single-component scalar field theory.

4.2 Model and observables

We consider a single-component relativistic scalar field theory with field variable $\phi(t, \mathbf{x})$, in $d = 2$ and $d = 3$ spatial dimensions with classical action

$$S[\phi] = \int_{t,\mathbf{x}} \left[\frac{1}{2} \partial^\mu \phi \partial_\mu \phi - \frac{m^2}{2} \phi^2 - \frac{\lambda}{4!} \phi^4 \right] , \tag{4.1}$$

where $\int_{t,\mathbf{x}} \equiv \int \mathrm{d}t \int \mathrm{d}^d x$, summation over repeated indices is implied, m is the bare mass and λ is the coupling constant. In the weak-coupling regime $\lambda \ll 1$ considered in this work, the quantum dynamics can be accurately mapped onto classical-statistical field theory (Truncated-Wigner approximation) for highly occupied systems at not too late times [71]. In classical-statistical simulations, one samples the fields over initial conditions,

$$\begin{aligned} \phi(0, \mathbf{p}) &= \sqrt{f(0,p)/p}\, c(\mathbf{p}) \,, \\ \pi(0, \mathbf{p}) &= \sqrt{p f(0,p)}\, \tilde{c}(\mathbf{p}) \,, \end{aligned} \tag{4.2}$$

where $p = |\mathbf{p}|$, with independent random numbers drawn from a Gaussian distribution that satisfy $\langle c(\mathbf{p})\, (c(\mathbf{q}))^* \rangle_{\mathrm{cl}} = V \delta_{\mathbf{p},\mathbf{q}}$, and similarly for $\tilde{c}$. Our initial condition sets high occupations for the infrared modes,

$$f(t = 0, \mathbf{p}) = \frac{n_0}{\lambda} \Theta(Q - p) \,, \tag{4.3}$$

up to a characteristic momentum scale Q, which is the physical scale governing the dynamics. Subsequently, each realisation is evolved according to the classical equations of motion,

$$\begin{aligned} \partial_t \phi(t, \mathbf{x}) &= \pi(t, \mathbf{x}) \,, \\ \partial_t \pi(t, \mathbf{x}) &= \partial_i \partial_i \phi(t, \mathbf{x}) - m^2 \phi(t, \mathbf{x}) - \frac{\lambda}{6} \phi(t, \mathbf{x})^3 . \end{aligned} \tag{4.4}$$

In the numerical approach, we discretise $\phi(t, \mathbf{x})$ and $\pi(t, \mathbf{x})$ on a spatial lattice with spacing a_s, volume $V = (N_s a_s)^d$ and time step $a_t = 0.05\, a_s$. In $d = 2$ dimensions, we use $N_s = 2048$, $a_s = 0.1\, Q^{-1}$, $m/Q = 2$, $n_0 = 80$. In $d = 3$ dimensions, we use $N_s = 256$, $a_s = 0.8\, Q^{-1}$, $m/Q = 0.25$, $n_0 = 100$, unless stated otherwise. Any dependence on the coupling constant drops out after the classical equations of motion and the initial conditions are rescaled according to $\phi \to \lambda^{1/2} \phi$, $\pi \to \lambda^{1/2} \pi$. This property stems from the underlying classical limit $\hbar \to 0$ or, equivalently, the weak coupling limit $\lambda \to 0$. The figures shown in the following sections all assume quantities in units of Q.

To study the excitation spectrum, we will compute two different unequal-time two-point correlation functions: the spectral function $\rho(t', t, \mathbf{p})$ and the statistical correlation function $F(t', t, \mathbf{p})$. The latter can be defined as the expectation value of an anticommutator of fields, which can be calculated in the classical-statistical framework as the classical expectation value of the corresponding product of fields,

$$F\,(t', t, \mathbf{p}) = \frac{1}{V} \left\langle \phi\,(t', \mathbf{p})\ \phi^*(t, \mathbf{p}) \right\rangle_{\mathrm{cl}} . \tag{4.5}$$

Based on this, we can also define the distribution function as

$$f(t, \mathbf{p}) = \left. \sqrt{F\,(t', t, \mathbf{p})\, \partial'_t \partial_t F\,(t', t, \mathbf{p})} \right|_{t'=t} \tag{4.6}$$

at equal times $t' = t$.

For the computation of the spectral function, the linear-response approach of [82] similar to [81, 153] is employed. This involves perturbing the system, at time t, as $\phi \to \phi + \delta\phi$ with a source term $j(t, \mathbf{x}) = j^0(\mathbf{x})\delta(t - t')$, drawn from a random Gaussian distribution that satisfies $\left\langle j^0(\mathbf{p}) \left(j^0(\mathbf{q})\right)^* \right\rangle_j = V\delta_{\mathbf{p},\mathbf{q}}$. The perturbation $\delta\phi$ is time evolved according to the linearised equations of motion $\partial_t'\delta\phi = \delta\pi$ and

$$\partial_t'\delta\pi = \partial_i\partial_i\delta\phi - \left(m^2 + \frac{\lambda}{6}\phi^2\right)\delta\phi - j^0\,\delta\left(t - t'\right) . \tag{4.7}$$

The retarded component of the spectral function follows from linear response theory as

$$\theta\left(t' - t\right)\rho\left(t', t, \mathbf{p}\right) = \frac{1}{V}\left\langle \langle \delta\phi\left(t', \mathbf{p}\right)\rangle_{\mathrm{cl}} \left(j^0(\mathbf{p})\right)^* \right\rangle_j . \tag{4.8}$$

Apart from the occupancy of excitations in the system, the correlators F and ρ also contain information about the frequency dependence of excitations, including the dispersion relations and damping rates of all of the relevant excitation species in the system. We consider these unequal-time correlation functions in momentum space and perform the Fourier transforms with respect to relative time $\Delta t = t' - t''$ as

$$F(t, \omega, \mathbf{p}) \equiv \int \mathrm{d}\Delta t\, \mathrm{e}^{\mathrm{i}\omega\Delta t} F\left(t', t'', \mathbf{p}\right) , \tag{4.9}$$

$$\rho(t, \omega, \mathbf{p}) \equiv -\mathrm{i}\int \mathrm{d}\Delta t\, \mathrm{e}^{\mathrm{i}\omega\Delta t} \rho\left(t', t'', \mathbf{p}\right) , \tag{4.10}$$

where $t \equiv \left(t' + t''\right)/2$ is the (central) time. In practice, we evaluate the correlations at $t'' = t$. This approximation can be justified provided the correlations do not change significantly over times of the order of their oscillation periods along the relative time Δt, which is fulfilled during the self-similar scaling dynamics [81]. Therefore, in our simulations, we compute the Fourier transforms while holding t fixed, as

$$F(t, \omega, \mathbf{p}) \approx 2\int_0^{\Delta t_{\mathrm{max}}} \mathrm{d}\Delta t\, \cos(\omega\Delta t)\, h(\Delta t)\, F\left(t + \Delta t, t, \mathbf{p}\right) , \tag{4.11}$$

$$\rho(t, \omega, \mathbf{p}) \approx 2\int_0^{\Delta t_{\mathrm{max}}} \mathrm{d}\Delta t\, \sin(\omega\Delta t)\, h(\Delta t)\, \rho\left(t + \Delta t, t, \mathbf{p}\right) , \tag{4.12}$$

typically using $\Delta t_{\mathrm{max}} \approx 300$ for spectral functions and $\Delta t_{\mathrm{max}} \approx 500$ for the statistical function. We have checked that the results are not sensitive to the exact value of Δt_{max}. We also employ a Hann window function,

$$h(\Delta t) = \frac{1}{2}\left(1 + \cos\frac{\pi\Delta t}{\Delta t_{\mathrm{max}}}\right) , \tag{4.13}$$

and zero padding to smoothen the resulting curves, and have checked that these do not alter the form of the displayed peaks. Expectation values of observables are obtained by averaging over the field trajectories that are solutions to the classical equations of motion. The results shown in the following use correlation functions averaged over 100 realisations in two and 40 realisations in three dimensions. Real-time classical-statistical simulations have been extensively used to study the dynamics of isolated systems in corresponding regimes of applicability for similar initial conditions [1, 2, 19, 48, 78, 79, 82, 116, 119, 125, 127–129, 131–133, 154–163].

4.3 Excitations and defects in O(1) theory

In this section, we discuss the different quasiparticle and topological defect contributions that we expect to be relevant for O(1) scalar field theory.

4.3.1 Low-energy effective theories of scalar fields

Relativistic O(N) scalar field theories are known to display nonrelativistic effects at low momenta in the presence of a mass gap. For the initial conditions considered here, such a mass gap $|p| \lesssim M$ with effective mass M emerges even when the underlying theory is originally massless [48], giving rise to nonrelativistic dynamics in the infrared. Hence, a single component field theory O(1) can be described by an emergent U(1) theory. This mapping can be made more rigorous by introducing nonrelativistic degrees of freedom emerging from the underlying relativistic ones

$$\psi = \mathrm{e}^{\mathrm{i}Mt}\left[\sqrt{\omega_x}\,\phi + \mathrm{i}/\sqrt{\omega_x}\,\pi\right]/\sqrt{2}\,, \tag{4.14}$$

with $\omega_x = \sqrt{M^2 - \nabla^2}$ [125, 164]. The emergent dynamics is governed by the Gross-Pitaevskii equation,

$$\mathrm{i}\partial_t\psi(t,\mathbf{x}) = -\frac{\nabla^2}{2M}\psi(t,\mathbf{x}) + g|\psi(t,\mathbf{x})|^2\psi(t,\mathbf{x})\,, \tag{4.15}$$

thus describing the real-time dynamics of a single-component Bose gas. While it is a well-known mapping, Ref. [125] considered it for the case of overoccupied isolated systems corroborated by numerical simulations in two dimensions, with initial conditions very similar to what is being considered here.

In contrast, for a nonrelativistic N-component Bose gas, a low-energy effective theory was considered in Ref. [105], describing interacting Goldstone modes of the total and relative phase excitations. There are N equations of motion for the U(N) theory, which give rise to $N-1$ Goldstone modes[1] with quadratic dispersion $\omega_{\mathrm{G}}(p)$ (relative phase excitations), and a Bogoliubov mode (total phase) with dispersion $\omega_{\mathrm{B}}(p)$,

$$\begin{aligned}\omega_{\mathrm{G}}(p) &= \frac{p^2}{2m}\,, \quad c = 1,\ldots,N-1\,,\\ \omega_{\mathrm{B}}(p) &= \sqrt{\frac{p^2}{2m}\left(\frac{p^2}{2m} + 2g\rho_0\right)}\,,\end{aligned} \tag{4.16}$$

where ρ_0 is the condensate density in the zero-mode. In Ref. [82], these dispersions were generalised to the relativistic case of O(N) models by computing the dispersions of possible excitations using classical field equations of motion. This gives rise to the gapless modes

$$\omega_{\mathrm{G,rel}}(p) = \sqrt{p^2 + M^2} - M \tag{4.17}$$

$$\omega_{\mathrm{B,rel}}(p) = \sqrt{p^2 + 2M\left(M + g\rho_0 - \sqrt{p^2 + (M+g\rho_0)^2}\right)}\,, \tag{4.18}$$

[1] Based on the underlying $U(N)$ theory, there are $2N-1$ broken generators, and $2N-2$ of them combine into the $N-1$ quadratic modes [105].

where $g\rho_0$ imprints the magnitude of the (local) condensate and is related to the effective mass M. These dispersion relations are provided as relative excitations on top of the local condensate that is the solution of the classical equation of motion. Therefore, they can be directly compared to the dispersions (4.16) of the nonrelativistic theories. However, we emphasise that in the relativistic case, one computes correlations of the scalar field ϕ instead of ψ and, before comparing to the stated dispersions, one has to remove the rotation frequency $\pm M$ in the frequency spectrum [82] that also emerges in the exponent of Eq. (4.14). We will take this into account in all the figures below by plotting $\omega - M$.

We note that in the large-N limit, the Bogoliubov mode is suppressed in the infrared. In this limit, large-N kinetic theories [48, 73, 74] that dominantly describe the scattering of quasiparticles with a quadratic dispersion agree with the low-energy effective theory (EFT) considered in Ref. [105]. For the single-component scalar field theory, the EFT considers only Bogoliubov modes and no quadratic excitations. However, the extraction of the excitation spectrum in U(1) and O(1) theories in Refs. [81, 82] reveals the existence of a dominant "transport peak" or "non-Lorentzian peak" at low momenta, in addition to the Bogoliubov modes, that drives the dynamics. This raises the question of what kind of quasiparticles are present in a single-component scalar field theory and, in particular, what the dominant degree of freedom is that none of the existing EFTs or kinetic theories are able to capture.

4.3.2 Topological defects in O(1) scalar field theory

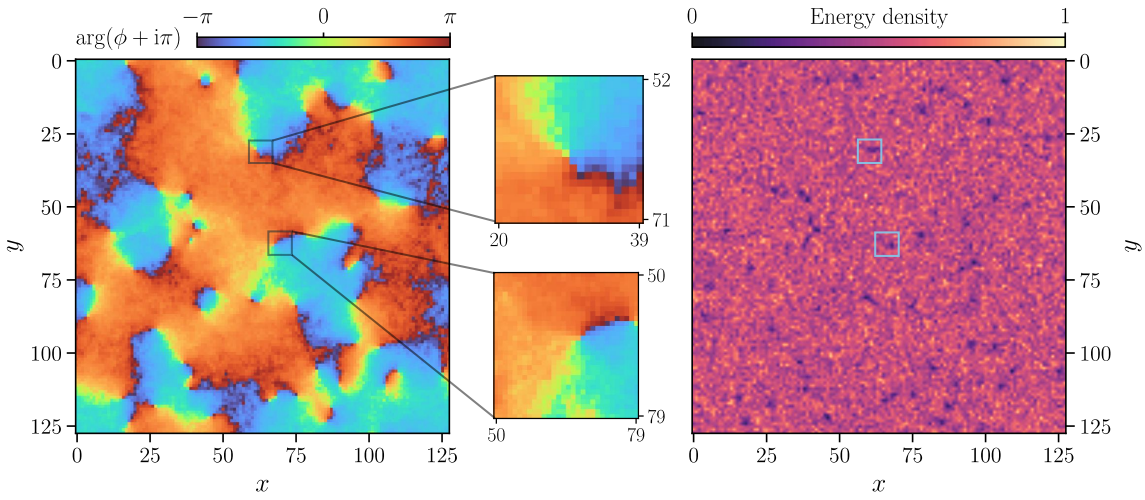

Figure 4.1. *Left:* Phase angle of the complex quantity $\theta = \phi + \mathrm{i}\pi$ defined from the relativistic degrees of freedom. Vortices/antivortices occur at a phase change $\pm 2\pi$, as magnified by the middle insets. *Right:* Vortex defects also show up as distinct minima in the local energy density on the lattice. We show coarse-grained plots to minimise the influence of lattice artefacts. Lengths are shown in units of Q^{-1}, cf. (4.3). The healing length $\xi_\mathrm{h} = p_{\xi_\mathrm{h}}^{-1} = [2g\rho_0 M]^{-1/2}$, which gives the scale of the diameter of the vortex cores is $\xi_\mathrm{h} \approx 0.83\, Q^{-1}$.

Approaching from a different perspective, an important consideration is the potential existence of topological defects in our systems. This could be especially significant for the

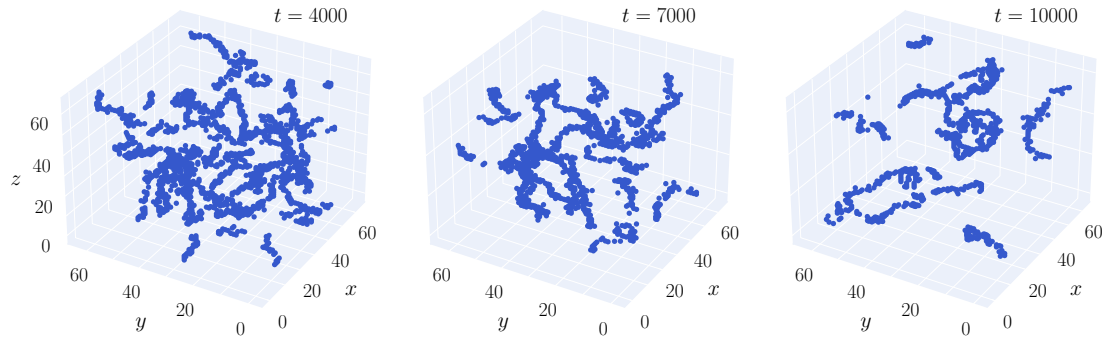

Figure 4.2. Tangles of vortex lines on a three-dimensional lattice shown at three different times and extracted from the low-energy depressions of the energy density fluctuations. Due to reconnections of vortex rings, leading to both larger and smaller rings and subsequent shrinking and dissolution of the smallest rings on the noisy background, the overall vortex line length decreases, corresponding to a coarsening process in the energy density.

$N = 1$ case, since the lower N is, the more constrained the topology of the underlying vacuum manifold becomes, making it more likely to support nontrivial topological structures.[2]

Due to the effective conservation of particle number in the infrared regime, which also occurs in the presence of a mass gap in the relativistic theories considered here, an inverse self-similar particle transport develops. This gradually transfers particles to low-momentum modes, ultimately building a condensate at zero momentum. However, causality imposes a limit on the rate at which information and correlations can propagate, preventing the instantaneous formation of a uniform condensate. Therefore, the condensate initially lacks long-range order, which it will gradually develop through ordering dynamics [67]. This dynamics may include topological defects depending on the number of field components N [80], and for a single component, $N = 1$, there are stable vortex defects. In this particular case, the formation of vortices and antivortices, and their annihilation process is of importance, since this allows for the growth of larger structures.

One way to identify these defects in our simulations would be performing the canonical transformation (4.14) on the relativistic degrees of freedom ϕ and π to obtain the complex $\psi(t, \mathbf{x})$. Then positions on the real-space lattice where depressions in the density of $|\psi(t, \mathbf{x})|^2$ occur along with a phase change of approximately $\pm 2\pi$ in $\arg[\psi(t, \mathbf{x})]$ would correspond to vortices and antivortices, respectively [125]. However, we find that it is also possible to obtain topological defects directly from the relativistic degrees of freedom ϕ and π without transforming into ψ, and also without applying any cooling effects in the simulations. For a relativistic theory with a sufficiently large mass gap, defects also show up as minima in energy density fluctuations [1], which coincide with a $\pm 2\pi$ winding in the relativistic phase angle defined by

$$\theta(t, \mathbf{x}) = \arg\left[\phi(t, \mathbf{x}) + \mathrm{i}\,\pi(t, \mathbf{x})\right] , \tag{4.19}$$

[2] For a mathematically more rigorous consideration of what plays the role of a vacuum manifold in the nonequilibrium dynamical theory considered here, see Refs. [1, 80].

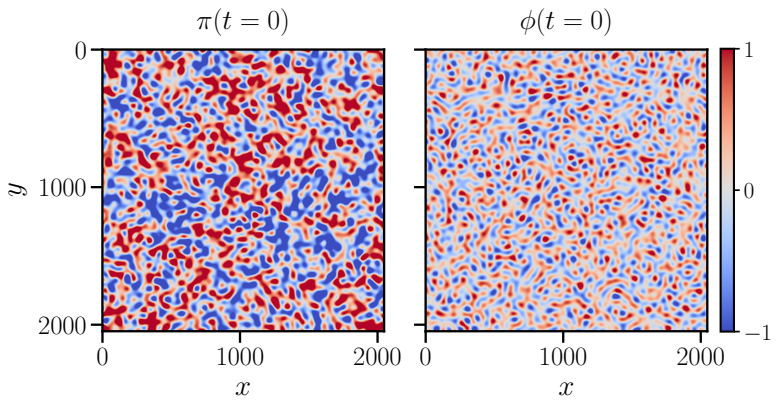

Figure 4.3. Initial spatial configurations of the fields $\phi(t_0, \mathbf{r})$ and $\pi(t_0, \mathbf{r})$ in $d = 2$ dimensions, $\mathbf{r} = (x, y)$, normalised to have values between -1 and 1. The "scrambled" pattern, containing many small domains, allows for numerous phase singularities in $\arg[\phi + \mathrm{i}\pi]$, which we identify as (anti)vortex defects. These domains then become larger, as throughout the coarsening process vortices annihilate with antivortices resulting in the growth of structures.

as shown in Fig. 4.1 for the two-dimensional case. We have cross-checked that the number and positions of (anti)vortices coincide in these two observables, the relativistic $\theta(t, \mathbf{x})$, and the nonrelativistic $\arg[\psi(t, \mathbf{x})]$. Such phase singularities in the nonrelativistic $\arg[\psi(t, \mathbf{x})]$ have been specifically matched with depressions in the complex field ψ in Refs. [79, 125] and their time evolution has been tracked in the context of vortex-antivortex annihilation events and the resulting coarsening of the domains. In this work, we will obtain results from purely relativistic quantities, namely the fields $\phi(t, \mathbf{x})$ and $\pi(t, \mathbf{x})$ entering $\theta(t, \mathbf{x})$.

Technically, one could first identify the minima in the energy density and check for a corresponding phase winding in $\theta(t, \mathbf{x})$. In practice, however, nearly all the $\pm 2\pi$ phase windings coincide with a minimum in the energy density, such that simply checking only one of these observables gives an accurate picture of the total vortex density. Similarly, for the three-dimensional case, vortex lines are revealed by looking for depressions in the energy density fluctuations, as seen in Fig. 4.2 for different times.

Since vortex configurations are solutions to the classical equation of motion, they can arise during the dynamics. However, it is worth mentioning that even though these vortices are not explicitly part of the initial conditions under consideration, our box initial condition (4.3) provides the right environment for vortices to emerge. This can be seen in Fig. 4.3, where the initial field configurations $\phi(t = 0, \mathbf{x})$ and $\pi(t = 0, \mathbf{x})$ are shown in position space. The "scrambled" look results from small domains that are characterised by sharp boundaries between low and high values of ϕ and π due to the step function in the distribution at the characteristic momentum Q. As already illustrated in Fig. 4.1, such sharp boundaries are ideal for phase singularities in $\theta(t = 0, \mathbf{x})$, which is a feature of vortices.

It is also important to note that using a smoother cutoff for the initial momentum space distribution instead of a step function, like a hyperbolic tangent function or a Gaussian function, did not reduce the number of vortex defects initially formed in the system, which we explicitly checked. As long as one has a relatively steep increase in occupation number in

momentum space near some characteristic momentum, this initially scrambled picture will emerge in position space, and vortices will always form very quickly in the dynamics. In this sense, it is not possible not to have, or to remove these defect configurations. For the case of $N = 1$ (and also $N = 2, 3$ but not higher N), they are stable configurations on topological grounds [1, 80].

4.3.3 Excitations on vortices

Another type of contribution yet to be considered is that the vortex defects themselves can support excitations, which appear as quasiparticles during the dynamics. For instance, phonons can be produced from vortex-antivortex annihilation processes [165], which are expected to yield a linear dispersion relation at low momenta. Beyond this, individual vortex lines in three dimensions, and vortex cores in two dimensions can be excited in a way that can be characterised as quasiparticles, which are distinct from the phonons arising from vortex annihilation. In anticipation of our findings, we briefly summarise the properties of such *kelvon* quasiparticles.

In three dimensional systems, vortex defects are extended objects and may be viewed as vortex lines, along which helical excitations can propagate as waves. These are known as Kelvin waves [137], and were originally described in the context of classical hydrodynamics. In the realm of quantum fluids, Kelvin waves arise as helical perturbations of quantised vortex lines, with the circulation being discretised as a direct consequence of the quantum mechanical phase winding around the vortex core [138, 140, 166, 167]. These excitations play a crucial role in the dynamics of quantum turbulence, mediating energy transfer from larger to smaller scales [141–144, 146, 148, 149], as Kelvin waves at a similar scale interact, exciting smaller scale Kelvin waves, ultimately dissipated by phonon emission. At larger scales, vortex reconnection is thought to dominate energy transfer [168], and such reconnection events excite Kelvin waves at scales close to the inter-vortex distance. Lord Kelvin obtained, for the small-amplitude wave excitations of a thin columnar vortex with a hollow core, with wave number p along the vortex line and azimuthal quantum number $n = 1$, the dispersions [137]

$$\omega_{\mathrm{K}}^{\pm}(p) = \frac{\Gamma}{2\pi r_{\mathrm{c}}^2}\left(1 \pm \sqrt{1 + r_{\mathrm{c}} p \frac{K_0(r_{\mathrm{c}}p)}{K_1(r_{\mathrm{c}}p)}}\right) , \tag{4.20}$$

where r_{c} is the vortex core radius, $\Gamma = \oint_{\mathcal{C}} \mathbf{v} \cdot \mathrm{d}\mathbf{r}$ the vortex circulation, with fluid velocity $\mathbf{v}$ and $\mathcal{C}$ some closed path around the core, and K_j are modified Bessel functions of order j. The low-momentum approximation of the dispersion ω^- has the form

$$\omega_{\mathrm{K}}^{-}(p) \simeq -\frac{\Gamma p^2}{4\pi}\left[\ln\left(\frac{2}{p r_{\mathrm{c}}}\right) - \gamma\right] , \quad (p r_{\mathrm{c}} \ll 1) , \tag{4.21}$$

where $\gamma \approx 0.577216\ldots$ is the Euler-Mascheroni constant. The Kelvin-wave dispersion (4.21) also applies to vortices in a superfluid [140] with integer winding number $w \in \mathbb{Z}$ and circulation $\Gamma = wh/m$ quantised in integer multiples of the Planck constant h over particle mass. The much larger $\omega^+(p \to 0) \simeq \Gamma/(\pi r_{\mathrm{c}}^2)$ is related to the Magnus force and the mass inside the core [169].

The dynamics of quantised vortices and their Kelvin-wave excitations with dispersion (4.20) is well captured by the Gross–Pitaevskii equation (GPE) (4.15) [151, 170–173]. As it is explicitly visible in the approximate expression (4.21), the p-dependence of the dispersion (4.20) is nearly quadratic at low momenta. Around $pr_\mathrm{c} = 1$ it is close to linear in p, while at higher momenta, it bends to a lower power than linear. Such a momentum dependence serves as a unique signature of Kelvin waves that is unlikely to be attributed to any other excitation with only linear or quadratic dispersions. Previous GPE studies of Kelvin waves mostly focused on weak wave turbulence, and a direct connection has not been made with nonthermal fixed points to date, where strong wave turbulence dominates the infrared region.

At first sight, Kelvin waves cannot occur in two dimensions, where vortices lack a linear extension along the core and are localised objects with circular symmetry. Similar quasiparticles, however, emerge even in two dimensions [152, 174], especially if the vortices are not point-like, but have a finite core size, which is precisely our case, as seen in the right panel of Fig. 4.1 depicting the energy density. As a result, the *boundary* of the vortex supports bound-state-like oscillations, which, in the azimuthal direction, are quantised in the same way as kelvons in three dimensions, looked at in a single fixed plane perpendicular to the vortex core. The lowest such azimuthal excitation corresponds to a circularly varying displacement of the centre of the vortex. As a result, also the density is modified in its radial dependence relative to the rotating position of the vortex, and in the large-volume limit, a continuum of kelvon states emerges, which can be distinguished again by a wave number p parametrising the radial dependence as well as the dispersion of the kelvon. Therefore, an analogy can be drawn between a Kelvin wave extended *along* a vortex line in three dimensions and a "Kelvin wave" representing, at lowest order, a circularly rotating displacement of the vortex position. We will also refer to these quasiparticles in two dimensions as kelvons, for which a dispersion with the same scaling (4.21) as in three dimensions has been found [152, 174]. Wave-like motion along vortex boundaries has also been discussed in the context of Kelvin waves in finite-size, quasi two-dimensional systems as realised in a trapping potential strongly confined in the third dimension [151, 152].

4.4 Universal scaling dynamics

4.4.1 Self-similar evolution of the momentum spectrum

The O(1) theory (4.1) in $d = 2$ spatial dimensions provides a particularly intriguing and valuable framework for the study of relevant degrees of freedom for our initial conditions. Comparable simulations in $d = 3$ for the massive O(1) theory [80, 82] have revealed the momentum distribution function (4.6) which evolves self-similarly according to

$$f(t,p) = t^{\alpha} f_\mathrm{s}\left(t^{\beta} p\right) , \tag{4.22}$$

with universal scaling exponents α and β and scaling function $f_\mathrm{s}(p)$. The distribution function takes the approximate form

$$f(t,p) \approx \left(\frac{\mathcal{N}(t)}{p_\mathrm{IR}^2(t) + p^2}\right)^{\kappa/2} , \tag{4.23}$$

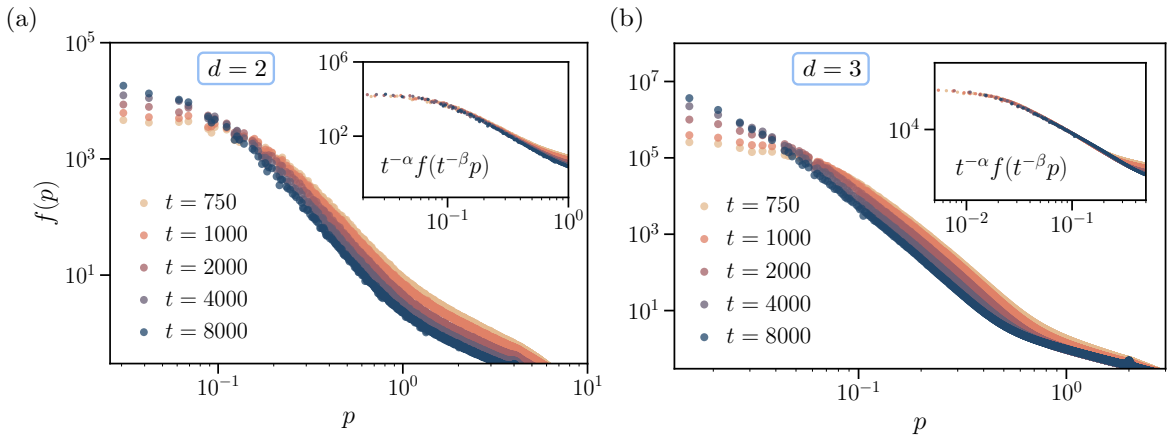

Figure 4.4. Distribution function $f(t,p)$, cf. (4.6), for a single-component scalar field theory in (a) two and (b) three dimensions, shown at five different evolution times t. The inset shows the functions rescaled according to (4.22), with $\beta = 0.25$ and $\alpha = 0.5$ in two dimensions, and $\beta = 0.5$ and $\alpha = 1.5$ in three dimensions. In (a), simulations were run on a 2048^2 lattice, while in (b) the lattice size was 512^3.

where the characteristic momentum scale $p_{\rm IR}$ marks the transition between a plateau in the infrared and power law fall-off $p^{-\kappa}$. For $p \to 0$, the function develops a plateau or increases with a power law much smaller than κ.

According to (4.22), the characteristic scale decreases in time as $p_{\rm IR}(t) \sim t^{-\beta}$, while the overall normalisation scales as $\mathcal{N}(t) \sim t^{2(\alpha/\kappa-\beta)}$. If particle number and thus the integral $\int \mathrm{d}^d p f(t,p)$ is conserved in time, in d dimensions, the relation $\alpha = d\beta$ must hold. Classical-statistical simulations gave the universal scaling exponents $\beta \approx 0.5$ and $\alpha \approx 1.5 \approx d\,\beta$, and $\kappa \approx 4.5$ in $d = 3$ dimensions [48, 80].

This self-similar scaling is confirmed by our results in Fig. 4.4b, where we show the evolution of $f(t,p)$ in $d = 3$ dimensions for different times as a function of momentum. One finds that the characteristic self-similar dynamics in Eq. (4.22) that builds up a condensate, i.e., a macroscopic occupation of the low-p modes, requires the stated values for α and β to obtain a time-insensitive scaling function $f_{\rm s}$ as visible in the inset. This form consists of a nearly constant part at the lowest momenta $p \lesssim p_{\rm IR}$ and the power law decrease $p^{-\kappa}$ at higher momenta $p \gtrsim p_{\rm IR}$ within the infrared momentum range below the inverse healing length $p \lesssim p_{\xi_{\rm h}} = \sqrt{2g\rho_0 M}$.

4.4.2 Coarsening dynamics

Based on the spectral and statistical functions, the above excitation dynamics for single-component scalar fields was found to be markedly different from what is observed and expected in the large-N limit [82], where we have an analytic understanding of these exponents [48, 72–74]. On the other hand, the exponent $\beta \approx 0.5$ is known to apply in qualitatively very different situations. As an alternative to the self-similar transport of free Goldstone quasiparticle excitations to lower momenta, which dominates the large-N limit [73, 105], it could also result from diffusion-type coarsening dynamics of the spatial field configuration,

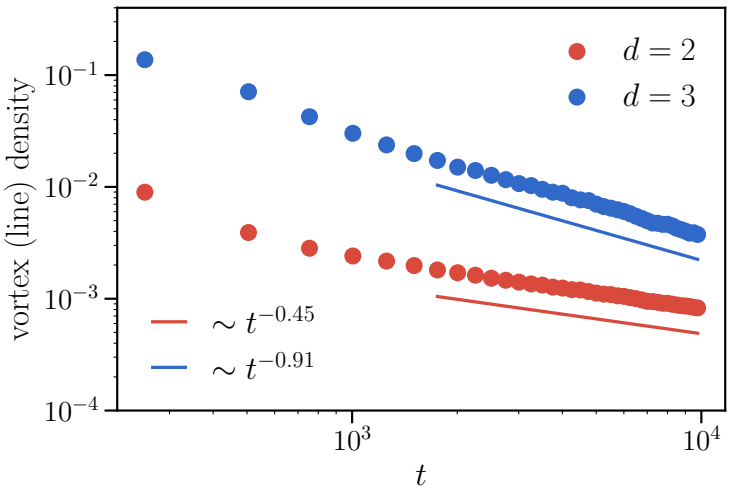

Figure 4.5. Vortex (line) density shown as a function of time, in $d = 2$ and $d = 3$ dimensions for O(1) scalar fields. The decay reveals a power law $N_\mathrm{v} \sim t^{-\xi}$ with $\xi \approx 0.45$ in two dimensions, and $\xi \approx 0.91$ in three dimensions.

e.g., as induced by mutual annihilation of vortices and antivortices excited in the system [79].

Yet, in two-dimensional O(1) simulations, the equal-time distribution function has only been found to scale with $\beta \approx 0.25$, $\alpha \approx 0.5$, and $\kappa \approx 4$ [125]. This is confirmed by our results in Fig. 4.4a, where we show the evolution of $f(t, p)$ for a two-dimensional system in the main panel and its self-similar scaling in the inset using the stated exponents. Despite scanning through a wide range of initial conditions, these results remained unchanged. In particular, we were unable to find a stable $\beta \approx 0.5$ scaling regime in $d = 2$. In contrast, for $N > 1$, we have easily recovered the expected scaling with $\beta \approx 0.5$ and $\alpha = d\beta \approx 1.0$.

A closely related scaling exponent to the $d = 2$ case of O(1) theory, $\beta \approx 0.2$ has been found in simulations of a nonrelativistic Bose gas in two dimensions upon imprinting vortices into the initial field configuration [79], also confirmed experimentally [117]. This scaling behaviour is phenomenologically understood as due to three-body collisions of bound vortex-antivortex pairs with nearby vortices or antivortices. Any such collision allows for an exchange of vortices after which the newly formed vortex-antivortex pair can be more strongly bound and thus potentially undergo fast subsequent vortex-antivortex annihilation [79]. Hence, pair annihilation is dominated by the three-body collision rate, which gives rise to the exponent $\beta \approx 0.2 \ll 0.5$. This stands in contrast to isolated vortex-antivortex annihilation due to background fluctuations, which is governed by a diffusion-type scaling with $\beta \approx 0.5$ [79, 117, 175, 176]. The relevance of three-body collisions was likewise identified in Ref. [125] for the O(1) model in two dimensions without imprinting vortices.

In both Refs. [79, 125] the average vortex density was found to decay as a power law, $n_\mathrm{v} \sim t^{-\xi}$ with $\xi \approx 0.41 \approx 2\beta$, which reflects that the decreasing infrared scale $p_\mathrm{IR}(t) \sim t^{-\beta}$ corresponds to a growing characteristic length scale, which can be associated with the mean inter-defect distance $\ell_\mathrm{v} \sim p_\mathrm{IR}^{-1} \sim t^{\beta}$. Hence, it is useful to define the exponent

$$\xi = 2\,\beta_\mathrm{L}\,, \tag{4.24}$$

which thus characterises the growth of the average free volume between vortex defects in $d = 2$ dimensions. Assuming that the self-similar scaling of the distribution function, (4.22), is related to the coarsening of topological defects, one has that $\beta_{\mathrm{L}} = \beta$.

An interesting question therefore is to what extent the spatiotemporal scaling of $f(t, p)$ and the momentum power law fall-off is, in general, driven by coarsening, or whether the two scaling phenomena are independent. After all, the value of the exponent κ and thus the steepness of the distribution determines whether and how particles can be transported towards the infrared and eventually allow condensation in the $p = 0$ mode. The buildup of such a transport process necessarily involves some underlying coarsening due to causality, as explained in Sec. 4.2.

Hence, before moving on to investigating the excitation spectrum from unequal-time correlation functions, we examine the dynamics of vortices in two dimensions and vortex lines in three dimensions explicitly and extract the respective β_{L} exponents from the spatial field configurations. As mentioned in Sec. 4.3, (anti)vortex defects are identified by a $\pm 2\pi$ phase winding in $\theta(t, \mathbf{x})$, which coincide with a depression in the energy density on the lattice. Based on this, we have extracted the total vortex (line) density in two and three dimensions, which we show as functions of time in Fig. 4.5. For additional details on the data analysis and the extraction of these quantities, see App. B.1.

This vortex density reveals a power law $\sim t^{-\xi}$ with $\xi \approx 0.45$ or $\beta_{\mathrm{L}} \approx 0.23$ for the O(1) model in two dimensions, which is consistent with the $\beta \approx 0.25$ self-similar scaling of the equal-time distribution function f. [3] In three dimensions, we find $\xi \approx 0.91$. It represents the decrease of the total vortex line length per unit volume, which corresponds to a dilution of the vortex rings and tangles as $\sim \ell_{\mathrm{v}}^{-2} \sim t^{-2\beta}$ [177, 178], where ℓ_{v} is the scale measuring the mean distance between vortex lines. Hence, also in $d = 3$, one has $\xi = 2\beta$, and the decrease of the vortex line density implies $\beta_{\mathrm{L}} \approx 0.46 \approx \beta$. While these numbers look convincing, a clearer link to the relevant quasiparticle excitations in f would be desirable. To make such a connection, in the next subsection we discuss the extraction of the frequency and momentum dependence of the correlation functions that are closely related to the distribution function (4.6) but additionally encode the systems' excitation spectra.

4.4.3 Unequal-time correlation functions

A slow self-similar scaling dynamics of the equal-time distribution function $f(t, p)$ with $\beta \approx 0.25$ for the O(1) theory has only been found in two dimensions. Therefore, this provides an interesting study case to investigate the unequal-time correlation functions in both two and three dimensions, focusing on understanding the differences in scaling exponents and also on the potential connections to the dynamics arising from topological defects.

For both the two- and three-dimensional theories, the statistical function F is dominated by a single peak at low momenta in the infrared, which is accurately captured by the (non-

[3] Note however that, in two dimensions, vortex coarsening could also be characterised by $\beta_{\mathrm{L}} \approx \beta \approx 0.5$, as seen for a nonrelativistic Bose gas in [79] and discussed above.

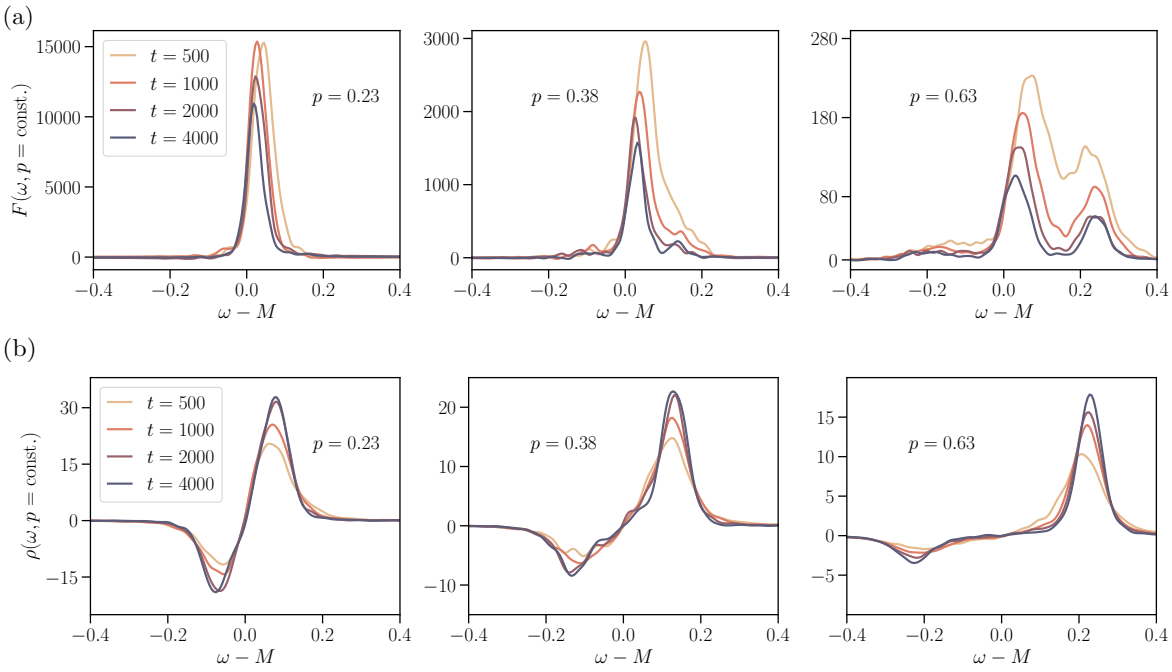

Figure 4.6. Fourier transform, (4.9), of the (a) unequal-time statistical function, $F(t, \omega, p)$, and the (b) spectral function $\rho(t, \omega, p)$ at different central times t and momenta p in $d = 2$ dimensions. They show the dominant transport peak in the vicinity of $\omega - M \approx 0$ in $F(t, \omega, p)$, with both branches of the Bogoliubov quasiparticle peak emerging to the left and right as larger momenta are considered. The spectral function is dominated by the Bogoliubov peak at all momenta. The curves are shown as functions of $\omega - M$, with zero-momentum mass gap M.

Lorentzian) hyperbolic secant function,[4]

$$F_{\mathrm{K}}(t, \omega, p) \simeq \frac{\pi}{2} \frac{A_{\mathrm{K}}(t, p)}{\gamma_{\mathrm{K}}(p)} \operatorname{sech}\left[\frac{\pi}{2} \frac{\omega - \omega_{\mathrm{K}}(t, p)}{\gamma_{\mathrm{K}}(p)}\right] . \tag{4.25}$$

Here, A_{K} is the peak amplitude, γ_{K} is the decay width of the peak and ω_{K} is the corresponding dispersion relation, which can be extracted by employing (4.25) as a fit function.

Example data extracted from numerical simulations for $F(t, \omega, p)$ and $\rho(t, \omega, p)$ is shown in Fig. 4.6 for two dimensions, as functions of frequency $\omega - M$ relative to the 'mass' gap of the dispersion, $\omega(p = 0) = M$, for different times t and different momenta p. To obtain a clearer picture, it is useful to depict the statistical function $F(t, \omega, p)$ in the frequency-momentum plane, as shown in Fig. 4.7, in both two (left) and three (right) dimensions, evaluated at time $t = 1000$. As already denoted on these figures and explained in the following section, the F_{K} peak is identified with Kelvin waves and their quantised excitations, kelvons, in three dimensions, as well as the analogous kelvon quasiparticles in two dimensions. From both representations, we can also see that at higher momenta, a second peak appears, which has been identified before as a Bogoliubov peak [82]. This Bogoliubov peak is more easily accessible from the spectral function $\rho(t, \omega, p)$, which is what we have used

[4] Regarding the notation: this peak corresponds to the "transport peak" in [81] and the "non-Lorentzian peak" (nL) in [82].

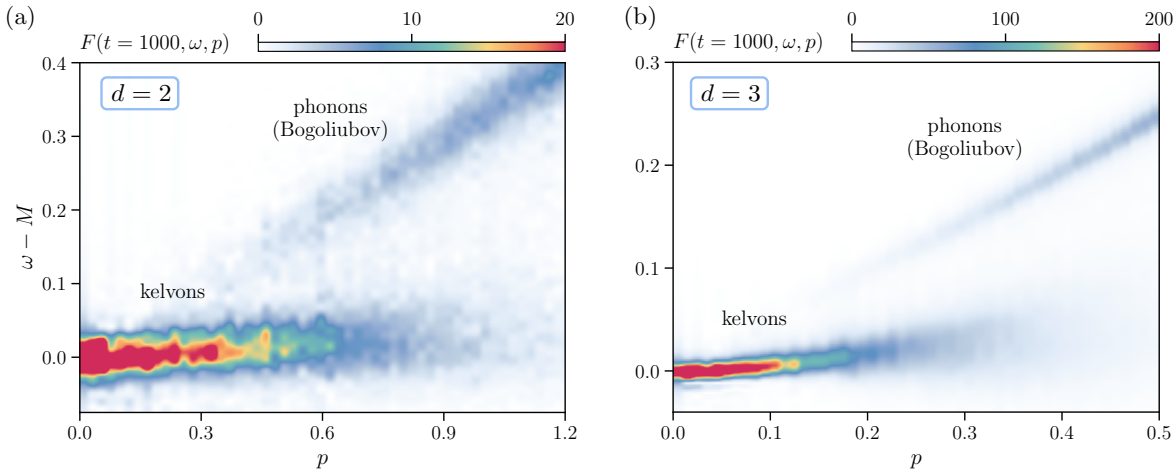

Figure 4.7. Frequency-momentum resolved representation of the statistical two-point correlator $F(t = 1000, \omega, p)$ in (a) two and (b) three dimensions, normalised by the occupation number $f(t, p)$. Momenta and frequencies are shown in units of Q.

at $p = 0$ to determine the effective mass gap M. The peak can be fitted by approximate Lorentzians of the form

$$\rho(t, \omega, p) \simeq \frac{2A_+(p)\gamma_+(t,p)}{[\omega - \omega(p)]^2 + \gamma_+(t,p)^2} - \frac{2A_-(p)\gamma_-(t,p)}{[\omega + \omega(p)]^2 + \gamma_-(t,p)^2}, \tag{4.26}$$

that capture the positive and negative branches of the Bogoliubov excitation. Moreover, its dispersion can be accurately fitted by using the relativistic generalisation (4.18) of the Bogoliubov dispersion [82], which is shown in Fig. 4.8.

The two-dimensional F_{K} looks qualitatively very similar to the three-dimensional one, although our curves are noisier as statistical convergence needs considerably more simulation runs to average over in lower dimensions. Nevertheless, we are still able to accurately extract the peak properties in two dimensions from the available data.

We note that in general, each of the excitations in F should have a counterpart in ρ. For the Bogoliubov peak, we confirm this for the two-dimensional theory in Fig. 4.6 and refer to Ref. [82] for a confirmation in $d = 3$. In contrast, the identification of the F_{K} peak given by (4.25) in ρ is challenging due to the peak's relative suppression in comparison to the Bogoliubov excitations. For $d = 3$, the existence of such a peak in ρ was demonstrated in Ref. [82] by carefully analysing high-statistics data. For $d = 2$, our level of statistics is insufficient to give a clear statement about its existence in ρ.

4.4.4 Kelvon dispersion relations

One of the most important aspects of distinguishing different kinds of quasiparticles and degrees of freedom is understanding their dispersion relation(s). To this end, we have extracted the positions of the different peaks at multiple times. As for the fit forms in the statistical function, up to $p < 0.17$, we have used (4.25), after which a two-peak fit is performed with one additional peak from Eq. (4.26) that takes the Bogoliubov excitation into account in order to improve the accuracy of the fits. Figure 4.9 shows the momentum-dependent position $\omega_{\mathrm{K}}(p)$ for the dominant infrared peak in (a) two and (b) three dimensions.

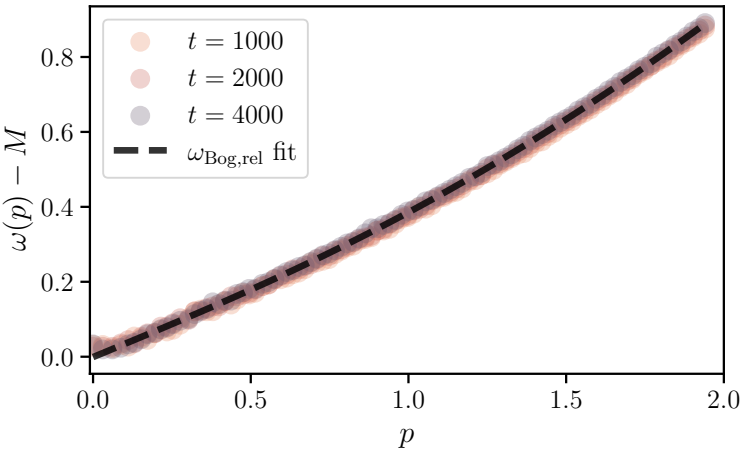

Figure 4.8. The dispersion relation extracted from the Bogoliubov peak in the two-dimensional spectral function. The fit corresponds to the relativistic generalisation of the Bogoliubov dispersion (4.18) and follows a linear, then quadratic, and finally again linear evolution. The healing-length momentum scale is $p_{\xi_\mathrm{h}} \approx 1.2\,Q$.

In three dimensions, the dispersion relation of this peak has been extracted before and was considered to be approximately linear [81, 82]. However, upon closer inspection, one can see that it is, in fact, quadratic at low momenta and linear at higher momenta, which is characteristic for kelvons [173]. Re-analysing the dispersion relation from Ref. [82], we find an excellent fit with the Kelvin wave dispersions as shown in Fig. 4.9b. We fitted the long-wavelength limit of (4.20), with the additional zero-momentum shift proposed in Ref. [171],

$$\omega\left(p_0 + p\right) = \omega_0 + \frac{\Gamma p^2}{4\pi} \ln\left(\frac{1}{|r_\mathrm{c} p|}\right), \quad |r_\mathrm{c} p| \ll 1\,, \tag{4.27}$$

where ω_0 is the frequency of the kelvon with the smallest momentum $p_0 \to 0$ relative to the mass gap M extracted from Bogoliubov excitations, Γ is the (here positive) vortex circulation and r_c is the vortex core radius. These quantities show a time dependence, which represents characteristics of the scaling dynamics not extracted previously. We find an increasing vortex core radius r_c, which reflects that in the course of the infrared transport, the number of coherent excitations at momenta on the order of the inverse healing length,[5] $p_\xi = \xi_\mathrm{h}^{-1} \approx 1.2\,Q$ in $d = 2$ and $p_\xi \approx 0.6\,Q$ in $d = 3$, decreases in time. This increase in the core radius as $r_c(t) \sim t^\beta$ is corroborated by the findings of [178], where the total volume enclosed by the vortex cores in decaying Vinen turbulence in a superfluid in $d = 3$ dimensions was found to settle to a constant at large times, while the vortex line density decays as t^{-1}. The gap ω_0, in $d = 3$, is found to be negative and its modulus decreases, as observed in Fig. 4.9(b). Altogether, the dispersions are found to obey the self-similar scaling relation

$$\omega_\mathrm{K}(t, p) - M = t^{-\beta z} \tilde{\omega}_S\left(t^\beta p\right)\,, \tag{4.28}$$

with exponent $\beta \approx 0.5$ and $z \approx 2$ [82], as also visible in the inset. Here, $z \approx 2$ reflects the dynamical scaling dimension of the Kelvin-wave dispersion relation.

[5] The healing length was extracted from the linear part of the Bogoliubov dispersion, where the speed of sound c_s and the healing length p_ξ are related via $c_\mathrm{s} = p_\xi/\sqrt{2}M$.

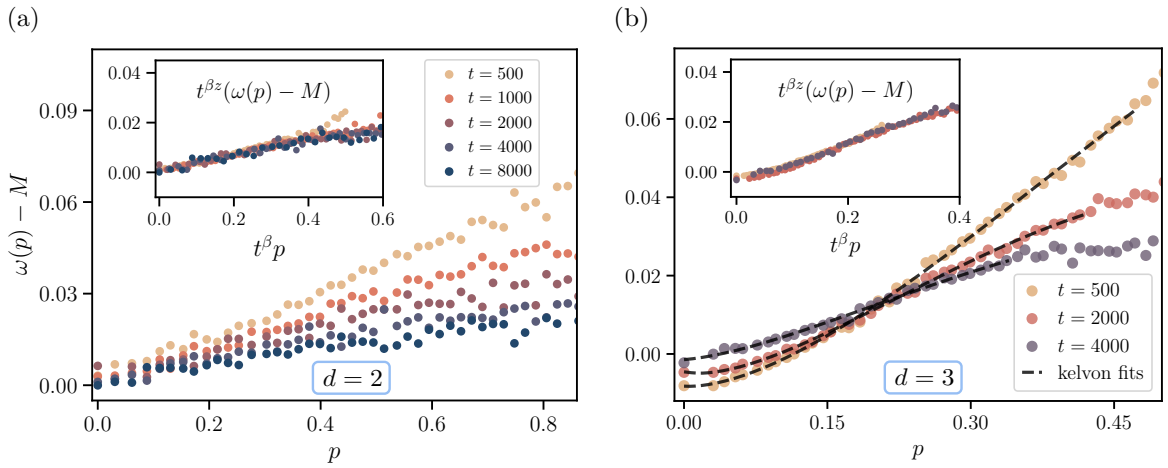

Figure 4.9. Time-dependent dispersion relations $\omega_{\mathrm{K}}(p)$ of the F_{K} peak for a single component scalar field theory: (a) In two dimensions, $\omega_{\mathrm{K}}(p)$ approximately follow straight lines. (b) In three dimensions, the curves are accurately fitted by the Kelvin wave dispersion relation (4.27). Here we show only 3 curves to make it visually clear how the data is captured by the fit. The insets show the rescaled dispersions. In two dimensions, we used $\beta = 0.25$, $z = 2$, while in three dimensions $\beta = 0.5$, $z = 2$.

At later times, we fit the dispersion (4.27) across a progressively smaller momentum range, as shown by the dashed lines in Fig. 4.9(b). This is necessary because the dispersion gradually starts to flatten at higher momenta, as clearly visible at $t = 4000$, deviating from the expected form and making the fit increasingly unreliable. As a result, the extracted parameters become less meaningful in this regime. A more detailed discussion of this behaviour can be found in App. B.2.

For two dimensions, we show the dispersion relation at different times in Fig. 4.9a. We find that it can be equally well fitted by both the kelvon and linear Bogoliubov dispersions, which we discuss more quantitatively in App. B.3 by investigating the residuals for both $d = 2, 3$ and both fits. The dispersion obeys the same self-similar scaling form (4.28) as in $d = 3$, but with exponents $\beta \approx 0.25$ and again $z \approx 2$, as shown in the inset of Fig. 4.9a.

As already discussed earlier in Sec. 4.3, Kelvin waves along the vortex core are not possible in two dimensions. However, as long as one has a finite vortex core, kelvon-like quasiparticles can emerge and be parametrised, besides an azimuthal quantum number, by wave number p. While the dispersion relation in Fig. 4.9(a) can be fitted equally well by both a linear curve and the kelvon dispersion (4.27), indicating the presence of phonons and/or kelvons, it looks qualitatively very similar to the dispersion in Fig. 4.9(b) which is more accurately described by the kelvon fit in $d = 3$ dimensions. With this in mind, we suggest that the dominant infrared peak in two dimensions also originates from kelvons. Apart from this, we also observe Bogoliubov phonons, which are excitations on top of the condensate and have larger dispersion values (4.18). Therefore, the dominant Bogoliubov peak can be generally found to the right of the kelvon peak in Fig. 4.6.

One of the prominent differences between two and three dimensions is that the peaks are considerably broader in two dimensions, as observed from the frequency-momentum resolved statistical function $F(t, \omega, p)$ in Fig. 4.7. A similar effect occurs in non-Abelian

gauge plasmas where the excitation spectrum in two dimensions exhibits a broad non-Lorentzian peak that remains broad even at late times [179] while the quasiparticle peak in three-dimensional plasmas becomes narrower with time [153]. In general, fluctuations are more significant in lower dimensions because of the reduced spatial volume available to average them out. This leads to more prominent noise and dissipation effects, which can then further broaden the peaks.

Additionally, the broadening in two dimensions might also reflect the stronger coupling between the different modes – kelvons and phonons from vortex interactions – due to the reduced dimensionality, where interactions and energy exchange between excitations are more pronounced. This interplay could obscure the distinction between different quasiparticle contributions, making it more challenging to isolate specific dispersion features as compared with the three-dimensional case. While in three dimensions, a distinct quadratic bending at the lowest momenta can be observed in Fig. 4.7b, extracting $F(t, \omega_{\text{max}}, p)$ as shown in Fig. 4.9b clarifies that, indeed, the dispersion is accurately described by a Kelvin-wave dispersion. Moreover, this three-dimensional representation also shows a striking similarity to the "space-time resolved mass spectrum" in Ref. [173], which used GPE simulations to study Kelvin and (Bogoliubov) sound waves.

Curiously, kelvons seem to dominate the dynamics of the infrared peak in $F(t, \omega, p)$, and we do not find any significant contribution from phonons arising, e.g., from vortex-ring annihilation. In two dimensions, this is likely the case as well, but the broader peaks make it more difficult to distinguish their contributions with certainty, leaving open the possibility that phonons may still play a role. How phonon generation occurs in vortex decay in two-dimensional superfluids is still a matter of active research, with different n-body processes put forward for the mechanisms [79, 175, 180–182]. We note that in our case, the process in two dimensions seems to be dominated by three-body collisions, where a vortex-antivortex pair and a lone vortex/antivortex are needed, as described in Sec. 4.4.2 and Refs. [79, 125].

We conclude that, while the topological defects themselves do not directly show up in the excitation spectra of F and ρ, excitations that arise on top of these defects do. Kelvons, quantised excitations of Kelvin waves, seem to be the dominant degree of freedom in the infrared regime of a three-dimensional single-component scalar field theory, while in two dimensions, kelvons, and potentially phonons that arise from the relaxation process of vortex-antivortex annihilation processes play a similar role.

4.4.5 Self-similar scaling and decay width

In Ref. [82] it was shown that the transport/kelvon peak in both $F(t, \omega, p)$ and $\rho(t, \omega, p)$ exhibits self-similar scaling in the three-dimensional $\mathrm{O}(1)$ theory. Similarly, in Ref. [81], self-similar scaling was demonstrated for the three-dimensional $\mathrm{U}(1)$ theory for the same peak in $F(t, \omega, p)$ with the exponents $\beta \approx 1/2$ and $z \approx 2$, and for the Bogoliubov peak in $\rho(t, \omega, p)$, with the same β and $z \approx 1$.

A natural question is whether we find scaling in F and ρ for both peaks in the two-dimensional $\mathrm{O}(1)$ system. Let us start with the Bogoliubov peak. It is more easily accessed from the spectral function, as the kelvon peak in ρ seems to be weak. The spectral function is shown in Fig. 4.10 for $d = 2$ as a function of frequency at different times and momenta

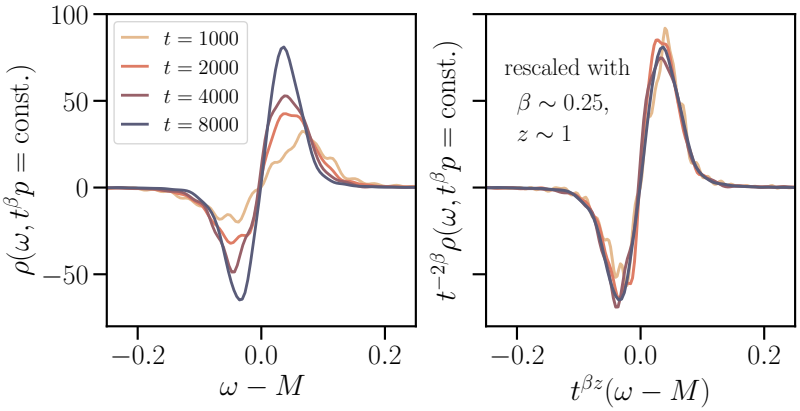

Figure 4.10. Self-similar evolution of the spectral function ρ in $d = 2$ showing the Bogoliubov peak (both positive and negative frequency branches) for constant slices of $t^\beta p$ with $\beta \approx 0.25$ at $p = 0.21, 0.15, 0.13, 0.11$, for the respective times from $t = 1000$ to $t = 8000$.

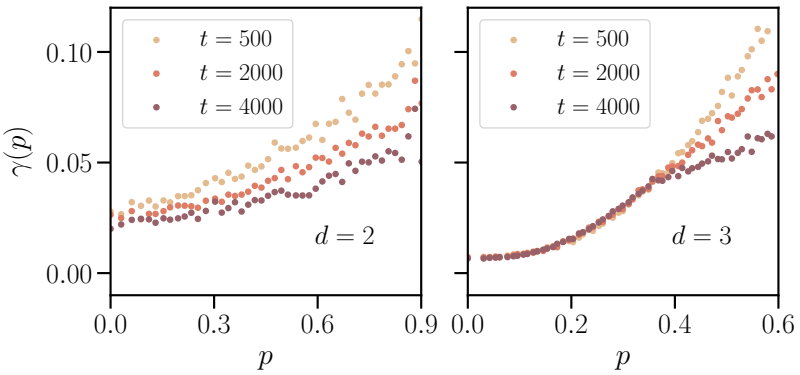

Figure 4.11. Time-dependent decay width of the kelvon peak for a single component scalar field theory in two (left) and three (right) dimensions.

whose combination $t^\beta p$ is kept fixed. The right panel demonstrates that it follows the self-similar scaling ansatz

$$\rho(t, \omega, p) = t^{\beta(2-\eta)} \rho_{\mathrm{s}} \left(t^{\beta z}(\omega - M), t^\beta p \right) , \tag{4.29}$$

with $\eta \approx 0$. While $z \approx 1$, as expected for phonons, we find $\beta \approx 0.25$, just like for the kelvon peak, while $\beta \approx 0.5$ in constant slices of $t^\beta p$ failed to reproduce self-similarity. These findings suggest that there might be an intrinsic connection between the Bogoliubov phonons and the kelvon peak.

In contrast to the Bogoliubov peak, we have found no evidence of a consistent self-similar scaling solution for the F_{K} peak of the two-dimensional O(1) theory. This is unexpected because the left panel of Fig. 4.9 displays self-similar scaling for the dispersion relation $\omega_{\mathrm{K}}(p)$. The problem lies rather in the decay width that scales appropriately in three dimensions but fails to scale in two dimensions.

The decay width of the kelvon peak as extracted from F using the fit form (4.25) is shown in Fig. 4.11 for two (left panel) and three (right) dimensions as a function of momentum at different times. In three dimensions, the decay width was found to be time-independent for low momenta and to have a quadratic form $\sim p^2$ [82], as we confirm in the right panel. In

contrast, as shown in the left panel, it depends on time in a nontrivial way in two dimensions. One finds a relatively large plateau, i.e., an approximately constant decay channel, in addition to a momentum-dependent decay width that decreases with time. This evolution spoils a simple scaling ansatz in $F(t, \omega, p)$.

We finally note that in both $d = 2$ and $d = 3$ dimensions there is a finite decay width even at zero momentum. However, it is worth noting that in $d = 2$, this offset seems to dominate $\gamma_{\mathrm{K}}(p)$ over a vast momentum region, while in $d = 3$, the decay width is dominated by a quadratic form $\sim p^2$ already at low momenta, facilitating the self-similar scaling solution found in [81, 82].

4.5 Discussion and outlook

We have investigated the universal nonequilibrium dynamics of single-component relativistic scalar field theories in $d = 2, 3$ dimensions. Our results reveal a direct connection between the dominant excitations in the infrared regime of nonthermal fixed points and topological defects through Kelvin waves in three dimensions, and the analogous kelvon quasiparticles in two dimensions. In three dimensions, the dominant excitation has a dispersion relation with an excellent fit by the Kelvin wave dispersion from Eq. (4.20), while a similar dominant excitation in two dimensions has a dispersion, which can be similarly well fitted by either a linear, or a kelvon momentum dependence. Both dispersion relations are time-dependent, which can indirectly result from the underlying vortex-antivortex annihilation processes.

A striking difference between two and three dimensions lies in the decay width of these excitations. In three dimensions, the kelvon peak exhibits a well-defined, time-independent width at low momenta, while in two dimensions, the peak is significantly broader, and the decay width does not scale in a simple manner in time. This suggests that the interactions between kelvons, phonons, and vortices in two dimensions are more intricate, potentially due to stronger mode coupling and increased dissipation. The inability to cleanly separate phononic contributions from kelvon-like excitations in the spectral function in two dimensions raises further questions about the interplay between different degrees of freedom in driving the infrared transport.

Regarding the role of vortex coarsening in the observed scaling behaviour, the decay of the vortex (line) density follows a power-law scaling in both two and three dimensions, with exponents consistent with those of the scaling evolution of the momentum-dependent distribution function. At the same time, the strong-wave-turbulence picture of the infrared dynamics of nonthermal fixed points is consistent with our results. However, the underlying degrees of freedom for the $N = 1$ component scalar field theory are notably distinct from what is included in large-N theories, which are free quasiparticles with quadratic dispersion.

Overall, our results complement existing large-N approaches and shed light on the origins of universal scaling behaviour and the importance of vortex and coarsening dynamics in single-component scalar field systems in the context of nonthermal fixed points. By combining a detailed analysis of the topological defects with the underlying excitation spectrum and its dynamical properties, our work paves the way towards a more comprehensive under-

standing of universal scaling behaviour in O(N) scalar models. In particular, this approach can also be applied to other low-N component systems to obtain a consistent picture of the contributing quasiparticle excitations relevant for nonthermal universal scaling phenomena. The results obtained here also mark an essential step in constructing a low-energy effective theory for the $N = 1$ system, which needs to be built upon the relevant degrees of freedom identified in this work.

Chapter 5

Topological defects and universal scaling far from equilibrium

This chapter is based on *"Detecting defect dynamics in relativistic field theories far from equilibrium using topological data analysis"* by V. Noel and D. Spitz, arXiv:2312.04959, Phys. Rev. D 109, 056011 (2024).

Nonthermal fixed points provide a powerful classification scheme for universality classes far from equilibrium, where relativistic scalar fields with global O(N) symmetry serve as an important paradigm. The corresponding universality classes are surprisingly large, where each N in both $d = 2$ and $d = 3$ dimensions, whether relativistic or nonrelativistic, appears to belong to the same universality class up to a possible anomalous dimension. As discussed in the previous chapter, a notable exception to this pattern is the two-dimensional $N = 1$ case. For both the two- and three-dimensional $N = 1$ theories, topological excitations were found to play a crucial role in the dynamics, which serves as a significant stepping stone in constructing an effective description to understand the universal scaling behaviour. However, this analysis has so far focused only on excitations supported by vortex and string defects that appear in the frequency-dependent unequal time correlation functions. In these strongly correlated nonequilibrium systems, the role of different phenomena such as nonlinear wave propagation and defect dynamics remains to be further clarified. For this, it is instructive to construct geometric observables that show more sensitivity to topological objects, as opposed to the two-point correlation functions, which are often used to study universal scaling behaviour in these theories. To this end, we employ *persistent homology* to infer topological features of our nonequilibrium many-body system for different numbers of field components N. Specifically, we show that the persistent homology of local energy density fluctuations can give rise to signatures of self-similar scaling associated with topological defects, distinct from the scaling behaviour of nonlinear wave modes.

In this chapter, after an introduction in Sec. 5.1, Sec. 5.2 describes the lattice simulations used, along with a discussion of topological defects in O(N) theories and their presence in local energy densities. Sec. 5.3 introduces persistent homology and details the signals of topological defects in *Betti number* distributions, for which appropriate definitions and a detailed explanation is presented in the same section. We then interpret the observations

in the context of coarsening dynamics of topological defects and energy transport, highlighting how the evolving topological features correspond to the emergence of large-scale structures over time with a distinct universal scaling exponent, which differs from the scaling behaviour typically observed in standard correlation functions. Finally, Sec. 5.4 provides a conclusion.

5.1 Introduction

Understanding the dynamics of nonequilibrium many-body systems is a fundamental challenge in theoretical physics. While these systems often evolve in a highly complex manner, certain collective phenomena can give rise to effective large-scale descriptions. Systems that are far from equilibrium can exhibit emergent universal scaling behaviour, where nonthermal fixed points provide a useful framework for grouping theories into different universality classes. These phenomena arise across a wide range of physical systems, from early-universe cosmology [10] to ultracold quantum gases [8], highlighting deep connections between seemingly unrelated areas of physics, where relativistic scalar fields with global O(N) symmetry serve as key models for exploring and understanding such far-from-equilibrium dynamics.

Recent experimental and theoretical studies of diverse systems indicate that for a small number of field components N, different initial conditions can lead to distinct nonthermal fixed points. They can be related to separate physical mechanisms: self-similar dynamics consistent with descriptions in the limit of many field components [21, 96], and topological defects undergoing coarsening dynamics for few field components [25, 26, 77–79, 116, 119, 121, 125, 127, 128, 132, 133, 183]. Also for the O(N) vector model in three spatial dimensions, a number of different, N-dependent topological defects are expected to contribute to the dynamics in the infrared [80]. Remarkably, for this model and typical overoccupied initial conditions, many types of equal-time correlation functions merely reveal scaling dynamics consistent with the large-N descriptions, even for low N, and in agreement with nonrelativistic complex U(N) vector models [48, 73, 74, 80–82, 105, 115]. This includes the momentum-resolved distribution function, which is computed from equal-time two-point correlation functions and forms the basis for many studies of far-from-equilibrium universality. The investigation of unequal-time two-point correlation functions has revealed differences among the excitation spectra for $N = 1$ as opposed to the large-N case [82], which is now directly connected to kelvon quasiparticles arising from vortex interactions, as described in Chapter 4. However, this may not necessarily contain clear links to the scaling behaviour related to the coarsening dynamics of the topological defects themselves. A thorough understanding of their role for nonthermal fixed point dynamics can be a prerequisite for the comprehensive classification of universal behaviour far from equilibrium, based on the experimentally and numerically found scaling dynamics. Hence, there is a need for topologically sensitive and computationally accessible observables.

Topological data analysis (TDA) [83, 84] can provide complementary information to correlation functions. Persistent homology, which is the primary tool from the TDA toolbox, gives access to the topology of a nested hierarchy of *complexes* constructed from the

field data. It has been successfully applied to describe nonthermal fixed points for two-dimensional nonrelativistic scalar and three-dimensional gluon fields [184, 185], accompanied by a corresponding mathematical analysis [86]. In the related context of phase transitions, persistent homology allowed for insights into critical phenomena and phase structures [186–197].

In this work, we examine the persistent homology of local energy density fluctuations in O(N) vector models in the classical-statistical regime, starting from overoccupied initial conditions without imprinting defects. Local energy densities can show clear signatures of dynamically built-up defects as we demonstrate. In particular, we show that the related Betti number distributions give rise to N-dependent topological structures reminiscent of the classification of defects in condensates of relativistic O(N) scalar fields, indicating topological dynamics consistent with phase-ordering kinetics [67].

5.2 O(N) vector model and topological defects

We consider a relativistic O(N)-symmetric scalar field theory with field variables $\phi_a(t, \mathbf{x})$, $a = 1, ..., N$, in $d = 3$ spatial dimensions with classical action

$$S[\phi] = \int_{t,\mathbf{x}} \left[\frac{1}{2} \partial^\mu \phi_a \partial_\mu \phi_a - \frac{m^2}{2} \phi_a \phi_a - \frac{\lambda}{4!N} \left(\phi_a \phi_a \right)^2 \right], \tag{5.1}$$

where $\int_{t,\mathbf{x}} \equiv \int \mathrm{d}t \int \mathrm{d}^3\mathbf{x}$, summation over repeated indices is implied, m is the bare mass and λ is the coupling constant. The action (5.1) is invariant under global O(N) rotations acting on the internal field components indexed by a: $\phi_a \mapsto R_{ab}\phi_b$ for $R \in \mathrm{O}(N)$.

5.2.1 Lattice simulations

Similarly to the previous chapter, we consider classical-statistical simulations on a lattice, which provide an adequate description of the quantum dynamics for large occupations, small coupling, and at not too late times [71]. We set overoccupied box initial conditions in momentum space for the scalar fields, where field configurations $\phi_a(t = 0, \mathbf{x})$ are sampled with large Gaussian fluctuations up to a characteristic momentum scale Q, described by

$$f(t = 0, \mathbf{p}) = \frac{N n_0}{\lambda} \Theta(Q - \mathbf{p}), \tag{5.2}$$

with zero macroscopic fields $|\phi(t = 0, \mathbf{x})| = 0$. The initial field configurations are time-evolved according to the equation of motion following from the action (5.1). For more details on this procedure we refer to Chapters 2 and 4.

We consider lattice simulations for $N_s^3 = 512^3$ spatial lattice sites and use a leapfrog solver with $Qa_s = 0.8$, where a_s is the spatial lattice constant, with temporal lattice spacing $\mathrm{d}t = 0.1\, a_s$, initial amplitude $n_0 = 125$ and renormalised mass squared $M^2 = 4Q^2$. The comparably large mass suppresses fluctuations on smaller length scales, which will allow us to reveal the presence of topological features associated with defects. In persistent homology as introduced below, the topological features appear less pronounced for smaller values of

the mass, see App. C.1. For later use we denote the spatial lattice by $\Lambda_s := \{0, a_s, \ldots, (N_s-1)a_s\}^3$.

In this work, we focus on the structures visible in local energy density fluctuations around the mean energy density. The local energy density corresponding to the action (5.1) is

$$T^{00}(t,\mathbf{x}) = \frac{1}{2}\pi_a^2 + \frac{1}{2}(\nabla\phi_a)^2 + \frac{m^2}{2}\phi_a\phi_a + \frac{\lambda}{4!N}(\phi_a\phi_a)^2, \tag{5.3}$$

where $\pi_a = \partial_t\phi_a$ and space-time arguments have been suppressed on the right-hand side.

We consider a single classical-statistical realisation in this work, based on the self-averaging property often encountered for observables in classical-statistical simulations. The latter also holds approximately for the later introduced Betti numbers due to the large number of contributing features.[1] In fact, the Betti numbers are expected to scale proportionally to the system volume for sufficiently large lattices [86, 198]. Specifically, we have verified the insensitivity of Betti numbers after division by the lattice volume for $N_s = 128, 256, 512$. We have also numerically verified their insensitivity to variations of the lattice spacing upon comparison with simulations for $Qa_s = 0.6$ and $Qa_s = 1.2$.

5.2.2 Topological defects in relativistic O(N) theories

Topological defects in condensates

The chosen initial condition sets high occupation numbers up to the momentum scale Q. As discussed in previous works [48, 199], the particle number redistributes towards the infrared via an inverse particle number cascade, which is a consequence of transient approximate particle number conservation. In this dynamical process, a condensate forms in the zero mode, which is initially absent and results from increasing occupancies in the deep infrared. Simultaneously, long-range order gradually builds up [80].[2]

Considering the ordering dynamics of the condensate, the phase space of spatial zero modes of the (Fourier transformed) field variables $\tilde{\phi}_a(t,\mathbf{p}) = \int_{\mathbf{x}} \phi_a(t,\mathbf{x}) \exp(-i\mathbf{p}\mathbf{x})$, formed by $(\tilde{\phi}_a, \partial_t\tilde{\phi}_a)_{a=1,\ldots,N}$ with $\tilde{\phi}_a \equiv \tilde{\phi}_a(t,\mathbf{p}=\mathbf{0})$, is of relevance. Approximate particle number conservation and energy minimisation provide two constraints for the realised condensate configurations [80]. Taking these into account, we denote the physically accessible condensate phase space by $\mathcal{C}_N$, which depends nontrivially on the number of field components N. In particular, the topology of $\mathcal{C}_N$ can be nontrivial, so that topologically nontrivial configurations (defects) can occur. These have been classified in [80], which we review in detail in App. C.2. Specifically, the condensate can feature string defects (vortex lines) for $N = 1, 2, 3$, domain walls for $N = 2$ and monopoles for $N = 4$. For three spatial dimensions, no other defects are expected, and condensates are defect-free for $N \geq 5$.

Note that, as discussed in Chapter 4, defects unavoidably arise during the evolution of the (classical) equation of motion, and are not explicitly part of the initial conditions under

[1] For mathematical details on self-averaging related to persistent homology (ergodicity in persistence) we refer to [86].

[2] As mentioned in the previous chapter, by causality, the formation of a condensate at finite evolution times requires a finite system volume. For infinite system volumes, modes in the deep infrared can mimic the dynamics of a condensate, but lack the related system-scale long-range order [80].

consideration. As described later in this work, defects typically annihilate each other with time via related coarsening dynamics [67], such that their number decreases. On longer time scales than considered here, the condensate itself is expected to decay again due to number-changing processes in the relativistic theory [199], suppressing topological defects as well.

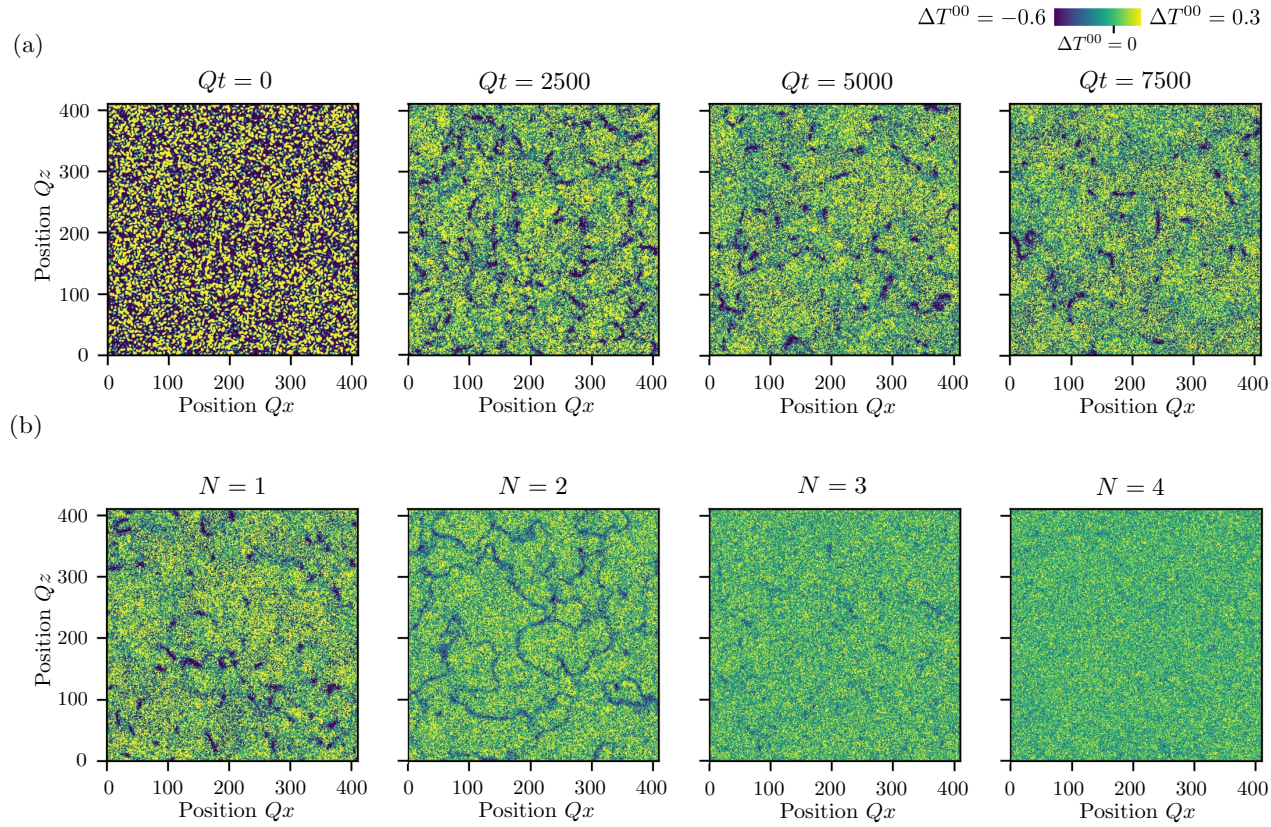

Figure 5.1. Two-dimensional slices of local energy density fluctuations around their mean value, given by $\Delta T^{00} = (T^{00} - \bar{T}^{00})/\bar{T}^{00}$. (a) Snapshots for $N = 1$ at different times, and (b) snapshots for different N at time $Qt = 5000$, showing signatures of string defects for $N = 1, 2, 3$ and of domain walls for $N = 2$.

Observation of defects in energy density fluctuations

We probe topological defects via their signatures in local energy density fluctuations around their mean values, given by

$$\Delta T^{00}(t, \mathbf{x}) := \frac{T^{00}(t, \mathbf{x}) - \bar{T}^{00}}{\bar{T}^{00}}, \tag{5.4}$$

where $\bar{T}^{00} := (1/N_s^3) \sum_{\mathbf{x} \in \Lambda_s} T^{00}(t, \mathbf{x})$ is time-independent due to energy conservation. In Fig. 5.1(a), we display two-dimensional slices of the time-evolving energy density fluctuations for $N = 1$. As time elapses, the initial fluctuations in local energy densities become gradually more homogeneous, with string-like structures distinctively emerging at

early times and minimal energy densities. We associate these with string defects, whose number appears to decline with time.

Comparing the two-dimensional snapshots of energy density fluctuations at a fixed time ($Qt = 5000$) for $N = 1, 2, 3, 4$, as displayed in Fig. 5.1(b), we observe similar string-like structures for $N = 2$ and $N = 3$. Moreover, for $N = 2$ we can also see indications of emerging domains separated by domain walls.[3] These appear at locally low energy densities as closed loops in the snapshots and are clearly distinguishable from the open elongated minima attributed to string-like structures. For $N = 4$ and higher N (not shown), the local energy densities become gradually more homogeneous without any distinct string- or domain-like structures forming, even when running the simulations for comparably long times up to $Qt = 50000$. Such defect structures agree with the classification outlined in Sec. 5.2.2, albeit with monopoles not seen for $N = 4$. Monopoles form point-like local minima in energy densities, similar to the many other fluctuations present in the system. The lattice configurations can therefore still contain monopoles, but might be indistinguishable from configurations without monopoles based on our methods.

The emergence of defect structures at minima in local energy density fluctuations can be heuristically understood based on energetic considerations. Defects locally minimise potential energy densities due to necessary zero-crossings in field amplitudes between oppositely-signed domains, at a string or within a monopole core, which manifest as zero local potential energy densities. Kinetic energy densities require more careful considerations. Defects move slowly in comparison to typical time scales associated with the inverse particle cascade, resulting in small contributions by $\sum_a \pi_a^2$ to T^{00} in (5.3). Moreover, spatial gradients in directions tangent to the curves formed by local energy density minima due to string defects or tangent to the corresponding surfaces for domain walls are naturally small, as in these directions local energy densities do not change much (see Fig. 5.1). In normal directions, defects come with related characteristic (healing) length scales. These can be comparably large, leading to a suppression of normal gradients as well, such that kinetic energy densities of defects are locally suppressed along with potential energy densities. We have observed this in our simulations for both kinetic and potential energy densities (not shown).

5.3 Persistent homology of energy density fluctuations

Persistent homology provides a method to calculate scale-dependent topological structures from data along with measures of their persistence. In Sec. 5.3.1, we present the concept of persistent homology for the investigated local energy density fluctuations. In Sec. 5.3.2, the persistent homology results are discussed in light of the previous discussion of topological defects in condensates. Sec. 5.3.3 considers the time dependence of Betti number distributions in relation to coarsening dynamics, while Sec. 5.3.4 provides an examination of its connection to energy transport towards the ultraviolet.

[3] These have been observed before in other observables, see e.g. [119, 124].

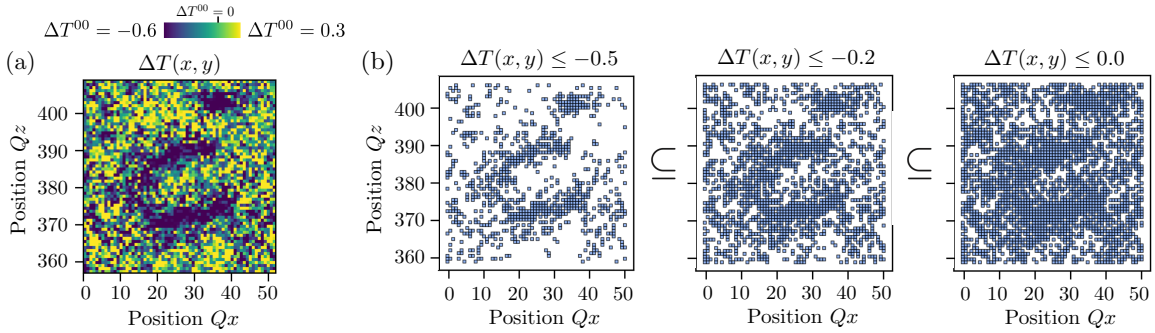

Figure 5.2. Pixelisation of lattice sublevel sets leads to a filtration of cubical complexes. (a): 64×64 pixels excerpt from the top-left corner of the $N = 1$ energy density fluctuation slice shown in Fig. 5.1(b). (b): Three nested cubical subcomplexes corresponding to the indicated sublevel sets of the image of (a), for filtration parameters $\nu \equiv \Delta T^{00} \leq -0.5, -0.2, 0.0$ from left to right.

5.3.1 Persistent homology of energy density fluctuation sublevel sets

Cubical complexes

In this work, persistent homology is computed for cubical complexes [200], which is ideally suited for data in pixel format. Here, we focus on a short, intuitive introduction, while App. C.3 provides mathematically more rigorous constructions. For more elaborate mathematical introductions to TDA we refer to [83, 84].

A cubical complex is a collection of cubes of different dimensions, closed under taking boundaries. For instance, the boundary of a 3-cube is the union of all its six faces, i.e., boundary squares, the boundary of a 2-cube (square) is the union of its four boundary edges, the boundary of a 1-cube (edge) consists of its two endpoints, and the boundary of a 0-cube (point) is empty. The full cubical complex for the spatial lattice under consideration consists of a 3-cube for each lattice site, with a lattice site located at each cube's center. For each 3-cube, all boundary cubes of lower dimensions are included in the full cubical complex.

Subcomplexes of the full cubical complex can be used to describe sublevel sets of functions on the spatial lattice. Intuitively, for a given function these are constructed by including a 3-cube in the subcomplex whenever the corresponding function value is below a chosen filtration parameter. While this fixes the filtration parameters when 3-cubes enter subcomplexes, the filtration parameters for lower-dimensional cubes are set inductively (the lower star filtration, see App. C.3). This way the subcomplex becomes indeed a cubical complex for every filtration parameter, which can be seen as a pixelisation of the corresponding lattice function sublevel set. In particular, a nested sequence of cubical complexes is formed upon increasing the filtration parameter. This procedure is illustrated in Fig. 5.2 for the example of an excerpt of the two-dimensional slice of the local energy density fluctuations shown in Fig. 5.1(b) ($N = 1$). While the two-dimensional slice is for illustrative purposes only, the analysis is carried out in all three spatial dimensions. For a given function on the lattice such as the image excerpt given in Fig. 5.2(a), the cubical complexes corresponding to the sequence of sublevel sets can resemble the structure of minima, see Fig. 5.2(b). In particular, note the persistence of the horseshoe-like accumulation of squares across filtration

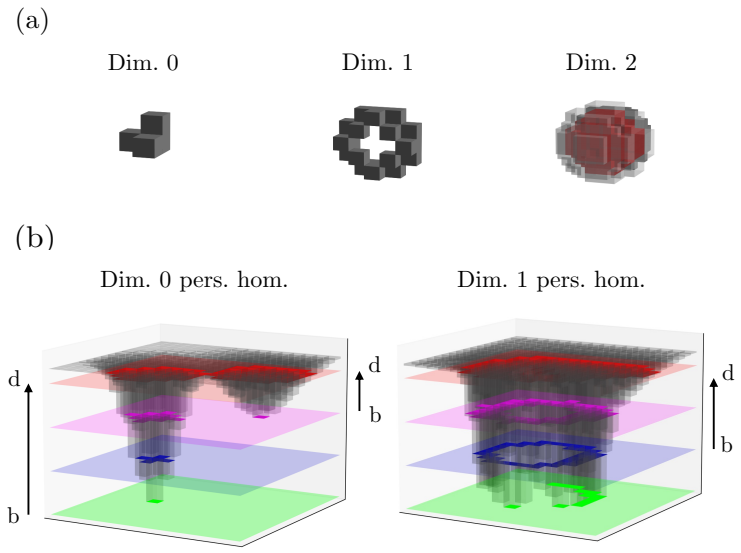

Figure 5.3. (a): Dimension-0, -1 and -2 homology classes from left to right, built with cubical complexes. Dimension-2 homology classes are enclosed volumes, indicated in red. (b): Dimension-0 and -1 holes in cubical complexes for different sublevel sets, giving rise to persistent homology classes.

parameters.

More formally, the evaluation of local energy density fluctuations for a given classical-statistical realisation $\phi(t, \mathbf{x})$ at time t provides a real-valued function $\Delta T^{00}(t, \cdot)$ on the spatial lattice Λ_s. Its sublevel sets are defined as

$$M_{\Delta T^{00}}(t, \nu) := \ (\Delta T^{00}(t, \cdot))^{-1}(-\infty, \nu] = \ \{\mathbf{x} \in \Lambda_s \,|\, \Delta T^{00}(t, \mathbf{x}) \leq \nu\}. \tag{5.5}$$

The described pixelisation procedure leads to the cubical complexes $\mathcal{C}_{\Delta T^{00}}(t, \nu)$, which are the cubical complexes of interest in this work. They form a filtration of the full cubical complex, i.e., a nested sequence of subcomplexes of the full cubical complex with

$$\mathcal{C}_{\Delta T^{00}}(t, \nu) \subseteq \mathcal{C}_{\Delta T^{00}}(t, \mu) \tag{5.6}$$

for all $\nu \leq \mu$. For ν smaller than the minimum value of $\Delta T^{00}(t, \cdot)$, the cubical complex $\mathcal{C}_{\Delta T^{00}}(t, \nu)$ is empty, while for ν larger or equal to the corresponding maximum value, the full cubical complex is recovered.

Persistent homology: holes in complexes

The full cubical complex of the three-dimensional lattice contains a 3-cube for each spatial lattice point. However, as energy density fluctuation values are swept through from the lowest to the highest, in general, the cubical complexes $\mathcal{C}_{\Delta T^{00}}(t, \nu)$ do not contain a cube for every spatial lattice point. Holes of different dimensions can appear, which are described by homology groups. For cubical complexes, such holes are illustrated in Fig. 5.3(a). Connected components are described by dimension-0 homology classes, dimension-1 homology classes describe planar-like holes (which in three dimensions can also be viewed as tunnels), and dimension-2 homology classes describe enclosed volumes.

Within the filtration, holes are born at a birth parameter b and die again with death parameter d, possibly deforming as the (energy density fluctuation) filtration is swept through, i.e., being present in the filtration for the filtration parameter interval $[b, d)$. The persistence $p = d - b$ is a measure of the dominance of a feature in the filtration. This is illustrated in Fig. 5.3(b), where two landscapes of example functions with distinct minima are displayed. The left function contains two distinct dips. As the sublevel set filtration is swept through, the cubical complex is empty as long as the filtration parameter ν is less than the minimum value of the function. As ν is increased, a dimension-0 homology class is born with birth parameter $b = \nu$ when the minimum value of the function is reached (green plane). Further increasing ν (blue plane), the single 2-cube turns into a set of 2-cubes, leaving this homology class unchanged. When the value of ν reaches the pink plane, a second dimension-0 homology class is born (on the right) corresponding to the second dip in the function. The two dimension-0 homology classes merge into one at the red plane, at which point the first homology class dies with death parameter $d = \nu$, and only the second one survives.

Turning to the right function in Fig. 5.3(b), a few dimension-0 homology classes are born (green plane), merging to form a dimension-1 homology class when ν is increased to the level of the blue plane, represented by the circular structure in the complex surrounding a hole. Further increasing ν, the homology is unchanged at the pink plane and the dimension-1 hole only disappears somewhere between the pink and red planes when it is fully filled by 2-cubes.

From the cubical complexes $\mathcal{C}_{\Delta T^{00}}(t, \nu)$, the different dimension-ℓ homology groups $H_\ell(\mathcal{C}_{\Delta T^{00}}(t, \nu))$ can be computed. For three spatial dimensions, the homology groups are generally nontrivial for $\ell = 0, 1, 2$, while the dimension-3 homology group only captures the toroidal lattice topology itself; all higher homology groups are trivial. Their dimensions, called Betti numbers, specify the number of independent dimension-ℓ holes (homology classes):

$$\beta_\ell(t, \nu) := \dim H_\ell(\mathcal{C}_{\Delta T^{00}}(t, \nu)). \tag{5.7}$$

We focus on Betti numbers as an informative persistent homology descriptor in this work.

Persistent homology has a number of useful features. Notably, it is stable against small perturbations of the input [83, 84] (local energy density values in this case) and well-defined large-volume asymptotics exist for suitable persistent homology descriptors such as Betti numbers, including notions of ergodicity [86, 198]. We compute the persistent homology of cubical complexes with $\mathbb{Z}_2$ coefficients and periodic boundary conditions using the open source TDA library GUDHI [201].

To summarise, the persistent homology of sublevel sets can be particularly sensitive to the extended structures formed by local minima and saddle points. We utilise this to investigate the structure of minima in energy density fluctuations, for which nontrivial defect dynamics is expected, based on the discussion in Sec. 5.2.2.

Blockwise averaging lattice functions

By construction, the persistent homology of cubical complexes does not contain spatial metric information. However, this also means that persistent homology computed from functions on the lattice does not differentiate between different length scales and therefore lat-

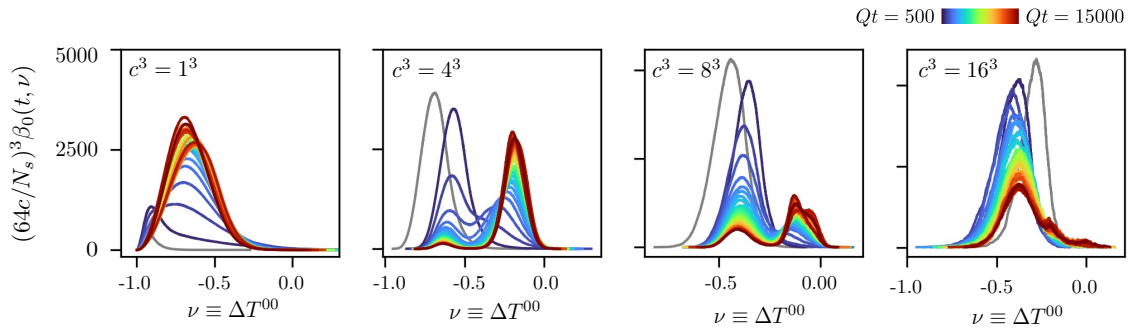

Figure 5.4. Dimension-0 Betti numbers for ΔT^{00} sublevel sets with local energy densities averaged over nearby blocks of every $c^3 = 1^3, 4^3, 8^3$ and 16^3 lattice sites (from left to right). Betti numbers have been normalised to 64^3 lattice size in accordance with their volume-scaling. Betti numbers at initial time $Qt = 0$ are shown in grey.

tice artefacts can enter the analysis. By blockwise averaging (coarsening) the local energy densities on the lattice over blocks of c^3 points for $c > 1$, both these artefacts and, partly, ultraviolet fluctuations are removed. This can pronounce contributions related to the infrared dynamics including topological defects, depending on the parameter c. We emphasise that the blockwise averaging procedure does not affect the dynamical evolution, since it is only applied *a posteriori* to the lattice configurations as part of the persistent homology read-out.

This is demonstrated in Fig. 5.4 for the case of $N = 1$ with dimension-0 Betti numbers. The number of persistent homology classes typically decreases as we average blockwise, since the number of lattice sites decreases accordingly. Betti numbers are expected to scale proportionally to system volume for sufficiently large lattices [86, 198], so that we can account for this by volume-normalising to a certain number of lattice sites, here chosen to be 64^3.[4] Without blockwise averaging, we see that the number of connected components specified by dimension-0 Betti numbers increases at earlier times. Averaging local energy densities over every 4^3 lattice blocks, we notice a twofold peak structure emerging: connected components accounting for the left peak decrease in numbers, while the right peak grows with time. Increasing to averaging over every 8^3 blocks, the left peak appears more pronounced, while the right peak decreases in height. This behaviour persists when coarsening by a factor of 16 in total in each direction.

Concerning the physical interpretation, we notice that the initially large occupations give rise to dynamics towards the infrared and growing wavelengths of correspondingly dominating modes as can be seen in the occupation number distributions, which are comparable to [48] (not shown here). The height of the left peak in dimension-0 Betti numbers decreases over time for energy densities averaged over blocks of $4^3, 8^3$ or 16^3 nearby lattice sites, which implies an increase in the average distance between the related connected components. This indicates that dimension-0 Betti numbers can probe the infrared dynamics for blockwise averaged configurations. In particular, the coarsening dynamics of topolog-

[4] We later focus on blockwise averaging by a factor of 8, so the effective lattice size for the persistent homology analysis is $(512/8)^3 = 64^3$.

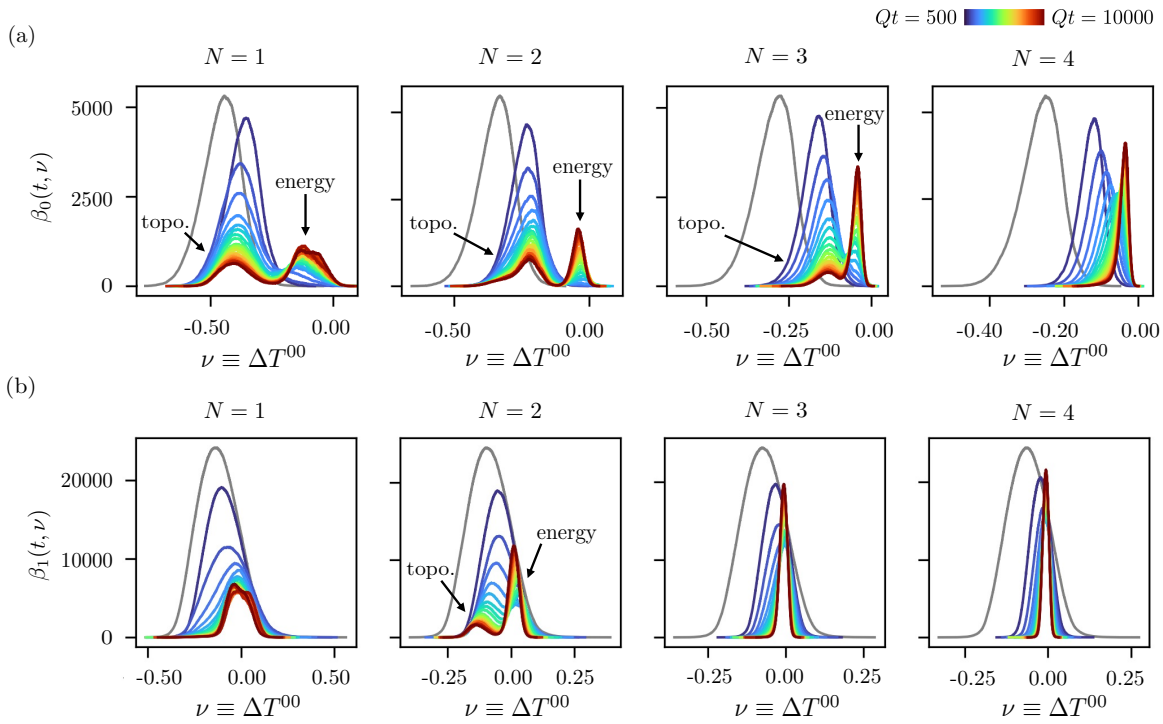

Figure 5.5. (a) Dimension-0 and (b) dimension-1 Betti numbers for ΔT^{00} sublevel sets and $N = 1$ to $N = 4$ field components (from left to right), with averaging over blocks of 8^3 lattice sites. Betti number distributions at initial time $Qt = 0$ are shown in grey. For Betti number distributions with twofold peak structures we label the peak associated with topological defects by "topo. ", and the peak corresponding to energy transport by "energy".

ical defects merging is typically also accompanied by a growth of respective characteristic length scales [67]. In the following, we show results for local energy densities blockwise averaged over cubes of 8^3 neighbouring lattice points. When quantitatively discussing the time dependence of Betti numbers below, it is investigated if the observed phenomena are stable with respect to further blockwise averaging.

5.3.2 Topological defects in Betti numbers

As shown in Fig. 5.5(a), upon investigating the time-evolving dimension-0 Betti numbers of local energy density fluctuations from $N = 1$ to $N = 4$ with averaging over blocks of 8^3 lattice sites, we observe two distinct peaks appearing for $N = 1, 2, 3$, while for $N = 4$ and higher N (not shown) there is only a single peak. Starting from the initial conditions (displayed in grey), for all N, the single peak in dimension-0 Betti numbers first moves to larger filtration parameters at early times, i.e., local minima shift to larger energy density values. For times larger than $Qt = 500$, the peak position stays approximately constant for $N = 1, 2, 3$, while the overall number of dimension-0 structures decreases with time. For $N = 1, 2, 3$, the single peak splits up into two distinct peaks, the left one decreasing, the right one increasing in height. For $N = 4$, no split-up happens, and the peak first decreases, then increases in height, and continuously shifts to larger filtration parameters.

Since dimension-0 Betti numbers count independent connected components, a decline in peak height implies that average length scales associated with the component configurations increase, which correspond to local energy density minima in the field configurations. Heuristically, we may thus associate the left peak and its decrease as a signature of dynamics towards larger length scales. Notably, for $N = 1, 2, 3$, the connected components making up the left peak appear for those ΔT^{00}-values where we have observed defects in the two-dimensional snapshots of ΔT^{00} in Fig. 5.1(b). This indicates that in terms of specific field configurations, it is the defects which dominate the declining left peaks in Betti numbers. Accordingly, the decrease in peak height can signal their coarsening dynamics, which we discuss in more detail later, see Sec. 5.3.3. Vice versa, Betti numbers increasing with time as for the right peak for $N = 1, 2, 3$, and for $N = 4$ for later times $Qt \gtrsim 4000$ implies refinement dynamics of the connected components, i.e., an increasing number of local minima appears. Corresponding length scales shrink in time. The peak shifting towards $\Delta T^{00} = 0$ indicates an ongoing homogenisation process of energy densities and can be suggestive of the transport of energy towards smaller length scales (larger momenta), which we analyse in more detail in Sec. 5.3.4.

Likewise, the analysis of dimension-1 Betti numbers shows qualitatively similar results for all N, but with only a single peak structure that decreases in amplitude, except for $N = 2$, for which two peaks appear. This is displayed in Fig. 5.5(b). More precisely, we notice a height decline of the peak for $N = 1, 3, 4$, which turns into an increase at later times. For $N = 2$, the behaviour is different: the height of the initial peak only decreases, and the single peak splits up into two peaks, where the right one forms at larger energy density values corresponding to $\Delta T^{00} \simeq 0$ and increases in height with time. The dimension-2 Betti numbers agree qualitatively for all N and do not come with twofold peak structures (not shown).

Still, a decline in dimension-1 Betti numbers indicates that length scales associated with the configurations of holes increase in time as for the dynamics towards the infrared. In particular, this applies to the left peak for $N = 2$, which constantly decreases in height and appears at energy densities, for which we have inferred the presence of defects from Fig. 5.1(b). Similarly to the previous discussion of dimension-0 Betti numbers, at later times, the increase in height for most peaks in dimension-1 Betti numbers together with their shift towards $\Delta T^{00} = 0$ can be indicative of refinement dynamics leading to a homogenisation of local energy densities.

To summarise, we observe potentially defect-related peaks in the dimension-0 Betti numbers shown in Fig. 5.5(a) for $N = 1, 2, 3$ but not for $N = 4$, and only for $N = 2$ in the dimension-1 Betti numbers displayed in Fig. 5.5(b). This is in line with the classification of topological defects for condensates outlined in Sec. 5.2.2 and reviewed in detail in App. C.2, provided that the left peak in dimension-0 Betti numbers is primarily due to strings and the left peak in dimension-1 Betti numbers is mostly due to domain walls. Indeed, this appears well-motivated from the structure of the defects along with fluctuations on top as inferred from the local energy density snapshots displayed in Fig. 5.1. For instance, closed strings manifest as loop-like minima in local energy densities and would thus naively appear as distinct dimension-1 persistent homology classes in the sublevel sets for correspondingly low filtration parameters (cf. also the discussion at the end of Sec. 5.2.2). Yet, smaller-scale

fluctuations on top result in a landscape of local minima and maxima, which adds to this and may interrupt the clean loop-like minima in energy densities. Accordingly, a closed string would not appear as a distinct dimension-1 homological feature anymore, but as a multitude of dimension-0 structures, which in addition cannot be distinguished from open strings. Similarly, domain walls would naively show up as empty volumes in energy density sublevel sets for correspondingly small filtration parameters, which would give rise to distinct dimension-2 persistent homology classes. The addition of smaller-scale fluctuations can yield local energy density maxima, which then pierce the enclosed volumes in the sublevel sets, yielding only scaffold-like networks which surround the empty volumes. These do not give rise to distinct dimension-2 persistent homology classes anymore, but to an abundance of dimension-1 features. The same reasoning applies to more exotic configurations of topological defects such as strings pinned to domain walls [132], which our persistent homology analysis cannot distinguish from the domain walls themselves.

5.3.3 Signatures of coarsening dynamics

On the time scales under consideration, the overoccupied initial conditions lead to nonthermal fixed point dynamics as characterised by dynamical self-similar scaling. The temporal dependence of the distribution function is restricted to spatial rescalings by time-dependent power laws while maintaining its shape in time [87]. Near a nonthermal fixed point, the Betti number distributions of energy density sublevel sets can also reveal self-similarity [185]. In this work, the shape of the Betti number distributions shown in Fig. 5.5 is not globally preserved in time, in particular for dimension 0 at $N = 1, 2, 3$, and dimension 1 at $N = 2$. Yet, for these, the shape of the peaks at lower ΔT^{00}-values remains approximately constant in time. We discuss this in detail in App. C.4 considering potential self-similar scaling.

For clarity, here we focus on the time-dependence of the corresponding dimension-0 Betti number peak values, $\beta^{\text{topo}}_{0,\text{max}}(t) = \max\{\beta_0(t,\nu) \,|\, \nu \in \text{left peak}\}$. This counts the maximum number of connected components formed by the pixelised sublevel sets as the filtration parameters corresponding to the peak are swept through, correlating with the number of defects. If a power law in time with exponent $-\vartheta_N$ can be identified from $\beta^{\text{topo}}_{0,\text{max}}(t)$, i.e.,

$$\beta^{\text{topo}}_{0,\text{max}}(t) \sim t^{-\vartheta_N}, \tag{5.8}$$

then in three-dimensional space, average length scales associated with the connected component configurations at the respective value of $\nu \equiv \Delta T^{00}$ grow as a power law with exponent $\vartheta_N/3$:

$$L_N(t) = \left(\frac{N_s^3 a_s^3}{\beta^{\text{topo}}_{0,\text{max}}(t)} \right)^{1/3} \sim t^{\vartheta_N/3}. \tag{5.9}$$

Such a power law growth of length scales can be indicative of the self-similar scaling of corresponding Betti number distributions. Since for $N = 1, 2, 3$, the lower-ΔT^{00} peak is defect-related as noted in Sec. 5.3.2, this length scale can be sensitive to the dynamics of defects. In particular, the number of strings correlating with the number of connected components of the ΔT^{00} sublevel sets (cf. Sec 5.2.2), $L_N(t)$ can serve as a proxy for the time-dependence of average length scales associated with string configurations.

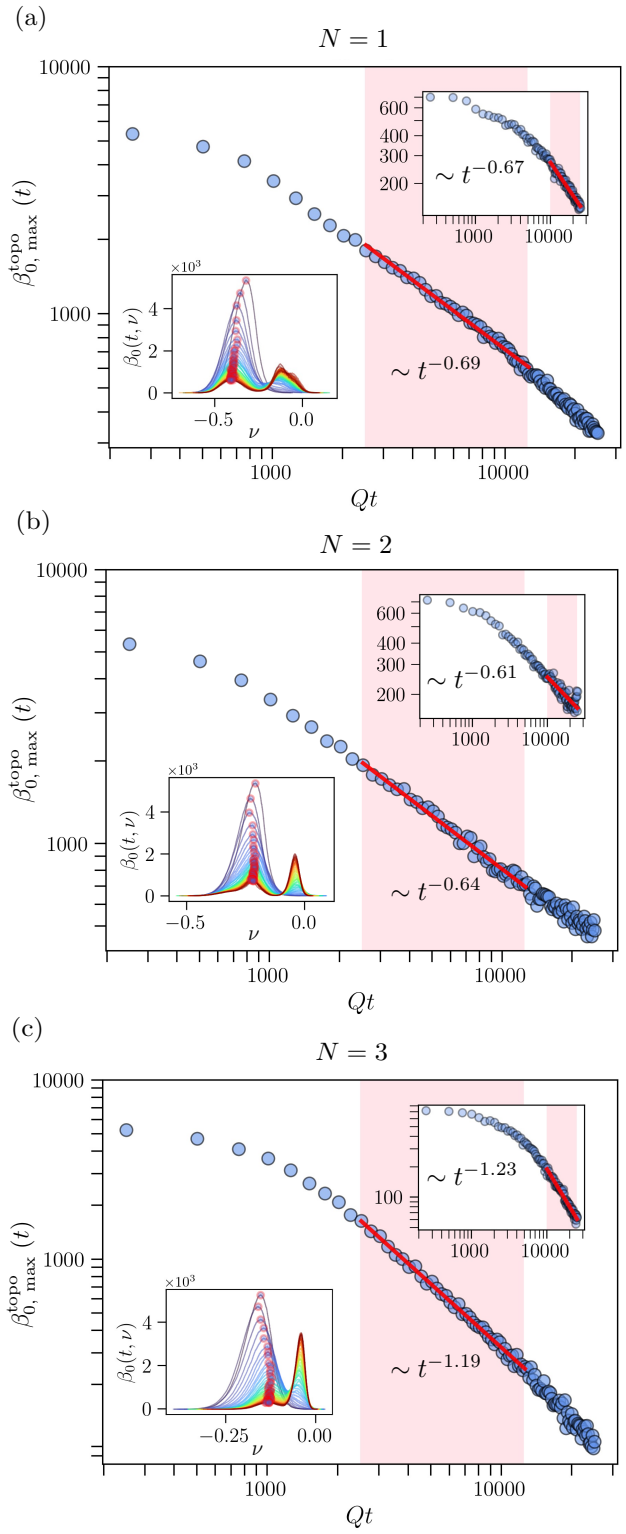

Figure 5.6. Temporal scaling of the left dimension-0 Betti number distribution peak values for (a) $N = 1$, (b) $N = 2$ and (c) $N = 3$, with averaging over blocks of 8^3 lattice sites. The bottom insets show the Betti number distributions, where the red circles indicate the peak positions. The top insets show peak values for averaging over every 16^3 blocks. The power law fits are based on the data in the red shaded Qt ranges.

In Fig. 5.6, we display the time-dependence of $\beta^{\text{topo}}_{0,\text{max}}(t)$ for (a) $N = 1$, (b) $N = 2$ and (c) $N = 3$. The main figures give results for averaging over every 8^3 blocks, while the upper insets show results for 16^3 blocks. All $\beta^{\text{topo}}_{0,\text{max}}(t)$ decrease in time, which indicates that average length scales associated with the connected component configurations grow, as discussed previously (cf. Sec. 5.3.2). The decrease of $\beta^{\text{topo}}_{0,\text{max}}(t)$ is of a power law form for long time ranges. Fitting a power law to these curves for the indicated times[5] via standard χ^2 fits yields $\vartheta_1 = 0.69 \pm 0.02$ ($N = 1$), $\vartheta_2 = 0.64 \pm 0.02$ ($N = 2$) and $\vartheta_3 = 1.19 \pm 0.01$ ($N = 3$) when averaging over every 8^3 blocks. We obtain $\vartheta_1 = 0.67 \pm 0.04$, $\vartheta_2 = 0.61 \pm 0.05$ and $\vartheta_3 = 1.23 \pm 0.03$ when averaging over 16^3 blocks. Thus, within errors these exponents are insensitive to blockwise averaging in the considered regime. They describe dynamics predominantly related to string defects, which appears well-separated from the dynamics on much smaller length scales based on the described insensitivity to blockwise averaging. This is in contrast to the analogous analysis for the potentially defect-related peak at $N = 2$ in dimension-1 Betti number distributions, for which the power law scaling behaviour is different when averaging over blocks of 8^3 versus 16^3 lattice points. For this reason, a more detailed analysis of the defect-related peak in $N = 2$ dimension-1 Betti number distributions is only described in App. C.5.

The fitted exponents ϑ_N correspond to the following power laws describing the time dependence of the length scales $L_N(t)$ (for averaging over every 8^3 blocks):

$$L_1(t) \sim t^{0.2}, \quad L_2(t) \sim t^{0.2}, \quad L_3(t) \sim t^{0.4}. \tag{5.10}$$

It is instructive to compare this with the known dynamics of topological defects as captured by phase-ordering kinetics [67], which describes the growth of order through coarsening dynamics when a system is quenched across a phase transition. Notably, phase-ordering kinetics captures the mutual annihilation of vortices and antivortices (strings) as well as the shrinking of domain walls with time. These processes can give rise to self-similar scaling which is characteristic of a nonthermal fixed point, with defect-related length scales displaying a power law in time. For instance, numerical studies of universal dynamics in one-dimensional Bose gases have revealed power law exponents of order 0.25 to 0.35 [127, 133, 202]. Recent experiments with ultracold atoms in a quasi-one-dimensional elongated optical trap have pointed towards a growth of length scales related to vector solitons as a power law in time with exponent 0.28 ± 0.05 [25]. In two spatial dimensions, it is known that inter-vortex distances can grow proportional to $t^{0.2}$ for nonrelativistic systems [79, 183, 184, 203], and similarly for a nonrelativistic projection of relativistic scalar theory [125]. For three spatial dimensions, signatures of defects in scalar field theories have been detected previously, albeit without analysing their self-similar scaling dynamics [77, 116, 119, 124]. Yet, even in this case, phase-ordering kinetics predicts scaling exponents for defect-related length scales in the range of 0.2 to 0.3, if conserved order parameters are considered [67]. Our results for $L_1(t)$ and $L_2(t)$ as deduced with persistent homology are well within this range. The scaling exponent of $L_3(t)$ is closer to 0.5, which is considered to be the relevant

[5] Note the different time intervals for 8^3 versus 16^3 blocks. This is due to initially slower dynamics in Betti number distributions for averaging over 16^3 blocks compared to 8^3 blocks, since part of the faster ultraviolet modes do not contribute to the former (cf. Fig. 5.4).

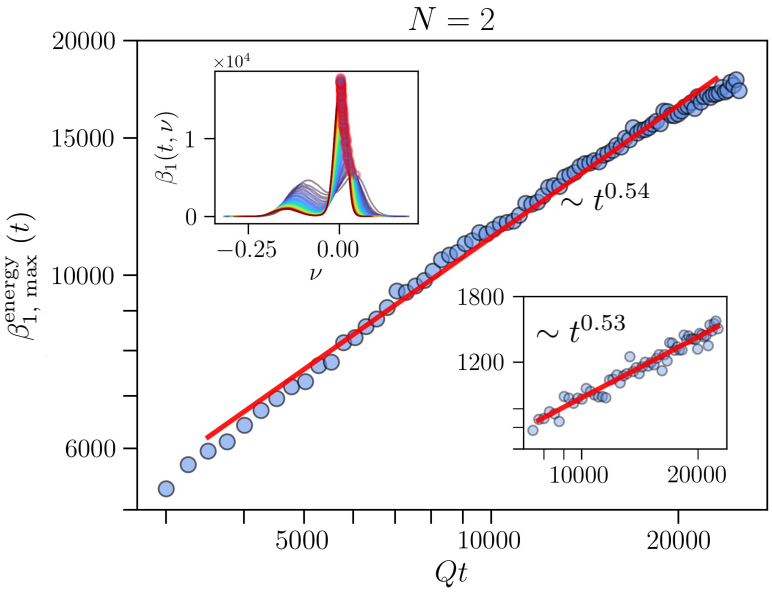

Figure 5.7. Temporal scaling of the right dimension-1 Betti number distribution peak values for $N = 2$. Averaging over blocks of 8^3 lattice sites has been employed. The top inset shows the actual Betti number distributions, where the red circles indicate the peak values. The bottom inset shows peak values for averaging over every 16^3 blocks. The power law fit is based on the data in the Qt range for which it is displayed. Note the smaller time interval shown here in comparison to Fig. 5.6.

exponent for length scale dynamics associated with the particle cascade in large-N expansions (up to anomalous dimensions) [48, 81, 82], where topological defects are absent. Still, topological defects can also give rise to such dynamics [67, 105].

Note that the association of persistent homology classes with defects is not a one-to-one correspondence, and not all persistent homology classes need to behave uniformly according to (5.10). Therefore, for our method we expect systematic errors on the deduced scaling dynamics of topological defects, which we do not consider here and are to be discussed in a future work.

5.3.4 Signatures of energy transport

In addition to the coarsening dynamics, there is an ongoing homogenisation process of local energy densities. This is apparent from the peaks with increasing amplitudes close to $\Delta T^{00} = 0$ in the Betti number distributions, which shifts towards the mean local energy density. Again, we study their maxima, in this case for dimension-1 Betti number distributions, denoted by $\beta_{1,\max}^{\text{energy}}(t) = \max\{\beta_1(t,\nu) \,|\, \nu \in \text{right peak}\}$.

In Fig. 5.7, we show $\beta_{1,\max}^{\text{energy}}(t)$ for $N = 2$ when averaging over every 8^3 blocks (main figure) and 16^3 blocks (bottom inset). Comparable outcomes can be obtained for other dimensions and N. We find that the number of features as counted by $\beta_{1,\max}^{\text{energy}}(t)$ in Fig. 5.7 grows in time, such that corresponding dimension-1 holes (tunnels) steadily decrease in size. Though slightly bent, the data can be approximately described by a power law, $\beta_{1,\max}^{\text{energy}}(t) \sim t^{-\vartheta_{\text{energy}}}$. Standard χ^2 fits yield $\vartheta_{\text{energy}} = -0.54 \pm 0.02$ for averaging over every 8^3 blocks and

$\vartheta_{\text{energy}} = -0.53 \pm 0.03$ for 16^3 blocks, such that $\vartheta_{\text{energy}}$ appears stable for this regime of blockwise averaging.

As before, we can estimate the time dependence of average length scales associated with the dimension-1 holes from the time dependence of $\beta_{1,\text{max}}^{\text{energy}}(t)$:

$$L_{\text{energy}}(t) = \left(\frac{N_s^3 a_s^3}{\beta_{1,\text{max}}^{\text{energy}}(t)} \right)^{1/3} \sim t^{\vartheta_{\text{energy}}/3}, \tag{5.11}$$

which leads to $L_{\text{energy}}(t) \sim t^{-0.18}$ for averaging over every 8^3 blocks. It is well known that turbulent energy transport towards the ultraviolet is accompanied by self-similar scaling behaviour characteristic of a nonthermal fixed point, for which related length scales dynamically shrink as $\sim t^{-1/7}$ [30, 31]. The power law behaviour $L_{\text{energy}}(t)$ is close to this, which suggests that the corresponding structures in Betti number distributions are due to excitations in local energy densities transported towards smaller length scales. Deviations can be caused by the blockwise averaging procedure and the tentative interpretation of features in the Betti number distributions with different physical phenomena, which are in general not perfectly separated. Moreover, while the maxima of the Betti number distributions can provide estimates for the overall number of structures associated with the corresponding peaks, this number partly remains ambiguous in light of non-uniform persistences of features in the filtration.

5.4 Conclusions

In this work, we have investigated the real-time dynamics of relativistic O(N) scalar fields in overoccupied scenarios. We have applied TDA to lattice configurations, which can provide complementary information to the traditionally investigated distribution functions computed from equal-time two-point correlations. More specifically, we have considered Betti numbers computed for sublevel sets of local energy density fluctuations. These have revealed clear signals of dynamically generated topological defects. The identification of defects in the Betti numbers is based on the comparison with defect structures visible in local energy density landscapes. Crucially, the N-dependent topological features visible in the Betti numbers have been consistent with the classification of defects for condensates in relativistic O(N) scalar fields [80].

The number of connected components associated with the topological defects has decreased in time as a power law, which is indicative of self-similar scaling dynamics. This behaviour corresponds to power law growth of length scales associated with their dilution, with scaling exponents ~ 0.2 for $N = 1$ and $N = 2$, and ~ 0.4 for $N = 3$. While the values for $N = 1, 2$ agree well with the findings for topological dynamics in a variety of simulations, the value for $N = 3$ is closer to the scaling behaviour of the model at large N. Yet, topological dynamics can also lead to the latter scaling dynamics [67, 105]. A thorough quantitative analysis of the relation to phase-ordering kinetics and a more careful study of possible dynamical contributions to the structures associated with defects in Betti numbers is beyond the scope of this paper.

In addition, we have observed signatures of energy transport and the related universal scaling behaviour in the Betti numbers. While for overoccupied scenarios the distribution

function reveals a dual cascade with particle and energy transport, the Betti numbers computed for local energy density fluctuations may therefore be able to distinguish topological dynamics from energy transport.

Our work hints at the importance of topologically sensitive observables in order to uncover defect dynamics in universal regimes far from equilibrium. In particular for three-dimensional systems, defect-driven temporal scaling dynamics can be hard to access with distribution functions and appears to be suppressed in overoccupied scenarios. Based on the present work, TDA-based observables are particularly promising to investigate along with distribution functions, since they can be sensitive to extended field configurations of arbitrary size.

This method is applicable without major modifications to the analysis of ultracold atom experiments. Local atom densities can play a similar role to the local energy densities considered in this work, with topological configurations also showing up as distinct minima. These features can be detected using standard absorption imaging techniques. In this spirit, a recent work has exploited TDA to detect dark solitons in condensate density images [204]. It is particularly beneficial that this method does not rely on more sophisticated experimental techniques such as response measurements to probe correlation functions at unequal times [81, 82, 136, 153, 205, 206].

Our work reinforces the potential of TDA to provide relevant information on the dynamics of strongly correlated many-body systems. The choice of cubical complexes has especially been advantageous to reveal the presence of nonlocal structures. TDA can facilitate the systematic study of the role of topological defects for nonequilibrium quantum many-body dynamics, with diverse regimes of applicability ranging from cold atoms to the collisions of heavy nuclei.

Chapter 6

Nonthermal scaling phenomena with the two-particle irreducible effective action

This chapter is based on *"Nonthermal scaling phenomena with the two-particle irreducible effective action"* by V. Noel, A. N. Mikheev, C. Huang, and J. Berges (in preparation).

Systems far from equilibrium can exhibit self-similar scaling behaviour in time and space near nonthermal fixed points. One of the primary approaches to studying this scaling is to derive evolution equations for correlation functions within a given model and analyse their scaling properties. However, this analytical approach is based on scaling analyses, where the resulting scaling exponents are either integers or simple rational fractions, under the assumption that the anomalous dimension η is zero. Without this assumption, the approach does not predict a specific value for η, which, if nonzero, is expected to be small, as numerical results remain close to the analytically obtained ones. This raises the question of whether such scaling analyses capture all possible nonthermal scaling solutions.

Nonthermal fixed points have also been investigated through numerical simulations, specifically using real-time classical statistical simulations and the Two-Particle Irreducible (2PI) formalism. In these approaches, usually, a highly overoccupied initial condition is prepared, after which the system dynamically evolves towards a nonthermal fixed point. This method relies on the system approaching an attractor solution far from equilibrium, where self-similar scaling behaviour emerges during its evolution. While this provides valuable insights into nonequilibrium dynamics, existing methods have limitations in accurately extracting scaling properties because scaling exponents can be influenced by the specific simulation code used, exhibit slight sensitivity to initial conditions, and are subject to errors arising from self-similar fitting procedures. It is also restricted to the case when the attractor solution is approached during the time evolution. Therefore, new methods are needed to describe scaling behaviour, not only to potentially improve the precision of scaling exponent extraction but also to extend the study of nonthermal scaling beyond attractor solutions typically associated with nonthermal fixed points.

In this chapter, we investigate scaling phenomena in strongly correlated systems, beginning with the well-established *Wilson–Fisher* fixed point in equilibrium, followed by an exploration of nonthermal scaling behaviour in nonequilibrium dynamics. We discuss how the

large-N expansion within the 2PI formalism provides a robust, nonperturbative framework for studying both cases. This chapter begins with an introduction in Sec. 6.1, highlighting the motivations behind the 2PI effective action approach. The framework for extracting scaling solutions is benchmarked for the thermal critical behaviour in Sec. 6.2, after which it is applied to nonthermal scaling phenomena in Sec. 6.3. By solving the self-consistent 2PI equation, a nonthermal scaling solution is extracted through the explicit computation of the self-energy integrals. Finally, a conclusion is presented in Sec. 6.4 with a possible outlook on future directions.

6.1 Introduction

Far-from-equilibrium systems can exhibit scaling behaviour and large fluctuations near nonthermal fixed points, similar to the features observed at second-order phase transitions in thermal equilibrium. In (near-)equilibrium systems, Wilson–Fisher fixed points have provided an important paradigm for continuous phase transitions, with a notable example being the three-dimensional O(N)-symmetric scalar field theory. The systems of interest can be vastly different in terms of energy scales; for instance, the O(4) model is expected to describe the high-temperature QCD phase transition for the case of two massless quark flavours [207], and the O(2) model characterises the relevant universality class for Bose-Einstein condensates [208], capturing the behaviour in certain ultracold quantum gases. Beyond these examples, for ferromagnetic phase transitions, the Ising model, characterised by O(1) symmetry, the XY model with O(2) symmetry, and the Heisenberg model with O(3) symmetry are of importance [209]. Additionally, the $N \to 0$ limit is relevant for describing the critical swelling of long polymer chains near the collapse transition [210], where the system undergoes a transition between a swollen and collapsed state, further illustrating the wide applicability of these universality classes.

In this context, the 2PI approach offers a powerful framework for understanding both equilibrium and nonequilibrium dynamics when applied to scaling phenomena. When combined with a large-N expansion in terms of the number of field components, this method offers a nonperturbative approach that does not rely on a small coupling parameter, enabling a controlled and systematic study of critical phenomena in both equilibrium and nonequilibrium settings. The 2PI $1/N$ expansion has been successfully applied before [211] to compute the universal properties directly at the critical temperature of a second-order phase transition in three dimensional O(N)-symmetric scalar fields. Specifically, it has recovered the N-dependent anomalous dimension $\eta(N)$, with values comparable to those obtained from Monte Carlo simulations and renormalisation group approaches. Beyond equilibrium, evolving the 2PI equations of motion has also enabled the study of nonthermal scaling phenomena by computing correlation functions and analysing their self-similar evolution in time. However, this has so far always relied on approaching an attractor solution, limiting the scope of scaling analysis. Therefore, a key challenge remains in characterising scaling behaviour out of equilibrium.

In the following, we present a numerical procedure to extract the scaling properties for relativistic scalar fields in a strongly correlated, nonthermal scaling regime. To validate

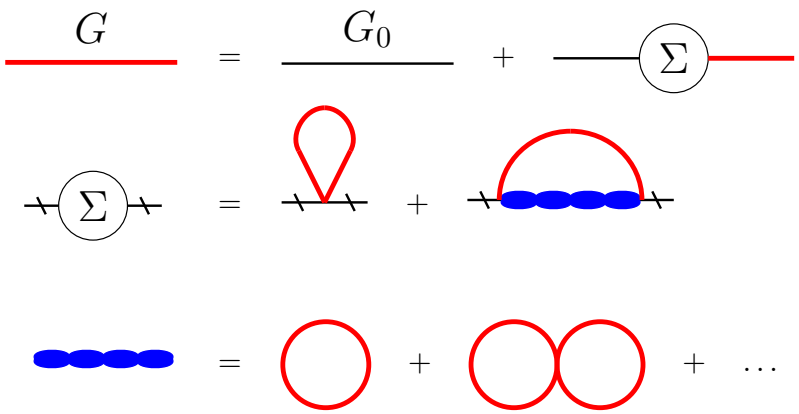

Figure 6.1. Diagrammatic representation of the self-consistent 2PI equation for the full propagator G at NLO order in a $1/N$ expansion. The top diagrams describe Eq. (6.3), expressing the resummed propagator G in terms of the classical one G_0 and the self-energy Σ. The middle diagrams show the self-energy expressed in terms of the LO contribution (tadpole) and the NLO contribution (blue chain sum) in the large-N expansion, while the chain sum is expressed at the bottom in terms of G.

our approach, we first benchmark it against existing analytical results from the 2PI large-N expansion for the Wilson–Fisher fixed point in three dimensions. We then extend the method to formulate the corresponding problem on the Keldysh contour for nonequilibrium dynamics.

6.2 Equilibrium criticality

We first consider a Euclidean field theory for a real, N-component scalar field φ_a with classical action

$$S[\varphi] = \int \mathrm{d}^d x \left(\frac{1}{2}\partial_\mu \varphi_a(x)\partial_\mu \varphi_a(x) + \frac{m^2}{2}\varphi_a(x)\varphi_a(x) + \frac{\lambda}{4!N}\left(\varphi_a(x)\varphi_a(x)\right)^2 \right), \quad (6.1)$$

where $a = 1, \ldots, N$, and summation over repeated indices is implied. We will focus on the case of $d = 3$, where O(N) models are known to undergo a second-order phase transition at a critical mass $m^2 = m_C^2(N, \lambda)$ for all N. Our analysis is conducted at this critical mass, where the correlation length diverges, rendering standard perturbative approaches invalid. As discussed in Chapter 2, the 2PI effective action provides a powerful framework for analysing this system, which is especially effective when combined with a large-N expansion [9, 212, 213]. Instead of relying on a small coupling parameter λ, the large-N expansion treats the number of field components N as the expansion parameter. A key advantage of this is that at next-to-leading order (NLO), it enables the resummation of an infinite number of diagrams to all orders in perturbation theory, as discussed in Sec. 2.3.3. This resummation significantly improves the accuracy of theoretical predictions in strongly correlated systems.

At the critical point, the universal behaviour of the system is characterised by the anomalous dimension η, which governs the power-law scaling of the propagator. In the limit

$\mathbf{p}^2/\Lambda^2 \to 0^+$, the propagator takes the form:

$$G(\mathbf{p}) = \frac{1}{\mathbf{p}^2}\left(\frac{\mathbf{p}^2}{\Lambda^2}\right)^{\eta/2}, \tag{6.2}$$

where Λ is an ultraviolet cutoff. In the following expressions, we ignore Λ as it does not affect the universal scaling properties, which we have numerically verified. As introduced in Sec. 2.3.3, for the resummed propagator

$$G^{-1}(\mathbf{p}) = \mathbf{p}^2 + m^2 + \Sigma(\mathbf{p}), \tag{6.3}$$

the expression for the 2PI large-N self-energy at NLO is given by

$$\Sigma(\mathbf{p}) = \lambda\frac{N+2}{6N}\int_{\mathbf{q}} G(\mathbf{q}) - \frac{\lambda}{3N}\int_{\mathbf{q}} G(\mathbf{p}-\mathbf{q})\mathbf{I}(\mathbf{q}), \tag{6.4}$$

with the chain sum

$$\mathbf{I}(\mathbf{q}) = 1 - \left(1 + \frac{\lambda}{6}\int_{\mathbf{r}} G(\mathbf{q}-\mathbf{r})G(\mathbf{r})\right)^{-1}. \tag{6.5}$$

This describes a closed set of self-consistent equations, which is shown in diagrammatic form in Fig. 6.1. At the critical point, $G^{-1}(\mathbf{p}=0) = 0$, therefore by taking the difference $G^{-1}(\mathbf{p}) - G^{-1}(\mathbf{p}=0)$, the local (divergent) part of the self-energy is subtracted, and with the evaluation of the chain sum, the fixed point equation becomes

$$G^{-1}(\mathbf{p}) = \mathbf{p}^2 + \frac{\lambda}{3N}\int_{\mathbf{q}} [G(\mathbf{p}-\mathbf{q}) - G(\mathbf{q})]\left[1 + \frac{\lambda}{6}\int_{\mathbf{r}} G(\mathbf{q}-\mathbf{r})G(\mathbf{r})\right]^{-1}. \tag{6.6}$$

At the critical point, the convolution integral over $\mathbf{r}$ becomes $\gg 1$, such that λ drops out of the equation in (6.6), which demonstrates the underlying universal behaviour, giving

$$G^{-1}(\mathbf{p}) = \mathbf{p}^2 + \frac{2}{N}\int_{\mathbf{q}} [G(\mathbf{p}-\mathbf{q}) - G(\mathbf{q})]\left[\int_{\mathbf{r}} G(\mathbf{q}-\mathbf{r})G(\mathbf{r})\right]^{-1}. \tag{6.7}$$

The convolution $\int_{\mathbf{r}} G(\mathbf{q}-\mathbf{r})G(\mathbf{r})$ may be solved using Feynman parametrisation to yield

$$\int_{\mathbf{r}} G(\mathbf{q}-\mathbf{r})G(\mathbf{r}) = \frac{1}{8\pi^{3/2}}\frac{\Gamma\left(\frac{1}{2}-\eta\right)\left(\Gamma\left(\frac{1+\eta}{2}\right)\right)^2}{\left(\Gamma\left(1-\frac{\eta}{2}\right)\right)^2\Gamma(1+\eta)}\left(\mathbf{q}^2\right)^{\eta-1/2}, \tag{6.8}$$

which provides an immense analytic simplification. Subsequently, the entire self-energy expression can be further simplified analytically in a $\mathbf{p} \to 0$ expansion [211] with the help of hypergeometric functions into a series

$$\Sigma(\mathbf{p}) = \beta(\eta)\mathbf{p}^{2-\eta} + \alpha(\eta)\mathbf{p}^2 + \ldots, \tag{6.9}$$

which then reduces the self-consistent equation (6.3) into simple power laws only. Thus, we have

$$\mathbf{p}^{2-\eta} = \mathbf{p}^2 + \beta(\eta)\mathbf{p}^{2-\eta} + \alpha(\eta)\mathbf{p}^2 + \ldots, \tag{6.10}$$

where the prefactors $\beta(\eta)$ and $\alpha(\eta)$ have been computed as

$$\beta(\eta) = \frac{4\eta(1-2\eta)\cos(\eta\pi)}{(3-\eta)(2-\eta)\sin^2(\eta\pi/2)}\frac{1}{N}, \tag{6.11}$$

and

$$\alpha(\eta) = -\frac{(1-\eta)(2-\eta)}{6\pi^2\eta\mathcal{A}(\eta)}\frac{1}{N}. \tag{6.12}$$

Since the (critical) $\mathbf{p} \to 0$ behaviour is dominated by the $\mathbf{p}^{2-\eta}$ term, one can simply compare coefficients on the left- and right-hand side of (6.10) to obtain the condition

$$\beta(\eta) \stackrel{!}{=} 1. \tag{6.13}$$

Previously, this approach was used to compute an analytic solution for $\eta(N)$ [211]. However, beyond computing a value for η, it offers additional insights by identifying scaling behaviour. By assuming a simple scaling ansatz for the propagator (6.2), this method enables the extraction of scaling properties of the self-energy and therefore the identification of scaling solutions. This could prove invaluable for nonthermal scaling phenomena, since the equation that follows from (6.13) goes beyond the results of simple scaling analyses, and is a genuine self-consistent equation for the scaling solution(s).

Concerning analytic solutions in the $\mathbf{p} \to 0$ limit for the self-energies on the Keldysh contour, things are much more challenging, and it is simpler to take a fully numeric route. To this end, first we will use the exact analytic expression from (6.11) to benchmark a fully numerical approach to extract the scaling behaviour of the self-energy (6.4). Subsequently, this numeric approach will be used to extract scaling solutions from the nonequilibrium self-energies.

6.2.1 Numerical approach

The numerical approach to extract scaling solutions relies on first defining a discrete η grid

$$\eta \in \{\eta_{\text{min}}, \ldots, \eta_{\text{max}}\} \tag{6.14}$$

with uniform spacing $\delta\eta$. This gives a set of distinct inputs for the propagator (6.2) that all have a slightly different scaling behaviour due to the different anomalous dimension assumed. Crucially, we perform our integrations with these propagators, where the η value is a variable input. Afterwards, we then compute the value of $\beta(\eta)$ by fitting a $\mathbf{p}^{2-\eta}$ power law to our numerical results obtained by computing the self-energy (6.4). In this case, $\beta(\eta)$ is merely an η-dependent prefactor to the self-energy, as seen in (6.9). However, this prefactor can also be essentially equated with the number of field components N as seen in (6.13), thereby giving $N(\eta)$. This can be inverted to obtain $\eta(N)$, which is a valid approach as long as it is a well-defined function and has an inverse.

Instead of directly solving (6.6) numerically, we first deal with the "inner" loop integral (6.8), where the momentum runs over the $\mathbf{r}$ variable. This convolution integral is solved numerically on some $\mathbf{q}$ grid for each η. The integrals are all evaluated in spherical polar coordinates, where the angular integrals are also suitably taken care of. For propagators involving the difference of vector quantities, we use

$$G(\mathbf{q}-\mathbf{r}) = \left((\mathbf{q}-\mathbf{r})^2\right)^{\eta/2-1} \equiv \left(\mathbf{q}^2+\mathbf{r}^2-2|\mathbf{q}||\mathbf{r}|\cos(\theta)\right)^{\eta/2-1}. \tag{6.15}$$

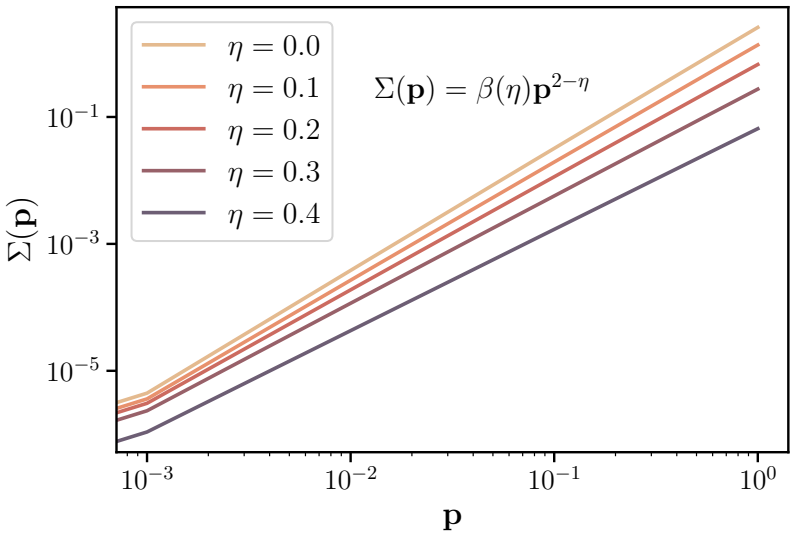

Figure 6.2. The self-energy shows a power law behaviour $\mathbf{p}^{2-\eta}$, with the precise scaling depending on the specific value of η used in the propagator (6.2) as an input.

Upon numerical integration, it can be observed that the power law behaviour of the convolution is

$$\int_{\mathbf{k}} G(\mathbf{q}-\mathbf{r})G(\mathbf{r}) = \mathcal{C}(\eta)(\mathbf{q}^2)^{\eta-1/2}, \tag{6.16}$$

which matches the analytic results obtained from Feynman parametrisation for such a loop integral. The $\mathcal{C}(\eta)$ is an η dependent prefactor and is precisely equal to (6.8), however, now we only have the numerical prefactor which we obtain by fitting the η-dependent power law $(\mathbf{q}^2)^{\eta-1/2}$ on the data obtained from numerical integration over a $\mathbf{q}$ grid. This power law fit with the correct prefactor can be used as an input function into the self-energy integral. This reduces the original equation from (6.6) to

$$G^{-1}(\mathbf{p}) = \mathbf{p}^2 + \frac{2}{N}\int_{\mathbf{q}} [G(\mathbf{p}-\mathbf{q}) - G(\mathbf{q})] \left[\mathcal{C}(\eta)(\mathbf{q}^2)^{\eta-1/2}\right]^{-1}. \tag{6.17}$$

While in an ideal case the self-energy integral should be solved numerically "at once", taking this intermediate step is an immense simplification numerically, and we have checked that this does not compromise the results, as long as the performed fit to the convolution integral is very accurate. Subsequently, the self-energy integral over the $\mathbf{q}$ variable is evaluated on a grid at discrete $\mathbf{p}$ values, which we show for several η values in Fig. 6.2.

This highlights the essence of our approach to extract scaling: for a series of input propagators with different η, we have shown that the self-energy follows a power law, which we can fit as a $\mathbf{p}^{2-\eta}$. In this fit, we minimise a loss function that compares the predicted and observed (numerically computed) data. The loss function is defined as

$$\text{Loss}(a, b, \eta, \text{data}) = \sqrt{\frac{\sum_i \left(\frac{y_i - \text{predicted}(p_i)}{\text{predicted}(p_i)}\right)^2}{n - n_{\text{vars}}}}, \tag{6.18}$$

where

$$\text{predicted}(p_i) = a p_i^2 + b p_i^{2-\eta}, \tag{6.19}$$

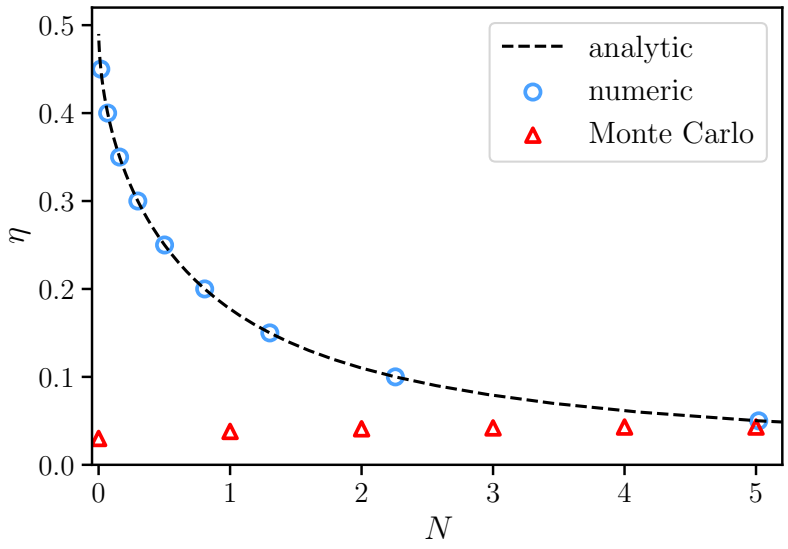

Figure 6.3. The value of $\eta(N)$ extracted from a fully numeric solution of the self-consistent equation (6.3). Our numeric approach recovers the analytic results very accurately.

n is the number of data points, and n_{vars} is the number of fit parameters. The global minimum of the loss function is found using simulated annealing, which provides the error on our fit. Since in this case we can simply equate the extracted prefactor $\beta(\eta)$ for each η with the value of N, we show $\eta(N)$ in Fig. 6.3. The analytic result from (6.11) and more accurate numerical results from Monte Carlo simulations [214] are also included for added clarity. As we can see, our fully numeric solution accurately recovers the analytic solution from [211]. We also note that in the limit of large-N, these results agree with Monte Carlo simulations. The errors to the fits are minimal and are below 0.1% of the values obtained.

In the next section, we will take a similar approach to the one presented above to extract nonthermal scaling solutions.

6.3 Nonthermal scaling

As detailed in Chapter 2, the Keldysh formalism provides a comprehensive method for describing real-time nonequilibrium phenomena. This approach effectively doubles the degrees of freedom, thereby doubling the number of propagators and self-energies, leading to a set of coupled equations. As discussed in Sec. 2.3.2, the equations corresponding to (6.3) within this framework are given by (2.68), more specifically for the two-point vertices as

$$\Gamma^R_{ab}(p) = \Gamma^R_{ab,0}(p) + \Sigma^R_{ab}(p), \tag{6.20}$$

for the retarded self-energy with the bare vertex $\Gamma^R_{ab,0}(p) = p^2 + m^2$, where $p \equiv (\omega, \mathbf{p})$ and

$$\Gamma^F_{ab}(p) = \Sigma^F_{ab}(p) \tag{6.21}$$

for the statistical components. The retarded and advanced self-energies are directly related to the spectral one via

$$\Sigma^\rho_{ab}(x,y) = \Sigma^R_{ab}(x,y) - \Sigma^A_{ab}(x,y). \tag{6.22}$$

In the following, we will mostly consider Σ^R_{ab} for practical calculations out of convenience instead of Σ^ρ_{ab} directly.

For the self-energies, we use the 2PI large-N expressions to NLO [87], which in Wigner space in a classical-statistical approximation (c.f. Sec. 2.3.4) are given by

$$\Sigma^F_{ab}(p) = -\frac{\lambda}{3N}\left[F_{ab} * \left(\Pi^F \cdot v_{\text{eff}}\right)\right](p), \tag{6.23}$$

$$\Sigma^R_{ab}(p) = \Sigma^{\text{loc}}_{ab} - \frac{\lambda}{3N}\left[F_{ab} * \left(\Pi^R \cdot v_{\text{eff}}\right) + G^R_{ab} * \left(\Pi^F \cdot v_{\text{eff}}\right)\right](p), \tag{6.24}$$

where the symbol $*$ refers to a convolution product, and the local part of the self-energy is given by

$$\Sigma^{\text{loc}}_{ab} = \lambda\frac{N+2}{6N}\int_{\nu,\mathbf{q}} F_{ab}(\nu,\mathbf{q}). \tag{6.25}$$

Similarly to the thermal case above, eventually we consider $\Sigma^R_{ab}(p) - \Sigma^R_{ab}(0)$, such that this local part gets subtracted. The different Π quantities are

$$\Pi^F(p) = \frac{\lambda}{6N}[(F_{ab} * F_{ba})(p) - \frac{1}{4}(\rho_{ab} * \rho_{ba})(p)], \tag{6.26}$$

$$\Pi^R(p) = \frac{\lambda}{3N}[(F_{ab} * G^R_{ba})(p)], \tag{6.27}$$

and the *effective coupling* is

$$v_{\text{eff}}(p) = \frac{1}{|1+\Pi^R(p)|^2}. \tag{6.28}$$

In deriving this effective coupling, a leading-order gradient expansion in time is assumed, as explained in Sec. 2.3.4. At this order, the spectral function remains time-independent, and therefore so does the retarded propagator. Assuming that a two-point function is the inverse of the propagator, we have $G^R(\omega,\mathbf{p}) = i\left[\Gamma^R(\omega,\mathbf{p})\right]^{-1}$.

At the critical point, the retarded propagator is expected to have the power law behaviour

$$G^R(\omega,\mathbf{p}) \sim \begin{cases} G^R(\omega\to 0,\mathbf{p}) \sim \mathbf{p}^{\eta-2} + \dots \\ G^R(\omega,\mathbf{p}\to 0) \sim \omega^{\frac{\eta-2}{z}} + \dots \end{cases}, \tag{6.29}$$

where we have introduced the *dynamical critical exponent* z. Therefore, the equation for $\Gamma^R_{ab}(p)$ is anticipated to become rather similar to the equilibrium case in the limit of $\omega = 0, \mathbf{p}\to 0$, assuming that the retarded self-energy scales as

$$\lim_{\mathbf{p}\to 0}\Sigma^R(\omega=0,\mathbf{p}) = \beta(\eta)\mathbf{p}^{2-\eta} + \alpha(\eta)\mathbf{p}^2 + \dots \tag{6.30}$$

which we expect by self-consistency. Hence, equation (6.20) is expected to reduce to

$$\mathbf{p}^{2-\eta} = \mathbf{p}^2 + \beta(\eta)\mathbf{p}^{2-\eta} + \alpha(\eta)\mathbf{p}^2 + \dots \tag{6.31}$$

in such a limit. This equation serves as a starting point for extracting the scaling behaviour of the retarded self-energy in nonthermal scaling phenomena. In the following, we focus on computing the nonthermal scaling behaviour from (6.31) by performing the first explicit semi-analytic computation of the self-energies on the Keldysh contour in this context. The equation for $\Gamma^F_{ab}(p)$ will be addressed separately in a future work.

6.3.1 Quasiparticle approximation

Unlike in the equilibrium case where integrals were only momentum-dependent, the integrals in the nonequilibrium case involve both frequency and momentum dependence. We simplify the computations of the frequency integrals by assuming a quasiparticle picture, as detailed in this section.

The self-energies to be computed are given in terms of F and G^R, where the latter is related to the spectral function ρ. In the following, by virtue of $\mathrm{O}(N)$ rotations, the quantities $\rho_{ab}(x,y) = \rho(x,y)\delta_{ab}$, and similarly for $F_{ab}(x,y) = F(x,y)\delta_{ab}$ are taken to be diagonal. In equilibrium, these two functions are connected via the *fluctuation-dissipation theorem*

$$F^{(\mathrm{eq})}(\omega,\mathbf{p}) = -\mathrm{i}\left(f(\omega)+\frac{1}{2}\right)\rho^{(\mathrm{eq})}(\omega,\mathbf{p}), \tag{6.32}$$

where $f(\omega)$ is the Bose-Einstein distribution function. Out of equilibrium, such a relation does not hold in general; nevertheless, one is free to use the parametrisation

$$F(t,\omega,\mathbf{p}) = -\mathrm{i}\left(f(t,\omega,\mathbf{p})+\frac{1}{2}\right)\rho(t,\omega,\mathbf{p}), \tag{6.33}$$

where t refers to the centre-coordinate $(t_1+t_2)/2$, also used in the gradient expansion. To further exploit the usefulness of such a parametrisation, it is instructive to first consider a free theory. In this case, the equation that governs the evolution of the spectral function is given by

$$\left(\partial^2 + m^2\right)\rho_0(x,y) = 0. \tag{6.34}$$

The solution to this is

$$\rho_0\left(x_0,y_0,\mathbf{p}\right) = \frac{1}{\omega_{\mathbf{p},0}}\sin\left[\omega_{\mathbf{p},0}\left(x_0-y_0\right)\right], \tag{6.35}$$

where $\omega_{\mathbf{p},0} = \sqrt{\mathbf{p}^2+m^2}$ is the free particle dispersion relation. The Wigner transform of (6.35) is given by

$$-\mathrm{i}\rho_0(t,\omega,\mathbf{p}) = \frac{\sin\left[\left(\omega-\omega_{\mathbf{p},0}\right)2t\right]}{\omega_{\mathbf{p},0}\left(\omega-\omega_{\mathbf{p},0}\right)} - \frac{\sin\left[\left(\omega+\omega_{\mathbf{p}}\right)2t\right]}{\omega_{\mathbf{p},0}\left(\omega+\omega_{\mathbf{p},0}\right)}, \tag{6.36}$$

which, at finite central time t has a rapidly oscillating behaviour, while at late times $t\to\infty$ approaches a δ peak in the form of

$$\rho_0(t,\omega,\mathbf{p}) = 2\pi\mathrm{i}\delta\left(\omega^2-\left(\omega_{\mathbf{p},0}\right)^2\right). \tag{6.37}$$

Therefore, using this for the spectral function, the parametrisation (6.33) puts the distribution function $f(t,\omega,\mathbf{p})$ on the mass-shell. While the spectral function in general has a more involved form in an interacting theory, it often retains a peaked structure with a modified dispersion relation $\omega_{\mathbf{p}}$. Specifically for the systems and dynamics considered here, it has been found to have a peaked structure with a finite decay width $\gamma(\mathbf{p})$ that approaches a δ-function in time [82, 136]. This reflects the presence of well-defined quasiparticles, and therefore

we assume the dynamics is dominated by quasiparticle excitations. Accordingly, we modify the dispersion relation to include a possible nonequilibrium anomalous dimension η as well,

$$\omega_{\mathbf{p}} = \sqrt{\mathbf{p}^{2-\eta} + m^2}. \tag{6.38}$$

For the spectral function, we keep the δ-like structure and use

$$\rho(\omega, \mathbf{p}) = 2\pi \mathrm{i}\delta\left(\omega^2 - \omega_{\mathbf{p}}^2\right) \tag{6.39}$$

as an ansatz, with the dispersion (6.38).

The retarded and advanced propagators are also directly related to the spectral function by

$$G^R(x,y) = \Theta\left(x^0 - y^0\right)\rho(x,y), \quad G^A(x,y) = -\Theta\left(y^0 - x^0\right)\rho(x,y), \tag{6.40}$$

where Θ is the Heaviside step function. Moving to Wigner space, the retarded propagator can be computed as

$$G^R(\omega, \mathbf{p}) = \lim_{\epsilon\to 0}\int \frac{\mathrm{d}\omega'}{2\pi\mathrm{i}}\frac{\rho\left(\omega', \mathbf{p}\right)}{\omega - \omega' + \mathrm{i}\epsilon}, \tag{6.41}$$

where the integral representation of the Heaviside function was used, given by

$$\Theta(x) = \lim_{\epsilon\to 0}\int \frac{\mathrm{d}\omega'}{2\pi\mathrm{i}}\frac{\mathrm{e}^{-\mathrm{i}\omega' x}}{\omega' + \mathrm{i}\epsilon}. \tag{6.42}$$

With the spectral function (6.39), this recovers the retarded propagator

$$G^R\left(\omega, \mathbf{p}\right) = \frac{1}{2\omega_{\mathbf{p}}}\left(\frac{1}{\omega - \omega_{\mathbf{p}} + i\epsilon} - \frac{1}{\omega + \omega_{\mathbf{p}} + i\epsilon}\right). \tag{6.43}$$

In order to compute the retarded self-energy (6.24), first the Π^R and Π^F quantities need to be obtained. In the on-shell approximation, using (6.39) and (6.43), the Π^R loop is

$$\begin{aligned}\Pi^R(\nu, \mathbf{q}) = &\lim_{\epsilon\to 0}\frac{\lambda}{12}\int_{\mathbf{r}}\frac{f(t, \mathbf{q}-\mathbf{r})}{\omega_{\mathbf{r}}\omega_{\mathbf{q}-\mathbf{r}}} \\ &\times\left[\frac{1}{\omega_{\mathbf{r}} + \omega_{\mathbf{q}-\mathbf{r}} - \nu - i\epsilon} + \frac{1}{\omega_{\mathbf{r}} - \omega_{\mathbf{q}-\mathbf{r}} - \nu - i\epsilon}\right. \\ &\left.+\frac{1}{\omega_{\mathbf{r}} - \omega_{\mathbf{q}-\mathbf{r}} + \nu + i\epsilon} + \frac{1}{\omega_{\mathbf{r}} + \omega_{\mathbf{q}-\mathbf{r}} + \nu + i\epsilon}\right],\end{aligned} \tag{6.44}$$

where we have excluded the time-dependence t in $\Pi^R(\nu, \mathbf{q})$, even though it appears in the distribution function $f(t, \mathbf{p})$. As we will see in the next section, t can be scaled out of the expressions considered here.

While the Π^F loop does not inherently have a causal structure in terms of retarded or advanced quantities and so does not include iϵ terms, as detailed in App. D.1, within the quasiparticle approximation, we can interpret this object as

$$\begin{aligned}\Pi^F(\nu, \mathbf{q}) = &\lim_{\epsilon\to 0}\frac{\lambda}{24}\int_{\mathbf{r}}\frac{f(t, \mathbf{q}-\mathbf{r})f(t, \mathbf{r})}{\omega_{\mathbf{r}}\omega_{\mathbf{q}-\mathbf{r}}} \\ &\times\left[\frac{1}{\omega_{\mathbf{r}} + \omega_{\mathbf{q}-\mathbf{r}} - \nu - i\epsilon} + \frac{1}{\omega_{\mathbf{r}} - \omega_{\mathbf{q}-\mathbf{r}} - \nu - i\epsilon}\right. \\ &\left.+\frac{1}{\omega_{\mathbf{r}} - \omega_{\mathbf{q}-\mathbf{r}} + \nu + i\epsilon} + \frac{1}{\omega_{\mathbf{r}} + \omega_{\mathbf{q}-\mathbf{r}} + \nu + i\epsilon}\right],\end{aligned} \tag{6.45}$$

which is what will be used later in the self-energy computations.

6.3.2 Nonequilibrium computations

The above description shares a number of similarities with the standard kinetic theory approach to nonthermal fixed points, which is based on obtaining an evolution equation for the occupation number $f(t, \mathbf{p})$ due to the elastic scatterings of quasiparticles with free dispersion. However, rather than directly solving for the full evolution, kinetic theory typically seeks self-similar solutions, which describe the universal late-time behaviour of the system. More specifically, the occupation number $f(t, \mathbf{p})$ exhibits self-similar evolution, where its functional form obeys

$$f(t, \mathbf{p}) = s^{\alpha/\beta} f\left(s^{-1/\beta} t, s\mathbf{p}\right), \tag{6.46}$$

in terms of the universal scaling exponents α and β. Similar scaling relations hold for the statistical function,

$$F\left(t, \omega, \mathbf{p}\right) = s^{\alpha/\beta+2z} F\left(s^{-1/\beta} t, s^z \omega, s\mathbf{p}\right), \tag{6.47}$$

as well as the spectral function

$$\rho\left(\omega, \mathbf{p}\right) = s^{2-\eta} \rho\left(s^z \omega, s\mathbf{p}\right), \tag{6.48}$$

and the dispersion relation

$$\omega(\mathbf{p}) = s^{-z} \omega(s\mathbf{p}). \tag{6.49}$$

If the total particle number is conserved, which is the case for the infrared transport process near nonthermal fixed points, this imposes an additional constraint on the scaling exponents. Specifically, the particle number

$$n = \int \frac{d^d p}{(2\pi)^d} f(t, \mathbf{p}) = t^{\alpha-\beta d} \int \frac{d^d q}{(2\pi)^d} f_S(\mathbf{q}), \tag{6.50}$$

must remain constant, which leads to the relation $\alpha = d\beta$. The full scaling analysis reveals [48] that

$$\beta = \frac{1}{2-\eta}, \quad \alpha = d\beta. \tag{6.51}$$

The exponents $\beta \approx 0.5$ and $\alpha \approx d\beta$ have been corroborated by numerical simulations as well [48, 136]. While the self-similar scaling ansätze above provide a robust framework for identifying universal properties, they rely on extracting exponents based on known scaling hypotheses rather than directly solving for scaling solutions. In this work, we take a different approach by directly computing the scaling solutions for the self-energies within the 2PI large-N formalism.[1] This allows us to identify scaling behaviour in a fully controlled, self-consistent manner and by an explicit calculation.

As seen in Eqs. (6.44) and (6.45), the Π^R and Π^F functions only depend on the occupation number $f(t, \mathbf{p})$ and the dispersion relation $\omega_{\mathbf{p}}$. For the latter, we use (6.38). As for the distribution function, without loss of generality, we can choose $s^{-1/\beta} t = 1$ for the scaling parameter s in (6.46) to obtain

$$f(t, \mathbf{p}) = t^{\alpha} f_S\left(t^{\beta} |\mathbf{p}|\right), \tag{6.52}$$

[1] Note also that substituting the above scaling forms into (6.20) with $s^{-1/\beta} t = 1$ yields the same exponents on the left and right-hand sides of the equation. Therefore, a simple scaling analysis in this case only provides a self-consistency check, and no constraints on the value of the exponents.

in terms of the universal scaling function f_S. Phenomenologically, this has been accurately fitted [48, 74] by the form

$$f_S(t^\beta|\mathbf{p}|) \simeq \frac{A\,(\kappa_> - \kappa_<)}{(\kappa_> - 2)\,(t^\beta|\mathbf{p}|/B)^{\kappa_<} + (2-\kappa_<)\,(t^\beta|\mathbf{p}|/B)^{\kappa_>}}. \tag{6.53}$$

System-dependent aspects are contained in the nonuniversal amplitudes, A and B. Numerically, $\kappa_< \approx 0.0 - 0.5$ and $\kappa_> \approx 4.0 - 4.5$ have been observed in different simulations [48, 74, 80]. Here, we simply use $\kappa_< = 0$, in which case, for all practical computations, we may use the distribution function

$$f(\mathbf{p}) = \frac{p_\Lambda^{\kappa-\alpha/\beta}}{p_\Lambda^\kappa + \mathbf{p}^\kappa}, \tag{6.54}$$

which satisfies (6.46), with $\kappa_> \equiv \kappa$ from above and where the momentum has been rescaled according to $t^\beta|\mathbf{p}| \to \mathbf{p}$. The term p_Λ signifies the *plateau* which scales as $p_\Lambda(t) \sim t^{-\beta}$ and also acts as an infrared cutoff.

The dispersion relation depends on the exponent η, and since $\alpha/\beta = d$ for conserved particle number, the distribution function is characterised by the exponent κ and we use $d = 3$. Therefore, our computations are governed by the exponents η and κ rather than by α and β. In this sense, the calculation presented below resembles *stationary transport*. This setup is time-translation invariant and can be realised in the presence of appropriate sources and sinks. In contrast, the isolated nonequilibrium systems we consider exhibit self-similar evolution and thus lack time-translation invariance. Stationary transport in the nonperturbative regime has been previously studied in the context of *strong-wave turbulence* [19, 20, 115], where scaling solutions to kinetic equations were analysed. In this work, we go beyond those studies by explicitly computing the self-energy expression for the first time.

Most of the results shown in the following have used the value $m = 0.6$ for the mass in (6.38), which is in line with the effective mass extracted for a relativistic scalar field theory in Ref. [48] from numerical simulations, relative to a plateau at $p_\Lambda \approx 1.0$ in the distribution function. However, we have explicitly verified that setting $m = 0$ does not qualitatively alter the scaling laws we obtained. Nevertheless, using a finite mass was numerically more convenient for our computations. Additionally, we confirmed that within the range $0.0 \leq m \leq 2.0$, and for varying the plateau between $0.001 \leq p_\Lambda \leq 1.0$, the scaling laws remain qualitatively unchanged.

Lastly, we emphasise that while we adopt this specific functional form for the distribution function in our computation, our approach is not limited to this choice, and scaling solutions can be explored using any suitable function. This makes our method more broadly applicable, and opens pathways beyond the standard form (6.53) found in the vicinity of nonthermal fixed points.

Effective vertex

In the strongly correlated infrared regime, a time- and momentum-dependent effective coupling appears,

$$\lambda^2 \to \lambda^2_{\text{eff}}[f](t, \mathbf{p}), \tag{6.55}$$

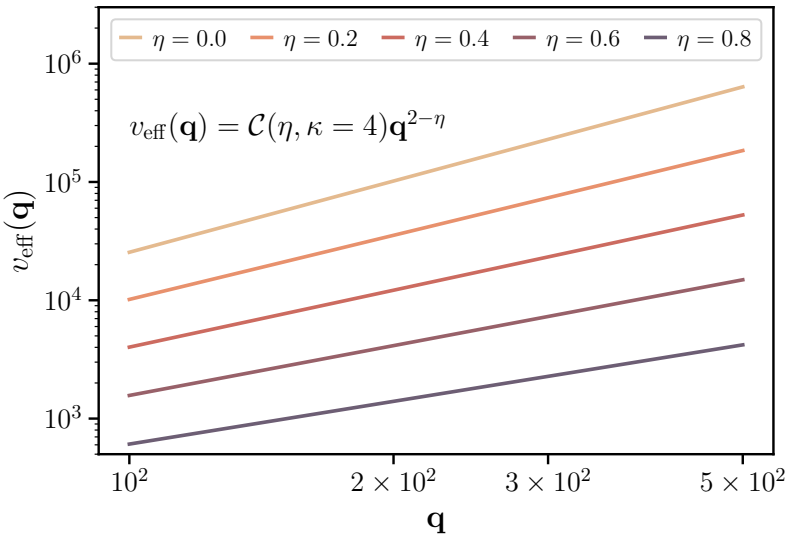

Figure 6.4. The effective vertex, shown for different values of η and $\kappa = 4.0$. The power law behaviour is $\sim \mathbf{q}^{2-\eta}$, such that the power law is η-dependent, while the prefactor depends on both η and κ.

reflecting the influence of nonperturbative effects. Its definition is given by

$$\lambda_{\text{eff}} = \frac{\lambda}{|1 + \Pi^R(p)|^2}, \tag{6.56}$$

such that the effective vertex in Eq. (6.28) takes the form $\lambda_{\text{eff}} = \lambda v_{\text{eff}}$. This effective interaction coupling is particularly relevant in far-from-equilibrium systems with large occupation numbers, where strong correlations and nonperturbative effects modify the scaling behaviour. While at high momenta Π^R is small and λ_{eff} remains close to the bare coupling λ, in the infrared regime, strong correlations lead to significant modifications where Π^R grows nonperturbatively large. In such cases, the effective interaction strength is determined self-consistently through a resummation of scattering processes, as illustrated in Fig. 6.1. This leads to a modified scaling behaviour that differs from naive perturbative expectations, which has been extensively studied before [48, 72–74]. In the following, we outline the computation of the effective vertex v_{eff} within our framework and will not investigate any λ-dependence, as we are only interested in how v_{eff} influences the emergence of scaling solutions. In the limit $\Pi^R \gg 1$, the coupling λ drops out of the expression for the retarded self-energy (6.24) in any case. Since this self-energy is the quantity we ultimately aim to compute, λ is irrelevant for our analysis.

The effective coupling has been found to obey a universal scaling form before [73, 74]. Motivated by this, we similarly assume that the Π^R loop is given by a power law, such that a scaling exponent and a prefactor to this can be extracted, which we compute on-shell $\Pi^R(\nu = \omega_{\mathbf{q}}, \mathbf{q})$. This gives us an expression for the effective vertex, which simplifies to $v_{\text{eff}}(\omega_{\mathbf{q}}, \mathbf{q}) \approx \left[|\Pi^R(\omega_{\mathbf{q}}, \mathbf{q})|\right]^{-1}$ in the infrared limit where $\Pi^R \gg 1$. The previous studies in Refs. [73, 74] have computed the effective coupling under the assumption of a zero anomalous dimension, which significantly simplified the computation. In contrast, we allow for a nonzero η by using the modified dispersion relation (6.38), at the cost of dealing with more involved integrals.

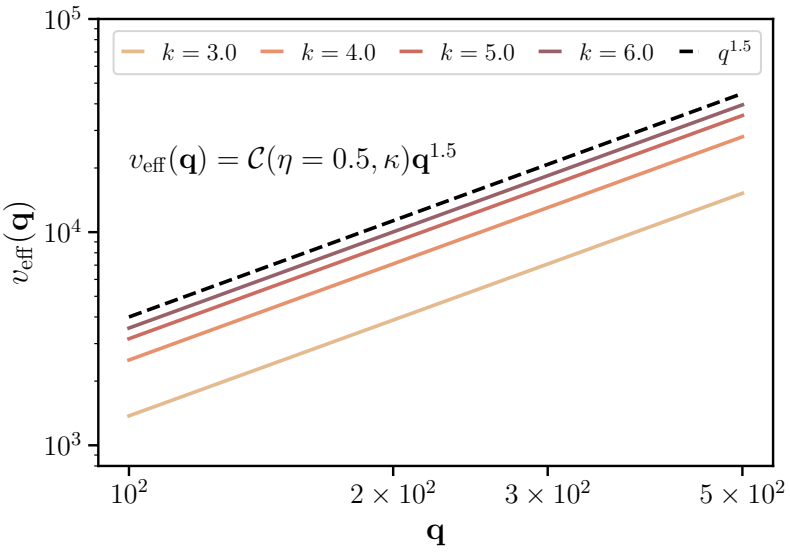

Figure 6.5. The effective vertex, shown for $\eta = 0.5$ and different κ exponents, verifying that its scaling behaviour is independent of κ. We have similarly checked for different values of η, and found no evidence for a κ dependence in the form of the power law.

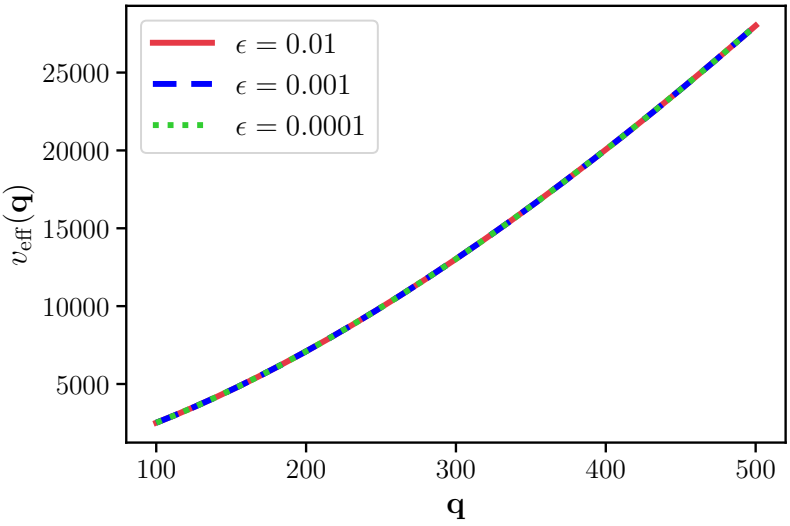

Figure 6.6. The effective vertex at different values of ϵ, showing that decreasing the ϵ term does not influence the numerical value of $v_{\text{eff}}(\mathbf{q})$. In this case, we specifically show results for $\eta = 0.4$ and $\kappa = 4.0$.

Explicitly evaluating (6.44) with $\nu = \omega_{\mathbf{q}}$ for a range of η appearing in the dispersion, we find an η-dependent effective vertex, which scales like

$$v_{\text{eff}}(\mathbf{q}) = \mathcal{C}(\eta, \kappa)\mathbf{q}^{2-\eta}, \tag{6.57}$$

as shown in Fig. 6.4. The prefactor to this power law depends on both η and κ. However, as we have also found, the scaling form of the effective vertex remains independent of the κ exponent, as shown in Fig. 6.5, which is consistent with previous findings [73, 74]. Moreover, we have verified the stability of our results as $\epsilon \to 0$ in the iϵ contributions of (6.44) by systematically decreasing ϵ in the integration, as shown in Fig. 6.6.

In summary, we have demonstrated that the effective vertex follows a universal scaling form, with its dependence on η and κ explicitly examined. We confirmed that the scaling exponent remains independent of κ and verified the stability of our results as $\epsilon \to 0$. Furthermore, our findings are consistent with the presence of a nonzero anomalous dimension in its scaling form. Moving forward, we will use the power law and the prefactor obtained here as input functions for the computation of the retarded self-energy.

Universal scaling of $\Pi^F(q)$

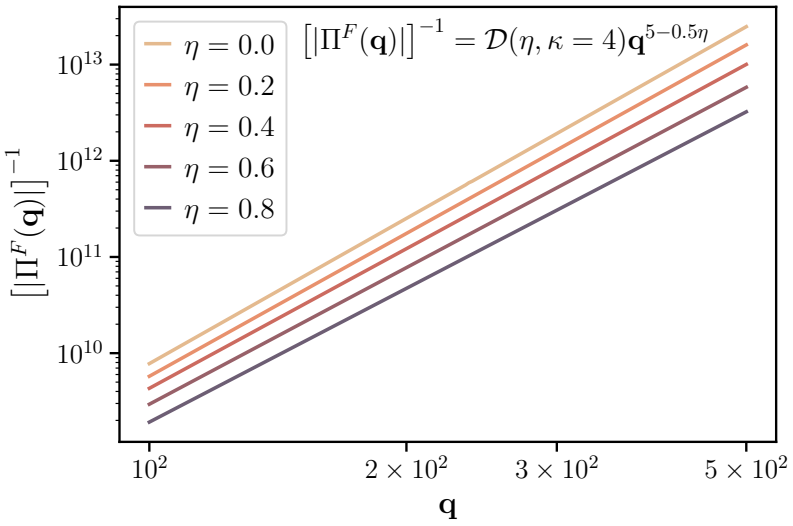

Figure 6.7. Universal scaling of $\left[|\Pi^F(\mathbf{q})|\right]^{-1}$ for different η at $\kappa = 4$, demonstrating the numerically obtained behaviour $\sim \mathbf{q}^{1+\kappa-0.5\eta}$ with a prefactor that depends on both η and κ.

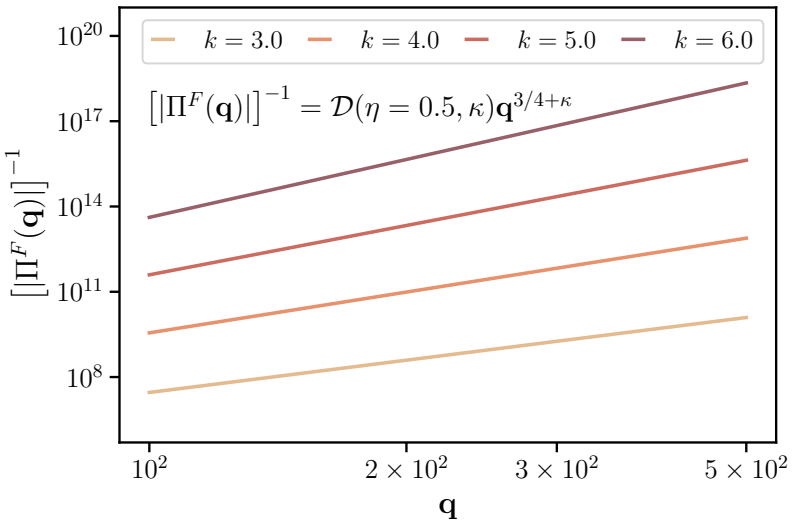

Figure 6.8. Universal scaling of $\left[|\Pi^F(\mathbf{q})|\right]^{-1}$ for different κ at $\eta = 0.5$, also showing the $\sim \mathbf{q}^{1+\kappa-0.5\eta}$ behaviour.

Before we can proceed with the computation of Σ^R, another loop quantity, Π^F also needs to be calculated. By explicitly solving (6.45) on-shell with $\nu = \omega_{\mathbf{q}}$, we find that, as expected,

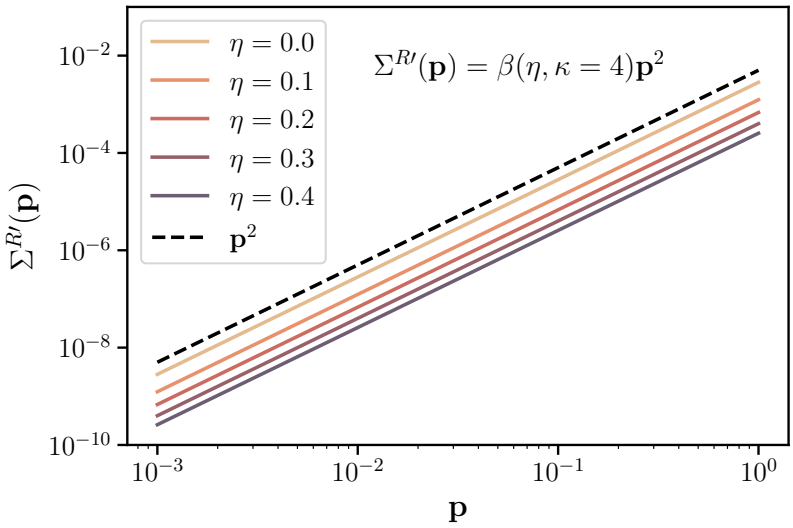

Figure 6.9. The universal scaling of the retarded self-energy shows only quadratic scaling $\mathbf{p}^2$, and no η or κ dependence in the scaling exponent. This specific plot has used $\kappa = 4$.

the solution reveals a power law behaviour. More specifically, we find a scaling form that depends on both η and κ and is given by

$$\left[|\Pi^F(\mathbf{q})|\right]^{-1} = \mathcal{D}(\eta, \kappa)\mathbf{q}^{1+\kappa-0.5\eta}. \tag{6.58}$$

In Fig. 6.7 we show the explicit η-dependence on the scaling for $\kappa = 4$, while in Fig. 6.8 we show the κ-dependence, holding η constant. To our knowledge, the power law behaviour of Π^F has not been studied extensively yet, and (6.58) provides a new insight into its scaling behaviour. This can be used as a quantitative foundation for further theoretical developments, especially analytical ones.

Self-energy

After the appropriate evaluations of the frequency integrals with the delta functions, the exact expressions we consider for the self-energy are given by

$$\Sigma^R(\omega = 0, \mathbf{p}) - \Sigma^R(0, 0) \equiv \Sigma^{R\prime}(\mathbf{p}), \tag{6.59}$$

where more explicitly we have

$$\Sigma^{R\prime}(\mathbf{p}) = -\frac{\lambda}{3N}\left[\int_{\mathbf{q}} \frac{f(\mathbf{p}-\mathbf{q})}{\omega_{\mathbf{p}-\mathbf{q}}} \Pi^R\left(\omega_{\mathbf{p}-\mathbf{q}}, \mathbf{q}\right) v_{\text{eff}}\left(\omega_{\mathbf{p}-\mathbf{q}}, \mathbf{q}\right) - \int_{\mathbf{q}} \frac{f(\mathbf{q})}{\omega_{\mathbf{q}}} \Pi^R\left(\omega_{\mathbf{q}}, \mathbf{q}\right) v_{\text{eff}}\left(\omega_{\mathbf{q}}, \mathbf{q}\right) \right.$$
$$\left. - \left(\int_{\mathbf{q}} \frac{\Pi^F(\omega_{\mathbf{p}-\mathbf{q}}, \mathbf{q})}{\omega_{\mathbf{p}-\mathbf{q}}} v_{\text{eff}}\left(\omega_{\mathbf{p}-\mathbf{q}}, \mathbf{q}\right) - \int_{\mathbf{q}} \frac{\Pi^F(\omega_{\mathbf{q}}, \mathbf{q})}{\omega_{\mathbf{q}}} v_{\text{eff}}\left(\omega_{\mathbf{q}}, \mathbf{q}\right) \right) \right]. \tag{6.60}$$

The derivation of this form is shown in more detail in App. D.1. Having computed power laws for both Π^R and Π^F, we can use the obtained expressions towards the computation of $\Sigma^{R\prime}$. As previously discussed in the context of the effective vertex, each Π^R and Π^F comes with a factor of λ, such that in the end for $\Pi^R \gg 1$, λ completely drops out of (6.60).

Explicitly evaluating this expression with the Π^R whose scaling depends on η, and Π^F, which depends on both η and κ, we find quadratic scaling behaviour in $\Sigma^{R\prime}(\mathbf{p}) \sim \mathbf{p}^2$ with no η or κ dependence, as illustrated in Fig. 6.9. This is in stark contrast to what was found in Sec. 6.2 for the Wilson–Fisher fixed point, where the self-energy showed $\mathbf{p}^{2-\eta}$ scaling behaviour, and where we could identify the prefactor of this power law with the number of field components N to yield a function $\eta(N)$. In this case, our prefactors are always very small numbers on the order of 10^{-3}, as shown in Fig. 6.10. Although, we have identified a trend that for larger η, the prefactor extracted does decrease, just like for the equilibrium case. As a key result, we have also identified a critical region, where an infrared divergence occurs

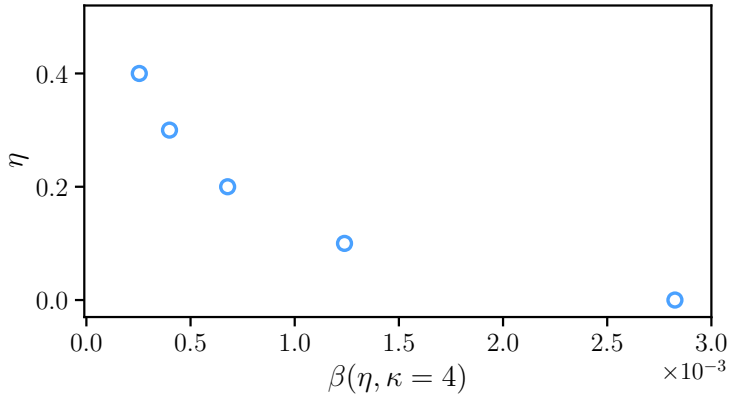

Figure 6.10. Prefactors to the $\mathbf{p}^2$ power law of the retarded self-energy from Fig. 6.9 for different η and $\kappa = 4.0$, shown along the x-axis. The numbers are comparably small for $\kappa = 3.0$ and $\kappa = 5.0$. The results shown here used $m = 0.6$ and $p_\Lambda = 1.0$, however, varying the mass $0.0 \leq m \leq 2.0$ and the plateau $0.001 \leq p_\Lambda \leq 1.0$, we have always found comparably small prefactors to the quadratic scaling.

in $\Sigma^{R\prime}$, specifically in the terms involving Π^F, and which depends on the input parameters η and κ. Within this region, we can extract a finite, quadratic scaling of the self-energy. Outside this critical region, however, we encounter the infrared divergences, which remain under active investigation. For the case $m = 0$ in the dispersion (6.38), we numerically found that the critical region is

$$4 - \kappa \leq \eta \leq 5 - \kappa, \tag{6.61}$$

which we have verified for $0 \leq \eta \leq 1$. Together, these two conditions constrain $3 \leq \kappa \leq 5$. We have also determined that having a finite mass shifts the critical region, thereby altering the range of η and κ values for which a finite scaling function can be extracted. This dependence will be studied more thoroughly in the future.

6.4 Conclusion and outlook

In this chapter, we investigated the emergence of nonthermal critical behaviour in relativistic scalar fields using the 2PI effective action framework. Our findings demonstrate that the self-consistent 2PI approach provides a robust method for extracting scaling exponents in

the strongly correlated, nonperturbative regime. Specifically, we employed a leading-order gradient expansion in time, and a quasiparticle approximation, treating the spectral function as a delta function to simplify the analysis. To ensure the reliability of our numerical approach, which explicitly computes self-energy integrals, we first applied it to thermal critical behaviour, benchmarking the results against established equilibrium scaling solutions.

We then examined the nonequilibrium effective vertex, identifying a nontrivial scaling behaviour where the scaling exponent depends on the anomalous dimension. However, further analysis of the self-energy revealed a self-similar quadratic scaling, ultimately showing no dependence on an anomalous dimension, even when its presence was initially assumed. We found that across a wide range of input parameters, the retarded self-energy consistently exhibits quadratic scaling behaviour. Our findings also highlight a critical region where the emergence of this quadratic scaling solution is closely linked to the initially assumed exponents and input parameters. In the future, further investigation is needed to better understand the critical region and its dependence on an effective mass.

Additionally, the quasiparticle approximation may impose significant limitations, making it essential to incorporate a finite width for the spectral function and explicitly evaluate the frequency integrals. This refinement could enable a more precise determination of the nonequilibrium anomalous dimension η, which, in our current computation appears to be consistent with zero.

A major open question remains whether a unified renormalisation group framework can be established for nonthermal fixed points, similar to equilibrium critical phenomena. While successful renormalisation group approaches exist for stationary nonequilibrium systems [20, 215, 216], and some studies have extended these ideas beyond the stationary case [217–219], a comprehensive framework within the renormalisation group remains under development [220]. The approach presented here complements existing methods based on scaling analyses of kinetic equations and numerical simulations, offering an alternative perspective on nonthermal scaling phenomena, and in principle, it can also be combined with functional renormalisation group methods.

Chapter 7

Discussion and outlook

In this chapter, the main findings of the thesis are summarised and discussed in the context of the broader research landscape in nonequilibrium quantum many-body dynamics. Along with reviewing the main results, which include the novel insights into symmetry restoration and the role of topological defects for universal scaling in the vicinity of nonthermal fixed points, as well as the search for new nonthermal scaling phenomena, potential future research directions are also briefly explored.

One of the primary objectives of this thesis was to advance the development of effective theories to describe the emergent macroscopic dynamics of isolated quantum many-body systems far from equilibrium. The projects presented examined various phenomena, including nonthermal fixed points, where universal self-similar scaling emerges, as well as the dynamics of spontaneous symmetry breaking and symmetry restoration in nonequilibrium systems. Chapter 3 explored the extraction of effective symmetries in a spinor Bose gas, with a focus on symmetry properties and their evolution in nonequilibrium conditions. Chapters 4 and 5 addressed challenges related to universal scaling behaviour far from equilibrium, with particular attention to the role of topological defects and the interplay between nonlinear wave propagation and defect dynamics. Finally, Chapter 6 investigated nonthermal scaling phenomena by applying the 2PI formalism to extract scaling solutions, extending beyond traditional scaling analyses of the self-consistent equations. This approach provided new insights into the robustness of scaling exponents beyond conventional attractor solutions.

One of the main findings was the observation of effective symmetry restoration long before equilibration in spinor Bose gases, demonstrating how symmetry properties can evolve in nonequilibrium conditions and manifest at the level of correlation functions. The findings emphasise that symmetry dynamics in isolated nonequilibrium systems can be complex, with lower-order correlation functions capturing effective restoration even when higher-order correlations retain memory of the initial symmetry breaking in an isolated system. This distinction between different orders of correlation functions underlines the importance of identifying the appropriate observables when constructing low-energy effective theories to describe emergent, macroscopic nonequilibrium phenomena, which are typically based on lower-order correlation functions. Additionally, spontaneous symmetry breaking was

detected from experimental data in the same spinor Bose gas system and defined also at the level of correlation functions. This highlights the importance of correlation functions as a tool for understanding both the preservation and emergence of symmetries in nonequilibrium dynamics, as well as the central role of symmetries in shaping the macroscopic behaviour of far-from-equilibrium quantum many-body systems.

The methods developed offer a framework for probing critical behaviour and nonequilibrium phase transitions in isolated quantum systems, which has relevance ranging from early-universe cosmology to ultracold atomic systems. Regarding universality classes far from equilibrium, these methods could also provide a classification scheme, drawing parallels to the established connection between symmetries and universality classes in equilibrium systems. Another major direction for future research is the experimental demonstration of explicit symmetry breaking and the subsequent symmetry restoration at the level of correlation functions, which remains an ongoing project under development.

Another key aspect explored in this thesis was the dynamics near nonthermal fixed points, which act as universal attractor solutions. They are characterised by self-similar scaling behaviour, governed by universal scaling exponents and functions that are largely independent of the system's microscopic details. This work focused on analysing the scaling properties in relativistic N-component scalar field theories, investigating the role of different degrees of freedom and their contribution to the scaling dynamics. The analysis extended the understanding of nonthermal fixed points by examining both quasiparticle excitations and topological defects, contributing new perspectives on how various physical processes shape the universal dynamics near these points. It was found that in two dimensions, a single-component scalar field theory shows markedly different scaling exponents compared to higher N-component theories, with these differences traced back to excitations originating from defect dynamics. In three dimensions, the relevant excitations in a single-component scalar field theory were also linked to defect-driven dynamics. However, at the macroscopic level, the system likely displays a similar effective description to that of large-N theories, since the dynamics is characterised by the same universal scaling exponents and scaling functions.

This serves as a major stepping stone towards a low-energy effective description of single-component scalar field theories, which need to be built upon the relevant degrees of freedom. It is also a significant contribution towards a more comprehensive understanding of far-from-equilibrium universality classes in N-component scalar fields, which now separates a single-component scalar field theory from the large-N limit for overoccupied initial conditions, in terms of different fixed points in two dimensions, and the same fixed point, but different microscopic descriptions in three dimensions. In the future, this could be used to gain a deeper understanding of the scaling behaviour obtained by imprinting topological defects on top of overoccupied initial conditions. The results also revealed yet unexplored connections between nonthermal fixed points and superfluid turbulence in terms of Kelvin waves, which could be further investigated in systems beyond scalar fields.

Similarly, in the context of nonthermal fixed points, geometric observables were constructed that showed more sensitivity to defect-driven dynamics than standard correlation functions. These observables captured details of the system's topological structure and re-

vealed scaling behaviour with exponents distinct from those obtained through conventional correlation functions, indicating that multiple scaling phenomena can coexist near a nonthermal fixed point. This underscores the complex nature of nonequilibrium many-body dynamics, where different processes, such as nonlinear wave propagation and coarsening dynamics can dominate or play a subdominant role depending on the observable being investigated. Understanding how these various phenomena contribute to scaling behaviour could offer new insights into the investigation of universality classes and effective descriptions of far-from-equilibrium systems. Furthermore, these findings point to the potential utility of geometric observables in future studies of turbulence and defect interactions in nonequilibrium quantum systems. They may also provide a means to probe emergent structures that are otherwise hidden in traditional correlation-based analyses.

Another important aspect investigated here was the refinement of methods for extracting scaling properties in nonequilibrium systems. While traditional methods, such as scaling analyses and numerical simulations have provided valuable insights, they often rely on specific assumptions. A new approach explored in this work applies the 2PI formalism with a large-N expansion to extend the study of nonthermal scaling behaviour. This approach has the potential to improve the precision of scaling exponent extraction and broaden the classification of nonthermal fixed points, and, in particular, it could offer a more systematic way to probe scaling solutions. By numerically solving the self-consistent 2PI equations, this work identified a stationary transport regime exhibiting universal quadratic scaling. These advancements will contribute to a more comprehensive framework for characterising universal scaling behaviour, with implications for both equilibrium and nonequilibrium scaling phenomena across a range of strongly correlated physical systems.

In summary, this thesis has contributed to a deeper understanding of far-from-equilibrium dynamics in quantum many-body systems by investigating phenomena such as symmetry restoration and the universal scaling behaviour near nonthermal fixed points. The findings highlight the rich and complex interplay between topological defects, quasiparticle excitations, and nonlinear wave dynamics in shaping macroscopic scaling behaviour. Through the development of new methods and observables, this work has laid the foundation for future research aimed at uncovering universal properties and effective descriptions of nonequilibrium systems. These insights are not only relevant to theoretical studies but also have the potential to inform experimental investigations across fields ranging from ultracold atomic gases to early-universe cosmology.

Appendix A

Appendix to Chapter 3

A.1 Experimental details and analysis

For our analysis, we use data obtained with a ^{87}Rb spinor BEC of $\sim 10^5$ atoms in the $F = 1$ hyperfine manifold with initial state $|F, m_F\rangle = |1, 0\rangle$. The atom cloud is contained in a quasi one-dimensional trapping geometry, which consists of a dipole trap formed by a 1030 nm laser beam with trapping frequencies $\left(\omega_{\parallel}, \omega_{\perp}\right) = 2\pi \times (1.6, 160)$ Hz, and with two end caps formed by beams at 760 nm, confining the atoms within the central part of the harmonic potential. The longitudinal harmonic potential is constant to a good approximation over the employed sizes, leading to a 1D box-like confinement, with size $\sim 100\,\mu$m in the measurements used. The atom cloud is subjected to a uniform magnetic field of $B = 0.894$ G throughout the experiment which leads to a quadratic Zeeman splitting of $q_{\mathrm{B}} \sim h \times 58$ Hz. The spin dynamics is controlled via off-resonant microwave dressing $q = q_{\mathrm{B}} + q_{\mathrm{MW}}$ with $q < 2n|c_1|$. The initial quench is implemented by the instantaneous switching on of the microwave power.

The transverse spin field $F_{\perp} = F_x + \mathrm{i}F_y$ readout is obtained via spin rotations and microwave coupling to the initially empty $F = 2$ hyperfine manifold prior to a Stern–Gerlach pulse and spatially resolved absorption imaging. For a more detailed account on the experimental setup and on how the measurements were obtained, see the supplementary material of Ref. [25]. While the spatial degree of freedom is continuous, it gets discretised in the analysis procedure by the finite pixel size of the camera and imaging resolution ($\approx 1.2\,\mu$m per three pixels). Our analysis focuses on the central ~ 100 pixels of the data since, as discussed in the main text in Sec. 3.3, establishing long-range coherence across the entire system requires some time.

The total number of experimental realisations at each time can be seen in Table A.1.

A.2 Physical interpretation of the symmetry breaking perturbation

Since the spin operators $\hat{F}_i$ are the generators of the rotational symmetry, they commute with a symmetric Hamiltonian and consequently with the evolution operator as well. This

Evolution Time (s)										
1	10	12	14	17	20	24	29	35	42	50
Number of Realisations										
68	237	236	237	236	239	238	269	296	298	296

Table A.1. Number of experimental realisations for each evolution time.

allows us to rewrite the generating functional as

$$\begin{aligned} Z_t[\boldsymbol{J}] &= \mathrm{Tr}\Big\{\mathcal{U}\,(t,t_0)\,\mathrm{e}^{\int \mathrm{d}x \boldsymbol{J}(x)\cdot\hat{\boldsymbol{F}}(x)/2}\,\hat{\rho}_{t_0}\,\mathrm{e}^{\int \mathrm{d}x \boldsymbol{J}(x)\cdot\hat{\boldsymbol{F}}(x)/2}\mathcal{U}^\dagger\,(t,t_0)\Big\} \\ &= \mathrm{Tr}\big\{\mathcal{U}\,(t,t_0)\,\hat{\rho}'_{t_0}(\boldsymbol{J})\,\mathcal{U}^\dagger\,(t,t_0)\big\}\,, \end{aligned} \tag{A.1}$$

where we have introduced the deformed initial density matrix

$$\hat{\rho}'_{t_0}(\boldsymbol{J}) \equiv \mathrm{e}^{\int \mathrm{d}x \boldsymbol{J}(x)\cdot\hat{\boldsymbol{F}}(x)/2}\,\hat{\rho}_{t_0}\,\mathrm{e}^{\int \mathrm{d}x \boldsymbol{J}(x)\cdot\hat{\boldsymbol{F}}(x)/2}\,. \tag{A.2}$$

Note that, provided the sources J_i are real, the deformed operator $\hat{\rho}'_{t_0}(\boldsymbol{J})$ is Hermitian. Furthermore, under the same condition, it is also positive semidefinite. Indeed,

$$\langle\psi|\,\hat{\rho}'_{t_0}(\boldsymbol{J})\,|\psi\rangle = \langle\psi_{\boldsymbol{J}}|\,\hat{\rho}_{t_0}\,|\psi_{\boldsymbol{J}}\rangle \geq 0\,, \tag{A.3}$$

with $|\psi_{\boldsymbol{J}}\rangle \equiv \mathrm{e}^{\int \mathrm{d}x \boldsymbol{J}(x)\cdot\hat{\boldsymbol{F}}(x)/2}\,|\psi\rangle$, and $\hat{\rho}_{t_0}$ is positive semidefinite being a density matrix by assumption. Thus, aside from normalization, $\hat{\rho}'_t$ satisfies all the conditions of a physical density matrix. This suggests a simple interpretation of the equal-time generating functional $Z_t[\boldsymbol{J}]$ in the absence of explicit symmetry violations: it represents the evolution of the symmetric density matrix $\hat{\rho}_{t_0}$ that has been deformed by means of linear sources coupled to the spin operators $\hat{F}_i$ at the initial time t_0, thus breaking the symmetry.

Let us remark that the above simple physical picture is, to a certain extent, unique for spin systems. The reason is that the linear-source term that enters the definition of the generating functional $Z_t[\boldsymbol{J}]$ and serves as a symmetry-breaking perturbation commutes, in this case, with the symmetric evolution operator $\mathcal{U}$ as the spin operators $\hat{F}_i$ are also generators of the symmetry group.

Nevertheless, provided the linear source $\boldsymbol{J}$ in the definition of $Z_t[\boldsymbol{J}]$ is coupled to operators that transform nontrivially under the symmetry group in question, the formalism developed in this work can still be applied to define spontaneous symmetry breaking in nonequilibrium systems, albeit lacking the appealing interpretation of the symmetry-breaking perturbation as a deformation of the initial state.

A.3 Calculation of correlation functions

Both experimentally and in TWA simulations, we have N_s samples (measurements) of the spin observable F_i in datasets $\left\{F_i^{(s)} \mid s = 1, \ldots, N_s\right\}$, from which we infer n-th order correlation functions as

$$\langle F_{i_1} \cdots F_{i_n}\rangle \approx \frac{1}{N_s}\sum_{s=1}^{N_s} F_{i_1}^{(s)} \cdots F_{i_n}^{(s)}. \tag{A.4}$$

The information in all of the n-point correlation functions is equivalently stored in the generating functional $Z[J]$ as described in the context of Eq. (3.7). The TWA simulations involve periodic boundary conditions, and while the experimental setup considered is a finite system without periodic boundary conditions, we find approximate translational invariance, which simplifies the calculation of connected correlators in momentum space. We first perform a discrete Fourier transform (DFT) for the spin observables F_i to momentum space

$$F_i^{(s)}(p) = \mathrm{DFT}_{x\to p}\left[F_i^{(s)}(x)\right] \equiv \sum_{j=1}^{N} \mathrm{e}^{-\mathrm{i}pj} F_i^{(s)}(j)\,, \tag{A.5}$$

where $p \in [p_L, 2p_L, \ldots, Np_L]$, $p_L = 2\pi/L$, and L is the system size. Subsequently, we compute connected correlation functions in momentum space using the Julia language package Cumulants.jl [221].

We have verified that this procedure gives equivalent results to first computing connected correlators in position space, and then performing the DFT. The former approach, however, is much more memory-efficient. Indeed, computing higher-order correlation functions requires a considerable amount of computer memory: for instance, a four-point cumulant is an $N \times N \times N \times N$ array, so the amount of required memory scales quartically with the system size. At the same time, as evident from Eqs. (3.17a) and (3.17b), the four-point functions entering the symmetry identities have one of the momenta set to zero, while the three remaining ones have to add up to zero due to momentum conservation. Therefore, one only needs a two-dimensional momentum-conserving surface, which can be encoded in an $N \times N$ matrix. By computing correlators directly in momentum space we avoid the need to store the full $N \times N \times N \times N$ array, and we can directly extract the relevant information by computing the two-dimensional momentum-conserving surface. For our numerical data, we consider correlation functions up to the inverse healing length, where the TWA description is expected to be reliable. For the plots, we have binned every 5 data points, while the correlators themselves were calculated on uncoarsened lattices.

Note that since perfect homogeneity and isotropy cannot be experimentally achieved, numerical artefacts always enter analyses. More specifically, in Eq. (3.16), while $E^{(2)}_{\pi\pi}(-p,p)$ and $E^{(2)}_{\sigma\sigma}(p,-p)$ are manifestly real, the three-point function $E^{(3)}_{\pi\pi\sigma}(0,p,-p)$ has in general a nonzero imaginary part. However, for the experimental data, the imaginary part is orders of magnitude below the real part, therefore, the magnitude of the correlator is dominated by the contribution from the real part. We similarly observe this with numerical data, apart from the very early initial times of a few t_s, where the imaginary part is more pronounced. In this case, and in all other cases, the magnitude of complex quantities is plotted.

Appendix B

Appendix to Chapter 4

B.1 Vortex (line) density detection algorithm

Vortex defects are characterised by phase singularities in $\arg(\phi+\mathrm{i}\pi)$ where a sharp minimum in the energy density also occurs on the lattice. In two dimensions, we compute the vortex density by counting the total number of (anti)vortices in the phase $\arg(\phi+\mathrm{i}\pi)$, and divide this by the (constant) area of the system. First, the input fields ϕ and π are blockwise averaged over every set of 8×8 lattice points to reduce lattice artefacts. In two dimensions, this process reduces the original 2048^2 lattice to a coarser 256^2 grid. For each point in the phase angle lattice, the algorithm then computes the phase differences around a closed loop. This loop consists of eight neighbouring points (excluding the edges of the lattice) arranged in a clockwise sequence, forming a square path centred around the point of interest. The phase differences between consecutive points in the loop are calculated by subtracting the phase angle at one point from the phase angle at the next point along the loop. Eventually, these differences are summed up and if the total phase change around the loop is approximately 2π, the point is identified as a vortex, and similarly, an antivortex is detected for a phase change of around -2π. This procedure is designed to avoid mistakenly identifying points as defects where the phase fluctuates between $\pm\pi$, as such fluctuations do not result in a uniform phase winding around the point, and therefore do not indicate the presence of a vortex core. Moreover, to avoid duplicate detections, which may still arise due to artefacts, the code enforces a minimum distance between detected vortices and antivortices. After a parameter scan, this minimum distance was chosen as 5 lattice points. This procedure is then repeated for each point on the 2048^2 lattice.

However, phase singularities in a three-dimensional lattice are more challenging to compute, and doing the computation in the two-dimensional planes, plane by plane, could be misleading. Therefore, we extract the vortex *line* density [177] from the energy density profiles, e.g. the ones shown in Fig. 4.2. We first blockwise average over every $6 \times 6 \times 6$ lattice points to reduce the original 368^3 lattice to a coarser grid. At this point, the energy density becomes quite uniform, and the vortex tangles in Fig. 4.2 are revealed by taking the points that are at $60 \ldots 70\%$ of the mean energy value on the lattice. We then compute the number of points that belong to vortex lines, and divide it by the total number of points on the lattice, giving us the density of vortex lines.

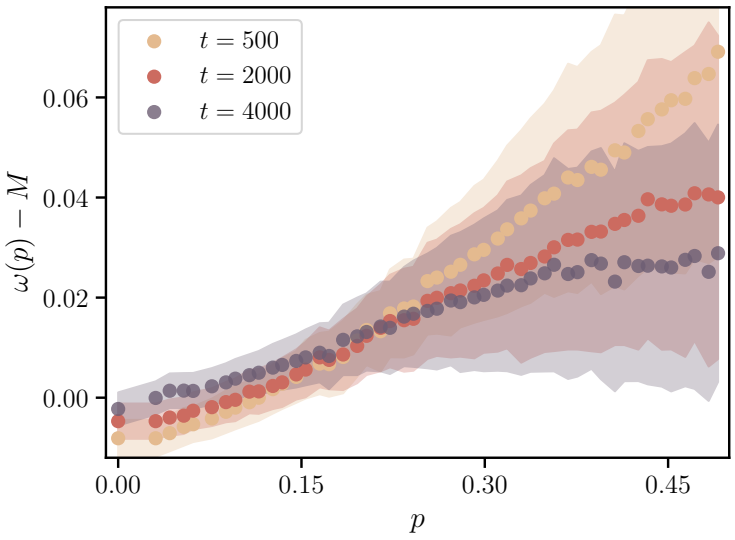

Figure B.1. The Kelvin wave dispersion from Fig. 4.9(b), with the shaded area showing the width of the peaks in $F_{\mathrm{K}}(t, \omega, p)$.

B.2 Flattening of the kelvon dispersion curves

As mentioned in the main text, the Kelvin wave dispersion (4.27) is fitted to the extracted dispersion relations over a progressively smaller momentum range at later times in three dimensions, since the fit becomes less reliable due to the flattening of the dispersion curves at higher momenta. This flattening is not part of the kelvon dispersion, therefore to reliably extract the fit parameters, we have to exclude this from the fit region. While the exact origin of this effect remains unclear, it is likely influenced by limitations in our data extraction procedure. In the statistical function $F(t, \omega, p)$, at later times, and for higher momenta, the kelvon peak becomes weaker as the Bogoliubov peak starts to dominate. This makes the extraction of the position of the maximum of the peak challenging, which is the quantity that yields ω_{K}. Even though we start using a two-peak fit form after $p \geq 0.17$, that includes both the kelvon (4.25) and the Bogoliubov peaks (4.26) in the fit function, the peak position of (4.25) becomes less certain. We also illustrate this by including the width γ_{K} from Fig. 4.11 as a shaded region around ω_{K} in Fig. B.1. While, naturally, the peak amplitude diminishes away from ω_{K}, as also visible in Fig. 4.7, the increasing breadth of the peak indicates the growing uncertainty in the maximum position with increasing momentum.

B.3 Analysing the fits to dispersion relation data

The comparison of linear and kelvon fits for the dispersion relation in $d = 2$ and $d = 3$ dimensions reveals specific differences, as shown in Fig. B.2. In $d = 3$, the kelvon fit clearly captures both the expected p^2 behaviour at low p and the bending of the data at higher p. This is reflected in the residuals, which are evenly distributed around zero for the kelvon fit, indicating that it accurately describes the data across the entire range. In contrast, the linear fit exhibits systematic deviations, as it fails to account for the p^2 scaling at low p and the curvature at higher p, leading to structured residuals. In $d = 2$, however, the data

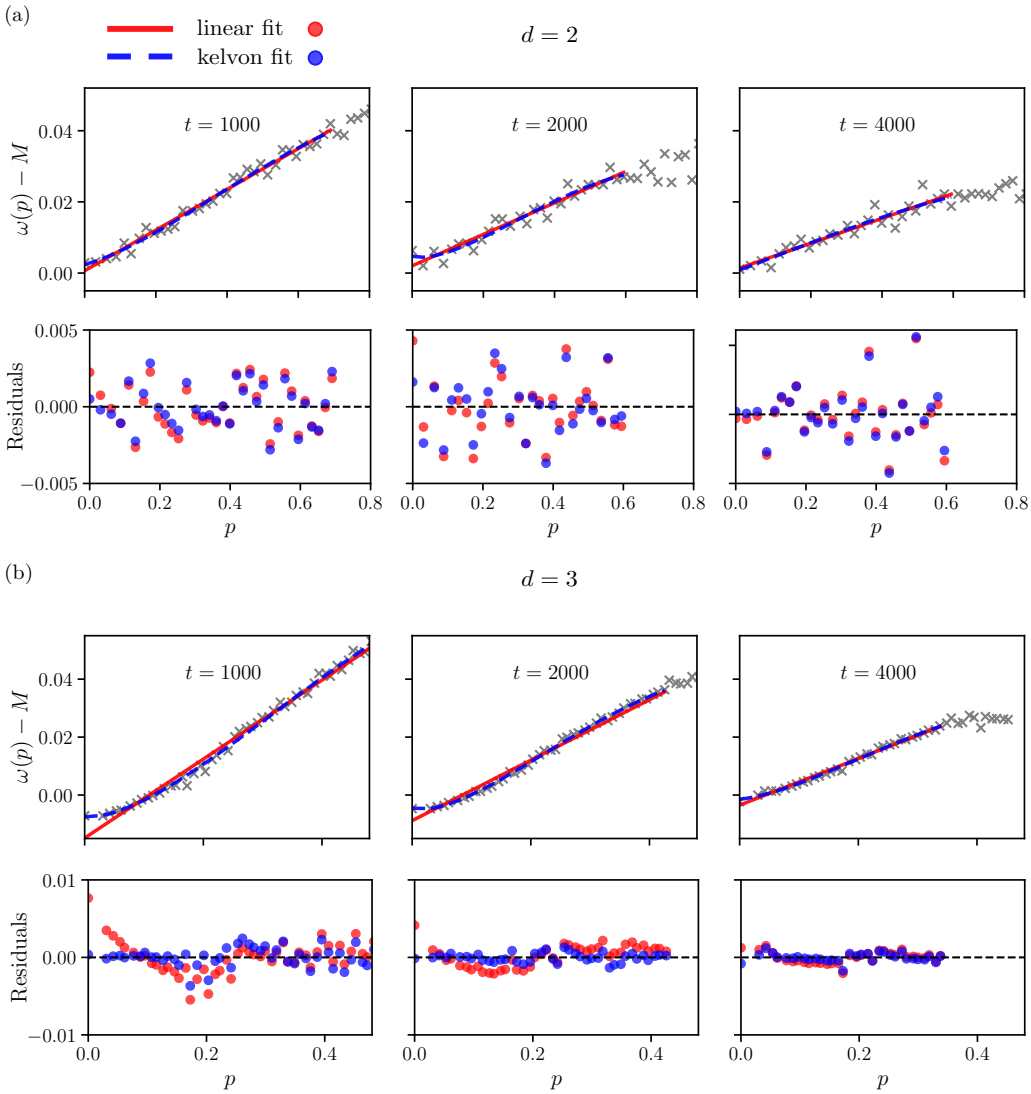

Figure B.2. Comparison of linear and kelvon fits for the dispersion relation of the dominant infrared excitation in (a) $d = 2$ and (b) $d = 3$ dimensions, including the corresponding residuals. In $d = 2$, it is challenging to determine which model provides a better fit, but the residuals strongly indicate that the kelvon fit captures the data more accurately in $d = 3$.

is significantly more scattered, making it difficult to determine a clear preference between the two models. Both fits result in residuals that appear evenly distributed around zero, suggesting that the noise in the data obscures any systematic deviations. Consequently, while the kelvon fit is strongly favoured in $d = 3$, the ambiguity in $d = 2$ prevents a definitive conclusion about which model captures the underlying dispersion relation better. However, since Fig. 4.7 shows that in $d = 2, 3$ dimensions, the behaviour is qualitatively the same, it is strongly suspected that kelvon-like excitations also exist in $d = 2$ dimensions.

Appendix C

Appendix to Chapter 5

C.1 Dependence of Betti numbers on the renormalised mass value

The simulations reported about in the main text have used a comparably large renormalised mass with $M = 2Q$. In this appendix, we discuss the dependence of the persistent homology results provided in Sec. 5.3.2 on this choice.

Fig. C.1 provides the dimension-0 Betti numbers for simulations with $N = 2$ field components and renormalised mass $M = Q/2$. Comparison with Fig. 5.5, which has given the corresponding results for $M = 2Q$, reveals that the right peak close to $\nu \equiv \Delta T^{00} = 0$ increases in height for the smaller mass value, while the height of the left peak appears roughly insensitive to the choice of mass. In particular, the scaling behaviour of $\beta^{\text{topo}}_{0,\text{max}}(t)$ remains the same compared to the larger mass (not shown).

We can heuristically understand this behaviour as follows. For the results displayed in Fig. 5.5 and Fig. C.1, we have employed averaging over blocks of 8^3 lattice sites. Removing ultraviolet fluctuations, this emphasises structures in the infrared, where the model is well-described by a nonrelativistic complex scalar field theory [48, 125]. The Hamiltonian of such a theory comes with a kinetic term $\sim \mathbf{k}^2/2M$, where $\mathbf{k}$ denotes the spatial momentum of a Fourier mode of the complex-valued field. A larger value for M therefore suppresses the contributions of spatial gradients of local fluctuations to energy densities, which pronounces structures with small spatial gradients, for instance topological defects.

Moreover, we have argued in favour of the association of the right peak in the dimension-0 Betti numbers with energy transport towards the ultraviolet, see Sec. 5.3.4. In the ΔT^{00} snapshots presented in Fig. 5.1, this corresponds to the local fluctuations on small length scales. A larger mass therefore suppresses these, such that the topological defects appear pronounced relative to the small-scale fluctuations, even though their number might remain roughly invariant under the choice of mass. This explains the behaviour of the dimension-0 Betti numbers shown in Fig. C.1.

For completeness, we note that the occupation number distributions computed for both mass values agree (not shown) and are similar to the results of [48].

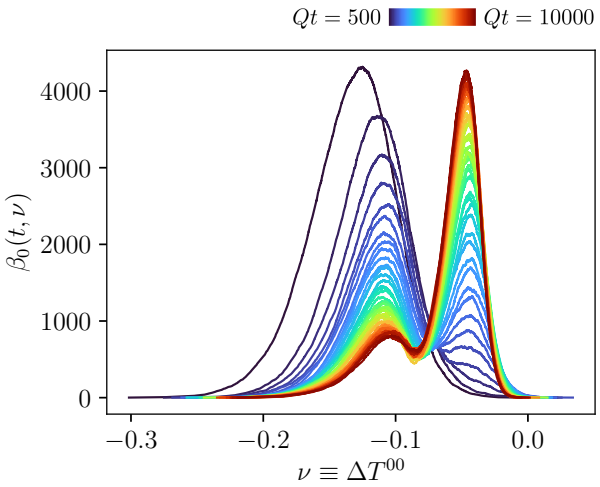

Figure C.1. Dimension-0 Betti numbers for ΔT^{00} sublevel sets for $N = 2$ field components, with averaging over blocks of 8^3 lattice sites. The renormalised mass used to generate these results is $M^2 = Q^2/4$.

C.2 The classification of topological defects in condensates of the O(N) vector model

In this appendix, we derive the classification of topological defects in condensates of the O(N) vector model in detail. The arguments are drawn from [80] and expanded here.

Intuitively, topological defects form when growing occupancies in the infrared organise into condensates along with the inverse particle cascade. To this end, the behaviour of spatial zero modes of the field variables is of relevance for the classification of topological defects. In particular, it is the topology of the phase space of zero modes of the field variables, $(\tilde{\phi}_a, \partial_t \tilde{\phi}_a)_{a=1,\dots,N}$, where $\tilde{\phi}_a \equiv \tilde{\phi}_a(t) \equiv \tilde{\phi}_a(t, \mathbf{p} = 0)$, along with dynamical constraints which determines the latter. Denoting this space for the O(N) vector model by $\mathcal{C}_N$, we first motivate its general construction from first principles based on the condensate dynamics. We subsequently describe the specific structure of the $\mathcal{C}_N$ and their topological properties, ultimately leading to the classification of defects in three spatial dimensions.

C.2.1 Dynamically realised condensate phase space

In our simulations, the modes in the infrared are highly occupied at early times for the considered initial conditions and are thus well-described classically. Here, we derive an approximate equation of motion for the condensate. First, the classical inverse propagator follows from the action (5.1) as

$$-i\frac{\delta^2 S[\phi]}{\delta\phi_a(x)\delta\phi_b(y)} = i\delta(x-y)\left[\delta_{ab}(\Box + m^2) + \frac{\lambda}{6N}\left(2\phi_a(x)\phi_b(x) + \delta_{ab}\sum_c \phi_c(x)^2\right)\right] \tag{C.1}$$

with $\Box \equiv \partial_\mu \partial^\mu$ and where we explicitly denoted the summation over the field components. This leads to the classical self-energy matrix

$$\Sigma^{\rm cl}_{ab}(x) = \frac{\lambda}{6N}\left(2\phi_a(x)\phi_b(x) + \delta_{ab}\sum_{c=1}^{N}\phi_c(x)^2\right). \tag{C.2}$$

Its spatial Fourier-transform is $\tilde{\Sigma}^{\rm cl}_{ab}(t,\mathbf{p}) = \int_{\mathbf{x}} \Sigma^{\rm cl}_{ab}(t,\mathbf{x})\exp(-i\mathbf{p}\mathbf{x})$. The action (5.1) yields an inhomogeneous Klein-Gordon equation as the classical equation of motion for spatial zero modes of the fields:

$$\sum_{b=1}^{N}\left[\delta_{ab}(\partial_t^2 + m^2)\tilde{\phi}_b(t) + \int_{\mathbf{p}}\tilde{\Sigma}^{\rm cl}_{ab}(t,-\mathbf{p})\tilde{\phi}_b(t,\mathbf{p})\right] = 0, \tag{C.3}$$

where $\int_{\mathbf{p}} \equiv \int \mathrm{d}^3\mathbf{p}/(2\pi)^3$ and the dependence on the classical self-energy matrix $\tilde{\Sigma}^{\rm cl}_{ab}(t,-\mathbf{p})$ has been explicitly denoted. We assume a large fraction of the particles occupies the zero mode, so that the momentum integral in (C.3) is dominated by momentum zero. This finally yields the equation

$$\sum_{b=1}^{N}[\delta_{ab}(\partial_t^2 + m^2) + \tilde{\Sigma}^{\rm cl}_{ab}(t,\mathbf{p}=0)]\tilde{\phi}_b(t) = 0, \tag{C.4}$$

which governs the time evolution of the condensate.

For a single field component ($N = 1$) $\tilde{\phi} \equiv \tilde{\phi}_{a=1}$ and the effective mass squared is $M^2 = m^2 + \tilde{\Sigma}^{\rm cl}_{11}$. (C.3) leads to the decomposition $\tilde{\phi} = \tilde{\phi}_0\cos(Mt+\delta)$, where $\tilde{\phi}_0$ is a real-valued peak amplitude of the field, δ a phase and M determines the oscillation frequency of the field. The amplitude $|\tilde{\phi}_0|$ is fixed by transient particle number conservation.[1] From a topological viewpoint, the $N = 1$ condensate phase space $\mathcal{C}_1$ is thus described by a circle, $\mathcal{C}_1 \simeq S^1$.

For $N \geq 2$ field components the solutions $\tilde{\phi} \equiv (\tilde{\phi})_{a=1,\ldots,N}$ to (C.4) generally have the form of oscillations sweeping out ellipses in the internal space of field components. These can interpolate between the extreme possibilities of $\tilde{\phi}$ and $\partial_t\tilde{\phi}$ parallel, so that oscillations happen along a line in this space, or $\tilde{\phi}$ and $\partial_t\tilde{\phi}$ orthogonal, so that oscillations happen along a circular orbit. It can be shown, that the energy-minimising condensate configurations are not straight lines and, therefore, have the topology of circular orbits. Indeed, repeating the argument provided in [80], we can understand this by comparing the energy cost of a circular orbit to that of a straight line in O(N) field space. The energy density ε of the zero mode of a single-component scalar field oscillating back and forth in a quartic potential is

$$\varepsilon = \frac{\lambda}{8}\tilde{\phi}_0^4 = \frac{1}{2}(\partial_t\tilde{\phi})^2 + \frac{\lambda}{8}\tilde{\phi}^4, \tag{C.5}$$

where we have neglected the mass term. This equation can be rearranged for $\partial_t\tilde{\phi}$ to obtain a periodic solution, which has oscillation frequency

$$\omega^2 = \frac{\pi\Gamma(3/4)^2}{\Gamma(1/4)^2}\lambda\tilde{\phi}_0^2. \tag{C.6}$$

[1] This is similar to nonrelativistic scalar fields for which particle number conservation is exact.

The particle number stored in the condensate is $n(\varepsilon) = \int_0^\varepsilon \mathrm{d}\varepsilon'/\omega = 4\varepsilon/(3\omega)$, and using (C.5), we obtain

$$\varepsilon = (8\pi^2)^{1/3} \left[\frac{3\Gamma(3/4)}{4\Gamma(1/4)}\right]^{4/3} \lambda^{1/3} n^{4/3}. \tag{C.7}$$

On the other hand, for a scalar field with two or more components with a circular orbital motion in the same potential, the energy density is

$$\varepsilon = \frac{1}{2}(\partial_t \tilde{\phi}_0)^2 + \frac{\lambda}{8}\tilde{\phi}_0^4 = \frac{3}{4}(\partial_t \tilde{\phi}_0)^2 = \frac{3\omega^2}{4}\tilde{\phi}_0^2 = \frac{3\lambda}{8}\tilde{\phi}_0^4, \tag{C.8}$$

where we have used the Virial theorem $(\partial_t \tilde{\phi})^2/2 = \lambda \tilde{\phi}_0^4/4$ and $\tilde{\phi}_0 = \tilde{\phi}(t_0)$ denotes the condensate configuration at some initial time t_0. Hence,

$$\omega^2 = \frac{\lambda}{2}\tilde{\phi}_0^2 = \frac{2^{1/2}}{3^{1/2}}\lambda^{1/2}\varepsilon^{1/2}. \tag{C.9}$$

Using the same arguments as before for $n(\varepsilon)$, we get that

$$\varepsilon = \frac{3}{2^{7/3}}\lambda^{1/3} n^{4/3}. \tag{C.10}$$

Therefore, comparing the numerical prefactors, at fixed particle number the energy cost of a circular orbit is lower than that of a straight line. We can conclude that energy-minimising orbits $\tilde{\phi}(t)$ are not straight lines and thus homotopy-equivalent to circles in the zero mode phase space. We expect that the addition of a non-zero mass term does not alter the topology of energy-minimising orbits. This is *a posteriori* reinforced by the consistency of our work with the defect classification outlined here, which relies on orbits being homotopy-equivalent to circles.

We thus proceed with the consideration of circular orbits in the zero mode phase space. For these the constancy of $|\tilde{\phi}|$ due to effective particle number conservation is complemented by $|\partial_t \tilde{\phi}|$ being constant due to the circular orbit geometry, along with the orthogonality constraint $\tilde{\phi} \perp \partial_t \tilde{\phi}$ in the internal field space. In general, a fixed-length $\tilde{\phi}$ is an element of the $(N-1)$-sphere $S^{N-1} \subset \mathbb{R}^N$. Any tangent vector to S^{N-1} at a point $\tilde{\phi} \in S^{N-1}$ is orthogonal to the vector $\tilde{\phi}$ itself within $\mathbb{R}^N$. The vectors $\partial_t \tilde{\phi}$ orthogonal to $\tilde{\phi}$ actually form the tangent manifold $T_{\tilde{\phi}} S^{N-1}$. The constancy constraint for $|\partial_t \tilde{\phi}|$ singles out tangent vectors of constant length. Since topology does not discriminate between the length of such tangent vectors, the constancy constraint for $|\partial_t \tilde{\phi}|$ can be taken care of upon restricting to normalised tangent vectors $\partial_t \tilde{\phi}$ with $|\partial_t \tilde{\phi}| = 1$.[2] Finally, for $N \geq 2$, the condensate phase space $\mathcal{C}_N$ is (homotopy-equivalent to) the unit tangent bundle of S^{N-1}, $\mathcal{C}_N \simeq T^1 S^{N-1}$, which as a set reads

$$T^1 S^{N-1} = \bigcup_{\tilde{\phi} \in S^{N-1}} \{(\tilde{\phi}, \partial_t \tilde{\phi}) \,|\, \partial_t \tilde{\phi} \in T_{\tilde{\phi}} S^{N-1},\ |\partial_t \tilde{\phi}| = 1\}. \tag{C.11}$$

C.2.2 Homotopy groups of $\mathcal{C}_N$

The topology of $\mathcal{C}_N$ can be nontrivial as quantified by the low-order homotopy groups, which is the mathematical origin of topological defects. Specifically, a nontrivial zeroth homotopy

[2] For the same reason we here ignored the mass dimension of $|\partial_t \tilde{\phi}|$.

group $\pi_0(\mathcal{C}_N)$ indicates that $\mathcal{C}_N$ comprises different connected components, i.e., the condensate is separated into different domains bounded by domain walls. If the fundamental group $\pi_1(\mathcal{C}_N)$ is nontrivial, $\mathcal{C}_N$ is not simply connected, and string defects can occur, i.e., vortex lines. If the second homotopy group $\pi_2(\mathcal{C}_N)$ is nontrivial, then monopole defects can occur. A nontrivial third homotopy group $\pi_3(\mathcal{C}_N)$ would indicate the possibility of textures. However, these have no defect core and are unstable [222], such that we exclude them from our analysis. Apart from textures, strings, domain walls and monopoles are all types of defects which can occur in three spatial dimensions. Investigating the presence of topological defects thus requires the computation of the homotopy groups $\pi_\ell(\mathcal{C}_N)$ for $\ell = 0, 1, 2$ and different N.

- $N = 1$

  For $N = 1$, the condensate phase space is $\mathcal{C}_1 \simeq S^1$, for which $\pi_1(S^1) \cong \mathbb{Z}$ and all other homotopy groups vanish, such that only string defects can occur.

- $N = 2$

  For $N = 2$, we have to consider $\mathcal{C}_2 \simeq T^1S^1$. The unit tangent line at any point in S^1 consists of exactly two points, such that $\mathcal{C}_2 \simeq S^1 \times \mathbb{Z}_2$. The homotopy groups of such products factorise [223], such that $\pi_\ell(\mathcal{C}_2) \cong \pi_\ell(S^1) \times \pi_\ell(\mathbb{Z}_2)$ for all $\ell \in \mathbb{N}$. We find the nontrivial homotopy groups $\pi_0(\mathcal{C}_2) \cong \pi_0(S^1) \times \pi_0(\mathbb{Z}_2) \cong 0 \times \mathbb{Z}_2 \cong \mathbb{Z}_2$ and $\pi_1(\mathcal{C}_2) \cong \pi_1(S^1) \times \pi_1(\mathbb{Z}_2) \cong \mathbb{Z} \times 0 \cong \mathbb{Z}$ and all other homotopy groups vanish. Hence, both domain walls and string defects can occur.

- $N = 3$

  For $N = 3$, we have to consider $\mathcal{C}_3 \simeq T^1S^2$. This space can be identified with SO(3), since $\tilde{\phi}$ describes a direction in $\mathbb{R}^3$ and $\partial_t\tilde{\phi}$ is orthogonal to it. Together with their cross product, they single out an orthonormal coordinate frame. The fundamental group is nontrivial: $\pi_1(\mathcal{C}_3) \cong \pi_1(\mathrm{SO}(3)) \cong \mathbb{Z}_2$ and all other homotopy groups vanish. There are thus string defects.

- $N = 4$

  For $N = 4$, we have to consider $\mathcal{C}_4 \simeq T^1S^3$. The 3-sphere is parallelisable, i.e., $TS^3 \cong S^3 \times \mathbb{R}^3$ is a trivial bundle above S^3. The unit tangent vector constraint then singles out $\mathcal{C}_4 \simeq S^3 \times S^2$. Again, the homotopy groups of such products factorise [223], such that $\pi_\ell(\mathcal{C}_4) \cong \pi_\ell(S^3) \times \pi_\ell(S^2)$ for all ℓ. With the homotopy groups of the spheres we find that $\pi_2(\mathcal{C}_4) \cong \mathbb{Z}$, $\pi_3(\mathcal{C}_4) \cong \mathbb{Z}^2$ and all other homotopy groups vanish. While the former (π_2) indicates that there are monopole defects, the latter (π_3) is irrelevant for defects in three spatial dimensions as considered here.

- $N \geq 5$

  For general $N \geq 5$ one needs to consider $\mathcal{C}_N \simeq T^1(S^{N-1}) \cong \mathrm{Spin}(N)/\mathrm{Spin}(N-2)$. The identification with the spin group quotient comes about since the elements of the unit tangent bundle of S^{N-1} single out orthonormal 2-frames in $\mathbb{R}^N$, which form the second Stiefel manifold $V_2(\mathbb{R}^N)$. Specifically, for $N \geq 3$ we have that $V_2(\mathbb{R}^N)$ is diffeomorphic to $\mathrm{SO}(N)/\mathrm{SO}(N-2)$ [223]. This in turn is diffeomorphic to the quotient $\mathrm{Spin}(N)/\mathrm{Spin}(N-2)$ for all $N \geq 3$, as can be seen with standard results for homogeneous spaces together with the consideration of relevant stabiliser subgroups of $\mathrm{SO}(N)$ and $\mathrm{Spin}(N)$.

The computation of the homotopy groups of this space requires more advanced methods from algebraic topology [223], which we only briefly outline here. Homotopy groups of the quotients $\mathrm{Spin}(N)/\mathrm{Spin}(N-2)$ can be computed with the long exact sequence of relative homotopy groups, which reduces their computation to the homotopy groups of the spin groups themselves. The spin groups are the universal covers of the special orthogonal groups for $N \geq 3$, as indicated by the related short exact sequence of groups:

$$1 \to \mathbb{Z}_2 \to \mathrm{Spin}(N) \to \mathrm{SO}(N) \to 1. \tag{C.12}$$

The spin groups are thus simply connected, so that $\pi_0(\mathrm{Spin}(N)) \cong \pi_1(\mathrm{Spin}(N)) \cong 0$ for all $N \geq 3$. Moreover, the short exact sequence (C.12) induces a long exact sequence of homotopy groups. Using $\pi_2(\mathrm{SO}(N)) \cong 0$ for all $N \geq 2$ (in the stable range), we then find $\pi_2(\mathrm{Spin}(N)) \cong 0$ for all $N \geq 2$. Together with the previously mentioned long exact sequence of relative homotopy groups this yields $\pi_0(\mathcal{C}_N) \cong 0$, $\pi_1(\mathcal{C}_N) \cong 0$ and $\pi_2(\mathcal{C}_N) \cong 0$ for all $N \geq 5$, while higher homotopy groups can be nontrivial. Yet, it is these homotopy groups which determine the topological defects for three spatial dimensions. Topological defects are thus absent in the considered three-dimensional $\mathrm{O}(N)$ vector model for all $N \geq 5$.

C.3 Details on the lower star filtration of cubical complexes and persistent homology

This appendix provides mathematical details on the construction of the lower star filtration of cubical complexes, homology groups and persistent homology. It closely follows similar expositions in [185].

C.3.1 Lower star filtration

We introduce the lower star filtration for a real-valued lattice function $f : \Lambda_s \to \mathbb{R}$ such as $\Delta T^{00}(t, \cdot)$, intuitively corresponding to a pixelisation of its lattice sublevel sets. To begin with, let $\mathcal{C}$ denote the full cubical complex of the lattice Λ_s, consisting of one 3-cube $\mathbf{x} + [-a_s/2, a_s/2]^3$ for each spatial lattice point $\mathbf{x} \in \Lambda_s$. $\mathcal{C}$ also includes all faces, edges and vertices of every 3-cube, such that it is closed under taking boundaries. $\mathcal{C}$ is equipped with

the information contained in the function f by means of inductively constructing a map $F : \mathcal{C} \to \mathbb{R}$. By construction, any 3-cube $C \in \mathcal{C}$ has a unique lattice point $\mathbf{x} \in \Lambda_s$ at its center, so that we can set $F(C) := f(\mathbf{x})$. For all 2-cubes $D \in \mathcal{C}$ we set

$$F(D) := \min\{F(C) \,|\, D \subset \partial C,\, C \in \mathcal{C} \text{ 3-cube}\}. \tag{C.13}$$

(C.13) is then applied inductively to construct F for lower-dimensional cubes from higher-dimensional ones, until F is defined on all $\mathcal{C}$. This construction is called the lower star filtration. We define cubical complexes corresponding to lattice sublevel sets of f as

$$\mathcal{C}_f(\nu) := F^{-1}(-\infty, \nu]. \tag{C.14}$$

Indeed, these are closed under taking boundaries. As stated in the main text, they form a filtration: whenever $\nu \leq \mu$, we have the inclusion $\mathcal{C}_f(\nu) \subseteq \mathcal{C}_f(\mu)$.

C.3.2 Homology groups

Let $\mathcal{C}$ be a cubical complex, although the construction of homology groups is the same as for simplicial complexes. More details can be found e.g., in [83] and references cited therein. In this work, we focus on chain complexes and homology groups with $\mathbb{Z}_2$-coefficients, such that the k-th chain complex $C_k(\mathcal{C})$ of $\mathcal{C}$ consists of formal sums of chains of k-cubes with $\mathbb{Z}_2$-coefficients. The boundary operator $\partial_k : C_k(\mathcal{C}) \to C_{k-1}(\mathcal{C})$ is defined to map a chain of k-cubes to its boundary, which is a $(k-1)$-chain. Since boundaries of such chain boundaries are empty, $\partial_{k-1} \circ \partial_k = 0$. We define the cycle group as $Z_k(\mathcal{C}) := \ker(\partial_k)$, which consists of all closed k-chains, i.e., k-chains without boundary. The boundary group can be defined as $B_k(\mathcal{C}) := \mathrm{im}(\partial_{k+1})$, consisting of all those k-chains, which are boundaries of $(k+1)$-chains. As subgroups, $B_k(\mathcal{C}) \subseteq Z_k(\mathcal{C})$, such that their quotient groups are well-defined:

$$H_k(\mathcal{C}) := Z_k(\mathcal{C})/B_k(\mathcal{C}). \tag{C.15}$$

These are called homology groups.

The topology of $\mathcal{C}$ can be studied via the homology groups $H_k(\mathcal{C})$. They capture similar topological information compared to homotopy groups of $\mathcal{C}$, but are often not the same. Elements of $H_k(\mathcal{C})$ are called homology classes and form equivalence classes of k-cycles, defined modulo higher-dimensional boundary contributions. Intuitively, they can be thought of as independent holes. Their number is given by the $\mathbb{Z}_2$-dimension of $H_k(\mathcal{C})$:

$$\beta_k(\mathcal{C}) := \dim_{\mathbb{Z}_2}(H_k(\mathcal{C})), \tag{C.16}$$

which is called the k-th Betti number.

C.3.3 Persistent homology groups

Let $\{\mathcal{C}_\nu\}_{\nu\in\mathbb{R}}$ be a filtration of complexes, such as $\mathcal{C}_\nu = \mathcal{C}_f(\nu)$ for the energy density sublevel set filtration considered in this work. Suppose we compute all their individual homology groups $\{H_k(\mathcal{C}_\nu)\}_\nu$. In addition, the filtration contains for all $\nu \leq \mu$ the inclusion maps $\mathcal{C}_\nu \hookrightarrow \mathcal{C}_\mu$, which induce maps on the homology groups:

$$\iota_k^{\nu,\mu} : H_k(\mathcal{C}_\nu) \to H_k(\mathcal{C}_\mu). \tag{C.17}$$

The $\iota_k^{\nu,\mu}$ map a homology class in $H_k(\mathcal{C}_\nu)$ either to one in $H_k(\mathcal{C}_\mu)$, if it is still present for $\mathcal{C}_\mu$, or to zero, if corresponding (potentially deformed) cycles appear as boundaries in $H_k(\mathcal{C}_\mu)$. Moreover, nontrivial cokernels can appear for $\iota_k^{\nu,\mu}$: new homology classes can appear in $\mathcal{C}_\mu$, which are not in $\mathcal{C}_\nu$. The parameter μ can be chosen, so that for sufficiently small $\epsilon > 0$:

$$H_k(\mathcal{C}_{\mu-\epsilon}) \subsetneq H_k(\mathcal{C}_\mu). \tag{C.18}$$

The collection $\{(H_k(\mathcal{C}_\nu), \iota_k^{\nu,\mu})\}_{\nu\leq\mu}$ forms a so-called persistence module, which is tame, if (C.18) holds only for finitely many distinct values of μ.

By the structure theorem of persistent homology (see e.g. [83] and references therein), any tame persistence module is isomorphic to its persistence diagram, i.e., the collection of all the birth-death pairs (b, d), $b < d \in \mathbb{R} \cup \{\infty\}$. Persistence diagrams are multisets, so the same birth-death pair may appear multiple times.

C.4 Self-similar scaling in persistent homology

In this appendix, we discuss the self-similarity of Betti number distributions as introduced in [184] and similarly employed in [185]. For this, we need to introduce the so-called persistence pair distribution. The persistent homology of the energy density filtration is fully described by the persistence diagram, which consists of all birth-death pairs (b, d). We denote it for dimension-ℓ features as $\mathrm{Dgm}_{\ell,i}(t)$, computed for a classical statistical realisation $\phi_i(t, \mathbf{x})$. The dimension-ℓ persistence pair distribution is then given by [184]

$$\mathfrak{P}_{\ell,i}(t, b, d) = \sum_{(b',d')\in \mathrm{Dgm}_{\ell,i}(t)} \delta(b - b')\delta(d - d'). \tag{C.19}$$

Its expectation value can exist and is in general no longer a sum of Dirac δ-functions anymore [86]. In particular, it scales self-similarly in time [184] if

$$\langle\mathfrak{P}_\ell\rangle(t, b, d) = (t/t')^{-\eta_2}\langle\mathfrak{P}_\ell\rangle(t', (t/t')^{-\eta_1}b, (t/t')^{-\eta_1}d),$$

where t, t' is any pair of times in the temporal regime of self-similar scaling and η_1, η_2 are suitable scaling exponents.

From $\langle\mathfrak{P}_\ell\rangle(t, b, d)$, the Betti number distribution can be computed as

$$\langle\beta_\ell\rangle(t, \nu) = \int_{-\infty}^{\nu} \mathrm{d}b \int_{\nu}^{\infty} \mathrm{d}d\, \langle\mathfrak{P}_l\rangle(t, b, d). \tag{C.20}$$

If $\langle\mathfrak{P}_\ell\rangle(t, b, d)$ scales self-similarly in time, the Betti number distributions $\langle\beta_\ell\rangle(t, \nu)$ fulfil

$$\langle\beta_\ell\rangle(t, \nu) = (t/t')^{2\eta_1-\eta_2}\langle\beta_\ell\rangle(t', (t/t')^{-\eta_1}\nu). \tag{C.21}$$

In Fig. C.2, we show dimension-0 Betti number distributions for (a) $N = 1$, (b) $N = 2$ and (c) $N = 3$, rescaled in time according to (C.21) (averaging over every 8^3 blocks). The fits take all times in the interval from $Qt = 2500$ to $Qt = 12500$ into account. They are done for those filtration parameter ranges which correspond to the defect-related peaks in Betti number distributions: for $N = 1$ from $\nu = -0.45$ to -0.29, for $N = 2$ from $\nu = -0.31$ to

-0.15, and for $N = 3$ from $\nu = -0.20$ to -0.09. This way, the optimised scaling exponents for $N = 1$ are

$$\eta_1 = 0.02 \pm 0.03, \qquad \eta_2 = 0.72 \pm 0.01, \tag{C.22}$$

for $N = 2$

$$\eta_1 = 0.01 \pm 0.02, \qquad \eta_2 = 0.69 \pm 0.03, \tag{C.23}$$

and for $N = 3$

$$\eta_1 = 0.01 \pm 0.02, \qquad \eta_2 = 1.20 \pm 0.01. \tag{C.24}$$

Indeed, rescaling the Betti number distributions with these scaling exponents consistently leads at least to approximate constancy in time, see Fig. C.2, in particular for $N = 1$ and $N = 3$. Yet, smaller systematic deviations remain, since the shape of the peaks is not fully independent of time. According to the Betti number scaling (C.21), the peak Betti number scales $\sim t^{2\eta_1-\eta_2}$. The numbers provided by the self-similarity fits, (C.22), (C.23), (C.24), match the analysis results provided in Sec. 5.3.3. There, we also discuss the value of the exponent $2\eta_1 - \eta_2$ in light of phase-ordering kinetics.

The value of η_1 is consistent with zero within errors. If connected components at these ΔT^{00} values are primarily due to defects, this can indicate that defects appear locally at particular *constant* energy density values. We note that a zero result for η_1 is not in line with the packing relation [86], which yields $\eta_2 = 3\eta_1$ for energy conservation, providing a one-dimensional constraint on the filtration. This is not in contradiction with [86], since the packing relation has been proven for self-similar scaling that applies to the entire filtration range. This is not the case here, where the ongoing homogenisation of small-scale structures in energy densities provides features in Betti number distributions which cannot be rescaled with the exponents of (C.22) to (C.24) (cf. the right peaks in Fig. C.2).

C.5 Maxima of dim-1 Betti number distributions at $N = 2$

This appendix discusses the defect-related left peak in the dimension-1 Betti number distributions for $N = 2$ (cf. 5.5). In Fig. C.3 we show maximum values of the peak depending on time. The main figure has been computed for averaging over every 8^3 blocks, the top inset for averaging over 16^3 blocks. As it is clearly visible, the numbers of dimension-1 features decline with time, such that the average distances associated with the structures grow. Qualitatively, the discussion of Sec. 5.3.3 applies here in an analogous way, so that we can associate this to the coarsening dynamics, potentially for domain walls. Again, for an intermediate time range a power law can be fitted. For averaging over every 8^3 blocks, the peak values decrease as a power law with exponent -0.85 ± 0.01, and with exponent -0.62 ± 0.03 for averaging over 16^3 blocks. While the corresponding length scales of dimension-1 features thus grow as power laws with exponents well within the regime expected for coarsening dynamics (see the discussion in Sec. 5.3.3), the numbers do not agree within uncertainties. This indicates that in dimension-1 Betti numbers the dynamics in the infrared is not well-separated from ultraviolet dynamics for averaging over every 8^3 or 16^3 blocks. Additional potential sources of uncertainties have been discussed at the end of Sec. 5.3.4.

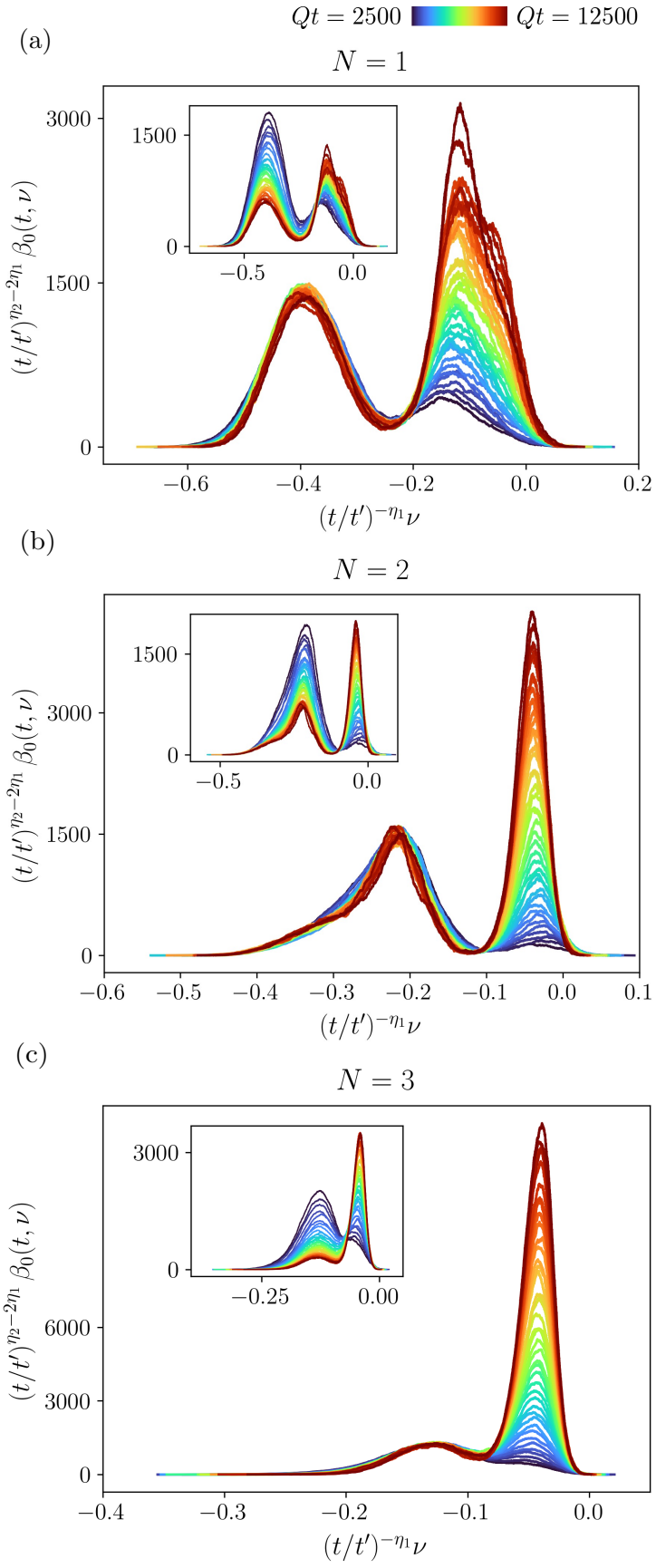

Figure C.2. Rescaled dimension-0 Betti number distributions for (a) $N = 1$, $\eta_1 = 0.02$, $\eta_2 = 0.73$, (b) $N = 2$, $\eta_1 = 0.02$, $\eta_2 = 0.65$, (c) $N = 3$, $\eta_1 = 0.01$, $\eta_2 = 1.20$. Blocks of 8^3 lattice points have been averaged. The insets show the non-rescaled distributions.

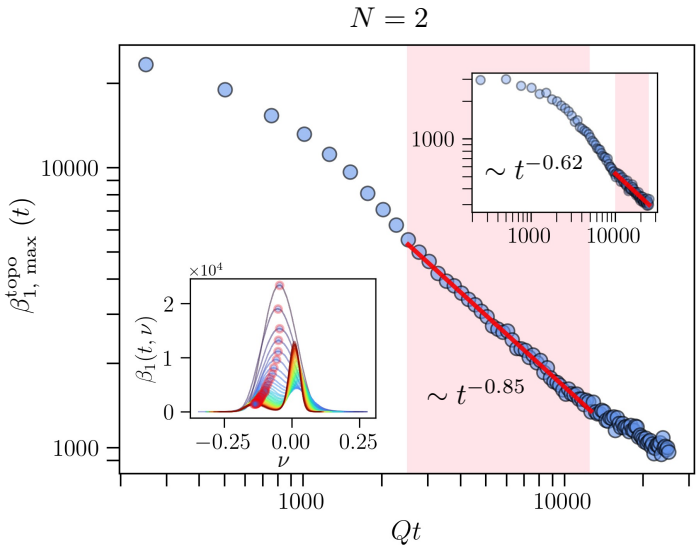

Figure C.3. Temporal scaling of the left dimension-1 Betti number distribution peak values for $N = 3$. Averaging over blocks of 8^3 lattice sites has been employed. The bottom inset shows the actual Betti number distributions, where the red circles indicate the peak values. The top inset shows peak values for averaging over every 16^3 blocks. The power law fits are based on the data in the red shaded Qt ranges.

Appendix D

Appendix to Chapter 6

D.1 Derivation of self-energy expressions

As already mentioned in the main sections, at next-to-leading order in $1/N$, the nonlocal part of the spectral self-energy on the Keldysh contour is given by

$$\Sigma^{\rho}(x,y) = -\frac{\lambda}{3N}\left(F(x,y)I^{\rho}(x,y) + \rho(x,y)I^{F}(x,y)\right). \tag{D.1}$$

Using a leading-order gradient expansion in time, the summation functions I^F and I^ρ can be majorly simplified in momentum space, as discussed in the main text. For the spectral self-energy in Wigner space, this leads to the expression

$$\Sigma^{\rho}(\omega,\mathbf{p}) = -\frac{\lambda}{3N}\int_{\nu,\mathbf{q}}\left[F(\omega-\nu,\mathbf{p}-\mathbf{q})\Pi^{\rho}(\nu,\mathbf{q}) - \rho(\omega-\nu,\mathbf{p}-\mathbf{q})\Pi^{F}(\nu,\mathbf{q})\right]v_{\text{eff}}(\nu,\mathbf{q}). \tag{D.2}$$

We also note that

$$\int_{\nu,\mathbf{q}} \equiv \int \frac{\mathrm{d}\nu}{2\pi}\frac{\mathrm{d}^3\mathbf{q}}{(2\pi)^3}. \tag{D.3}$$

The next step is to evaluate the frequency integrals, which is done by the quasiparticle approximation. Assuming delta-functions for the spectral function,

$$\rho(\omega,\mathbf{p}) = \frac{2\pi\mathrm{i}}{2\omega_{\mathbf{p}}}\left(\delta\left(\omega-\omega_{\mathbf{p}}\right) - \delta\left(\omega+\omega_{\mathbf{p}}\right)\right), \tag{D.4}$$

and a generalised fluctuation-dissipation relation for the statistical and spectral functions,

$$F(t,p) = -\mathrm{i}\left(f(t,p)+\frac{1}{2}\right)\rho(p), \tag{D.5}$$

first, the Π^{ρ} loop can be simplified to

$$\begin{aligned}\Pi^{\rho}(\nu,\mathbf{q}) &= \frac{\lambda}{3N}\int_{\mu,\mathbf{r}} F(\nu-\mu,\mathbf{q}-\mathbf{r})\rho(\mu,\mathbf{r}) \\ &= \frac{\lambda}{3N}\int_{\mu,\mathbf{r}} f(\nu-\mu,\mathbf{q}-\mathbf{r})\frac{2\pi}{2\omega_{\mathbf{q}-\mathbf{r}}}\left[\delta\left(\nu-\mu-\omega_{\mathbf{q}-\mathbf{r}}\right)-\delta\left(\nu-\mu+\omega_{\mathbf{q}-\mathbf{r}}\right)\right] \\ &\quad\times\frac{2\pi\mathrm{i}}{2\omega_{\mathbf{r}}}\left[\delta\left(\mu-\omega_{\mathbf{r}}\right)-\delta\left(\mu+\omega_{\mathbf{r}}\right)\right] \\ &= \frac{\lambda}{3N}\int_{\mathbf{r}}\frac{2\pi\mathrm{i}f(\mathbf{q}-\mathbf{r})}{4\omega_{\mathbf{q}-\mathbf{r}}\omega_{\mathbf{r}}}\Big[\delta\left(\nu-\omega_{\mathbf{r}}+\omega_{\mathbf{q}-\mathbf{r}}\right)+\delta\left(\nu-\omega_{\mathbf{r}}-\omega_{\mathbf{q}-\mathbf{r}}\right) \\ &\quad-\delta\left(\nu+\omega_{\mathbf{r}}+\omega_{\mathbf{q}-\mathbf{r}}\right)-\delta\left(\nu+\omega_{\mathbf{r}}-\omega_{\mathbf{q}-\mathbf{r}}\right)\Big].\end{aligned} \tag{D.6}$$

In a similar manner, the Π^{F} loop can also be computed as

$$\begin{aligned}\Pi^{F}(\nu,\mathbf{q}) =& \frac{\lambda}{6N}\int_{\mu,\mathbf{r}} F(\nu-\mu,\mathbf{q}-\mathbf{r})F(\mu,\mathbf{r}) \\ =& \frac{\lambda}{6N}\int_{\mu,\mathbf{r}} f(\nu-\mu,\mathbf{q}-\mathbf{r})\frac{2\pi}{2\omega_{\mathbf{q}-\mathbf{r}}}\left[\delta\left(\nu-\mu-\omega_{\mathbf{q}-\mathbf{r}}\right)-\delta\left(\nu-\mu+\omega_{\mathbf{q}-\mathbf{r}}\right)\right] \\ &\times f(\mu,\mathbf{r})\frac{2\pi}{2\omega_{\mathbf{r}}}\left[\delta\left(\mu-\omega_{\mathbf{r}}\right)-\delta\left(\mu+\omega_{\mathbf{r}}\right)\right] \\ =& \frac{\lambda}{6N}\int_{\mathbf{r}}\frac{2\pi f(\mathbf{q}-\mathbf{r})f(\mathbf{r})}{4\omega_{\mathbf{q}-\mathbf{r}}\omega_{\mathbf{r}}}\Big[\delta\left(\nu-\omega_{\mathbf{r}}+\omega_{\mathbf{q}-\mathbf{r}}\right)+\delta\left(\nu-\omega_{\mathbf{r}}-\omega_{\mathbf{q}-\mathbf{r}}\right) \\ &-\delta\left(\nu+\omega_{\mathbf{r}}-\omega_{\mathbf{q}-\mathbf{r}}\right)-\delta\left(\nu+\omega_{\mathbf{r}}+\omega_{\mathbf{q}-\mathbf{r}}\right)\Big].\end{aligned} \tag{D.7}$$

Then, when explicitly writing the self-energy out from (D.2), for the first term, we get

$$\begin{aligned}\int_{\nu,\mathbf{q}} F(\omega-\nu,\mathbf{p}-\mathbf{q})\Pi^{\rho}(\nu,\mathbf{q})v_{\mathrm{eff}}(\nu,\mathbf{q}) &= \frac{-\lambda}{3N}\int_{\nu,\mathbf{q}}\frac{2\pi f(\omega-\nu,\mathbf{p}-\mathbf{q})}{2\omega_{\mathbf{p}-\mathbf{q}}}\Pi^{\rho}(\nu,\mathbf{q})v_{\mathrm{eff}}(\nu,\mathbf{q}) \\ &\quad\times\left[\delta\left(\omega-\nu-\omega_{\mathbf{p}-\mathbf{q}}\right)-\delta\left(\omega-\nu+\omega_{\mathbf{p}-\mathbf{q}}\right)\right] \\ &= \frac{-\lambda}{3N}\int_{\mathbf{q}}\frac{f(\mathbf{p}-\mathbf{q})}{\omega_{\mathbf{p}-\mathbf{q}}}\Pi^{\rho}\left(\omega_{\mathbf{p}-\mathbf{q}},\mathbf{q}\right)v_{\mathrm{eff}}\left(\omega_{\mathbf{p}-\mathbf{q}},\mathbf{q}\right),\end{aligned} \tag{D.8}$$

and for the second term, it is

$$\begin{aligned}\int_{\nu,\mathbf{q}} \rho(w-\nu\cdot\mathbf{p}-\mathbf{q})\Pi^{F}(\nu,\mathbf{q})v_{\mathrm{eff}}(\nu,\mathbf{q}) &= \frac{-\lambda}{3N}\int_{\nu,\mathbf{q}}\frac{2\pi\mathrm{i}}{2\omega_{\mathbf{p}-\mathbf{q}}}\Pi^{F}(\nu,\mathbf{q})v_{\mathrm{eff}}(\nu,\mathbf{q}) \\ &\quad\times\left[\delta(\omega-\nu-\omega_{\mathbf{p}-\mathbf{q}})-\delta(\omega-\nu+\omega_{\mathbf{p}-\mathbf{q}})\right] \\ &= \frac{-\lambda}{3N}\int_{\mathbf{q}}\frac{\mathrm{i}}{\omega_{\mathbf{p}-\mathbf{q}}}\Pi^{F}(\omega_{\mathbf{p}-\mathbf{q}},\mathbf{q})v_{\mathrm{eff}}(\omega_{\mathbf{p}-\mathbf{q}},\mathbf{q}).\end{aligned} \tag{D.9}$$

To consider the relationship between the retarded and spectral self-energies, we recall

$$\Sigma^{R}(\omega,\mathbf{p}) = \lim_{\epsilon\to 0}\int\frac{\mathrm{d}\omega'}{2\pi\mathrm{i}}\frac{\Sigma^{\rho}\left(\omega',\mathbf{p}\right)}{\omega-\omega'+\mathrm{i}\epsilon}. \tag{D.10}$$

This overall turns the expression (D.6) into (6.44) and (D.7) into (6.45), as found in the main text.

Afterword and acknowledgements

First and foremost, I am grateful, for I have been blessed with enough perseverance and skills so that I get to do what I wish to do in life. It has been my long-standing aspiration to become a *quantum physicist* for half my life, as everything else seemed to be lacking. I'm a curious person, and I always wanted to know how "the universe works". I still don't quite understand it, however, I did learn all sorts of new physics throughout my doctoral studies as a result of the intriguing research projects I undertook.

While acknowledgements are typically meant to recognise the people whose support I've appreciated during this phase of my life, I don't feel particularly inclined to list them all out. I trust that those to whom I'm grateful already know it, and, in all likelihood, so do those to whom I'm not. That said, I do deeply appreciate the useful support I've received over the years, especially from my teachers, collaborators, and friends. In particular, I would like to express my gratitude to Jürgen for his remarkable patience.

Bibliography

[1] V. Noel and D. Spitz, "Detecting defect dynamics in relativistic field theories far from equilibrium using topological data analysis", Phys. Rev. D **109**, 056011 (2024), arXiv:2312.04959 [hep-ph].

[2] A. N. Mikheev, V. Noel, I. Siovitz, H. Strobel, M. K. Oberthaler, and J. Berges, "Extracting the symmetries of nonequilibrium quantum many-body systems", SciPost Phys. **18**, 044 (2025), arXiv:2407.17913 [cond-mat.quant-gas].

[3] V. Noel, T. Gasenzer, and K. Boguslavski, "Kelvin waves in nonequilibrium universal dynamics of relativistic scalar field theories", (2025), arXiv:2503.01771 [cond-mat.quant-gas].

[4] V. Noel, A. N. Mikheev, C. Huang, and J. Berges, "Nonthermal scaling phenomena with the two-particle-irreducible effective action (in preparation)", (2025).

[5] V. de Jonge, V. Noel, J. M. Pawlowski, and F. Sattler, "Far-from-equilibrium universality in driven-dissipative scalar fields (in preparation)", (2025).

[6] A. Molle, J. P. Drennhaus, V. Noel, N. Kolev, and A. Bande, "Time-Resolved Rubidium-Assisted Electron Capture by Barium (II) Cation", (2023), arXiv:2306.09580.

[7] M. Srednicki, "Chaos and quantum thermalization", Physical review e **50**, 888 (1994).

[8] A. Polkovnikov, K. Sengupta, A. Silva, and M. Vengalattore, "Nonequilibrium dynamics of closed interacting quantum systems", Rev. Mod. Phys. **83**, 863 (2011), arXiv:1007.5331 [cond-mat.stat-mech].

[9] J. Berges and J. Cox, "Thermalization of quantum fields from time reversal invariant evolution equations", Phys. Lett. B **517**, 369–374 (2001), arXiv:hep-ph/0006160.

[10] J. Eisert, M. Friesdorf, and C. Gogolin, "Quantum many-body systems out of equilibrium", Nature Phys. **11**, 124 (2015), arXiv:1408.5148 [quant-ph].

[11] J. Berges, S. Borsanyi, and C. Wetterich, "Prethermalization", Phys. Rev. Lett. **93**, 142002 (2004), arXiv:hep-ph/0403234.

[12] M. Gring, M. Kuhnert, T. Langen, T. Kitagawa, B. Rauer, M. Schreitl, I. Mazets, D. A. Smith, E. Demler, and J. Schmiedmayer, "Relaxation and Prethermalization in an Isolated Quantum System", Science **337**, 1224953 (2012).

[13] C.-L. Hung, V. Gurarie, and C. Chin, "From Cosmology to Cold Atoms: Observation of Sakharov Oscillations in Quenched Atomic Superfluids", Science **341**, 1213–1215 (2013), arXiv:1209.0011 [cond-mat.quant-gas].

[14] B. Rauer, S. Erne, T. Schweigler, F. Cataldini, M. Tajik, and J. Schmiedmayer, "Recurrences in an isolated quantum many-body system", Science **360**, aan7938 (2018).

[15] T. Kinoshita, T. Wenger, and D. S. Weiss, "A quantum Newton's cradle", Nature **440**, 900–903 (2006).

[16] M. Schreiber, S. S. Hodgman, P. Bordia, H. P. Lüschen, M. H. Fischer, R. Vosk, E. Altman, U. Schneider, and I. Bloch, "Observation of many-body localization of interacting fermions in a quasirandom optical lattice", Science **349**, aaa7432 (2015).

[17] R. Nandkishore and D. A. Huse, "Many body localization and thermalization in quantum statistical mechanics", Ann. Rev. Condensed Matter Phys. **6**, 15–38 (2015), arXiv:1404.0686 [cond-mat.stat-mech].

[18] C. J. Turner, A. A. Michailidis, D. A. Abanin, M. Serbyn, and Z. Papić, "Weak ergodicity breaking from quantum many-body scars", Nature Phys. **14**, 745–749 (2018).

[19] J. Berges, A. Rothkopf, and J. Schmidt, "Non-thermal fixed points: Effective weak-coupling for strongly correlated systems far from equilibrium", Phys. Rev. Lett. **101**, 041603 (2008), arXiv:0803.0131 [hep-ph].

[20] J. Berges and G. Hoffmeister, "Nonthermal fixed points and the functional renormalization group", Nucl. Phys. B **813**, 383–407 (2009), arXiv:0809.5208 [hep-th].

[21] M. Prüfer, P. Kunkel, H. Strobel, S. Lannig, D. Linnemann, C.-M. Schmied, J. Berges, T. Gasenzer, and M. K. Oberthaler, "Observation of universal dynamics in a spinor Bose gas far from equilibrium", Nature **563**, 217–220 (2018), arXiv:1805.11881 [cond-mat.quant-gas].

[22] S. Erne, R. Bücker, T. Gasenzer, J. Berges, and J. Schmiedmayer, "Universal dynamics in an isolated one-dimensional Bose gas far from equilibrium", Nature **563**, 225–229 (2018), arXiv:1805.12310 [cond-mat.quant-gas].

[23] C. Eigen, J. A. Glidden, R. Lopes, E. A. Cornell, R. P. Smith, and Z. Hadzibabic, "Universal prethermal dynamics of Bose gases quenched to unitarity", Nature **563**, 221–224 (2018), arXiv:1805.09802 [cond-mat.quant-gas].

[24] J. A. P. Glidden, C. Eigen, L. H. Dogra, T. A. Hilker, R. P. Smith, and Z. Hadzibabic, "Bidirectional dynamic scaling in an isolated Bose gas far from equilibrium", Nature Phys. **17**, 457–461 (2021), arXiv:2006.01118 [cond-mat.quant-gas].

[25] S. Lannig, M. Prüfer, Y. Deller, I. Siovitz, J. Dreher, T. Gasenzer, H. Strobel, and M. K. Oberthaler, "Observation of two non-thermal fixed points for the same microscopic symmetry", (2023), arXiv:2306.16497 [cond-mat.quant-gas].

[26] S. Huh, K. Mukherjee, K. Kwon, J. Seo, S. I. Mistakidis, H. R. Sadeghpour, and J.-y. Choi, "Classifying the universal coarsening dynamics of a quenched ferromagnetic condensate", (2023), arXiv:2303.05230 [cond-mat.quant-gas].

[27] A. D. García-Orozco, L. Madeira, M. A. Moreno-Armijos, A. R. Fritsch, P. E. S. Tavares, P. C. M. Castilho, A. Cidrim, G. Roati, and V. S. Bagnato, "Universal dynamics of a turbulent superfluid Bose gas", Phys. Rev. A **106**, 023314 (2022), arXiv:2107.07421 [cond-mat.quant-gas].

[28] S. Schlichting and D. Teaney, "The First fm/c of Heavy-Ion Collisions", Ann. Rev. Nucl. Part. Sci. **69**, 447–476 (2019), arXiv:1908.02113 [nucl-th].

[29] J. Berges, M. P. Heller, A. Mazeliauskas, and R. Venugopalan, "QCD thermalization: Ab initio approaches and interdisciplinary connections", Rev. Mod. Phys. **93**, 035003 (2021), arXiv:2005.12299 [hep-th].

[30] R. Micha and I. I. Tkachev, "Relativistic turbulence: A Long way from preheating to equilibrium", Phys. Rev. Lett. **90**, 121301 (2003), arXiv:hep-ph/0210202.

[31] R. Micha and I. I. Tkachev, "Turbulent thermalization", Phys. Rev. D **70**, 043538 (2004), arXiv:hep-ph/0403101.

[32] I. Bloch, J. Dalibard, and S. Nascimbene, "Quantum simulations with ultracold quantum gases", Nature Physics **8**, 267–276 (2012).

[33] C. Gross and I. Bloch, "Quantum simulations with ultracold atoms in optical lattices", Science **357**, 995–1001 (2017).

[34] M. Rigol, V. Dunjko, and M. Olshanii, "Thermalization and its mechanism for generic isolated quantum systems", Nature **452**, 854–858 (2008), arXiv:0708.1324.

[35] N. Navon, A. L. Gaunt, R. P. Smith, and Z. Hadzibabic, "Critical dynamics of spontaneous symmetry breaking in a homogeneous bose gas", Science **347**, 167–170 (2015).

[36] L. E. Sadler, J. M. Higbie, S. R. Leslie, M. Vengalattore, and D. M. Stamper-Kurn, "Spontaneous symmetry breaking in a quenched ferromagnetic spinor Bose–Einstein condensate", Nature **443**, 312–315 (2006).

[37] M. Greiner, O. Mandel, T. Esslinger, T. W. Hänsch, and I. Bloch, "Quantum phase transition from a superfluid to a Mott insulator in a gas of ultracold atoms", Nature **415**, 39–44 (2002).

[38] T. Langen, T. Gasenzer, and J. Schmiedmayer, "Prethermalization and universal dynamics in near-integrable quantum systems", J. Stat. Mech. **1606**, 064009 (2016), arXiv:1603.09385 [cond-mat.quant-gas].

[39] K. Aamodt et al. (ALICE), "Elliptic flow of charged particles in Pb-Pb collisions at 2.76 TeV", Phys. Rev. Lett. **105**, 252302 (2010), arXiv:1011.3914 [nucl-ex].

[40] J. Adams et al. (STAR), "Experimental and theoretical challenges in the search for the quark gluon plasma: The STAR Collaboration's critical assessment of the evidence from RHIC collisions", Nucl. Phys. A **757**, 102–183 (2005), arXiv:nucl-ex/0501009.

[41] S. Chatrchyan et al. (CMS), "Multiplicity and Transverse Momentum Dependence of Two- and Four-Particle Correlations in pPb and PbPb Collisions", Phys. Lett. B **724**, 213–240 (2013), arXiv:1305.0609 [nucl-ex].

[42] J. Berges, B. Schenke, S. Schlichting, and R. Venugopalan, "Turbulent thermalization process in high-energy heavy-ion collisions", Nucl. Phys. A **931**, edited by P. Braun-Munzinger, B. Friman, and J. Stachel, 348–353 (2014), arXiv:1409.1638 [hep-ph].

[43] A. H. Guth, "The Inflationary Universe: A Possible Solution to the Horizon and Flatness Problems", Phys. Rev. D **23**, edited by L.-Z. Fang and R. Ruffini, 347–356 (1981).

[44] A. D. Linde, "A New Inflationary Universe Scenario: A Possible Solution of the Horizon, Flatness, Homogeneity, Isotropy and Primordial Monopole Problems", Phys. Lett. B **108**, edited by L.-Z. Fang and R. Ruffini, 389–393 (1982).

[45] B. Ryden, *Introduction to cosmology* (Cambridge University Press, 2017).

[46] L. Kofman, A. D. Linde, and A. A. Starobinsky, "Reheating after inflation", Phys. Rev. Lett. **73**, 3195–3198 (1994), arXiv:hep-th/9405187.

[47] L. Kofman, A. D. Linde, and A. A. Starobinsky, "Towards the theory of reheating after inflation", Phys. Rev. D **56**, 3258–3295 (1997), arXiv:hep-ph/9704452.

[48] A. Piñeiro Orioli, K. Boguslavski, and J. Berges, "Universal self-similar dynamics of relativistic and nonrelativistic field theories near nonthermal fixed points", Phys. Rev. D **92**, 025041 (2015), arXiv:1503.02498 [hep-ph].

[49] E. Noether, "Invariant variation problems", Transport theory and statistical physics **1**, 186–207 (1971).

[50] J. C. Ward, "An identity in quantum electrodynamics", Physical Review **78**, 182 (1950).

[51] Y. Takahashi, "On the generalized ward identity", Nuovo Cim. **6**, 371–375 (1957).

[52] J. Taylor, "Ward identities and charge renormalization of the yang-mills field", Nucl. Phys. B **33**, 436–444 (1971).

[53] A. A. Slavnov, "Ward identities in gauge theories", Theor. Math. Phys. **10**, 99–104 (1972).

[54] S. Weinberg, *The quantum theory of fields* (Cambridge University Press, 1995).

[55] A. Altland and B. D. Simons, *Condensed matter field theory*, 2nd ed. (Cambridge University Press, 2010).

[56] F. Ares, S. Murciano, and P. Calabrese, "Entanglement asymmetry as a probe of symmetry breaking", Nature Commun. **14**, 2036 (2023), arXiv:2207.14693.

[57] F. Ares, S. Murciano, L. Piroli, and P. Calabrese, "An entanglement asymmetry study of black hole radiation", arXiv:2311.12683 [hep-th].

[58] L. Rossi, L. Barbiero, J. C. Budich, and F. Dolcini, "Long-time rigidity to flux-induced symmetry breaking in quantum quench dynamics", Phys. Rev. B **108**, 155420 (2023), arXiv:2307.03580 [cond-mat.quant-gas].

[59] A. N. Mikheev, I. Siovitz, and T. Gasenzer, "Universal dynamics and non-thermal fixed points in quantum fluids far from equilibrium", Eur. Phys. J. ST **232**, 3393–3415 (2023), arXiv:2304.12464 [cond-mat.quant-gas].

[60] B. Widom, "Equation of state in the neighborhood of the critical point", The Journal of Chemical Physics **43**, 3898–3905 (1965).

[61] L. P. Kadanoff, "Scaling laws for ising models near t c", Physics Physique Fizika **2**, 263 (1966).

[62] K. G. Wilson, "Renormalization group and critical phenomena. i. renormalization group and the kadanoff scaling picture", Physical review B **4**, 3174 (1971).

[63] K. G. Wilson, "Renormalization group and critical phenomena. ii. phase-space cell analysis of critical behavior", Physical Review B **4**, 3184 (1971).

[64] P. C. Hohenberg and B. I. Halperin, "Theory of Dynamic Critical Phenomena", Rev. Mod. Phys. **49**, 435–479 (1977).

[65] V. E. Zakharov, V. S. L'vov, and G. Falkovich, *Kolmogorov spectra of turbulence I: wave turbulence* (Springer, Berlin, Germany, 2012).

[66] S. Nazarenko, *Wave turbulence*, Vol. 825 (Springer, 2011).

[67] A. J. Bray, "Theory of phase-ordering kinetics", Adv. Phys. **43**, 357 (1994), arXiv:cond-mat/9501089.

[68] P. Calabrese and A. Gambassi, "Ageing properties of critical systems", Journal of Physics A: Mathematical and General **38**, R133–R193 (2005).

[69] A. Chiocchetta, M. Tavora, A. Gambassi, and A. Mitra, "Short-time universal scaling in an isolated quantum system after a quench", Phys. Rev. B **91**, 220302 (2015).

[70] L. M. Sieberer, S. D. Huber, E. Altman, and S. Diehl, "Dynamical critical phenomena in driven-dissipative systems", Physical Review Letters **110**, 10.1103/physrevlett.110.195301 (2013).

[71] A. Polkovnikov, "Phase Space Representation of Quantum Dynamics", Annals Phys. **325**, 1790–1852 (2010), arXiv:0905.3384 [cond-mat.stat-mech].

[72] J. Berges and D. Sexty, "Strong versus weak wave-turbulence in relativistic field theory", Phys. Rev. D **83**, 085004 (2011), arXiv:1012.5944 [hep-ph].

[73] I. Chantesana, A. Piñeiro Orioli, and T. Gasenzer, "Kinetic theory of nonthermal fixed points in a Bose gas", Phys. Rev. A **99**, 043620 (2019), arXiv:1801.09490 [cond-mat.quant-gas].

[74] R. Walz, K. Boguslavski, and J. Berges, "Large-N kinetic theory for highly occupied systems", Phys. Rev. D **97**, 116011 (2018), arXiv:1710.11146 [hep-ph].

[75] J. Berges, K. Boguslavski, S. Schlichting, and R. Venugopalan, "Universality far from equilibrium: From superfluid Bose gases to heavy-ion collisions", Phys. Rev. Lett. **114**, 061601 (2015), arXiv:1408.1670 [hep-ph].

[76] J. Berges, K. Boguslavski, M. Mace, and J. M. Pawlowski, "Gauge-invariant condensation in the nonequilibrium quark-gluon plasma", Phys. Rev. D **102**, 034014 (2020), arXiv:1909.06147 [hep-ph].

[77] B. Nowak, D. Sexty, and T. Gasenzer, "Superfluid turbulence: nonthermal fixed point in an ultracold bose gas", Phys. Rev. B **84**, 020506 (2011), arXiv:1012.4437 [cond-mat.quant-gas].

[78] J. Schole, B. Nowak, and T. Gasenzer, "Critical Dynamics of a Two-dimensional Superfluid near a Non-Thermal Fixed Point", Phys. Rev. A **86**, 013624 (2012), arXiv:1204.2487 [cond-mat.quant-gas].

[79] M. Karl and T. Gasenzer, "Strongly anomalous non-thermal fixed point in a quenched two-dimensional Bose gas", New J. Phys. **19**, 093014 (2017), arXiv:1611.01163 [cond-mat.quant-gas].

[80] G. D. Moore, "Condensates in Relativistic Scalar Theories", Phys. Rev. D **93**, 065043 (2016), arXiv:1511.00697 [hep-ph].

[81] A. Piñeiro Orioli and J. Berges, "Breaking the fluctuation-dissipation relation by universal transport processes", Phys. Rev. Lett. **122**, 150401 (2019), arXiv:1810.12392 [cond-mat.quant-gas].

[82] K. Boguslavski and A. Piñeiro Orioli, "Unraveling the nature of universal dynamics in $O(N)$ theories", Phys. Rev. D **101**, 091902 (2020), arXiv:1911.04506 [hep-ph].

[83] N. Otter, M. A. Porter, U. Tillmann, P. Grindrod, and H. A. Harrington, "A roadmap for the computation of persistent homology", EPJ Data Sci. **6**, 1–38 (2017), arXiv:1506.08903 [math.AT].

[84] F. Chazal and B. Michel, "An introduction to topological data analysis: fundamental and practical aspects for data scientists", Front. Artif. Intell. Appl. **4**, https://doi.org/10.3389/frai.2021.667963 (2021), arXiv:1710.04019 [math].

[85] D. Cohen-Steiner, H. Edelsbrunner, and J. Harer, "Stability of persistence diagrams", Discrete Comput. Geom. **37**, 103–120 (2007).

[86] D. Spitz and A. Wienhard, "The self-similar evolution of stationary point processes via persistent homology", (2020), arXiv:2012.05751 [math.PR].

[87] J. Berges, "Nonequilibrium Quantum Fields: From Cold Atoms to Cosmology", (2015), arXiv:1503.02907 [hep-ph].

[88] J. Schwinger, "Brownian motion of a quantum oscillator", Journal of Mathematical Physics **2**, 407–432 (1961).

[89] L. V. Keldysh, "Diagram technique for nonequilibrium processes", Zh. Eksp. Teor. Fiz **47**, 151–165 (1964).

[90] L. P. Kadanoff, *Quantum statistical mechanics* (CRC Press, 2018).

[91] S. Y. Khlebnikov and I. I. Tkachev, "Classical decay of the inflaton", Physical Review Letters **77**, 219 (1996).

[92] F. Ihssen, J. M. Pawlowski, F. R. Sattler, and N. Wink, "Toward quantitative precision for QCD at large densities", Phys. Rev. D **111**, 036030 (2025), arXiv:2309.07335 [hep-th].

[93] F. Ihssen, J. M. Pawlowski, F. R. Sattler, and N. Wink, "Towards quantitative precision in functional QCD I", (2024), arXiv:2408.08413 [hep-ph].

[94] M. A. Amin, M. P. Hertzberg, D. I. Kaiser, and J. Karouby, "Nonperturbative Dynamics Of Reheating After Inflation: A Review", Int. J. Mod. Phys. D **24**, 1530003 (2014), arXiv:1410.3808 [hep-ph].

[95] T. V. Zache, T. Schweigler, S. Erne, J. Schmiedmayer, and J. Berges, "Extracting the field theory description of a quantum many-body system from experimental data", Phys. Rev. X **10**, 011020 (2020), arXiv:1909.12815 [cond-mat.quant-gas].

[96] M. Prüfer, T. V. Zache, P. Kunkel, S. Lannig, A. Bonnin, H. Strobel, J. Berges, and M. K. Oberthaler, "Experimental extraction of the quantum effective action for a non-equilibrium many-body system", Nature Phys. **16**, 1012–1016 (2020), arXiv:1909.05120 [cond-mat.quant-gas].

[97] R. Ott, T. V. Zache, M. Prüfer, S. Erne, M. Tajik, H. Pichler, J. Schmiedmayer, and P. Zoller, "Hamiltonian Learning in Quantum Field Theories", arXiv:2401.01308 [cond-mat.quant-gas].

[98] F. Ares, S. Murciano, E. Vernier, and P. Calabrese, "Lack of symmetry restoration after a quantum quench: An entanglement asymmetry study", SciPost Phys. **15**, 089 (2023), arXiv:2302.03330 [cond-mat.stat-mech].

[99] A. J. Beekman, L. Rademaker, and J. van Wezel, "An Introduction to Spontaneous Symmetry Breaking", SciPost Phys. Lect. Notes **11**, 1 (2019), arXiv:1909.01820 [hep-th].

[100] E. P. Wigner, *Group Theory and its Application to the Quantum Mechanics of Atomic Spectra* (Academic Press, 1959).

[101] G. Chiribella, E. Aurell, and K. Życzkowski, "Symmetries of quantum evolutions", Phys. Rev. Res. **3**, 033028 (2021), arXiv:2101.04962 [quant-ph].

[102] P. Kunkel, M. Prüfer, S. Lannig, R. Rosa-Medina, A. Bonnin, M. Gärttner, H. Strobel, and M. K. Oberthaler, "Simultaneous readout of noncommuting collective spin observables beyond the standard quantum limit", Phys. Rev. Lett. **123**, 063603 (2019).

[103] N. D. Mermin and H. Wagner, "Absence of ferromagnetism or antiferromagnetism in one-or two-dimensional isotropic heisenberg models", Physical Review Letters **17**, 1133 (1966).

[104] M. Prüfer, D. Spitz, S. Lannig, H. Strobel, J. Berges, and M. K. Oberthaler, "Condensation and thermalization of an easy-plane ferromagnet in a spinor Bose gas", Nature Phys. **18**, 1459–1463 (2022), arXiv:2205.06188 [cond-mat.quant-gas].

[105] A. N. Mikheev, C.-M. Schmied, and T. Gasenzer, "Low-energy effective theory of nonthermal fixed points in a multicomponent Bose gas", Phys. Rev. A **99**, 063622 (2019), arXiv:1807.10228 [cond-mat.quant-gas].

[106] B. Bertini, K. Klobas, M. Collura, P. Calabrese, and C. Rylands, "Dynamics of charge fluctuations from asymmetric initial states", Phys. Rev. B **109**, 184312 (2024), arXiv:2306.12404 [cond-mat.stat-mech].

[107] L. Capizzi and V. Vitale, "A universal formula for the entanglement asymmetry of matrix product states", arXiv:2310.01962 [quant-ph].

[108] F. Ferro, F. Ares, and P. Calabrese, "Non-equilibrium entanglement asymmetry for discrete groups: the example of the XY spin chain", J. Stat. Mech. **2402**, 023101 (2024), arXiv:2307.06902 [cond-mat.stat-mech].

[109] S. Yamashika, F. Ares, and P. Calabrese, "Time evolution of entanglement entropy after quenches in two-dimensional free fermion systems: A dimensional reduction treatment", Phys. Rev. B **109**, 125122 (2024), arXiv:2310.18160 [cond-mat.stat-mech].

[110] S. Liu, H.-K. Zhang, S. Yin, and S.-X. Zhang, "Symmetry restoration and quantum Mpemba effect in symmetric random circuits", arXiv:2403.08459 [quant-ph].

[111] D. J. Strachan, A. Purkayastha, and S. R. Clark, "Non-Markovian Quantum Mpemba effect", arXiv:2402.05756 [quant-ph].

[112] L. K. Joshi et al., "Observing the Quantum Mpemba Effect in Quantum Simulations", Phys. Rev. Lett. **133**, 010402 (2024), arXiv:2401.04270 [quant-ph].

[113] J. Zhang, G. Xia, C.-W. Wu, T. Chen, Q. Zhang, Y. Xie, W.-B. Su, W. Wu, C.-W. Qiu, P.-x. Chen, W. Li, H. Jing, and Y.-L. Zhou, "Observation of quantum strong Mpemba effect", arXiv:2401.15951 [quant-ph].

[114] S. Aharony Shapira, Y. Shapira, J. Markov, G. Teza, N. Akerman, O. Raz, and R. Ozeri, "Inverse Mpemba Effect Demonstrated on a Single Trapped Ion Qubit", Phys. Rev. Lett. **133**, 010403 (2024), arXiv:2401.05830 [quant-ph].

[115] C. Scheppach, J. Berges, and T. Gasenzer, "Matter Wave Turbulence: Beyond Kinetic Scaling", Phys. Rev. A **81**, 033611 (2010), arXiv:0912.4183 [cond-mat.quant-gas].

[116] B. Nowak, J. Schole, D. Sexty, and T. Gasenzer, "Nonthermal fixed points, vortex statistics, and superfluid turbulence in an ultracold Bose gas", Phys. Rev. A **85**, 043627 (2012), arXiv:1111.6127 [cond-mat.quant-gas].

[117] S. P. Johnstone, A. J. Groszek, P. T. Starkey, C. J. Billington, T. P. Simula, and K. Helmerson, "Evolution of large-scale flow from turbulence in a two-dimensional superfluid", Science **364**, 1267–1271 (2019), arXiv:1801.06952v2 [cond-mat.quant-gas].

[118] G. Martirosyan, M. Gazo, J. Etrych, S. M. Fischer, S. J. Morris, C. J. Ho, C. Eigen, and Z. Hadzibabic, "A universal speed limit for spreading of quantum coherence", (2024), arXiv:2410.08204 [cond-mat.quant-gas].

[119] T. Gasenzer, B. Nowak, and D. Sexty, "Charge separation in Reheating after Cosmological Inflation", Phys. Lett. B **710**, 500–503 (2012), arXiv:1108.0541 [hep-ph].

[120] T. Gasenzer, L. McLerran, J. M. Pawlowski, and D. Sexty, "Gauge turbulence, topological defect dynamics, and condensation in Higgs models", Nucl. Phys. A **930**, 163 (2014), arXiv:1307.5301 [hep-ph].

[121] C. Ewerz, T. Gasenzer, M. Karl, and A. Samberg, "Non-Thermal Fixed Point in a Holographic Superfluid", JHEP **05**, 070 (2015), arXiv:1410.3472 [hep-th].

[122] J. Berges, K. Boguslavski, S. Schlichting, and R. Venugopalan, "Nonequilibrium fixed points in longitudinally expanding scalar theories: infrared cascade, Bose condensation and a challenge for kinetic theory", Phys. Rev. D **92**, 096006 (2015), arXiv:1508.03073 [hep-ph].

[123] J. Berges and B. Wallisch, "Nonthermal Fixed Points in Quantum Field Theory Beyond the Weak-Coupling Limit", Phys. Rev. D **95**, 036016 (2017), arXiv:1607.02160 [hep-ph].

[124] J. Berges, K. Boguslavski, A. Chatrchyan, and J. Jaeckel, "Attractive versus repulsive interactions in the Bose-Einstein condensation dynamics of relativistic field theories", Phys. Rev. D **96**, 076020 (2017), arXiv:1707.07696 [hep-ph].

[125] J. Deng, S. Schlichting, R. Venugopalan, and Q. Wang, "Off-equilibrium infrared structure of self-interacting scalar fields: Universal scaling, Vortex-antivortex superfluid dynamics and Bose-Einstein condensation", Phys. Rev. A **97**, 053606 (2018), arXiv:1801.06260 [hep-th].

[126] C.-M. Schmied, A. N. Mikheev, and T. Gasenzer, "Prescaling in a far-from-equilibrium Bose gas", Phys. Rev. Lett. **122**, 170404 (2019), arXiv:1807.07514.

[127] C.-M. Schmied, M. Prüfer, M. K. Oberthaler, and T. Gasenzer, "Bidirectional universal dynamics in a spinor Bose gas close to a nonthermal fixed point", Phys. Rev. A **99**, 033611 (2019), arXiv:1812.08571 [cond-mat.quant-gas].

[128] C. .-. Schmied, T. Gasenzer, and P. B. Blakie, "Violation of single-length scaling dynamics via spin vortices in an isolated spin-1 Bose gas", Phys. Rev. A **100**, 033603 (2019), arXiv:1904.13222 [cond-mat.quant-gas].

[129] L. Gresista, T. V. Zache, and J. Berges, "Dimensional crossover for universal scaling far from equilibrium", Phys. Rev. A **105**, 013320 (2022), arXiv:2107.11749 [cond-mat.quant-gas].

[130] A. N. Mikheev, A. Mazeliauskas, and J. Berges, "Stability analysis of nonthermal fixed points in longitudinally expanding kinetic theory", Phys. Rev. D **105**, 116025 (2022), arXiv:2203.02299 [hep-ph].

[131] I. Siovitz, A.-M. E. Glück, Y. Deller, A. Schmutz, F. Klein, H. Strobel, M. K. Oberthaler, and T. Gasenzer, "Double sine-Gordon class of universal coarsening dynamics in a spin-1 Bose gas", (2024), arXiv:2412.13986 [cond-mat.quant-gas].

[132] M. Karl, B. Nowak, and T. Gasenzer, "Universal scaling at nonthermal fixed points of a two-component Bose gas", Phys. Rev. A **88**, 063615 (2013), arXiv:1307.7368 [cond-mat.quant-gas].

[133] I. Siovitz, S. Lannig, Y. Deller, H. Strobel, M. K. Oberthaler, and T. Gasenzer, "Universal Dynamics of Rogue Waves in a Quenched Spinor Bose Condensate", Phys. Rev. Lett. **131**, 183402 (2023), arXiv:2304.09293 [cond-mat.quant-gas].

[134] P. Heinen, A. N. Mikheev, and T. Gasenzer, "Anomalous scaling at nonthermal fixed points of the sine-Gordon model", Phys. Rev. A **107**, 043303 (2023), arXiv:2212.01163 [cond-mat.quant-gas].

[135] D. Spitz, J. Berges, M. Oberthaler, and A. Wienhard, "Finding self-similar behavior in quantum many-body dynamics via persistent homology", SciPost Physics **11**, 060 (2021).

[136] L. Shen and J. Berges, "Spectral, statistical and vertex functions in scalar quantum field theory far from equilibrium", Phys. Rev. D **101**, 056009 (2020), arXiv:1912.07565 [hep-ph].

[137] W. Thomson (Lord Kelvin), "3. vibrations of a columnar vortex", Proceedings of the Royal Society of Edinburgh **10**, 443–456 (1880).

[138] L. P. Pitaevskii, "Vortex lines in an imperfect Bose gas", [Zh. Eksp. Teor. Fiz. 40, 646 (1961)] Sov. Phys. JETP **13**, 451 (1961).

[139] E. Gross, "Structure of a quantized vortex in boson systems", Il Nuovo Cimento **20**, 454–477 (1961).

[140] R. J. Donnelly, *Quantized vortices in liquid He II*, Cambridge Studies in Low Temperature Physics (CUP, Cambridge, UK, 2005).

[141] W. Vinen, "Decay of superfluid turbulence at a very low temperature: the radiation of sound from a kelvin wave on a quantized vortex", Phys. Rev. B **64**, 134520 (2001).

[142] W. Vinen, M. Tsubota, and A. Mitani, "Kelvin-wave cascade on a vortex in superfluid h e 4 at a very low temperature", Phys. Rev. Lett. **91**, 135301 (2003), arXiv:cond-mat/0306191.

[143] E. Kozik and B. Svistunov, "Kelvin-wave cascade and decay of superfluid turbulence", Phys. Rev. Lett. **92**, 035301 (2004), arXiv:cond-mat/0308193.

[144] E. Kozik and B. Svistunov, "Vortex-phonon interaction", Phys. Rev. B **72**, 172505 (2005), arXiv:cond-mat/0505020.

[145] E. V. Kozik and B. V. Svistunov, "Theory of decay of superfluid turbulence in the low-temperature limit", J. Low Temp. Phys. **156**, 215 (2009), arXiv:0904.1379 [cond-mat.stat-mech].

[146] V. S. L'vov and S. Nazarenko, "Spectrum of kelvin-wave turbulence in superfluids", JETP Letters **91**, 428–434 (2010), arXiv:0911.2065.

[147] J. Laurie, V. S. L'vov, S. Nazarenko, and O. Rudenko, "Interaction of kelvin waves and nonlocality of energy transfer in superfluids", Phys. Rev. B **81**, 104526 (2010).

[148] L. Boué, R. Dasgupta, J. Laurie, V. L'vov, S. Nazarenko, and I. Procaccia, "Exact solution for the energy spectrum of kelvin-wave turbulence in superfluids", Phys. Rev. B **84**, 064516 (2011), arXiv:1103.5967.

[149] L. Boué, V. S. L'vov, Y. Nagar, S. V. Nazarenko, A. Pomyalov, and I. Procaccia, "Energy and vorticity spectra in turbulent superfluid he 4 from t= 0 to t λ", Phys. Rev. B **91**, 144501 (2015), arXiv:1504.00632.

[150] T. Isoshima and K. Machida, "Vortex stabilization in bose-einstein condensate of alkali-metal atom gas", Phys. Rev. A **59**, 2203–2212 (1999).

[151] T. Simula, "Collective dynamics of vortices in trapped bose-einstein condensates", Phys. Rev. A **87**, 023630 (2013), arXiv:1303.0947.

[152] T. Simula, "Vortex mass in a superfluid", Phys. Rev. A **97**, 023609 (2018), arXiv:1704.08410.

[153] K. Boguslavski, A. Kurkela, T. Lappi, and J. Peuron, "Spectral function for overoccupied gluodynamics from real-time lattice simulations", Phys. Rev. D **98**, 014006 (2018), arXiv:1804.01966 [hep-ph].

[154] G. Aarts and J. Berges, "Classical aspects of quantum fields far from equilibrium", Phys. Rev. Lett. **88**, 041603 (2002), arXiv:hep-ph/0107129.

[155] J. Berges, K. Boguslavski, S. Schlichting, and R. Venugopalan, "Basin of attraction for turbulent thermalization and the range of validity of classical-statistical simulations", JHEP **05**, 054 (2014), arXiv:1312.5216 [hep-ph].

[156] K. Boguslavski, A. Kurkela, T. Lappi, and J. Peuron, "Highly occupied gauge theories in 2+1 dimensions: A self-similar attractor", Phys. Rev. D **100**, 094022 (2019), arXiv:1907.05892 [hep-ph].

[157] M. Mace, N. Mueller, S. Schlichting, and S. Sharma, "Chiral Instabilities and the Onset of Chiral Turbulence in QED Plasmas", Phys. Rev. Lett. **124**, 191604 (2020), arXiv:1910.01654 [hep-ph].

[158] J. Hofmann, S. S. Natu, and S. Das Sarma, "Coarsening dynamics of binary bose condensates", Phys. Rev. Lett. **113**, 095702 (2014), arXiv:1403.1284.

[159] A. Schachner, A. Piñeiro Orioli, and J. Berges, "Universal scaling of unequal-time correlation functions in ultracold Bose gases far from equilibrium", Phys. Rev. A **95**, 053605 (2017), arXiv:1612.03038 [cond-mat.quant-gas].

[160] L. A. Williamson and P. B. Blakie, "Universal coarsening dynamics of a quenched ferromagnetic spin-1 condensate", Phys. Rev. Lett. **116**, 025301 (2016), arXiv:1504.06404 [cond-mat.quant-gas].

[161] J. F. Rodriguez-Nieva, A. Piñeiro Orioli, and J. Marino, "Far-from-equilibrium universality in the two-dimensional Heisenberg model", Proc. Nat. Acad. Sci. **119**, e2122599119 (2022), arXiv:2106.00023 [cond-mat.stat-mech].

[162] P. Heinen, A. N. Mikheev, C.-M. Schmied, and T. Gasenzer, "Non-thermal fixed points of universal sine-Gordon coarsening dynamics", (2022), arXiv:2212.01162 [cond-mat.quant-gas].

[163] D. Spitz, K. Boguslavski, and T. Preis, "Condensation and prescaling in spatial Polyakov loop correlations far from equilibrium", (2024), arXiv:2411.05582 [hep-ph].

[164] M. H. Namjoo, A. H. Guth, and D. I. Kaiser, "Relativistic corrections to nonrelativistic effective field theories", Phys. Rev. D **98**, 016011 (2018), arXiv:1712.00445.

[165] C. F. Barenghi, R. J. Donnelly, and W. Vinen, *Quantized vortex dynamics and superfluid turbulence*, Vol. 571 (Springer Science & Business Media, 2001).

[166] P. H. Roberts, "On vortex waves in compressible fluids. i. the hollow-core vortex", Proc. Roy. Soc. Lond. A: Math., Phys. Eng. Sci. **459**, 331–352 (2003).

[167] P. H. Roberts, "On vortex waves in compressible fluids. ii. the condensate vortex", Proc. Roy. Soc. Lond. A: Math., Phys. Eng. Sci. **459**, 597–607 (2003).

[168] D. P. Meichle, C. Rorai, M. E. Fisher, and D. Lathrop, "Quantized vortex reconnection: fixed points and initial conditions", Phys. Rev. B **86**, 014509 (2012).

[169] U. Giuriato, G. Krstulovic, and S. Nazarenko, "How trapped particles interact with and sample superfluid vortex excitations", Phys. Rev. Res. **2**, 023149 (2020).

[170] T. P. Simula, T. Mizushima, and K. Machida, "Kelvin waves of quantized vortex lines in trapped bose-einstein condensates", Phys. Rev. Lett. **101**, 020402 (2008), arXiv:0803.2574.

[171] T. Simula, T. Mizushima, and K. Machida, "Vortex waves in trapped bose-einstein condensates", Phys. Rev. A **78**, 053604 (2008), arXiv:0809.0993.

[172] A. W. Baggaley and J. Laurie, "Kelvin-wave cascade in the vortex filament model", Phys. Rev. B **89**, 014504 (2014), arXiv:1204.4034.

[173] P. Clark Di Leoni, P. D. Mininni, and M. E. Brachet, "Spatiotemporal detection of kelvin waves in quantum turbulence simulations", Phys. Rev. A **92**, 063632 (2015), arXiv:1509.05316.

[174] T. Simula, "Gravitational vortex mass in a superfluid", Phys. Rev. A **101**, 063616 (2020), arXiv:2001.03302.

[175] A. W. Baggaley and C. F. Barenghi, "Decay of homogeneous two-dimensional quantum turbulence", Phys. Rev. A **97**, 033601 (2018), arXiv:1711.07533.

[176] A. J. Groszek, P. Comaron, N. P. Proukakis, and T. P. Billam, "Crossover in the dynamical critical exponent of a quenched two-dimensional bose gas", Phys. Rev. Res. **3**, 013212 (2021).

[177] W. Vinen, "Mutual friction in a heat current in liquid helium II. III. Theory of the mutual friction", Proc. Roy. Soc. Lond. Ser. A: Math. Phys. Sci. **242**, 493 (1957).

[178] A. Villois, D. Proment, and G. Krstulovic, "Evolution of a superfluid vortex filament tangle driven by the gross-pitaevskii equation", Phys. Rev. E **93**, 061103 (2016).

[179] K. Boguslavski, A. Kurkela, T. Lappi, and J. Peuron, "Broad excitations in a 2+1D overoccupied gluon plasma", JHEP **05**, 225 (2021), arXiv:2101.02715 [hep-ph].

[180] A. J. Groszek, T. P. Simula, D. M. Paganin, and K. Helmerson, "Onsager vortex formation in bose-einstein condensates in two-dimensional power-law traps", Phy. Rev. A **93**, 043614 (2016), arXiv:1511.06552.

[181] X. Yu, T. P. Billam, J. Nian, M. T. Reeves, and A. S. Bradley, "Theory of the vortex-clustering transition in a confined two-dimensional quantum fluid", Phys. Rev. A **94**, 023602 (2016), arXiv:1512.05517.

[182] T. Kanai and C. Zhang, "Dynamical transition of quantum vortex-pair annihilation in a bose-einstein condensate", (2024), arXiv:2407.14627.

[183] S. P. Johnstone, A. J. Groszek, P. T. Starkey, C. J. Billington, T. P. Simula, and K. Helmerson, "Evolution of large-scale flow from turbulence in a two-dimensional superfluid", Science **364**, 1267–1271 (2019), arXiv:1801.06952.

[184] D. Spitz, J. Berges, M. K. Oberthaler, and A. Wienhard, "Finding self-similar behavior in quantum many-body dynamics via persistent homology", SciPost Phys. **11**, 060 (2021), arXiv:2001.02616 [cond-mat.quant-gas].

[185] D. Spitz, K. Boguslavski, and J. Berges, "Probing universal dynamics with topological data analysis in a gluonic plasma", Phys. Rev. D **108**, 056016 (2023), arXiv:2303.08618 [hep-ph].

[186] I. Donato, M. Gori, M. Pettini, G. Petri, S. De Nigris, R. Franzosi, and F. Vaccarino, "Persistent homology analysis of phase transitions", Phys. Rev. E **93**, 052138 (2016), arXiv:1601.03641 [cond-mat.stat-mech].

[187] T. Hirakida, K. Kashiwa, J. Sugano, J. Takahashi, H. Kouno, and M. Yahiro, "Persistent homology analysis of deconfinement transition in effective Polyakov-line model", Int. J. Mod. Phys. A **35**, 2050049 (2020), arXiv:1810.07635 [hep-lat].

[188] L. Speidel, H. A. Harrington, S. J. Chapman, and M. A. Porter, "Topological data analysis of continuum percolation with disks", Phys. Rev. E **98**, 012318 (2018), arXiv:1804.07733 [cond-mat.stat-mech].

[189] F. A. Santos, E. P. Raposo, M. D. Coutinho-Filho, M. Copelli, C. J. Stam, and L. Douw, "Topological phase transitions in functional brain networks", Phys. Rev. E **100**, 032414 (2019).

[190] B. Olsthoorn, J. Hellsvik, and A. V. Balatsky, "Finding hidden order in spin models with persistent homology", Phys. Rev. Res. **2**, 043308 (2020), arXiv:2009.05141 [cond-mat.stat-mech].

[191] N. Sale, J. Giansiracusa, and B. Lucini, "Quantitative analysis of phase transitions in two-dimensional XY models using persistent homology", Phys. Rev. E **105**, 024121 (2022), arXiv:2109.10960 [cond-mat.stat-mech].

[192] Q. H. Tran, M. Chen, and Y. Hasegawa, "Topological persistence machine of phase transitions", Phys. Rev. E **103**, 052127 (2021), arXiv:2004.03169 [cond-mat.stat-mech].

[193] A. Cole, G. J. Loges, and G. Shiu, "Quantitative and interpretable order parameters for phase transitions from persistent homology", Phys. Rev. B **104**, 104426 (2021), arXiv:2009.14231 [cond-mat.stat-mech].

[194] K. Kashiwa, T. Hirakida, and H. Kouno, "Persistent Homology Analysis for Dense QCD Effective Model with Heavy Quarks", Symmetry **14**, 1783 (2022), arXiv:2103.12554 [hep-lat].

[195] D. Sehayek and R. G. Melko, "Persistent homology of Z2 gauge theories", Phys. Rev. B **106**, 085111 (2022), arXiv:2201.09856 [cond-mat.stat-mech].

[196] N. Sale, B. Lucini, and J. Giansiracusa, "Probing center vortices and deconfinement in SU(2) lattice gauge theory with persistent homology", Phys. Rev. D **107**, 034501 (2023), arXiv:2207.13392 [hep-lat].

[197] D. Spitz, J. M. Urban, and J. M. Pawlowski, "Confinement in non-Abelian lattice gauge theory via persistent homology", Phys. Rev. D **107**, 034506 (2023), arXiv:2208.03955 [hep-lat].

[198] Y. Hiraoka, T. Shirai, and K. D. Trinh, "Limit theorems for persistence diagrams", Ann. Appl. Prob. **28**, 2740–2780 (2018), arXiv:1612.08371 [math.PR].

[199] J. Berges and D. Sexty, "Bose condensation far from equilibrium", Phys. Rev. Lett. **108**, 161601 (2012), arXiv:1201.0687 [hep-ph].

[200] H. Wagner, C. Chen, and E. Vuçini, "Efficient computation of persistent homology for cubical data", in *Topological methods in data analysis and visualization ii* (Springer, 2012), pp. 91–106.

[201] C. Maria, J.-D. Boissonnat, M. Glisse, and M. Yvinec, "The gudhi library: simplicial complexes and persistent homology", in International congress on mathematical software (Springer, 2014), pp. 167–174.

[202] K. Fujimoto, R. Hamazaki, and M. Ueda, "Flemish strings of magnetic solitons and a nonthermal fixed point in a one-dimensional antiferromagnetic spin-1 bose gas", Phys. Rev. Lett. **122**, 173001 (2019), arXiv:1812.03581 [cond-mat.quant-gas].

[203] M. T. Wheeler, H. Salman, and M. O. Borgh, "Relaxation dynamics of half-quantum vortices in a two-dimensional two-component bose-einstein condensate (a)", Europhys. Lett. **135**, 30004 (2021), arXiv:2110.02671 [cond-mat.quant-gas].

[204] D. Leykam, I. Rondon, and D. G. Angelakis, "Dark soliton detection using persistent homology", Chaos **32**, 073133 (2022), arXiv:2107.14594 [physics.atom-ph].

[205] K.-c. Chou, Z.-b. Su, B.-l. Hao, and L. Yu, "Equilibrium and Nonequilibrium Formalisms Made Unified", Phys. Rept. **118**, 1–131 (1985).

[206] P. Uhrich, S. Castrignano, H. Uys, and M. Kastner, "Noninvasive measurement of dynamic correlation functions", Phys. Rev. A **96**, 022127 (2017), arXiv:1611.08123 [quant-ph].

[207] R. D. Pisarski and F. Wilczek, "Remarks on the Chiral Phase Transition in Chromodynamics", Phys. Rev. D **29**, 338–341 (1984).

[208] A. Griffin, D. W. Snoke, and S. Stringari, *Bose-einstein condensation* (Cambridge University Press, 1996).

[209] H. E. Stanley, *Phase transitions and critical phenomena*, Vol. 7 (Clarendon Press, Oxford, 1971).

[210] P.-G. De Gennes, *Introduction to polymer dynamics* (CUP Archive, 1990).

[211] M. Alford, J. Berges, and J. M. Cheyne, "Critical phenomena from the two particle irreducible 1/N expansion", Phys. Rev. D **70**, 125002 (2004), arXiv:hep-ph/0404059.

[212] J. Berges, "Controlled nonperturbative dynamics of quantum fields out-of-equilibrium", Nucl. Phys. A **699**, 847–886 (2002), arXiv:hep-ph/0105311.

[213] G. Aarts, D. Ahrensmeier, R. Baier, J. Berges, and J. Serreau, "Far from equilibrium dynamics with broken symmetries from the 2PI - 1/N expansion", Phys. Rev. D **66**, 045008 (2002), arXiv:hep-ph/0201308.

[214] A. Pelissetto and E. Vicari, "Critical phenomena and renormalization-group theory", Physics Reports **368**, 549–727 (2002).

[215] J. Berges and D. Mesterhazy, "Introduction to the nonequilibrium functional renormalization group", Nucl. Phys. B Proc. Suppl. **228**, edited by B. .-. Schaefer, R. Alkofer, and C. S. Fischer, 37–60 (2012), arXiv:1204.1489 [hep-ph].

[216] S. Mathey, T. Gasenzer, and J. M. Pawlowski, "Anomalous scaling at nonthermal fixed points of Burgers' and Gross-Pitaevskii turbulence", Phys. Rev. A **92**, 023635 (2015), arXiv:1405.7652 [cond-mat.quant-gas].

[217] L. Corell, A. K. Cyrol, M. Heller, and J. M. Pawlowski, "Flowing with the temporal renormalization group", Phys. Rev. D **104**, 025005 (2021), arXiv:1910.09369 [hep-th].

[218] T. Gasenzer, S. Kessler, and J. M. Pawlowski, "Far-from-equilibrium quantum many-body dynamics", Eur. Phys. J. C **70**, 423–443 (2010), arXiv:1003.4163.

[219] T. Gasenzer and J. M. Pawlowski, "Towards far-from-equilibrium quantum field dynamics: A functional renormalisation-group approach", Phys. Lett. B **670**, 135–140 (2008), arXiv:0710.4627 [cond-mat.other].

[220] A. N. Mikheev, "Far-from-equilibrium universal scaling dynamics in ultracold atomic systems and heavy-ion collisions", PhD thesis (Heidelberg University Library, Heidelberg U., Heidelberg University, Jan. 2023).

[221] K. Domino, P. Gawron, and Ł. Pawela, "Efficient computation of higher order cumulant tensors", SIAM J. Sci. Comput. **40**, A1590–A1610 (2018), arXiv:1701.05420 [cs.NA].

[222] N. Turok, "Global Texture as the Origin of Cosmic Structure", Phys. Rev. Lett. **63**, 2625 (1989).

[223] A. Hatcher, *Algebraic topology* (Cambridge University Press, Cambridge, United Kingdom, 2002).